Exploring Condensed Phase Equilibrium Dynamics via Ultrafast Two-Dimensional Infrared Spectroscopy

by

Jessica M. Anna

A dissertation submitted in partial fulfillment
of the requirements for the degree of
Doctor of Philosophy
(Chemistry)
in The University of Michigan
2011

Doctoral Committee:

Assistant Professor Kevin J. Kubarych, Chair
Professor Eitan Geva
Professor Raoul Kopelman
Professor Roseanne J. Sension
Assistant Professor Jennifer P. Ogilvie

To Patrick

Acknowledgements

I am immensely thankful for the mentorship and encouragement of my advisor, Kevin Kubarych. Without his guidance, patience, insights, and dedication, this work would not have been possible.

I am grateful to both former and current group members for their suggestions and guidance. Specifically, I would like to thank Dr. Matthew Nee who introduced me to the experimental setup, and Dr. Carlos Baiz and Dr. Robert McCanne for stimulating discussions and invaluable suggestions.

I would also like to thank my committee members, Professor Eitan Geva, Professor Raoul Kopelman, Professor Kevin Kubarych, Professor Jennifer Ogilvie, and Professor Roseanne Sension for taking the time to serve on my committee.

I am greatly appreciative to my parents, Dan and Karen, and siblings, Brittany and Danny, for their encouragement and support.

Finally, I would like to thank Patrick for his unconditional love and encouragement. Without his support, this experience would not have been possible.

Table of Contents

List of Figures

List of Tables

Abstract

Understanding condensed phase equilibrium dynamics is essential to describing and predicting chemical reactions and their outcomes. To gain insight into equilibrium dynamics, ultrafast two-dimensional infrared (2DIR) spectroscopy is applied to metal carbonyl systems in order to observe two dynamic equilibrium processes: picosecond isomerization and intramolecular vibrational energy transfer.

The picosecond isomerization between two of the different isomers of a fluxional metal carbonyl complex, dicobalt octacarbonyl, is characterized using 2DIR spectroscopy. The isomerization times are extracted from the congested spectra using the well characterized coherent modulation –a signature of non-exchanging signals – to isolate the exchange contribution to the signal. From temperature dependent 2DIR spectra, the temperature dependent rate constants are extracted. Analysis of the temperature dependent rate constants through the Arrhenius and Eyring equations enables the extraction of both the activation energy and the entropic contribution associated with the barrier crossing process.

Using this well characterized reaction as a probe, the solvent's influence on a barrier crossing process is systematically investigated. It was found that for a series of linear alkanes, the potential energy surface does not change as a function of the solvent, indicating that any changes in solvent-dependent rate constants are solely due to the dynamic solvent effect. Through a combination of linear FT-IR measurements and quantum and classical computations, the static and dynamic contributions to the rate constant are separated, enabling the first direct test of Kramers theory in the time domain on a picosecond reaction occurring on the ground electronic state. The

experimental data show agreement with a simple Markovian Kramers theory for the isomerization rate constant's dependence on solvent viscosity.

Intramolecular vibrational energy redistribution (IVR) in two metal complexes, $(Cp)_2Fe_2(CO)_4$ and its ruthenium analog, $(Cp)_2Ru_2(CO)_4$, is also studied via 2DIR spectroscopy. The equilibrium energy transfer dynamics between different vibrational modes of the *cis*-B $(Cp)_2Fe_2(CO)_4$ and the *gauche*-NB $(Cp)_2Ru_2(CO)_4$ isomers is observed. Treating the energy transfer as an equilibrium process, rate constants associated with both the uphill and downhill transfer of vibrational energy are obtained. It was found that the difference in the rate constants maps to the difference in the energy gap between the two modes involved in IVR.

Chapter 1

Introduction

1.1 Equilibrium Dynamics

Most reactions of interest in chemistry and biology occur in the solution phase, making the study of condensed phase chemical reactions and dynamics a prevailing topic throughout the scientific community. For example, in the absence of strong coupling to the environment, the rate of a reaction can be solely predicted from static energetic parameters.[1] However, in solution the dynamic nature of the solvent may influence the barrier crossing process.[2-5] Specifically, the solvent dynamics dictate the rate of a chemical reaction with the frictional forces of the solvent leading to barrier recrossings. Barrier crossings are not the only processes affected by the solvent; many other processes may also be influenced by the solvent, including energy transfer processes[5, 6], both intramolecular and intermolecular; photochemical reactions[7, 8]; electron and proton transfer[9-11]; charge transfer reactions[12, 13]; and protein conformational changes[14-16]. Understanding the dynamic role the solvent plays in these processes will ultimately lead to predictions of condensed phase reaction dynamics.

This thesis focuses on the study of condensed phase equilibrium dynamics. By applying two-dimensional infrared (2DIR) spectroscopy to fluxional metal carbonyl systems, we are able to directly observe equilibrium isomerization between different species and systematically investigate the dynamic influence of the solvent on a barrier crossing process occurring on the ground electronic state. Along with

investigating a barrier crossing process, we also explore energy transfer between different vibrational modes in an iron metal carbonyl complex and its ruthenium analog.

1.2 Infrared Spectroscopy

Molecular dynamics simulations can be used to predict equilibrium dynamics in the condensed phase, where the motion of the solute and solvent atoms are recorded as a function of time.[17] Experimentally probing molecular dynamics requires a technique that has both high spatial and time resolution. Nuclear motions occur on the picosecond timescale, making infrared spectroscopy, where transitions have periods on the 10s of femtoseconds timescale, an ideal candidate for monitoring nuclear motions.[18] Another benefit associated with infrared spectroscopy arises from the fact that specific groups of nuclei have distinct vibrational features that are sensitive to the solvent environment, whether the solvent be a hydrogen bonding liquid or a complex protein.[19-21] These aspects make vibrational probes ideal for exploring solvent dynamics.

1.3 Linear Versus Two-Dimensional Infrared Spectroscopy

Using vibrational transitions as reporters for equilibrium dynamics results in a probe with high intrinsic time resolution that is sensitive to its surroundings. In infrared spectra, much of the dynamic information is manifested in the lineshapes of the peaks. There is no inherent reason why linear IR spectra cannot be used to obtain dynamic information; however, extracting this information is not generally possible without recourse to models, an approach that essentially relies on circular reasoning.

The linear spectrum can be thought of as an ensemble average, and though dynamic information is contained in the lineshapes of the peaks in the spectra, the different contributions to the lineshapes cannot be assigned unambiguously.[22, 23] Specifically, in linear spectra homogeneous and inhomogeneous line broadening mechanisms cannot be distinguished.[24, 25] In the condensed phase, the solute is

interacting with the solvent bath, and system-bath interactions can lead to fluctuations in the energy gap between the ground and excited states. When the energy gap fluctuations are very rapid the system is said to be homogeneously broadened (Fig. 1.1a). An inhomogeneously broadened peak is a result of different microscopic solvent environments; the energy gap fluctuations are slow compared to the experimentally probed timescale resulting in distinct local environments (Fig. 1.1b). Fig. 1.1 compares two cartoon linear spectra that are homogeneously and inhomogeneously broadened. There is no obvious difference between the two line lineshapes in the linear spectrum. Two-dimensional spectroscopy spreads information contained in a linear spectrum over two frequency axes, effectively creating a frequency-frequency correlation map, separating homogeneous and inhomogeneous

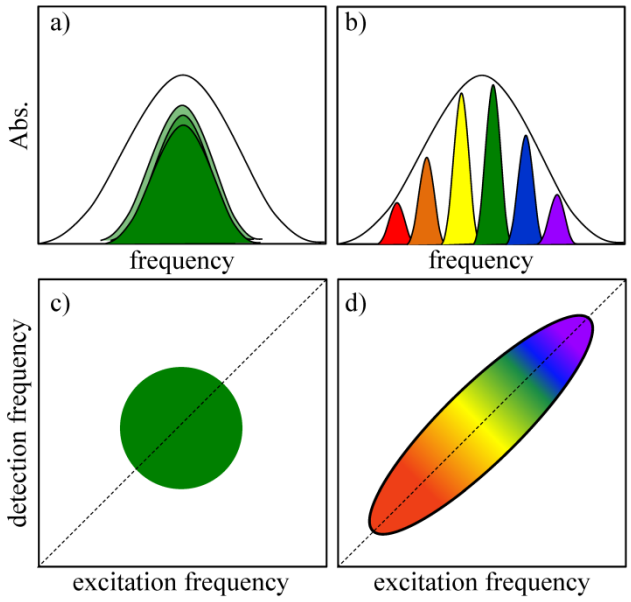

Figure 1.1. Linear spectra of a homogeneously broadened peak (a) and inhomogeneously broadened peak (b). Two dimensional spectra of a homogeneously broadened peak (c) and inhomogeneously broadened peak (d).

broadening.[26, 27] Figure 1.1c-d displays the corresponding 2D spectra. An inhomogeneous broadened peak (Fig. 1.1d) will be elongated along the diagonal, indicating a correlation between excitation and detection frequencies, while a homogeneous broadened peak will be symmetric about the diagonal (Fig. 1.1c). It is

important to note that these are limiting cases, and in general most real molecular systems will lie somewhere between the two extremes.

Obtaining a two-dimensional spectrum requires measuring the field emitted by the sample following three field matter interactions, as opposed to linear spectroscopy, where the signal results from one field matter interaction.[22] For linear spectroscopy, the incoming laser pulse creates a coherence, which leads to the emission of the signal. In two-dimensional spectroscopy, the first excitation pulse creates a coherence that serves to effectively label each molecule. The arrival of the second pulse creates either a population or an excited state coherence ending the t_1 time period and marking the beginning of the t_2 time period, the waiting time. The system evolves during the waiting time which ends upon the arrival of the third excitation pulse. The third excitation pulse marks the beginning of the t_3 time period by creating another coherence, effectively recording the final state of each molecule labeled during t_1. A Fourier transform along t_1 and t_3 results in the ω_{excite} and ω_{detect} axes. The pulse sequence and time delays are shown in Fig. 1.2. The incoming pulses are on the few to 100 fs timescale allowing for the ultrafast dynamics to be directly probed in the time domain by varying the waiting time t_2. Probing dynamics directly in the time domain avoids complications arising from the extraction of dynamic information from linear spectra in the frequency domain. In linear spectra, this dynamic information is typically extracted by mapping line broadening to dephasing models, which have been shown to not always be reliable.[24, 25]

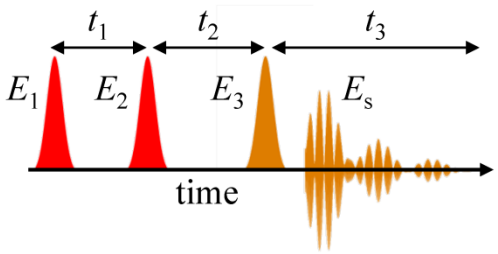

Figure 1.2 Pulse sequence.

So far we have considered how information contained in a linear spectrum is represented in a two-dimensional spectrum; however, the signal leading to the 2D spectrum is a result of the third order nonlinear polarization and contains more information than the signal resulting in the linear spectrum. Linear spectroscopy probes transitions between the ground and first excited state manifold while third order nonlinear optical spectroscopy probes transitions between the first and second excited state manifolds. Two-dimensional infrared spectroscopy, like infrared pump-probe spectroscopy, can be used to observe both ground state bleaches as well as excited state absorptions, where the difference between the two is a measure of the vibrational anharamonicity. In fact, the projection of the 2D spectra on to the ω_{detect} axis is equivalent to the pump-probe spectrum.[28] In comparing the 1D pump-probe spectrum to the 2D spectrum, the second dimension enables the direct observation of coupling between different transitions through the presence of crosspeaks, which is not directly observable from 1D pump-probe spectra.[26, 27]

1.4 Two-Dimensional Spectroscopy

There are two main experimental methods for obtaining 2D optical spectra: a collinear pump-probe geometry, where the signal is emitted along the same direction as the probe beam, and a non-collinear 2D photon echo geometry, where the signal is emitted in a background free direction.[26] Both can be used to obtain 2D spectra.

The first experimental 2DIR spectra were obtained using the collinear pump-probe geometry.[29] A 2D spectrum was constructed by performing a series of dynamic hole burning experiments, where a narrow band pump pulse excited a specific transition and a broad band probe was used for detection. The detection axis, corresponding to ω_{detect} from the previous section 1.3, was obtained experimentally by dispersing the probe pulse. The excitation axis, corresponding to ω_{excite} in section 1.3, was obtained by tuning the frequency of the pump pulse via a Fabry-Perot interferometer. Later, a self-heterodyne pump-probe method of 2DIR spectroscopy

was demonstrated where two broadband pulses were used as the pump and a third pulse was used as a probe, and the ω_1 axis was obtained by scanning t_1 (the time delay between the two pump pulses) in the time domain and performing a Fourier transform to obtain the frequency axis.[30] More recently, the following benefits of using the pump-probe geometry have been demonstrated: the "phasing problem" associated with obtaining absorptive spectra has been avoided[31]; single shot detected IR[32] and electronic 2D spectra[33] have been obtained; phase-cycling has been exploited to suppress certain peaks[34]; pulse-shaping can be used to actively control vibrational populations[35]; and a broadband probe pulse was developed to broaden the spectral range[36].

The non-collinear 2D photon echo method of obtaining 2D spectroscopy was also demonstrated in the late 1990's and early 2000's.[37-40] In the non-collinear setup, a sequence of three ultrafast pulses interacts with the sample where the pulses are arranged in space so that the signal is emitted in a background free direction. Heterodyne detection is used so that both the signal phase and amplitude can be determined. One of the benefits to using the background-free method lies in the ability to isolate different Liouville pathways through phase matching. For example, the rephasing and nonrephasing spectra are obtained separately using the background free method, where for the pump-probe geometry these two different signals are collected simultaneously. Current advances in the background free method of detection include: using a chirped-pulse to upconvert the mid-IR signal to the visible region enabling detection via a CCD camera[41, 42]; the use of polarization dependent pulses to enhance/suppress specific peaks in the spectrum[43, 44]; the use of diffractive optics for phase stabilization required in 2D electronic spectroscopy[45, 46]; and the measurements of the relative phase between pulse pairs needed for "phasing" an absorptive spectrum in the non-collinear geometry.[47, 48]

The use of multidimensional optical spectroscopy, whether obtained via the background-free geometry or the pump-probe geometry, has been established in the

study of molecular systems in the condensed phase.[26, 49-57] In the next sections we focus on a few examples of 2DIR spectroscopy. First, we highlight the ability of 2DIR spectroscopy to aid in assigning linear spectra and determine structure. We next focus on examples of using 2DIR spectroscopy to study equilibrium dynamics, such as vibrational energy redistribution, spectral diffusion and chemical exchange. We then briefly discuss non-equilibrium 2DIR spectroscopy and the use of modeling in obtaining a microscopic picture of equilibrium dynamics.

1.4.1 Assignment and Structure

As was previously discussed, linear spectra can be congested, making the unambiguous assignment of the spectral features a challenge. 2D spectroscopy can aid in the assignment of linear spectra. When there are two or more transitions arising from a single molecular species, and these transitions lie within the bandwidth of the incoming laser pulses, there will be crosspeaks between the corresponding diagonal peaks in the 2D spectrum.

To demonstrate this point, consider the cartoon spectra in Fig. 1.3. The linear spectrum consists of two peaks resulting from two different species, A and B, where A has one absorption feature at frequency ω_a and B has two absorptions at $\omega_{b'}$ and $\omega_{b''}$. The linear spectrum consists of two peaks, and there is no indication that the

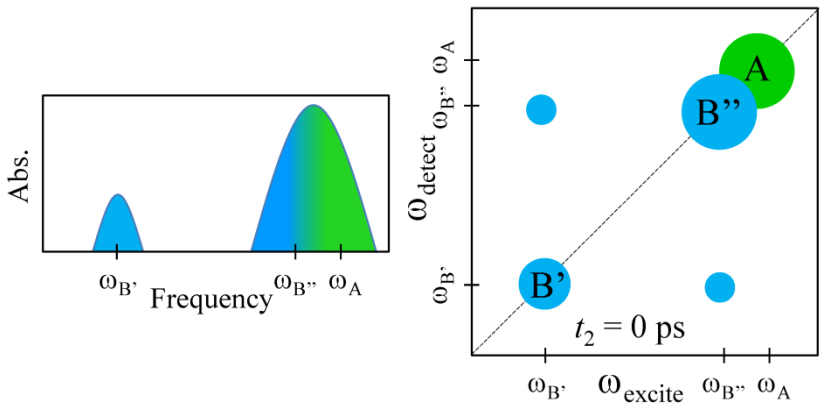

Figure 1.3 The linear spectrum (left) and corresponding 2D spectrum (right) are shown.

higher frequency peak has two contributions from different species. A cartoon 2DIR spectrum is also shown in Fig. 1.3. The peaks lying along the diagonal correspond to those in the linear spectrum. The presence of crosspeaks at t_2=0 ps, excitation immediately followed by detection, indicates that the two transitions have a common ground state and lie within the bandwidth of the excitation and detection pulses. We denote these crosspeaks as "inherent crosspeaks". When there are two or more transitions lying within the bandwidth of the incoming pulse, the first laser pulse will create a coherence between the ground state and one of the states in the first excited state manifold. The second pulse could create either a ground state or an excited state population or an excited state coherence. The inherent crosspeaks arise from pathways that create a ground state population during the waiting time. Because of the creation of the ground state population during t_2, the third incoming pulse creates a coherence between the ground state and any of the transitions lying within the bandwidth of the pulse. This will result in the appearance of a diagonal peak when the second coherence is created between the ground state and the same excited state as the first coherence. A crosspeak results when the second coherence is created between the ground state and a different excited state compared to the first coherence.

In the cartoon spectra at t_2=0 ps there are inherent crosspeaks from the two transitions of species B. The transition frequency of the higher frequency mode can be determined from the ω_{detect} frequency of the crosspeak. In this way the 2DIR spectrum can be used to effectively gain spectral resolution in the sense that the transition frequencies can be determined from the crosspeaks, whereas they could not be determined unambiguously from the linear spectrum.

Asbury *et. al.* first demonstrated the ability of 2DIR spectroscopy to aid in the assignment of linear spectra.[58] They demonstrated this using a mixture of two metal carbonyl complexes, where each metal carbonyl complex has two transitions in the terminal carbonyl region. Four distinct transitions were present in the linear FTIR

spectrum, and without prior knowledge of the sample it was not obvious that there were two different molecular species present. For example, either all four peaks could arise from one molecular species or there could be four distinct species present. They showed, from a single 2DIR spectrum at t_2=0 ps, that from the presence of inherent crosspeaks it was evident that there are two molecular species giving rise to the spectral features. More recently 2DIR spectroscopy was used to confirm the previous assignment of a metal-carbonyl complexes existing as multiple isomeric forms in equilibrium[59-61] and to assign photoproducts to parent structures[62-64], to name a few examples.

Inherent crosspeaks arise because there are multiple transitions lying within the bandwidth of the incoming pulses. However, crosspeaks have also been observed in two-color infrared 2D spectra.[65, 66] These crosspeaks arise because the two vibrations leading to the corresponding diagonal peaks are coupled. From the amplitudes and polarization dependence of the crosspeaks in a 2D spectrum, structural information along with the coupling strength can be obtained. For example the dicarbonyl compound, dicarbonylacetylacetonato rhodium (RDC), has two strongly coupled carbonyl stretching modes in the terminal carbonyl region. Golonzka and Tokmakoff determined the angle between the two transition dipole moments for each carbonyl units from the amplitude of the crosspeaks in the 2D spectra.[67] Information on the structure of small peptides, such as trialanine[68] and acetylproline-NH_2[69], has also been obtained from the crosspeaks in 2DIR spectra.[70] From crosspeaks in relaxation assisted 2DIR spectroscopy, information on bond connectivity and distance measurements can be obtained for larger molecules.[71]

1.4.2 Intramolecular Vibrational Energy Redistribution

The flow of vibrational energy can influence chemical reactions, making the study of vibrational energy redistribution important in determining reaction mechanisms and understanding dynamics.[6, 72] 2DIR spectroscopy can facilitate the observation of intramolecular vibrational energy redistribution. Monitoring the

waiting time dependent amplitude of crosspeaks between two coupled vibrations allows for the time scale of intramolecular vibrational energy redistribution to be determined.

In the gas phase, IVR is a result of anharmonic coupling to lower frequency modes of the solute; in solution, because of the anharmonic coupling to the lower frequency modes of the solvent, the liquid phonon modes, IVR is typically faster.[6] Fig. 1.4 shows a representative energy level diagram for a molecule having two transitions in the terminal carbonyl stretching region, where the transitions are

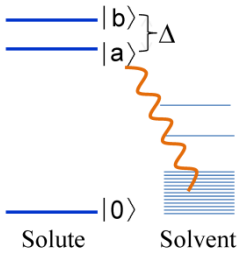

Figure 1.4 Energy level diagram demonstrating IVR process.

separated in frequency by Δ. If Δ is less than 200 cm^{-1} (kT at room temperature) then the low frequency solvent modes, the liquid phonon modes, are significantly populated and act as accepting states. The liquid phonons at Δ can act as accepting states when vibrational energy is transferred from the higher frequency mode to the lower frequency mode, assuring that energy is conserved.

To give a few examples, 2DIR spectroscopy has been used to study intramolecular vibrational energy redistribution (IVR) in metal carbonyl systems.[73-75] It was found that for two different metal carbonyl systems that the solvent's role in the IVR process was different. In one system it was found that the solvent hindered IVR[73] and in another system it was found that the solvent assisted the IVR process[75]. IVR in the peptide system acetlyproline-NH_2 has also been studied with 2DIR spectroscopy.[76]

1.4.3 Spectral Diffusion

In the condensed phase, the solute molecule is affected by the dynamics of the solvent. The random force exerted on the solute by the solvent can lead to fluctuations in the energy gap between states of the solute molecule. In Fig. 1.5a the change in the frequency between states 0 and 1 is plotted as a function of time where the width of the fluctuations is represented by Δ. The frequency-frequency correlation function (FFCF) can be used to characterize these fluctuations as a function of time (Eq. 1.1)

$$C(t) = \left\langle \delta\omega_{01}(t)\delta\omega_{01}(0) \right\rangle \qquad \textbf{Eq. 1.1}$$

The correlation function resulting from the frequency trajectory is also plotted in Fig. 1.5b. In many commonly used models, the resulting FFCF will decay exponentially, described by Eq. 1.2 where τ_c is the timescale of the fluctuations.

$$C(t) = \Delta^2 e^{-\frac{t}{\tau_c}} \qquad \textbf{Eq. 1.2}$$

Solvent interactions can be probed using three pulse photon echo spectroscopies, where the signal is a result of the third order nonlinear polarization.[77] From waiting-time dependent 2DIR optical spectroscopies, which also measure the third order nonlinear polarization, the time evolution of the frequency distributions can be directly observed.[78]

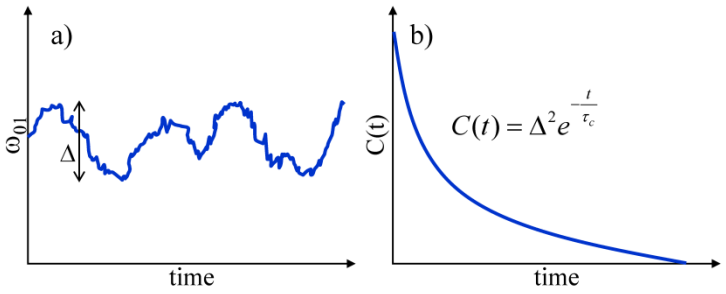

Figure 1.5 (a) Plot of the time dependent fluctuations in the frequency corresponding to the transition between the ground and first excited state. (b) Plot of the corresponding time correlation function, the frequency-frequency correlation function.

In 2D spectra, the waiting-time dependent lineshapes of the peaks are related to the FFCF, and hence are related to the solvent interactions.[79] For 2D spectra, where the timescale of the frequency fluctuations, τ_c, is slower than the timescale probed by the experiment, t_2, the resulting peak will be elongated along the diagonal and the peak is said to be inhomogeneously broadened. In Fig. 1.1, cartoon linear and corresponding 2D spectra are shown for both the homogeneously and inhomogeneously broadened cases. The corresponding 2D spectra are different even though the linear spectra show the same lineshapes for both cases. In the homogeneously broadened case, the peak is symmetric about the diagonal; the microscopic solvent environments are being fully sampled on the timescale being probed. Viewed another way, the sampling of distinct solvation environments does not lead to changes in the optically probed transition frequency. In the inhomogeneously broadened case there are distinct microscopic solvent environments, and each excitation frequency is correlated to a specific detection frequency, resulting in a peak that is elongated along the diagonal in the 2D spectra. For the case of the inhomogeneously broadened peak, as the waiting time increases, more microscopic environments can be sampled leading to a decrease in the inhomogeneity, and the peak becomes more round. Eventually, when the waiting time is long compared to τ_c, the different microscopic environments will be fully sampled and the peak will be homogeneously broadened; the peak will be symmetric about the diagonal in the 2D spectrum (Fig. 1.6). The decay of inhomogeneity as a function of waiting-time is referred to as spectral diffusion and can be directly related to interactions between the solute and solvent.[80]

There are several ways to map experimental observables in 2D spectra to the FFCF.[79, 81-84] It has been shown that the measure of the ellipticity of the peak is identical to the FFCF.[84] However, there are several other methods of obtaining the FFCF. One method is to use the so-called "inhomogeneous index," which measures the difference in amplitude between the rephasing and nonrephasing spectra.[79]

Asbury *et. al.* showed that the dynamic linewidth, the waiting time dependent width of the diagonal peak along ω_{excite}, is related to the FFCF.[81] Hamm used the covariance to determine the FFCF.[82] More recently it has been shown that the inverse of the center line slope, where the center line slope is the node between the peak resulting from the ground state bleach and the peak corresponding to the excited state absorption, can also be used to obtain the FFCF.[83] Experimentally, the study of the spectral diffusion in metal carbonyl systems has led to a detailed understanding of how the solute and solvent interact.[73, 74, 85] The dynamics of water have also been studied using 2DIR spectroscopy to observe spectral diffusion.[81, 86, 87] Insight into protein dynamics and mechanisms has also been gained by studying spectral diffusion via 2DIR spectroscopy.[88]

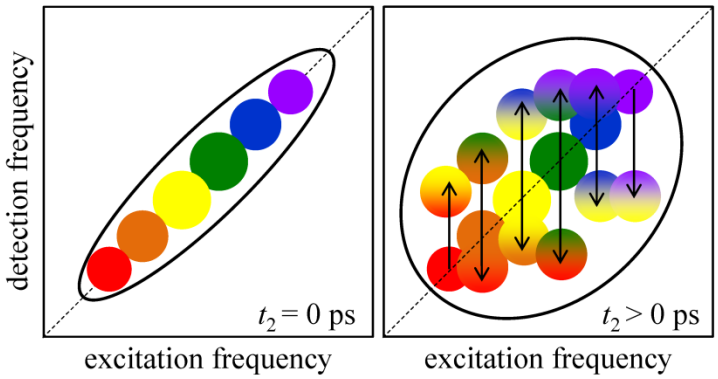

Figure 1.6 Cartoon spectra depicting spectral diffusion. At early waiting times the peak is elongated along the diagonal (left) and as the waiting time increases the peak becomes more symmetrical (right).

1.4.4 Chemical Exchange

Many fast, equilibrium, structural changes occur on the electronic ground state at room temperature. Studying these structural changes gives insight into equilibrium dynamics. Consider for example two different species A and B that interconvert on the picosecond timescale. The potential energy surface is shown in Fig. 1.7a, where species A lies lower in energy than species B and the height of the barrier is on the order of a few kcal/mol, corresponding to a picosecond isomerization time. A cartoon linear spectrum is shown in Fig. 1.7b where species A has one absorbance at

frequency ω_a and species B absorbs at frequency ω_b. Assuming the oscillator strength

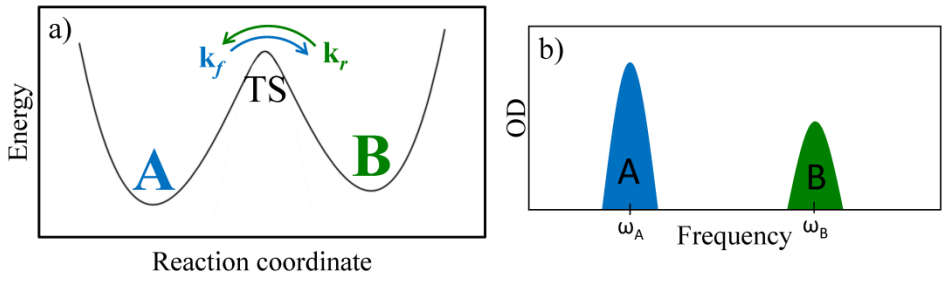

Figure 1.7 (a) 1D potential energy surface describing the isomerization between species A and B with the corresponding (b) linear spectrum.

is the same for both transitions, the absorbance feature corresponding to A is larger than that of B due to species A being more populated because it lies lower in energy. From the linear spectrum we can obtain thermodynamic information on the two stable species. In principle the linear IR spectrum contains information on the interconversion between A and B in the lineshapes of the peaks in that the interconversion between the two species, could act as a dephasing mechanism which would contribute to spectral broadening. However, separating the spectral broadening due to exchange from other processes is not always possible in the linear spectrum.[24, 25] Using 2DIR spectroscopy, chemical exchange can be directly observed as the appearance and growth of crosspeaks in the 2D spectra.

Fig. 1.8 displays cartoon 2D spectra. At earlier waiting times, before exchange can take place, we see two peaks lying along the diagonal. These peaks correspond to the peaks in the linear spectrum. As the waiting time increases, we see the appearance of crosspeaks. Crosspeak AB corresponds to exciting species A, waiting some time corresponding to t_2, and detecting species B; isomer A has converted to isomer B during the waiting time. We refer to these crosspeaks as "exchange crosspeaks". From the waiting-time dependent amplitude of the exchange crosspeaks, the isomerization time can be obtained directly in the time-domain.

Woutersen *et. al.* were the first to use 2DIR spectroscopy to study chemical exchange.[89] They observed the conformation change between two different states of

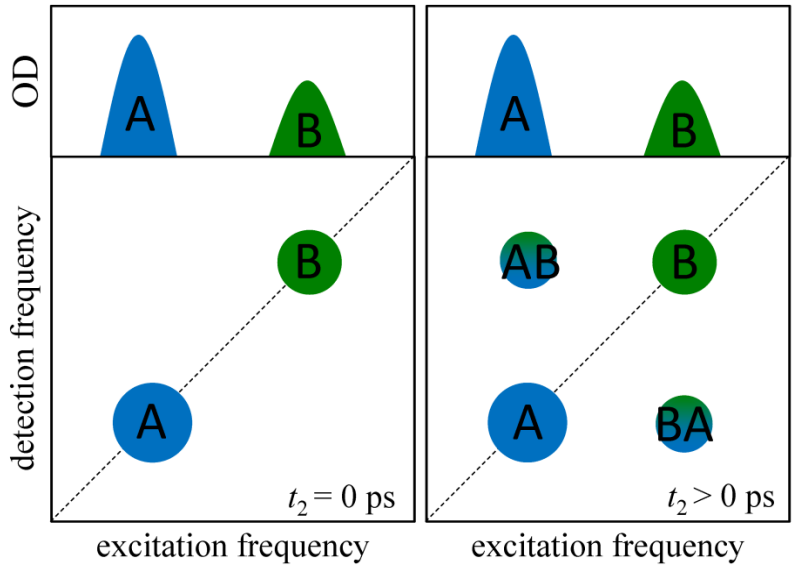

Figure 1.8 Cartoon 2D spectra depicting chemical exchange. (left) At early waiting times we see two peaks along the diagonal. (right) As the waiting time increases we see the appearance of crosspeaks indicating chemical exchange.

N-methylacetamide (NMA). In methanol, NMA exists as two states having distinct transitions. The red-shifted transition corresponds to species where the carbonyl group is hydrogen bonded to the solvent, and the blue shifted transition results from species where the carbonyl group is free of hydrogen bonds. As the waiting time was increased, crosspeaks between the two states appeared, indicating that chemical exchange occurred. Chemical exchange has also been used to study other systems including rotation about a carbon-carbon single bond[90]; hydrogen bond migration[91]; solvent-solute complexation[92]; hydrogen bond formation[89, 93]; and fluxional metal carbonyl complexes.[59, 60, 94]

1.4.5 Non-equilibrium 2DIR Spectroscopy

All the previous examples have focused on applying 2DIR spectroscopy to equilibrium systems to study how equilibrium ensembles evolve in time. Here we briefly address the study of non-equilibrium systems. In studying non-equilibrium

systems, insight on mechanistic pathways of photochemical reactions and dynamics of the electronic excited states can be gained.[55]

Here we focus on two types of non-equilibrium 2DIR spectroscopies: transient 2DIR (T-2DIR) and triggered exchange 2DIR (TE-2DIR) spectroscopy. In T-2DIR spectroscopy, a visible/UV pulse first excites the system and 2DIR spectroscopy is used to probe the non-equilibrium ensemble.[95] For TE-2DIR spectroscopy, the visible/UV arrives during the waiting time in the 2DIR pulse sequence –after the first two IR pulses but before the arrival of the third IR pulse.[64] This allows for vibrational modes of photoproducts to be directly mapped to vibrational modes of the reactants.

Non-equilibrium 2DIR spectroscopy has been used to study the following phenomena: geminate rebinding reactions[62]; orientational dynamics of photoproducts[96]; photoproducts of an iron hydrogenase enzyme model compound [63]; photoproducts mapping to parent structures[64]; photoswitchable proteins[55], and protein unfolding[97].

1.4.6 Modeling 2DIR Spectroscopy

From 2DIR spectra we can obtain transition frequencies, and timescales for dynamical processes, such as spectral diffusion and energy transfer. However, a detailed molecular understanding of these dynamic processes cannot be directly realized from the experimental spectra. In modeling 2DIR spectra, a detailed microscopic understanding of dynamical processes in the condensed phase is obatined.[26, 98-100] The use of modeling 2DIR spectra to obtain a microscopic picture of dynamics has been used to understand population transfer in peptides[101], vibrational energy transfer between amide I and amide II modes in N-methyacetanmide[102], hydrogen bonding complexes[103], photodissociation of metal carbonyl complexes[104] and intermolecular motion of water[105], to name a few examples.

1.5 Thesis Outline

This thesis focuses on the study of equilibrium dynamics in the condensed phase using 2DIR spectroscopy. Specifically I focus on the study of the equilibrium isomerization between two isomers of the fluxional metal carbonyl complex, dicobalt octacarbonyl, and the transfer of energy between different vibrational modes of two metal carbonyl complexes, iron cyclopentadienyl dicarbonyl dimer and its ruthenium analog.

In chapter 2 the theoretical background of 2DIR spectroscopy is presented along with a detailed account of the experimental setup. The focus of chapter 3 is on obtaining absorptive spectra using chirped pulse upconversion 2DIR spectroscopy. Sum frequency mixing the mid-infrared signal with a chirped pulse centered at 800 nm converts the signal from the mid-IR to the visible so that a CCD camera can be used for detection. The advantages of detecting the upconverted mid-IR signal are compared to the direct detection of the mid-IR signal. One of the disadvantages associated with the upconversion process arises from the inherent phase distortions due to cross-phase modulation. The procedure for correcting for these phase distortions is described in detail along with our technique for phasing rephasing and nonrephasing spectra. In chapter 4, the study of the equilibrium isomerization between two isomers of dicobalt octacarbonyl is described. A detailed account of our method used for the extraction of the exchange signal from congested spectra by using the quantum oscillations of inherent crosspeaks is given. Temperature dependent studies were also performed to determine the height of the barrier, and the influence of the solvent on these measurements is also discussed. In chapter 5, this well characterized reaction is used as a probe to determine how the solvent influences equilibrium chemical reaction occurring on the ground electronic state. Using classical and quantum mechanical computations along with linear FTIR measurements, the static solvent effect is separated from the dynamic solvent effect. This enables, for the first time, a direct test of Kramers theory in a ground electronic state in the time

domain. In chapter 6, the focus shifts to di-iron and di-ruthenium carbonyl complexes, where the ability of 2DIR spectroscopy to separate spectroscopic signatures from different isomeric forms is demonstrated. The transition frequencies associated with the different isomeric forms, which could not be determined from the linear FTIR spectra, were determined using 2DIR spectroscopy. Along with assigning the spectra, the timescale for vibrational energy transfer between different vibrational modes of the *cis*-B isomer for the iron complex and the *gauche*-NB isomer for the ruthenium complex was obtained.

References:

1. Pechukas, P., *TRANSITION-STATE THEORY*. Annual Review of Physical Chemistry, 1981. **32**: p. 159-177.

2. Hanggi, P., P. Talkner, and M. Borkovec, *REACTION-RATE THEORY - 50 YEARS AFTER KRAMERS*. Reviews of Modern Physics, 1990. **62**(2): p. 251-341.

3. Talkner, P. and P. Hanggi, *New Trends in Kramers' Reaction Rate Theory*. 1995, Netherlands: Kluwer Academic Publishers.

4. Truhlar, D.G., B.C. Garrett, and S.J. Klippenstein, *Current status of transition-state theory*. J. Phys. Chem., 1996. **100**(31): p. 12771-12800.

5. Fleming, G.R. and P. Hanggi, *Activated Barrier Crossing: Applications in Physics, Chemistry and Biology*, ed. G.R. Fleming and P. Hanggi. 1993, Singapore: World Scientific Publishing Co. Pte. Ltd.

6. Elles, C.G. and F.F. Crim, *Connecting chemical dynamics in gases and liquids*. Annual Review of Physical Chemistry, 2006. **57**: p. 273-302.

7. Rothenberger, G., D.K. Negus, and R.M. Hochstrasser, *Solvent Influence on Photo-Isomerization Dynamics*. Journal of Chemical Physics, 1983. **79**(11): p. 5360-5367.

8. Waldeck, D.H., *PHOTOISOMERIZATION DYNAMICS OF STILBENES*. Chem. Rev., 1991. **91**(3): p. 415-436.

9. Calef, D.F. and P.G. Wolynes, *CLASSICAL SOLVENT DYNAMICS AND ELECTRON-TRANSFER .1. CONTINUUM THEORY*. J. Phys. Chem., 1983. **87**(18): p. 3387-3400.

10. Maroncelli, M., J. Macinnis, and G.R. Fleming, *POLAR-SOLVENT DYNAMICS AND ELECTRON-TRANSFER REACTIONS*. Science, 1989. **243**(4899): p. 1674-1681.

11. Borgis, D. and J.T. Hynes, *MOLECULAR-DYNAMICS SIMULATION FOR A MODEL NONADIABATIC PROTON-TRANSFER REACTION IN SOLUTION*. Journal of Chemical Physics, 1991. **94**(5): p. 3619-3628.

12. Jimenez, R., G.R. Fleming, P.V. Kumar, and M. Maroncelli, *FEMTOSECOND SOLVATION DYNAMICS OF WATER*. Nature, 1994. **369**(6480): p. 471-473.

13. Hynes, J.T., *CHEMICAL-REACTION DYNAMICS IN SOLUTION*. Annual Review of Physical Chemistry, 1985. **36**: p. 573-597.

14. Beece, D., L. Eisenstein, H. Frauenfelder, D. Good, M.C. Marden, L. Reinisch, A.H. Reynolds, L.B. Sorensen, and K.T. Yue, *Solvent Viscosity and Protein Dynamics*. Biochemistry, 1980. **19**(23): p. 5147-5157.

15. Ansari, A., C.M. Jones, E.R. Henry, J. Hofrichter, and W.A. Eaton, *The Role of Solvent Viscosity in the Dynamics of Protein Conformational-Changes*. Science, 1992. **256**(5065): p. 1796-1798.

16. Fenimore, P.W., H. Frauenfelder, B.H. McMahon, and F.G. Parak, *Slaving: Solvent fluctuations dominate protein dynamics and functions*. Proceedings of the National Academy of Sciences of the United States of America, 2002. **99**(25): p. 16047-16051.

17. Chandler, D., *Introduction to Modern Statistical Mechanics*. 1987, New York: Oxford University Press.

18. Zewail, A.H., *Femtochemistry: Atomic-scale dynamics of the chemical bond*. Journal of Physical Chemistry A, 2000. **104**(24): p. 5660-5694.

19. Laberge, M., *Intrinsic protein electric fields: basic non-covalent interactions and relationship to protein-induced Stark effects*. Biochim. Biophys. Acta-Protein Struct. Molec. Enzym., 1998. **1386**(2): p. 305-330.

20. Boxer, S.G., *Stark Realities*. J. Phys. Chem. B, 2009. **113**(10): p. 2972-2983.

21. Suydam, I.T. and S.G. Boxer, *Vibrational Stark effects calibrate the sensitivity of vibrational probes for electric fields in proteins*. Biochemistry, 2003. **42**(41): p. 12050-12055.

22. Mukamel, S., *Principles of Nonlinear Optical Spectroscopy*. 1995, New York: Oxford University Press.

23. Mukamel, S., *Multidimensional femtosecond correlation spectroscopies of electronic and vibrational excitations*. Annu. Rev. Phys. Chem., 2000. **51**: p. 691-729.

24. Loring, R.F. and S. Mukamel, *Selectivity in Coherent Transient Raman Measurements of Vibrational Dephasing in Liquids*. Journal of Chemical Physics, 1985. **83**(5): p. 2116-2128.

25. Tanimura, Y. and S. Mukamel, *2-Dimensional Femtosecond Vibrational Spectroscopy of Liquids*. Journal of Chemical Physics, 1993. **99**(12): p. 9496-9511.

26. Cho, M.H., *Coherent two-dimensional optical spectroscopy*. Chem. Rev., 2008. **108**(4): p. 1331-1418.

27. Jonas, D.M., *Two-dimensional femtosecond spectroscopy*. Annual Review of Physical Chemistry, 2003. **54**: p. 425-463.

28. Faeder, S. and D. Jonas, *Two-dimensional electronic correlation and relaxation spectra: Theory and model calculations*. J. Phys. Chem. A, 1999. **103**(49): p. 10489-10505.

29. Hamm, P., M. Lim, and R.M. Hochstrasser, *Structure of the Amide I Band of Peptides Measured by Femtosecond Nonlinear-Infrared Spectroscopy*. The Journal of Physical Chemistry B, 1998. **102**(31): p. 6123-6138.

30. Hamm, P., M. Lim, W.F. DeGrado, and R.M. Hochstrasser, *Pump/probe self heterodyned 2D spectroscopy of vibrational transitions of a small globular peptide*. Journal of Chemical Physics, 2000. **112**(4): p. 1907-1916.

31. DeFlores, L., R. Nicodemus, and A. Tokmakoff, *Two dimensional Fourier transform spectroscopy in the pump-probe geometry*. Opt. Lett., 2007. **32**(20): p. 2966-2968.

32. DeCamp, M., L. DeFlores, K. Jones, and A. Tokmakoff, *Single-shot two-dimensional infrared spectroscopy*. OPTICS EXPRESS, 2007. **15**(1): p. 233-241.

33. DeCamp, M. and A. Tokmakoff, *Single-shot two-dimensional spectrometer*. Opt. Lett., 2006. **31**(1): p. 113-115.

34. Tian, P., D. Keusters, Y. Suzaki, and W. Warren, *Femtosecond phase-coherent two-dimensional spectroscopy*. Science, 2003. **300**(5625): p. 1553-1555.

35. Shim, S., D. Strasfeld, Y. Ling, and M. Zanni, *Automated 2D IR spectroscopy using a mid-IR pulse shaper and application of this technology to the human islet amyloid polypeptide*. PROCEEDINGS OF THE NATIONAL ACADEMY OF SCIENCES OF THE UNITED STATES OF AMERICA, 2007. **104**(36): p. 14197-14202.

36. Tekavec, P., J. Myers, K. Lewis, and J. Ogilvie, *Two-dimensional electronic spectroscopy with a continuum probe*. Opt. Lett., 2009. **34**(9): p. 1390-1392.

37. Lepetit, L. and M. Joffre, *Two-dimensional nonlinear optics using Fourier-transform spectral interferometry*. Opt. Lett., 1996. **21**(8): p. 564-566.

38. Hybl, J., A. Albrecht, S. Faeder, and D. Jonas, *Two-dimensional electronic spectroscopy*. Chem. Phys. Lett., 1998. **297**(3-4): p. 307-313.

39. Asplund, M.C., M.T. Zanni, and R.M. Hochstrasser, *Two-dimensional infrared spectroscopy of peptides by phase-controlled femtosecond vibrational photon echoes*. Proceedings of the National Academy of Sciences of the United States of America, 2000. **97**(15): p. 8219-8224.

40. Likforman, J.P., M. Joffre, and V. ThierryMieg, *Measurement of photon echoes by use of femtosecond Fourier-transform spectral interferometry*. Opt. Lett., 1997. **22**(14): p. 1104-1106.

41. Nee, M., R. McCanne, K. Kubarych, and M. Joffre, *Two-dimensional infrared spectroscopy detected by chirped-pulse upconversion*. Opt. Lett., 2007. **32**(6): p. 713-715.

42. Anna, J.M., M.J. Nee, C.R. Baiz, R. McCanne, and K.J. Kubarych, *Measuring absorptive two-dimensional infrared spectra using chirped-pulse upconversion detection*. J. Opt. Soc. Am. B, 2010. **27**: p. 382-393.

43. Hochstrasser, R.M., *Two-dimensional IR-spectroscopy: polarization anisotropy effects.* Chemical Physics, 2001. **266**(2-3): p. 273-284.

44. Zanni, M.T., N.H. Ge, Y.S. Kim, and R.M. Hochstrasser, *Two-dimensional IR spectroscopy can be designed to eliminate the diagonal peaks and expose only the crosspeaks needed for structure determination.* Proceedings of the National Academy of Sciences of the United States of America, 2001. **98**(20): p. 11265-11270.

45. Cowan, M., J. Ogilvie, and R. Miller, *Two-dimensional spectroscopy using diffractive optics based phased-locked photon echoes.* Chem. Phys. Lett., 2004. **386**(1-3): p. 184-189.

46. Brixner, T., T. Mancal, I. Stiopkin, and G. Fleming, *Phase-stabilized two-dimensional electronic spectroscopy.* J. Chem. Phys., 2004. **121**(9): p. 4221-4236.

47. Bristow, A.D., D. Karaiskaj, X.C. Dai, and S.T. Cundiff, *All-optical retrieval of the global phase for two-dimensional Fourier-transform spectroscopy.* OPTICS EXPRESS, 2008. **16**(22): p. 18017-18027.

48. Backus, E., S. Garrett-Roe, and P. Hamm, *Phasing problem of heterodyne-detected two-dimensional infrared spectroscopy.* Opt. Lett., 2008. **33**(22): p. 2665-2667.

49. Miller, R.J.D., A. Paarmann, and V.I. Prokhorenko, *Diffractive Optics Based Four-Wave, Six-Wave, ..., v-Wave Nonlinear Spectroscopy.* Accounts of Chemical Research, 2009. **42**(9): p. 1442-1451.

50. Ginsberg, N., Y. Cheng, and G. Fleming, *Two-dimensional electronic spectroscopy of molecular aggregates.* Accounts of Chemical Research, 2009. **42**: p. 1352-1363.

51. Zhuang, W., T. Hayashi, and S. Mukamel, *Coherent Multidimensional Vibrational Spectroscopy of Biomolecules: Concepts, Simulations, and Challenges.* ANGEWANDTE CHEMIE-INTERNATIONAL EDITION, 2009. **48**(21): p. 3750-3781.

52. Fayer, M., *Dynamics of Liquids, Molecules, and Proteins Measured with Ultrafast 2D IR Vibrational Echo Chemical Exchange Spectroscopy.* ANNUAL REVIEW OF PHYSICAL CHEMISTRY, 2009. **60**: p. 21-38.

53. Kim, Y. and R. Hochstrasser, *Applications of 2D IR Spectroscopy to Peptides, Proteins, and Hydrogen-Bond Dynamics.* J. Phys. Chem. B, 2009. **113**(24): p. 8231-8251.

54. Roberts, S.T., K. Ramasesha, and A. Tokmakoff, *Structural Rearrangements in Water Viewed Through Two-Dimensional Infrared Spectroscopy*. ACCOUNTS OF CHEMICAL RESEARCH, 2009. **42**(9): p. 1239-1249.

55. Hamm, P., J. Helbing, and J. Bredenbeck, *Two-dimensional infrared spectroscopy of photoswitchable peptides*. ANNUAL REVIEW OF PHYSICAL CHEMISTRY, 2008. **59**: p. 291-317.

56. Strasfeld, D., S. Shim, and M. Zanni, *NEW ADVANCES IN MID-IR PULSE SHAPING AND ITS APPLICATION TO 2D IR SPECTROSCOPY AND GROUND-STATE COHERENT CONTROL*. ADVANCES IN CHEMICAL PHYSICS, VOL 141, 2009. **141**: p. 1-28.

57. Ogilvie, J.P. and K.J. Kubarych, *Multidimensional Electronic and Vibrational Spectroscopy: An Ultrafast Probe of Molecular Relaxation and Reaction Dynamics*. Adv Atom Mol Opt Phy, 2009. **57**: p. 249-321.

58. Asbury, J.B., T. Steinel, and M.D. Fayer, *Using ultrafast infrared multidimensional correlation spectroscopy to aid in vibrational spectral peak assignments*. Chemical Physics Letters, 2003. **381**(1-2): p. 139-146.

59. Anna, J.M., M.R. Ross, and K.J. Kubarych, *Dissecting Enthalpic and Entropic Barriers to Ultrafast Equilibrium Isomerization of a Flexible Molecule Using 2DIR Chemical Exchange Spectroscopy*. Journal of Physical Chemistry A, 2009. **113**(24): p. 6544-6547.

60. Anna, J.M. and K.J. Kubarych, *Watching solvent friction impede ultrafast barrier crossings: A direct test of Kramers theory*. Journal of Chemical Physics, 2010. **133**(17).

61. Kania, R., A.I. Stewart, I.P. Clark, G.M. Greetham, A.W. Parker, M. Towrie, and N.T. Hunt, *Investigating the vibrational dynamics of a 17e(-) metallocarbonyl intermediate using ultrafast two dimensional infrared spectroscopy*. Phys. Chem. Chem. Phys., 2010. **12**(5): p. 1051-1063.

62. Baiz, C.R., R. McCanne, and K.J. Kubarych, *Structurally Selective Geminate Rebinding Dynamics of Solvent-Caged Radicals Studied with Nonequilibrium Infrared Echo Spectroscopy*. Journal of the American Chemical Society, 2009. **131**(38): p. 13590-+.

63. Stewart, A.I., J.A. Wright, G.M. Greetham, S. Kaziannis, S. Santabarbara, M. Towrie, A.W. Parker, C.J. Pickett, and N.T. Hunt, *Determination of the Photolysis Products of FeFe Hydrogenase Enzyme Model Systems using Ultrafast Multidimensional Infrared Spectroscopy*. Inorg. Chem., 2010. **49**(20): p. 9563-9573.

64. Bredenbeck, J., J. Helbing, and P. Hamm, *Labeling vibrations by light: Ultrafast transient 2D-IR spectroscopy tracks vibrational modes during photoinduced charge transfer.* Journal of the American Chemical Society, 2004. **126**(4): p. 990-991.

65. Rubtsov, I., J. Wang, and R. Hochstrasser, *Dual frequency 2D-IR of peptide amide-A and amide-I modes.* JOURNAL OF CHEMICAL PHYSICS, 2003. **118**(17): p. 7733-7736.

66. Rubtsov, I.V., J.P. Wang, and R.M. Hochstrasser, *Dual-frequency 2D-IR spectroscopy heterodyned photon echo of the peptide bond.* Proceedings of the National Academy of Sciences of the United States of America, 2003. **100**(10): p. 5601-5606.

67. Golonzka, O., M. Khalil, N. Demirdoven, and A. Tokmakoff, *Coupling and orientation between anharmonic vibrations characterized with two-dimensional infrared vibrational echo spectroscopy*. Journal of Chemical Physics, 2001. **115**(23): p. 10814-10828.

68. Woutersen, S. and P. Hamm, *Structure determination of trialanine in water using polarization sensitive two-dimensional vibrational spectroscopy*. J. Phys. Chem. B, 2000. **104**(47): p. 11316-11320.

69. Zanni, M.T., S. Gnanakaran, J. Stenger, and R.M. Hochstrasser, *Heterodyned two-dimensional infrared spectroscopy of solvent-dependent conformations of acetylproline-NH2*. J. Phys. Chem. B, 2001. **105**(28): p. 6520-6535.

70. Ganim, Z., H. Chung, A. Smith, L. Deflores, K. Jones, and A. Tokmakoff, *Amide I two-dimensional infrared Spectroscopy of proteins.* ACCOUNTS OF CHEMICAL RESEARCH, 2008. **41**(3): p. 432-441.

71. Rubtsov, I.V., *Relaxation-Assisted Two-Dimensional Infrared (RA 2DIR) Method: Accessing Distances over 10 angstrom and Measuring Bond Connectivity Patterns.* ACCOUNTS OF CHEMICAL RESEARCH, 2009. **42**(9): p. 1385-1394.

72. Crim, F.F., *Vibrational state control of bimolecular reactions: Discovering and directing the chemistry.* Accounts of Chemical Research, 1999. **32**(10): p. 877-884.

73. King, J.T., J.M. Anna, and K.J. Kubarych, *Solvent-hindered intramolecular vibrational redistribution.* Phys. Chem. Chem. Phys., 2011.

74. Khalil, M., N. Demirdoven, and A. Tokmakoff, *Coherent 2D IR spectroscopy: Molecular structure and dynamics in solution.* J. Phys. Chem. A, 2003. **107**(27): p. 5258-5279.

75. Stewart, A.I., I.P. Clark, M. Towrie, S.K. Ibrahim, A.W. Parker, C.J. Pickett, and N.T. Hunt, *Structure and vibrational dynamics of model compounds of the FeFe - hydrogenase enzyme system via ultrafast two-dimensional infrared spectroscopy.* J. Phys. Chem. B, 2008. **112**(32): p. 10023-10032.

76. Rubtsov, I. and R. Hochstrasser, *Vibrational dynamics, mode coupling, and structural constraints for acetylproline-NH2.* J. Phys. Chem. B, 2002. **106**(35): p. 9165-9171.

77. de Boeij, W.P., M.S. Pshenichnikov, and D.A. Wiersma, *Ultrafast solvation dynamics explored by femtosecond photon echo spectroscopies.* Annual Review of Physical Chemistry, 1998. **49**: p. 99-123.

78. Hybl, J.D., Y. Christophe, and D.M. Jonas, *Peak shapes in femtosecond 2D correlation spectroscopy.* Chemical Physics, 2001. **266**(2-3): p. 295-309.

79. Roberts, S.T., J.J. Loparo, and A. Tokmakoff, *Characterization of spectral diffusion from two-dimensional line shapes.* JOURNAL OF CHEMICAL PHYSICS, 2006. **125**(8): p. -.

80. Fleming, G.R. and M.H. Cho, *Chromophore-solvent dynamics.* Annual Review of Physical Chemistry, 1996. **47**: p. 109-134.

81. Asbury, J.B., T. Steinel, C. Stromberg, S.A. Corcelli, C.P. Lawrence, J.L. Skinner, and M.D. Fayer, *Water dynamics: Vibrational echo correlation spectroscopy and comparison to molecular dynamics simulations.* Journal of Physical Chemistry A, 2004. **108**(7): p. 1107-1119.

82. Hamm, P., *Three-dimensional-IR spectroscopy: Beyond the two-point frequency fluctuation correlation function.* Journal of Chemical Physics, 2006. **124**(12).

83. Kwak, K., S. Park, I.J. Finkelstein, and M.D. Fayer, *Frequency-frequency correlation functions and apodization in two-dimensional infrared vibrational echo spectroscopy: A new approach.* Journal of Chemical Physics, 2007. **127**(12).

84. Lazonder, K., M. Pshenichnikov, and D. Wiersma, *Easy interpretation of optical two-dimensional correlation spectra.* Opt. Lett., 2006. **31**(22): p. 3354-3356.

85. Demirdoven, N., M. Khalil, and A. Tokmakoff, *Correlated vibrational dynamics revealed by two-dimensional infrared spectroscopy.* Physical Review Letters, 2002. **89**(23).

86. Eaves, J., J. Loparo, C. Fecko, S. Roberts, A. Tokmakoff, and P. Geissler, *Hydrogen bonds in liquid water are broken only fleetingly.* PROCEEDINGS OF THE NATIONAL ACADEMY OF SCIENCES OF THE UNITED STATES OF AMERICA, 2005. **102**(37): p. 13019-13022.

87. Loparo, J.J., S.T. Roberts, and A. Tokmakoff, *Multidimensional infrared spectroscopy of water. I. Vibrational dynamics in two-dimensional IR line shapes.* JOURNAL OF CHEMICAL PHYSICS, 2006. **125**(19): p. -.

88. Woutersen, S., Y. Mu, G. Stock, and P. Hamm, *Subpicosecond conformational dynamics of small peptides probed by two-dimensional vibrational spectroscopy.* Proc. Natl. Acad. Sci. U. S. A., 2001. **98**(20): p. 11254-11258.

89. Woutersen, S., Y. Mu, G. Stock, and P. Hamm, *Hydrogen-bond lifetime measured by time-resolved 2D-IR spectroscopy: N-methylacetamide in methanol.* Chemical Physics, 2001. **266**(2-3): p. 137-147.

90. Zheng, J., K. Kwak, J. Xie, and M. Fayer, *Ultrafast carbon-carbon single-bond rotational isomerization in room-temperature solution.* SCIENCE, 2006. **313**(5795): p. 1951-1955.

91. Rosenfeld, D.E., K. Kwak, Z. Gengeliczki, and M.D. Fayer, *Hydrogen Bond Migration between Molecular Sites Observed with Ultrafast 2D IR Chemical Exchange Spectroscopy.* J. Phys. Chem. B, 2010. **114**(7): p. 2383-2389.

92. Zheng, J., K. Kwak, J. Asbury, X. Chen, I. Piletic, and M. Fayer, *Ultrafast dynamics of solute-solvent complexation observed at thermal equilibrium in real time.* SCIENCE, 2005. **309**(5739): p. 1338-1343.

93. Kim, Y.S. and R.M. Hochstrasser, *Chemical exchange 2D IR of hydrogen-bond making and breaking.* Proceedings of the National Academy of Sciences of the United States of America, 2005. **102**(32): p. 11185-11190.

94. Cahoon, J., K. Sawyer, J. Schlegel, and C. Harris, *Determining Transition-State Geometries in Liquids using 2D-IR.* Science, 2008. **319**: p. 1820-1823.

95. Bredenbeck, J., J. Helbing, R. Behrendt, C. Renner, L. Moroder, J. Wachtveitl, and P. Hamm, *Transient 2D-IR spectroscopy: Snapshots of the nonequilibrium ensemble during the picosecond conformational transition of a small peptide.* J. Phys. Chem. B, 2003. **107**(33): p. 8654-8660.

96. Baiz, C.R., R. McCanne, M.J. Nee, and K.J. Kubarych, *Orientational Dynamics of Transient Molecules Measured by Nonequilibrium Two-Dimensional Infrared Spectroscopy.* Journal of Physical Chemistry A, 2009. **113**(31): p. 8907-8916.

97. Chung, H.S., Z. Ganim, K.C. Jones, and A. Tokmakoff, *Transient 2D IR spectroscopy of ubiquitin unfolding dynamics.* Proceedings of the National Academy of Sciences of the United States of America, 2007. **104**(36): p. 14237-14242.

98. McRobbie, P.L., G. Hanna, Q. Shi, and E. Geva, *Signatures of Nonequilibrium Solvation Dynamics on Multidimensional Spectra.* Accounts of Chemical Research, 2009. **42**(9): p. 1299-1309.

99. Jansen, T.L.C. and J. Knoester, *Waiting Time Dynamics in Two-Dimensional Infrared Spectroscopy.* Accounts of Chemical Research, 2009. **42**(9): p. 1405-1411.

100. Tanimura, Y. and A. Ishizaki, *Modeling, Calculating, and Analyzing Multidimensional Vibrational Spectroscopies.* Accounts of Chemical Research, 2009. **42**(9): p. 1270-1279.

101. Jansen, T.L.C. and J. Knoester, *Two-dimensional infrared population transfer spectroscopy for enhancing structural markers of proteins.* Biophysical Journal, 2008. **94**(5): p. 1818-1825.

102. Bloem, R., A.G. Dijkstra, T.L.C. Jansen, and J. Knoester, *Simulation of vibrational energy transfer in two-dimensional infrared spectroscopy of amide I and amide II modes in solution.* Journal of Chemical Physics, 2008. **129**(5).

103. Hanna, G. and E. Geva, *Computational study of the signature of hydrogen-bond strength on the infrared spectra of a hydrogen-bonded complex dissolved in a polar liquid.* Chemical Physics, 2010. **370**(1-3): p. 201-207.

104. Baiz, C.R., P.L. McRobbie, N.K. Preketes, K.J. Kubarych, and E. Geva, *Two-Dimensional Infrared Spectroscopy of Dimanganese Decacarbonyl and Its Photoproducts:*

An Ab Initio Study. Journal of Physical Chemistry A, 2009. **113**(35): p. 9617-9623.

105. Yagasaki, T. and S. Saito, *Molecular Dynamics Simulation of Nonlinear Spectroscopies of Intermolecular Motions in Liquid Water*. Accounts of Chemical Research, 2009. **42**(9): p. 1250-1258.

Chapter 2

Theory and Experimental Setup

2.1 Overview: Chapter 2

This section first discusses the theory behind two-dimensional spectroscopy followed by a description of the experimental setup used to obtain 2DIR spectra.

2.2 Theory and Background

In its most popularly implemented form, two-dimensional spectroscopy in centrosymmetric media is a background-free, four-wave mixing technique where three incident fields, E_1, E_2, and E_3, having wavevectors, $\mathbf{k_1}$, $\mathbf{k_2}$, and $\mathbf{k_3}$, induce a third-order polarization ($P^{(3)}$) which radiates a signal field E_s with wavevector $\mathbf{k_s}$.[1, 2] The pulse sequence is illustrated in Fig. 2.1 where the time delays between the pulses are t_1 and t_2. The signal field that emits during t_3 is measured using Fourier transform

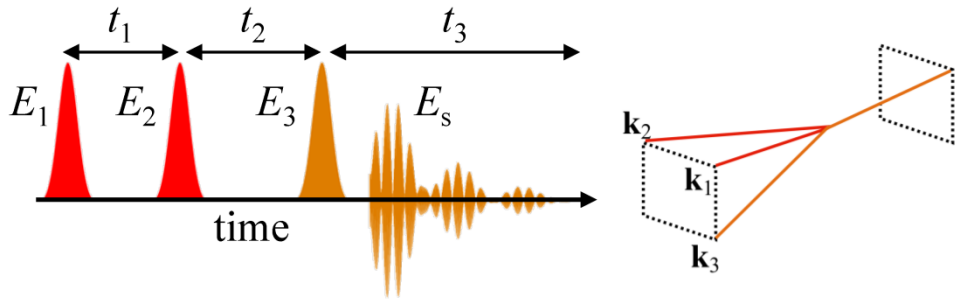

Figure 2.1 Pulse sequence (left) with box beam geometry (right).

spectral interferometry (FTSI) by combining the emitted signal with a fully characterized reference field that acts as a local oscillator for heterodyne detection.[3-7] The frequency-domain spectral interferogram is Fourier transformed to the time

domain, and the complex signal peaking at the signal-local-oscillator delay Δt is isolated by a numerical filter. Inverse Fourier transformation returns to the frequency domain, where the linear spectral phase due to the delay Δt is subtracted, yielding the spectral amplitude and phase to within a constant phase offset. With the signal field thus determined for each value of t_1—the delay between the first two pulses—Fourier transformation with respect to t_1 yields the excitation frequency axis ω_1.

Besides the background-free detection method, there are alternate strategies for obtaining 2DIR spectra, such as the collinear pump-probe geometry where either an interferometer or a pulse shaper generates the first two pulses of the three-pulse sequence.[8-10] However, regardless of the experimental implementation, 2DIR spectroscopy is a third-order nonlinear optical spectroscopy.

For third-order nonlinear optical spectroscopy the radiated signal is directly proportional to the third-order macroscopic optical polarization, which in turn is linearly proportional to the expectation value of the dipole operator over the third-order density matrix.[11] Knowing how the density matrix evolves in time after the three field-matter interactions, allows one to model and interpret 2D spectra. In the next section we address the time-evolution of the density operator.

2.2.1 Perturbation Theory

In the case of 2DIR spectroscopy, where the incoming electric fields are weak, we can treat the field-matter interaction perturbatively. The following derivation in this section is based on the derivation in Mukamel's *Principles of Nonlinear Optical Spectroscopy*.[11]

The Hamiltonian describing the system of interest is given by Eq. 2.1, where H_0 is the material Hamiltonian and H_{int} describes the electric field-matter interaction.

$$\hat{H}_T = \hat{H}_0 + \hat{H}_{\text{int}}(t) \qquad \textbf{Eq. 2.1}$$

In the above equation the field-matter interaction is time-dependent due to the time-dependent incoming laser pulse. Making the dipole approximation, assuming the molecule can be described by a point dipole, H_{int} is given by Eq. 2.2 where $E(\mathbf{r},t)$ is the incoming electric field and $\hat{V}$ is the dipole operator of the material.

$$\hat{H}_{\text{int}}(t) = -E(r,t)\hat{V} \qquad \textbf{Eq. 2.2}$$

The time evolution of the system is described by the Liouville equation (Eq. 2.3), where the first term accounts for the material response and the second term describes the field-matter interaction.

$$\frac{d\hat{\rho}}{dt} = -\frac{i}{\hbar}\left[\hat{H}_T, \hat{\rho}\right] = -\frac{i}{\hbar}\left[\hat{H}_0, \hat{\rho}\right] - \frac{i}{\hbar}\left[\hat{H}_{Int}, \hat{\rho}\right] \qquad \textbf{Eq. 2.3}$$

Substituting Eq. 2.2 into Eq.2.3 results in Eq. 2.4.

$$\frac{d\hat{\rho}}{dt} = -\frac{i}{\hbar}\left[\hat{H}_0, \hat{\rho}\right] - \frac{i}{\hbar}E(r,t)\left[\hat{V}, \hat{\rho}\right] \qquad \textbf{Eq. 2.4}$$

We now introduce the Liouvillian operators, $\boldsymbol{L}$ and $\boldsymbol{L}_{int}$, which are sometimes referred to as superoperators because they act on other operators. For a general operator $\hat{A}$, Eqs. 2.5-2.7 define the Liouvillian operators $\boldsymbol{L}$, $\boldsymbol{L}_{int}$, and $\boldsymbol{V}$.

$$\boldsymbol{L}\hat{A} = [\hat{H}, \hat{A}] \qquad \textbf{Eq. 2.5}$$

$$\boldsymbol{L}_{int}(t)\hat{A} = -E(r,t)[\hat{V}, \hat{A}] \qquad \textbf{Eq. 2.6}$$

$$\boldsymbol{V}\hat{A} = [\hat{V}, \hat{A}] \qquad \textbf{Eq. 2.7}$$

Using these operators, the equation of motion for the density operator (Eq. 2.4) can be rewritten as the following.

$$\frac{d\hat{\rho}}{dt} = -\frac{i}{\hbar}\boldsymbol{L}\hat{\rho} - \frac{i}{\hbar}\boldsymbol{L}_{int}(t)\hat{\rho} \qquad \textbf{Eq. 2.8}$$

2DIR spectroscopy is a four wave mixing spectroscopy where three incoming fields interact with the sample leading to the emission of the signal. Taking into account the three field matter interactions, the solution to Eq. 2.8, follows.

$$\hat{\rho}^{(3)}(t) = -\frac{i}{\hbar}\int_{t_0}^{t} d\tau_3 \int_{t_0}^{\tau_3} d\tau_2 \int_{t_0}^{\tau_2} d\tau_1 \boldsymbol{G}(t-\tau_3)\boldsymbol{L}_{int}(\tau_3)\boldsymbol{G}(\tau_3-\tau_2)\boldsymbol{L}_{int}(\tau_2)\boldsymbol{G}(\tau_2-\tau_1)\boldsymbol{L}_{int}(\tau_1)\hat{p}$$ **Eq. 2.9**

In the above equation we have introduced the Liouville space Green function, $\boldsymbol{G}$(t), given in Eq. 2.10, where θ(t) is the Heaviside step function.

$$\boldsymbol{G}(t) = \theta(t)\exp^{-\frac{i}{\hbar}\boldsymbol{L}(t)}$$ **Eq. 2.10**

Changing time variables so that t_1=τ2-τ1, t_2=τ3-τ2, and t_3=t-τ3 and using Eqs. 2.6-2.7 Eq. 2.9 can be rewritten as follows.

$$\hat{\rho}^{(3)}(t) = -\frac{i}{\hbar}\int_{0}^{\infty} dt_3 \int_{0}^{\infty} dt_2 \int_{0}^{\infty} dt_1 \boldsymbol{G}(t_3)\boldsymbol{V}\boldsymbol{G}(t_2)\boldsymbol{V}\boldsymbol{G}(t_1)\boldsymbol{V}\hat{p}(0)$$ **Eq. 2.11**

$$\times E(r,t-t_3)E(r,t-t_3-t_2)E(r,t-t_3-t_2-t_1)$$

The above equation describes the time dependence of the density matrix after three field matter interactions. The density matrix at t=0 is given by Eq. 2.12 and is just the equilibrium Boltzmann distribution of the states.

$$\hat{\rho}(0) = \frac{e^{-\frac{\hat{H}}{k_B T}}}{Tr\left[e^{-\frac{\hat{H}}{k_B T}}\right]}$$ **Eq. 2.12**

The first field matter interaction initiates the t_1 time, and is accounted for by acting on the density operator with the dipole operator, $\boldsymbol{V}$, multiplied by the incoming electric field. After the field matter interaction the system evolves in time under the field free Hamiltonian for the duration of t_1. The second field matter interaction initiates the t_2 time and the third field matter interaction initiates the beginning of t_3. After each field-matter interaction the system evolves under the field free Hamiltonian.

The macroscopic third order polarization, which is measured using 2DIR spectroscopy, is equivalent to the expectation value of the dipole operator (Eq. 2.13).

$$P^{(3)}(t) = Tr\left[Vp^{(3)}(t)\right] \qquad \textbf{Eq. 2.13}$$

Substituting Eq. 2.11 into the above equation (Eq. 2.13) results in the following.

$$P^{(3)}(t) = \int_0^\infty dt_3 \int_0^\infty dt_2 \int_0^\infty dt_1 S^{(3)}(t_3,t_2,t_1) E(r,t-t_3) E(r,t-t_3-t_2) E(r,t-t_3-t_2-t_1) \qquad \textbf{Eq. 2.14}$$

Where $S^{(3)}$ is the third order optical response function and is given by Eq. 2.15.

$$S^{(3)}(t_3,t_2,t_1) = \left(\frac{i}{\hbar}\right)^3 \theta(t_1)\theta(t_2)\theta(t_3)\left\langle\left[\left[\left[\hat{V}(t_3+t_2+t_1),\hat{V}(t_2+t_1)\right],\hat{V}(t_1)\right],\hat{V}(t_0)\right]\rho(0)\right\rangle \qquad \textbf{Eq. 2.15}$$

Evaluating the above nested commutators results in a total of 8 terms with 4 of the terms being independent. Evaluating the commutators results in the following expression.

$$S^{(3)}(t_3,t_2,t_1) = \left(\frac{i}{\hbar}\right)^3 \theta(t_1)\theta(t_2)\theta(t_3)\sum_{\alpha=1}^{4}\left[R_\alpha(t_3,t_2,t_1) - R_\alpha^*(t_3,t_2,t_1)\right] \qquad \textbf{Eq. 2.16}$$

In Eq. 2.16, there are four Liouville space pathways, R_α, that are given in Eq. 2.17-2.20.

$$R_1(t_3,t_2,t_1) = \left\langle \hat{V}(t_1)\hat{V}(t_1+t_2)\hat{V}(t_1+t_2+t_3)\hat{V}(0)\rho(0)\right\rangle \qquad \textbf{Eq. 2.17}$$

$$R_2(t_3,t_2,t_1) = \left\langle \hat{V}(0)\hat{V}(t_1+t_2)\hat{V}(t_1+t_2+t_3)\hat{V}(t_1)\rho(0)\right\rangle \qquad \textbf{Eq. 2.18}$$

$$R_3(t_3,t_2,t_1) = \left\langle \hat{V}(0)\hat{V}(t_1)\hat{V}(t_1+t_2+t_3)\hat{V}(t_1+t_2)\rho(0)\right\rangle \qquad \textbf{Eq. 2.19}$$

$$R_4(t_3,t_2,t_1) = \left\langle \hat{V}(t_1+t_2+t_3)\hat{V}(t_1+t_2)\hat{V}(t_1)\hat{V}(0)\rho(0)\right\rangle \qquad \textbf{Eq. 2.20}$$

In this section, we see that the third-order polarization is just the convolution of the incoming electric field pulses with the third order optical response function, and the optical response function can be written in terms of four Liouville space

pathways (Eq. 2.17-2.20). Accounting for the complex conjugates of the Liouville space pathways, there are eight contributing Liouville pathways. By not specifying the order of the incoming fields, there are 48 pathways contributing to the signal. However, in making the rotating wave approximations, neglecting the highly oscillatory terms, and by taking advantage of the fact that the wavevector of the signal can be selected, specific Liouville pathways can be chosen. In the next section we introduce two graphical methods used to describe the Liouville space pathways.

2.2.2 Diagrammatic Perturbation Theory

Diagrammatic perturbation theory can be used to keep track of the time-evolution of the density matrix after field matter interactions. In this section, we describe two useful graphical methods; double sided Feynman diagrams and ladder diagrams.[11]

For Feynman diagrams, each field interaction propagates one side of the density matrix, where the bra is on the left and the ket is on the right (Fig. 2.2a). Time

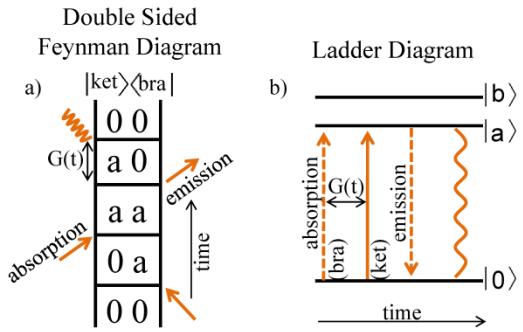

Figure 2.2 Examples of a double sided Feynman diagram (a) and a ladder diagram (b).

increases moving up the diagram. After a field matter interaction represented by a horizontal line, the system is free to propagate under the field free Hamiltonian until the next field-matter interaction. For the ladder diagrams (Fig. 2.2b), the states are arranged vertically and time propagates to the right. Arrows between states indicates field interactions and between field interactions the system is free to propagate under the field free Hamiltonian. Dashed lines act to propagate the bra and solid lines act to propagate the ket side of the density matrix. For the ladder diagrams, arrows pointing

up indicate absorption and arrows pointing down indicate emission, while for Feynman diagrams arrows pointing towards the diagram indicate absorption and arrows pointing away from the diagram indicate emission.

2.2.3 2DIR Spectra

Two phase-matching conditions are relevant for resonant 2D spectroscopy: $\mathbf{k}_{\pm} = \pm \mathbf{k}_1 \mp \mathbf{k}_2 + \mathbf{k}_3$, denoted "nonrephasing" ($\mathbf{k}_+$) and "rephasing" ($\mathbf{k}_-$). The terminology has its origin in the relative signs of the wave vectors $\mathbf{k}_1$ and $\mathbf{k}_3$: during the two evolution periods t_1 and t_3, the system evolves as a coherence (i.e. off-diagonal density matrix element); for the rephasing signal, the two coherences are phase reversed, whereas for the nonrephasing signal they are not phase reversed. Thus, the rephasing signal is capable of producing an echo by rephasing an inhomogeneously broadened set of oscillators. It was recognized in the context of nuclear magnetic resonance that to measure a two-dimensional lineshape with purely absorptive information (i.e. free of dispersive distortions), both the rephasing and nonrephasing signals must be recorded and their real parts added.[5, 12-14]

The double sided Feynman diagrams that give rise to the signal when both the

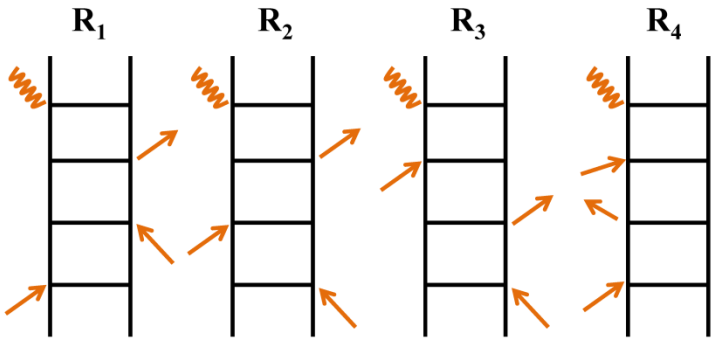

Figure 2.3 Liouville pathways contributing to the signal.

wave-matching and rotating wave approximation are taken into account are shown in Fig. 2.3[11], where pathways R_1 and R_4 and R_3* contribute to the nonrephasing signal and pathways R_2 and R_3 and R_1* contribute to the rephasing signal.[2, 11] In the time-

domain the signal is proportional to the following, where the contributing Liouville space pathways are depicted in Fig. 2.3.

$$S(k_s,t_1,t_2,t_3) \propto \mathrm{Re}\left[S^{(3)}(t_3,t_2,t_1) \right] \qquad \textbf{Eq. 2.21}$$

A double Fourier transform along t_1 and t_2 results in a two-dimensional infrared spectrum (Eq. 2.22).

$$S(k_s,\omega_1,t_2,\omega_3) \propto \mathrm{Re}\left[\int_{-\infty}^{\infty} dt_1 \int_{-\infty}^{\infty} dt_3 S(k_s,t_3,t_2,t_1) e^{i\omega_1 t_1} e^{i\omega_3 t_3} \right] \qquad \textbf{Eq. 2.22}$$

Experimentally, in the background-free geometry heterodyne detection is used so that both the amplitude and phase of the signal are measured. The intensity of the detected signal depends on both the signal field and the incoming local oscillator field (Eq. 2.23).[3]

$$I_{sig} \propto \left| E_{LO} + E_S \right|^2 = \left| E_{LO} \right|^2 + \left| E_S \right|^2 + 2\,\mathrm{Re}\left[E_{LO}^{*} E_{sig} \right] \qquad \textbf{Eq. 2.23}$$

The contribution from the local oscillator is removed by Fourier transformation along t_3, filtering the signal, and inverse Fourier transformation back to the time domain. In the background-free method we detect the rephasing and nonrephasing signals separately, so in order to obtain a 2DIR absorptive spectrum, the rephasing and nonrephasing signals must be added together (Eqs. 2.24-2.25).[5, 12, 15]

$$S(k_s,t_1,t_2,t_3) = S_R(k_s,t_1,t_2,t_3) + S_{NR}(k_s,t_1,t_2,t_3) \qquad \textbf{Eq. 2.24}$$

$$S(k_s,\omega_1,t_2,\omega_3) = \mathrm{Re}\left[\int_{-\infty}^{\infty} dt_1 \int_{-\infty}^{\infty} dt_3 S_R(t_1,t_2,t_3) e^{-i\omega_1 t_1} e^{\omega_3 t_3} + \int_{-\infty}^{\infty} dt_1 \int_{-\infty}^{\infty} dt_3 S_{NR}(t_1,t_2,t_3) e^{i\omega_1 t_1} e^{\omega_3 t_3} \right] \qquad \textbf{Eq. 2.25}$$

In the next section we describe the experimental setup we use to obtain 2DIR spectra.

2.3 Experimental Setup

The experimental setup used to obtain chirped pulse upconversion 2DIR spectra is shown in Fig. 2.4.[16-20] Two independently tuned optical parametric amplifiers (OPAs) are pumped with 100 fs 800 nm pulses generated by a Ti:Sapphire regenerative amplifier (Spectra-Physics Spitfire Pro). The signal and idler output of

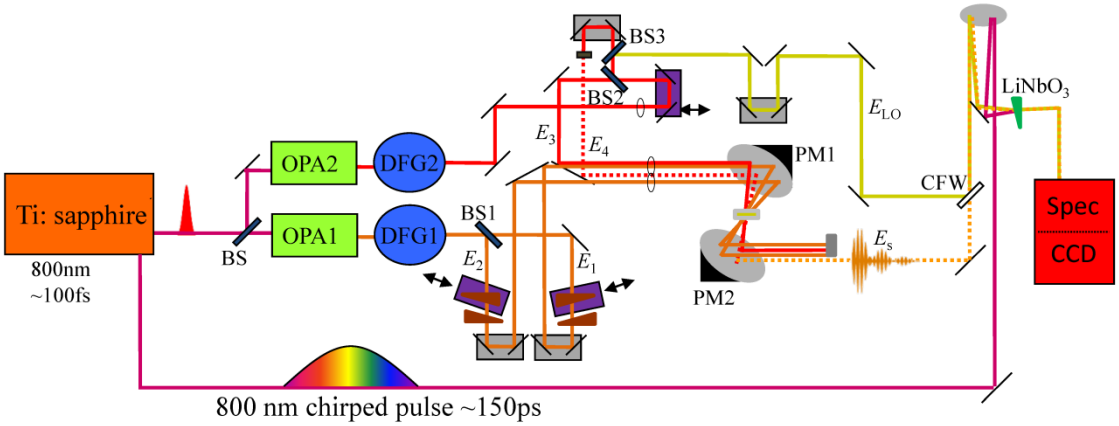

Figure 2.4 Experimental setup.

each OPA are difference frequency mixed in separate GaSe crystals to generate mid-IR pulses (FWHM = 100 cm^{-1}). The two mid-IR pulses are split to obtain a total of five pulses. The output of OPA1 is split by a beam splitter (BS1) into two beams E_1 and E_2 having wavevectors $\mathbf{k}_1$ and $\mathbf{k}_2$ while the output of OPA2 is split into three beams, E_3, E_4, and E_{LO}, having wavevectors $\mathbf{k}_3$, $\mathbf{k}_4$, and $\mathbf{k}_{LO}$, by BS2 and BS3. Pulses E_1, E_2, E_3, and E_4 are arranged in a box geometry (Fig. 2.1) so that the signal, E_S, is emitted in the background free direction $\mathbf{k}_\pm = \pm\,\mathbf{k}_1 \mp \mathbf{k}_2 + \mathbf{k}_3$ (E_4 is a tracer beam used for alignment purposes that is blocked during collection of the 2D spectrum). The first parabolic mirror (PM1) focuses the four beams at the sample and the second parabolic mirror (PM2) acts to collimate the beams. Three 1 meter focal length calcium fluoride lenses ensure the IR beams cross and focus at the same place at the sample. A wedged calcium fluoride window (CFW) is used to overlap the mid-IR signal with the local oscillator which are then sum-frequency mixed with the chirped pulse in a slightly wedged 5% MgO doped $LiNbO_3$ crystal. The $LiNbO_3$ crystal (1 cm on a side) thickness varies from 0.3 to 0.8 mm, providing a degree of analog gain, and minimizing back reflections which can interfere with the incoming

beams leading to temporal and spectral modulations. The mid-IR signal field and chirped field are upconverted non-collinearly using a folded spherical mirror of 30 cm focal length. The interference between the local oscillator and the signal is collected using a 1340x100 pixel, thermoelectrically-cooled CCD camera (Roper Scientific PIXIS).

The chirped pulse is taken from the output of the regenerative amplifier before the entrance to the compressor; using a half-wave plate and a cube polarizer a fraction of the uncompressed beam is selected with typical energies ranging from 100-300 μJ. The wave plate/polarizer combination enables another opportunity for analog gain when detecting weaker signals. A several-meter time delay is needed to temporally overlap the IR signal with the chirped pulse. To ensure that the signal is coincident with the same spectral component of the chirped pulse in the long time delay, the chirped pulse reflects off of a hollow corner cube mounted on the translation stage that controls the E_3 pulse. As the third pulse in the 2DIR sequence is scanned, the chirped pulse remains locked in time, eliminating the frequency shift (i.e. linear temporal phase) and amplitude modulation that would accompany the time delay.

A 2D spectrum is obtained by scanning the t_1 axis continuously for a given value of t_2. Two pairs of ZnSe wedges (7.3° apex angle, 25.4mm length, AR coated 3.5-7.5 μm) are used to scan the t_1 axis.[21] Scanning the wedges gives a maximum t_1 delay of 12 ps which corresponds to 2.78 cm^{-1} resolution. For each pair of wedges, one is held stationary and the other is mounted to a translation stage actuated by a DC motor. The DC motor (Newport LTA-HS) is driven using a home-built digital signal processer controller; a data acquisition (DAQ) board (NI M-series) records the motor's optical encoder output (resolution of 7.4 nm). The DAQ board and CCD camera are synchronized to the laser amplifier such that for each laser pulse the motor positions and spectra are saved. In order to map the encoder positions to time delays, the wedges are calibrated using interferograms between the upconverted

scatter of E_1 and E_2 recorded as each ZnSe wedge is scanned. The calibration of the wedges is discussed in detail in Chapter 3.

References:

1. Jonas, D.M., *Two-dimensional femtosecond spectroscopy*. Annual Review of Physical Chemistry, 2003. 54: p. 425-463.

2. Khalil, M., N. Demirdoven, and A. Tokmakoff, *Coherent 2D IR spectroscopy: Molecular structure and dynamics in solution*. J. Phys. Chem. A, 2003. 107(27): p. 5258-5279.

3. Lepetit, L., G. Cheriaux, and M. Joffre, *Linear techniques of phase measurement by femtosecond spectral interferometry for applications in spectroscopy*. Journal of the Optical Society of America B-Optical Physics, 1995. 12(12): p. 2467-2474.

4. Dorrer, C., N. Belabas, J. Likforman, and L. Joffre, *Experimental implementation of Fourier-transform spectral interferometry and its application to the study of spectrometers*. Appl. Phys. B-Lasers Opt., 2000. 70: p. S99-S107.

5. Hybl, J., A. Albrecht, S. Faeder, and D. Jonas, *Two-dimensional electronic spectroscopy*. Chem. Phys. Lett., 1998. 297(3-4): p. 307-313.

6. Gallagher, S., A. Albrecht, T. Hybl, B. Landin, B. Rajaram, and D. Jonas, *Heterodyne detection of the complete electric field of femtosecond four-wave mixing signals*. J. Opt. Soc. Am. B-Opt. Phys., 1998. 15(8): p. 2338-2345.

7. Lepetit, L. and M. Joffre, *Two-dimensional nonlinear optics using Fourier-transform spectral interferometry*. Opt. Lett., 1996. 21(8): p. 564-566.

8. Strasfeld, D., S. Shim, and M. Zanni, *NEW ADVANCES IN MID-IR PULSE SHAPING AND ITS APPLICATION TO 2D IR SPECTROSCOPY AND GROUND-STATE COHERENT CONTROL*. ADVANCES IN CHEMICAL PHYSICS, VOL 141, 2009. 141: p. 1-28.

9. Shim, S., D. Strasfeld, Y. Ling, and M. Zanni, *Automated 2D IR spectroscopy using a mid-IR pulse shaper and application of this technology to the human islet amyloid polypeptide*. PROCEEDINGS OF THE NATIONAL ACADEMY OF SCIENCES OF THE UNITED STATES OF AMERICA, 2007. 104(36): p. 14197-14202.

10. DeFlores, L., R. Nicodemus, and A. Tokmakoff, *Two dimensional Fourier transform spectroscopy in the pump-probe geometry.* Opt. Lett., 2007. 32(20): p. 2966-2968.

11. Mukamel, S., *Principles of Nonlinear Optical Spectroscopy*. 1995, New York: Oxford University Press.

12. Khalil, M., N. Demirdoven, and A. Tokmakoff, *Obtaining absorptive line shapes in two-dimensional infrared vibrational correlation spectra.* Phys. Rev. Lett., 2003. 90(4): p. 047401.

13. Ernst, R., G. Bodenhausen, and A. Wokaun, *Principles of Nuclear Magnetic Resonance in One and Two Dimensions*. 1987, Oxford: Clarendon Press.

14. Nagayama, K., P. Bachmann, K. Wuetrich, and R. Ernst, *USE OF CROSS-SECTIONS AND OF PROJECTIONS IN 2-DIMENSIONAL NMR-SPECTROSCOPY*. JOURNAL OF MAGNETIC RESONANCE, 1978. 31(1): p. 133-148.

15. Park, S., K. Kwak, and M. Fayer, *Ultrafast 2D-IR vibrational echo spectroscopy: a probe of molecular dynamics.* LASER PHYSICS LETTERS, 2007. 4: p. 704-718.

16. Baiz, C.R., M.J. Nee, R. McCanne, and K.J. Kubarych, *Ultrafast nonequilibrium Fourier-transform two-dimensional infrared spectroscopy.* Opt. Lett., 2008. 33(21): p. 2533-2535.

17. Anna, J.M., M.R. Ross, and K.J. Kubarych, *Dissecting Enthalpic and Entropic Barriers to Ultrafast Equilibrium Isomerization of a Flexible Molecule Using 2DIR Chemical Exchange Spectroscopy.* Journal of Physical Chemistry A, 2009. 113(24): p. 6544-6547.

18. Anna, J.M., M.J. Nee, C.R. Baiz, R. McCanne, and K.J. Kubarych, *Measuring absorptive two-dimensional infrared spectra using chirped-pulse upconversion detection.* J. Opt. Soc. Am. B, 2010. 27: p. 382-393.

19. Nee, M., R. McCanne, K. Kubarych, and M. Joffre, *Two-dimensional infrared spectroscopy detected by chirped-pulse upconversion.* Opt. Lett., 2007. 32(6): p. 713-715.

20. Nee, M.J., C.R. Baiz, J.M. Anna, R. McCanne, and K.J. Kubarych, *Multilevel vibrational coherence transfer and wavepacket dynamics probed with multidimensional IR spectroscopy.* JOURNAL OF CHEMICAL PHYSICS, 2008. 129(8): p. -.

21. Ding, F., P. Mukherjee, and M. Zanni, *Passively correcting phase drift in two-dimensional infrared spectroscopy*. Opt. Lett., 2006. 31(19): p. 2918-2920.

Chapter 3

Obtaining Two-Dimensional Infrared Absorptive Spectra Using Chirped Pulse Upconversion

The work presented in this chapter has been published in the following paper:

> Jessica M. Anna, Matthew J. Nee, Carlos R. Baiz, Robert McCanne, and Kevin J. Kubarych, "*Measuring absorptive two-dimensional infrared spectra using chirped-pulse upconversion detection*," Journal of the Optical Society of America B, 27, 2010, 382-393.

3.1 Overview: Chapter 3

This chapter demonstrates how to obtain two-dimensional infrared absorptive spectra using chirped-pulse upconversion (CPU). The benefits along with the disadvantages associated with using CPU for detection of the mid-infrared signal field are compared to the more conventional method of directly detecting the mid-infrared signal field using a HgCdTe (MCT). One of the drawbacks to using CPU arises from the inherent cross-phase modulation. The resulting distortions are revealed when a system has narrow spectral features or when phase sensitive spectra are desired. The removal of these phase distortions from all of the measurements required to obtain an absorptive 2DIR spectrum using CPU, including delay stage calibrations as well as

the requisite nonlinear signals, is demonstrated. Also, this chapter details the phasing procedure used to obtain absorptive spectra. This procedure is shown to operate well for both inhomogeneous and homogeneous broadened spectra.

3.2 Chirped-Pulsed Upconversion 2DIR Spectroscopy

One of the challenges in 2DIR spectroscopy lies in the detection of the emitted IR signal field. Most ultrafast IR spectroscopy is currently done using various 1D HgCdTe (MCT) arrays of 32, 64, or 128-pixels, sometimes in pairs to provide a reference. These detectors are costly, and are only useful in the IR, while suffering from complicated electronics and low intrinsic sensitivity as parameterized by the so-called specific detectivity D*. Using CPU, we are able to circumvent this limitation by using sum-frequency generation (SFG) to shift the emitted IR field to the visible which can be detected using a silicon CCD camera mated to a conventional spectrometer.[1-3] Specifically, we mix a highly chirped near-IR pulse centered at 800 nm with an emitted IR signal near 5 μm. The resulting ~700 nm light is easily detected on a 100x1340-pixel CCD array, providing an order-of-magnitude multiplex advantage over a 128-pixel IR detector array. The use of a chirped pulse is primarily a matter of convenience: the uncompressed output of a regenerative amplifier is perfectly synchronized to the IR pulse, while the high degree of chirp leads to a narrow bandwidth that is temporally coincident with the few-picosecond IR field, adding minimal spectral broadening in the upconverted output. Fig. 3.1 demonstrates this point. Figure 3.1 shows a cartoon spectrum of the chirped pulse along with a narrow (green) and broad (blue) spectral feature and the corresponding Fourier transforms. From Fig. 3.1, it can be seen that a signal having a short dephasing time (broad spectral features) will be effectively upconverted with a single frequency; however, for signals with longer dephasing times (narrow spectral features), different parts of the signal will be upconverted with slightly different frequencies of the chirped pulse leading to the spectral phase distortions.

For many applications, especially those where the phase of the signal is not particularly important or where the IR spectral features are sufficiently broad, there is no need to correct for the spectral phase distortion—due to cross-phase modulation during the SFG process—imparted by the chirped pulse.[4] However, in order to optimize the spectral resolution or to measure absorptive 2DIR signals the distortions caused by chirped-pulse upconversion are deleterious and must be corrected

The use of a chirped pulse is primarily a matter of convenience: the uncompressed output of a regenerative amplifier is perfectly synchronized to the IR pulse, and, as is shown in Fig. 3.1 broad spectral features are not significantly distorted. However, it is not necessary to use a chirped pulse: a narrow-band, transform limited pulse could also be used to upconvert the mid-IR signal. Assuming

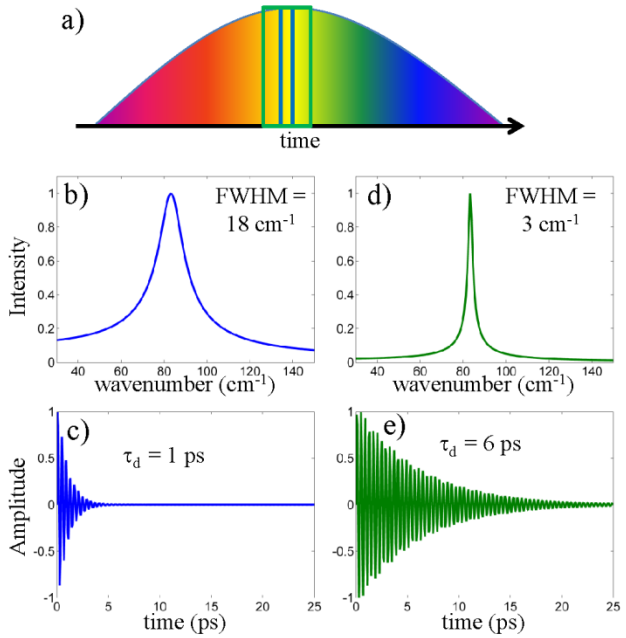

Figure 3.1 (a) Cartoon representation of a chirped-pulse with the temporal extent of the broad (blue box) and narrow (green box) spectral features indicated. (b) Broad spectral feature with corresponding time-domain signal (c). (d) Narrow spectral feature with corresponding time-domain signal (e).

that the cross-phase modulation of the SFG signal is due solely to the second-order upconversion process, there is no limitation of the present phase correction scheme to a particular magnitude or functional form of the chirped-pulse's spectral phase—

provided it is accurately measured. Since a transform-limited pulse is simply one with zero quadratic or higher-order spectral phase, there is no reason such a pulse could not be used. The only practical requirement for the mixing pulse is that it temporally overlaps the mid-IR signal. Since the SFG process is a time-domain product, the upconverted field will be the spectral convolution of the mid-IR and mixing pulses. Achieving maximal spectral resolution requires deconvolving the mixing pulse's spectral amplitude. Indeed, the numerical manipulations of the recorded spectra would be identical to those described here, except that the emphasis of the correction would be on the temporal amplitude of the transform-limited mixing pulse since its phase is trivial (i.e. first order or lower). Given that upconversion using either a chirped or a transform-limited pulse requires the same correction, our approach eliminates the need to implement a spectral filter to produce a narrow-band mixing pulse from our 130 cm^{-1} bandwidth amplifier output. Also, it is important to note that it should be possible to increase upconversion efficiency by tailoring the chirped pulse duration to match the temporal extent of the mid-IR signal to be measured, particularly for the case of transient absorption. When using a shorter pulse, however, both the amplitude and phase of the SFG signal will require correction, and care must be taken to avoid third-order cross-phase modulation. Such an optimization has yet to be shown experimentally, but work is currently underway in our laboratory. It should also be noted that Tokmakoff *et al.* have implemented an alternative approach to using upconversion for IR signal detection without a chirped pulse that relies on upconverting the dispersed mid-IR light in a spectrometer.[5, 6]

This chapter focuses on obtaining 2DIR spectra using the background-free method for detection, but there are alternate strategies to measure two-dimensional spectra in a modified pump-probe geometry where either an interferometer or a pulse shaper generates the first two pulses of the three-pulse sequence.[7-9] As has recently been demonstrated in the visible[10], the pump-probe method enables the use of a continuum probe.[11] In the mid-IR it is more difficult to produce an ultra-broadband continuum, but recent progress has been made.[12-15] In order for the full bandwidth of

the IR probe to be useful in a multichannel spectrometer, one requires a detector with a very large multiplex detection capability. For example, with a 4 cm^{-1} spectral resolution, a current state-of-the-art, 128-pixel MCT detector array is only able to cover 512 cm^{-1} of the IR spectrum, effectively negating the benefit of the broadband continuum (which can span more than 2000 cm^{-1}). Using the full spectral coverage of a typical CCD camera, at 4 cm^{-1} resolution it is possible to cover the entire IR spectral range. The limitation of CPU is the phase-matched sum-frequency process, but this can be addressed using a thin upconversion crystal combined with increased near-IR intensity. Using the known material dispersion, we calculate the mixing bandwidth for a mid-IR field centered at 2105 cm^{-1} upconverted with a field centered at 800 nm to be 3000 cm^{-1} when a 0.1 mm thick $LiNbO_3$ crystal is used at a single angle.[16] Sum-frequency bandwidth can be further extended by dithering the crystal or by using achromatic imaging approaches.[17, 18] Further, the amplitude filtering of the upconverted light due to the finite phase-matching bandwidth can be calculated, enabling the spectra to be corrected. Since any phase shifts due to imperfect phase matching will be common to the signal and the local oscillator (i.e. the probe), only the spectral amplitude requires correction. Chirped-pulse upconversion offers an attractive ultra-broadband technique to record single-shot mid-IR continuum probes that may become a popular option for ultrafast transient IR and 2DIR spectroscopy.

3.3 Simulated Effect of Spectral Phase Distortions

Considering a model 2D response function the FTSI procedure is illustrated while demonstrating the effect of chirped pulse upconversion. Early work in 2DIR by Tokmakoff on a rhodium dicarbonyl (RDC) complex, dicarbonylacetylacetonato rhodium(I) (Fig. 3.2), provided a complete picture of the molecule's CO vibrational eigenstates, along with the excited states that reveal the vibrational anharmonicity.[19-23] With knowledge of the transition energies and their associated transition dipole moments, it is possible to simulate nearly perfectly the measured 2DIR spectrum in a weakly interacting non-polar solvent such as hexane. Using the previously reported

analytical 2D response function[20], we illustrate the added complications that arise due to CPU detection. The key finding is both the absolute-value rephasing signal and the recovered signal phase are affected by the CPU process. The distortions typically arise as a series of small peaks to higher frequencies of the peaks in the spectrum. Because the lineshapes of the peaks in the spectra are affected by the distortions, correcting for the cross-phase modulation is mandatory for measuring meaningful absorptive 2D lineshapes. It is these lineshapes that contain much of the dynamical information that 2D spectroscopy seeks to extract.[19, 24-28]

Figure 3.2 shows a schematic representation of both the FTSI and CPU processes. The chirped field, E_{CP}, has a positive linear chirp due to a purely second

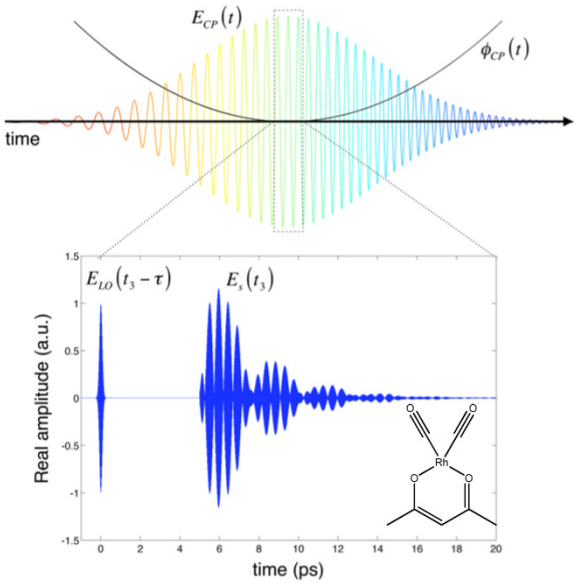

Figure 3.2 Chirped pulse amplitude (undersampled) and phase. (top) The dashed rectangle shows the temporal extent of the IR fields. (bottom) Real part of the amplitude of the *LO* and the emitted echo signal for the case of $t_1 = t_2 = 0$ with the molecular structure of RDC shown.

order phase. The experimental value was measured by frequency-resolved sum-frequency generation with the compressed 100-fs 800-nm pulse, and is the only auxiliary experimental measurement that must be performed to correct the distortion caused by CPU for absorption and echo spectra. Since the chirped pulse has a time-bandwidth product of roughly 1200, it would be classified as being highly complex,

and a challenge to measure with self-referencing methods such as frequency resolved optical gating or spectral phase interferometry for direct electric field reconstruction.

Moreover, it is very easy to map out the instantaneous frequency by SFG with the mid-IR pulse directly within the 2D spectrometer, and such measurements yield the same chirp value as is obtained by SFG with an 800 nm pulse. Fitting the center of the resulting SFG spectrum gives the instantaneous frequency of the chirped pulse

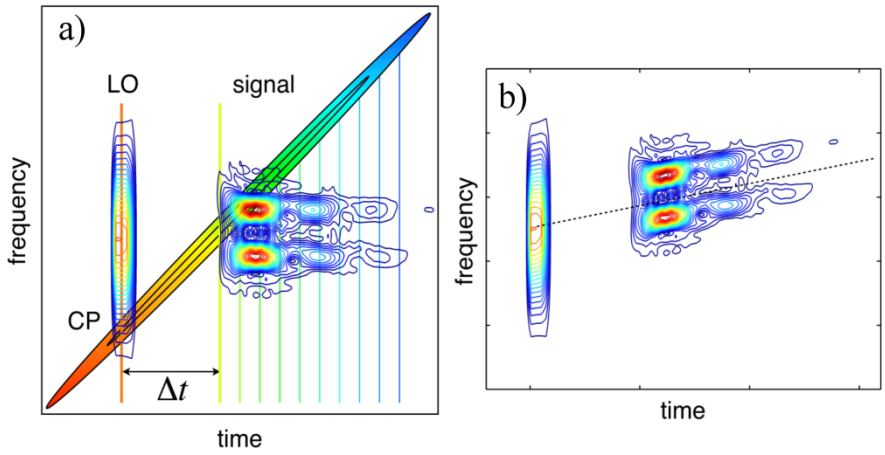

Figure 3.3 (a) Sonogram of the *LO* and signal fields, separated in time by Δ*t*, superimposed on a cartoon sonogram of the positively chirped near-IR pulse. (b) Simulated sonogram of the upconverted field the dotted line indicates the linear chirp of the signal imparted by the chirped pulse.

as a function of time since the short gate pulse is known to be centered at 800 nm. Fitting the variation of frequency gives a chirp rate of 0.5 cm^{-1}/ps, which is equivalent to a 8.33-ps^2 second-order temporal phase.[1] The local oscillator (LO), E_{LO}, is simulated to be advanced 10 ps relative to E_3 and the signal is emitted following the arrival of E_3. Since the dephasing times for the transitions considered here are long, no accounting for finite pulse durations is made except that the local oscillator is simulated to have a bandwidth that matches our experimental conditions (~150 cm^{-1}). The dotted box in the center of the chirped pulse field shows the temporal extent of the IR field—signal and LO—to be upconverted. Ignoring the effects of phase matching for the SFG process, the resulting upconverted field, E_{CPU}, is given by (Eq. 3.1)[4]:

$$E_{CPU}(t) = \left[E_S(t) + E_{LO}(t)\right] E_{CP}(t) \qquad \textbf{Eq. 3.1}$$

By representing the chirped field and IR field as a sonogram (Fig. 3.3), it is clear that the chirp imposes a quadratic spectral phase on the upconverted field, resulting in a linear chirp of the echo signal. Fig 3.3a displays the chirped, signal and LO fields before the upconversion processes, and Fig 3.3b displays the resulting upconverted fields. The chirped field is given in Eq. 3.2 where ω_0 is the center frequency of the chirped pulse and $\varphi^{(2)}$ is the quadratic phase of the chirped pulse, and the upconverted LO field is given in Eq. 3.3.[4]

$$E_{CP}(t) = A(t) e^{-i\omega_0 t} e^{-i\frac{t^2}{2\varphi^{(2)}}} \qquad \textbf{Eq. 3.2}$$

$$E_{LO,CPU}(t) \propto E_{LO}(t) e^{-i\omega_0 t} \qquad \textbf{Eq. 3.3}$$

The LO is transform limited and does not vary with time. This leads to the desired effect: the upconverted LO field is translated in frequency without any significant contribution from the quadratic spectral phase of the chirped pulse, which is evident from Fig. 3.3b and Eq. 3.3. The signal field varies arbitrarily with time, and the temporal extent of the signal depends on the molecular system being studied. The resulting upconverted signal field is given in Eq. 3.4.[4]

$$E_{S,CPU}(t) = E_S(t) e^{-i\omega_0 t} e^{-i\frac{t^2}{2\varphi^{(2)}}} \qquad \textbf{Eq. 3.4}$$

Along with the translation in frequency space, there is also some contribution from the second order quadratic phase of the chirped pulse to the echo signal. As can be seen from Eq. 3.4 and Fig. 3.3b the resulting upconverted echo signal has a linear chirp. In the experiment, the frequency of the echo signal increases as a function of time with a rate corresponding to 0.5 cm^{-1}/ps.

Analysis of a simulated spectral interferogram of the upconverted field E_{CPU} and an exact IR interferogram (i.e. E_s + E_{LO}) demonstrates the effect of the chirp on the signal. Transforming the data to the time domain, applying a filter to remove E_{LO},

inverse Fourier transforming the filtered complex data and removal of the linear phase due to the time delay Δt yields an absolute-magnitude spectrum shown in Fig. 3.4 with the real and imaginary parts of the signal shown in Fig. 3.4b-c. Comparing the exact and upconverted results we see the main distortions imparted by the chirped pulse as small modulations to the higher frequency side of the peaks in the spectra. The modulations appear at higher frequencies because the chirped pulse is positively chirped. As depicted in Fig. 3.3 when the signal is mixed with the chirped pulse different parts of the signal will be upconverted with slightly different frequencies leading to spectral modulations. A positive chirp, will lead to distortions

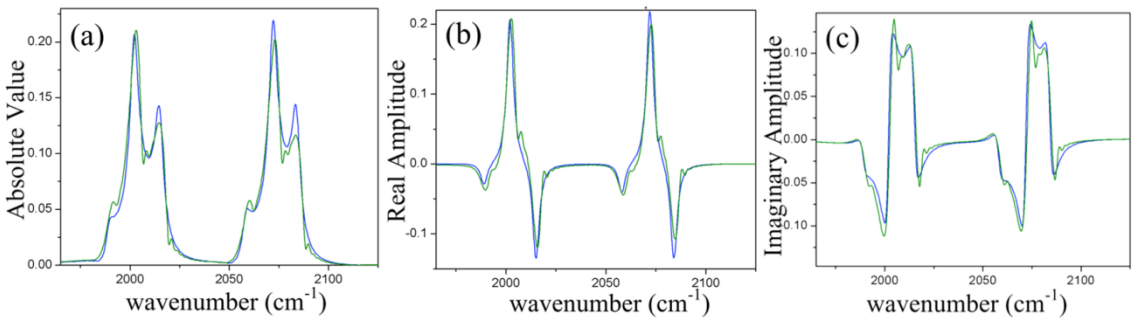

Figure 3.4 Simulated RDC absolute value (a), real (b) and imaginary (c) parts of the echo signal as would be measured directly (blue) and using CPU (green).

at slightly higher frequencies, while a negative chirp will lead to distortions at slightly lower frequencies of the peaks. For an extremely chirped pulse, the frequency of the mixing pulse will be practically constant over the signal range minimizing the distortions. Although this simulation only considers the rephasing signal, similar distortions will appear in the nonrephasing signal.

3.4 Correction of Vibrational Echo Signal

To correct the 2DIR vibrational echo signal we apply the correction to each interferogram collected for a given value of t_1. The steps for the correction procedure are depicted in Figure 3.5. Each step was performed using the RDC model to simulate a signal that is upconverted with an 800-nm pulse with the same chirp characteristics as our experimental pulse. The figure shows the resulting real,

imaginary and absolute values of the amplitudes for the corrected upconverted data, (black) and the exact simulated data (i.e. the simulated data without upconversion)

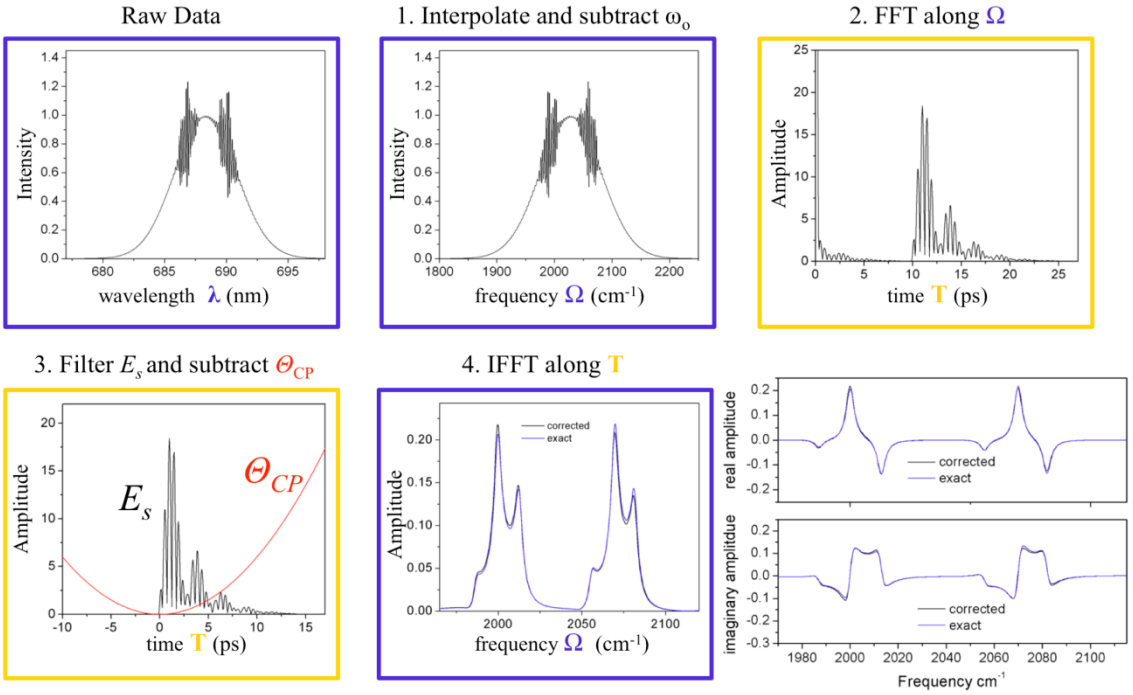

Figure 3.5 Steps required for removal of the distortions caused by CPU using simulated data for the RDC system (see text for details). Blue (orange) boxes correspond to data in the frequency (time) domain. Final pane shows real and imaginary amplitudes of the signal for the corrected data (black) versus the exact simulation (blue).

(blue). A more detailed description of each step in the correction process follows. Since the detected interferograms are collected as a function of wavelength, the first step in the correction process is to interpolate the interferograms to be evenly spaced in the frequency domain, ω_{det}. The frequencies are then shifted to the mid-IR region, $\Omega=\omega_{det}-\omega_o$ where ω_o is the center frequency of the chirped pulse; this accounts for the removal of the linear temporal phase (i.e. frequency shift) contribution of the chirped pulse, $\exp(-i\omega_o t)$. The center frequency of the chirped pulse is determined by comparing the frequencies of the peaks along the ω_3 axis to the frequencies of the peaks obtained from a linear FT-IR spectrum. The center frequency ω_o is the difference between the detected frequencies along ω_3 axis and the frequencies determined from the FT-IR. The second step is to Fourier transform with respect to

Ω to the time domain (denoted by T) where a filter is applied to remove the local oscillator, leaving the signal field plus the added linear phase due to the signal-LO delay, Δt. After removing the local oscillator, the quadratic phase of the chirped pulse, Θ_{CP}, is removed from the signal by multiplying the complex signal in the time domain by $\exp(iT^2/2\varphi^{(2)})$, where $\varphi^{(2)}$ is the measured quadratic phase of the chirped pulse.[4] It is important to note that the phase function, $\exp(iT^2/2\varphi^{(2)})$, is shifted so that its origin corresponds to the temporal origin of the signal (this is depicted in step 3 of Fig. 3.5) which is determined from an interferogram between the local oscillator and scatter from E_3. Shifting the function ensures that the added linear phase from the signal-LO delay is not being taken into account during the chirp correction. The final step is to apply an inverse Fourier transform along T resulting in the corrected signal field.

We have applied this correction method to a rephasing spectrum of a 3 mM solution of dimanganese decacarbonyl, $Mn_2(CO)_{10}$, in *n*-hexane.[29] In Figure 3.6a the absolute value of the amplitude of a slice taken from the 2D rephasing spectrum

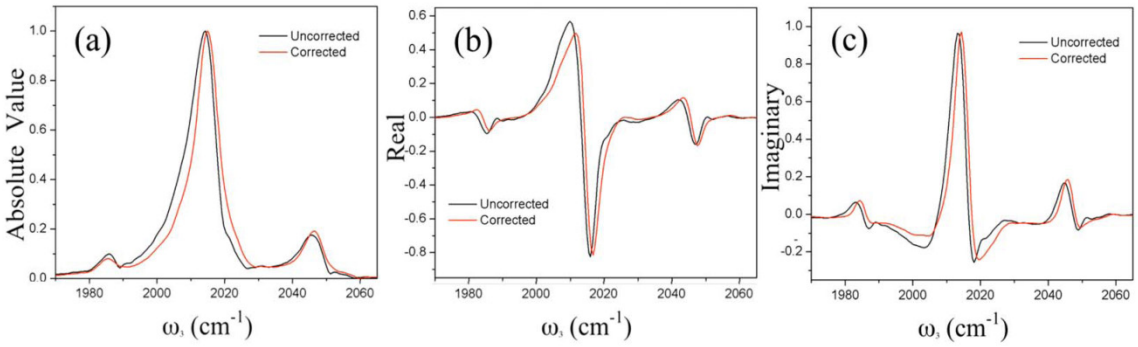

Figure 3.6 Normalized absolute value (a), real (b) and imaginary(c) amplitude of a slice along ω_3 at ω_1=2015 cm^{-1} for the rephasing spectrum of $Mn_2(CO)_{10}$ at t_2=5 for corrected (red) and uncorrected (black) data.

along ω_3 for ω_1= 2015 cm^{-1} is shown for the corrected data (red) and the uncorrected data (black) and Figure 3.6b-c shows the real and imaginary amplitudes of the slice for the corrected and uncorrected data. Comparing the slices isolates the distortions of the signal due to CPU. The uncorrected data has modulations on the blue side of

the peaks, which is a predicted distortion from the chirped pulse whereas the modulations are not present in the corrected data.

3.5 Calibration of Scanned t_1 Time Delay

In order to obtain a 2DIR spectrum, the time delay between the first two pulses, t_1, is scanned continuously for a given t_2, and a Fourier transform with respect to t_1 results in the ω_{excite} axis of the 2DIR spectrum. A pair of ZnSe wedges is used to scan the t_1 time delay.[30] In order to calibrate the wedges we obtain a series of interferograms which have distortions imparted by the chirped pulse. In this section we describe both the wedge calibration procedure along with the correction procedure for the removal of the distortions from the interferograms.

For each pair of wedges, one is held stationary and the other is mounted to a translation stage actuated by a DC motor which is used to scan the t_1 axis. To map the motor encoder positions to time delays, the wedges are calibrated using interferograms between the upconverted scatter of E_1 and E_2 recorded as each ZnSe wedge is scanned. Scanning the wedges gives a maximum t_1 delay of 12 ps which corresponds to 2.78 cm^{-1} resolution. For typical scans (10,000 interferograms) the spacing between the time points is ~1 fs; however, a minimum spacing of 0.4 fs—limited by the slowest practical motor movement—can be obtained by scanning the motors at a slower rate. A moving window Fourier transform method is used to correct for shifts in the frequency of the pixel, which is assigned using a known absorption feature. Since the chirped pulse's spectrum is roughly 130 cm^{-1} (FWHM) broad, there is an uncertainty in the upconverted signal wavelength. The tracer is used to set the absolute frequency of the detection axis by using spectral interference, via scatter, with either E_1 or E_2 with a molecular sample present, and then setting the delay to zero by nulling the fringes. With multiple bands present in the IR absorption spectrum, a polynomial can be used to map pixel to IR wavenumber.

Before calibrating the wedges we first remove the distortions from the interferograms using a procedure very similar to the correction of the 2DIR

vibrational echo, with the only difference occurring in step three of Figure 3.5; the shifting of the phase function. The phase function, $\exp(iT^2/2\varphi^{(2)})$, is shifted so that the origin of the function corresponds to the origin of the signal, so that the linear phase contribution from the time delay between E_1 and E_2, Δt_c, is not being compensated in the correction. For the calibrations, the value of Δt_c will necessarily change for each interferogram, so at each time step Δt_c is determined by fitting the peak in the time domain to a Gaussian function.

In Figure 3.7a, the absolute value of the Fourier transform of the uncalibrated pixel corresponding to 2015 cm^{-1} is shown for the uncorrected (black) and corrected

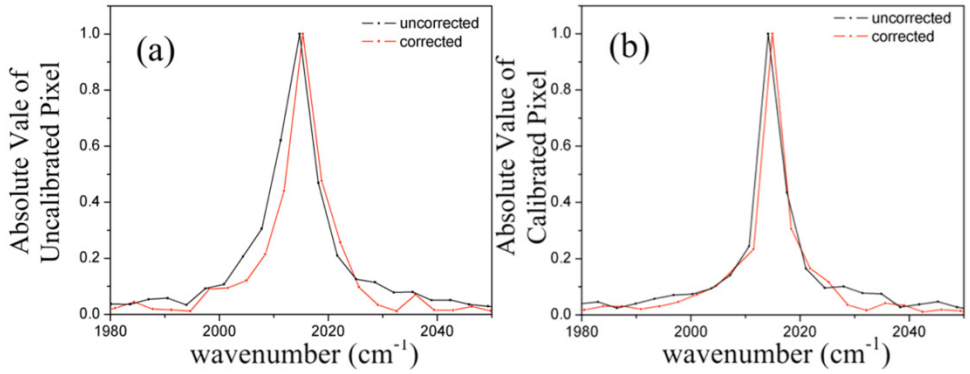

Figure 3.7 (a) Absolute value of the Fourier transform of the uncalibrated corrected (red) and uncorrected (black) data for the pixel corresponding to 2015 cm^{-1}. (b) Absolute value of the Fourier transform of the calibrated uncorrected (black) and corrected (red) data.

(red) data. This comparison isolates the distortions caused by the CPU alone. Comparing the two, we see a narrowing of the peak due to correcting the distortions. Figure 3.7b shows the absolute value of the Fourier transform of the calibrated pixel for the corrected (red) and uncorrected (black) data. Comparing the two peaks we see a slight difference; however, the spectral width seems comparable for the peaks indicating that the calibration itself corrects for some of the spectral phase contributions of the chirped pulse. In both figures, the data points for the corrected and uncorrected peaks are not at the exact same frequency; this is inherent to the calibration, as the mapping of the encoder positions to time delays is slightly different

for the corrected and uncorrected peaks resulting in a slightly different frequency spacing.

3.6 Correction of Pump-Probe Spectrum

Using the background free method for detecting both rephasing and nonrephasing spectra, and without further measurements of the absolute phase, the pump-probe spectrum is required for obtaining an absorptive spectrum. In this section we describe the procedure for the removal of the distortions imparted by the chirped pulse to the pump-probe spectrum. The IR-pump/IR-probe spectrum is obtained by subtracting the pumped tracer absorption from the unpumped absorption, but before subtraction, the individual absorption spectra are independently corrected according to the procedure described by Lee *et. al.*.[4] The correction procedure is similar to Fig 3.5 with the difference lying in step 3. In step 3, a filter is no longer applied, and Θ_{CP} is subtracted by multiplying the signal by $\exp(sign(T)*iT^2/2\varphi^{(2)})$, that is, by the anti-symmetrized phase, which reflects the causality of the absorption signal. We illustrate this method using a 3 mM solution of $Mn_2(CO)_{10}$ in *n*-hexane. The corrected (red) and uncorrected (black) pump-probe

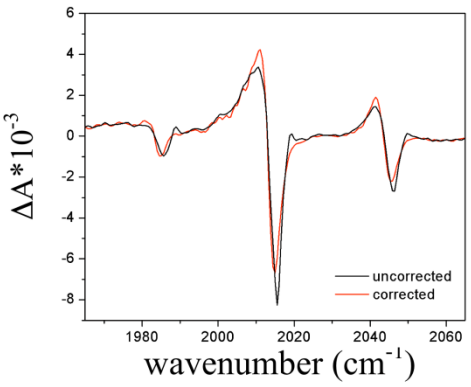

Figure 3.8 Corrected (red) and uncorrected (black) pump-probe spectra of $Mn_2(CO)_{10}$ at a delay time of 5 ps.

spectra are shown in Fig. 3.8. Comparing the two spectra we see the distortions present as small peak-like features to the blue of the ground state absorptions for the uncorrected spectrum. These features are absent in the corrected spectrum.

3.7 Obtaining Absorptive Spectra

After correcting for the phase distortions induced by the chirped pulse, the 2D absorptive spectrum can be obtained by adding the real parts of the rephasing and nonrephasing spectra (Eq. 3.5):[24, 31]

$$S(\omega_1, t_2, \omega_3) = \mathrm{Re}\left[\int_0^\infty dt_1 \int_0^\infty dt_3 S_R(t_1, t_2, t_3) e^{i\omega_3 t_3} e^{-i\omega_1 t_1} + \int_0^\infty dt_1 \int_0^\infty dt_3 S_{NR}(t_1, t_2, t_3) e^{i\omega_1 t_1} e^{i\omega_3 t_3}\right] \quad \textbf{Eq. 3.5}$$

Before the signals are added they must first be "phased." Typical phasing procedures call for the multiplication of the signal by a phase $\exp(i\Phi)$ where $\Phi(\omega_1, \omega_3) = \omega_1 \Delta t_1 + \omega_3 \Delta t_3 + \theta$.[32, 33] The two linear phase terms $\omega_1 \Delta t_1$ and $\omega_3 \Delta t_3$ account for distortions of the spectral phase of the signals arising from the inability to determine precisely the origins of t_1 and t_3 in Eq. 3.5. The constant phase, θ, accounts for the constant relative phase difference between the rephasing and nonrephasing signals.

3.8 Phasing the Corrected Rephasing and Nonrephasing Signals

Using a set of interferograms between the scatter of E_1 and E_2 and an interferogram between E_3 and E_{LO}, the origins of the t_1 and the t_3 axes are determined to within sufficient precision that the linear phase contributions in $e^{i\Phi}$, $\omega_1 \Delta t_1$ and $\omega_3 \Delta t_3$, can be neglected. Experimentally we determine the origin of the t_1 axis ($t_1 = 0$) from the same data used to calibrate the wedges. Each interferogram is transformed to the time domain, where the peak due to the interference is fit to a Gaussian enabling the time difference to be determined to within 1 fs. The time differences are then fit to a line (R^2=0.995) and extrapolated to t_1=0. An interferogram between the E_{LO} and scatter from E_3 is used to determine the difference in timing between E_3 and the E_{LO} to within 1 fs eliminating the need for the linear phase term along ω_3. Using these measurements we are able to neglect the linear phase contributions due to the timing errors; however, the constant phase,

which accounts for the relative phase difference between the rephasing and nonrephasing spectra, still needs to be determined. To determine θ_R and θ_{NR} we use a genetic algorithm searching method with a fitness function consisting of two parts, $f_{\omega 3}$ along ω_3, and $f_{\omega 1}$, along ω_1. Making use of the projection slice theorem we define $f_{\omega 3}$ to be minimized when the projection of the absorptive spectrum on to the ω_3 axis equals the pump-probe spectrum.[25, 34] The $f_{\omega 1}$ contribution is minimized when the normalized projections of the absolute value of the rephasing and nonrephasing spectra on to ω_1 match the normalized projection of the absolute value of the absorptive spectrum on to ω_1. The values of θ_R and θ_{NR} are obtained when the total fitness function, $f = f_{\omega 1} + f_{\omega 3}$, is minimized.

Figure 3.9a displays an absorptive spectrum of a 3 mM solution of $Mn_2(CO)_{10}$ in *n*-hexane at t_2= 5 ps. The color scheme is such that blue peaks are negative,

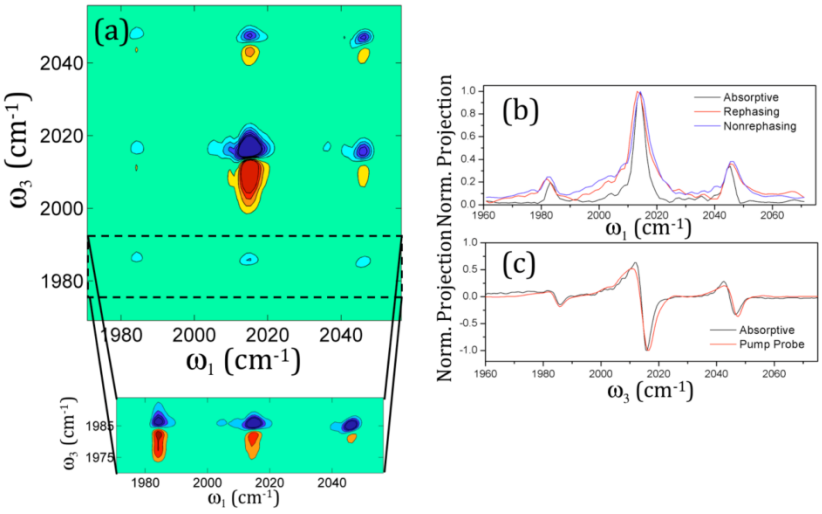

Figure 3.9 (a) Absorptive 2DIR spectrum of $Mn_2(CO)_{10}$ at t_2 = 5 ps. (b) Normalized projections of the absolute value of the absorptive (black), rephasing (red) and nonrephasing (blue) spectra on to ω_1. (c) Projection of the absorptive spectrum (black) on to $\omega_3$and the corrected pump-probe spectrum (red).

corresponding to ground-state bleach and stimulated emission, and red peaks are positive, corresponding to induced excited-state absorption. As expected, the 2DIR spectrum of DMDC consists of a set of nine negative peaks due to the coupling between the three bands observed in the linear FT-IR spectrum. Below each negative

peak is a positive peak at lower detection frequency, corresponding to the red-shifted excited state absorption. It is typically the case for molecular vibrations that the potential gives rise to positive anharmonicity, where the transition between the first and second excited state is lower in energy than the transition from the ground state to the first excited state. Zooming in on the peaks at ω_3=1980 cm^{-1} clearly shows the presence of the induced absorption peaks. The induced absorption peaks along the diagonal seem to be elongated; this minor effect could be due to faster dephasing or to the contribution of fifth order processes to the signal. The spectrum was obtained using the phasing procedure described above. Figure 3.9b displays the normalized projection of the absolute value of the correctly phased absorptive spectra on to ω_1 (black) and the normalized projection of the absolute value of the rephasing (red) and nonrephasing (blue) on to the ω_1 axis. Figure 3.9c shows the projection of the absorptive spectrum on to the ω_3 axis (red) along with the corrected pump-probe spectrum (black).

We have also applied the phasing procedure to rephasing and nonrephasing spectra that have not been corrected for CPU. Figure 3.10 shows the absorptive

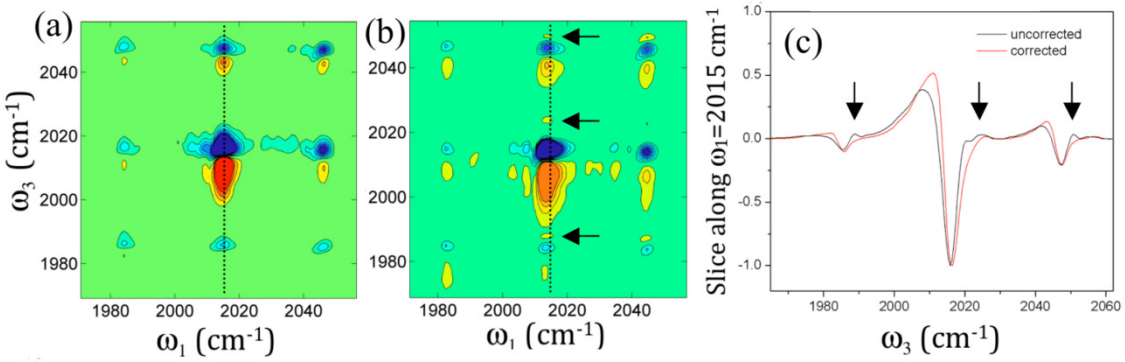

Figure 3.10 Absorptive 2DIR spectrum with the distortions from the chirped pulse removed (a) and not removed (b). (c) Slice along ω_3 at ω_1 = 2015 cm^{-1} for the corrected (red) and uncorrected (black) data. Distortions along the ω_3 axis are indicated with arrows.

spectra of $Mn_2(CO)_{10}$ in *n*-hexane at t_2=5ps obtained from the corrected (a) and the uncorrected (b) data. For the uncorrected data we see distortions of the lineshapes along with small peaks (indicated with arrows) along the ω_3 axis lying at a higher

frequency relative to the peaks from $Mn_2(CO)_{10}$. A slice along ω_3 at ω_1=2015 cm^{-1} (Fig. 3.10c) is plotted for the corrected (red) and uncorrected (black) data with the distortions indicated with arrows. Since each absorptive spectrum requires only roughly 20 seconds of experimental acquisition time (10 s for each rephasing and nonrephasing scan), spectra for many waiting times can be recorded in relatively rapid succession. Here we test the robustness of our phasing parameters for spectra measured with different waiting times. The origin of t_1 determined from the set of interferograms between E_1 and E_2 is approximately equivalent for each t_1 as t_2 is stepped. The reason for this reproducibility lies in our ability to return motors to the within ±20 encoder positions of the starting position, corresponding to ±0.1 fs. The origin of t_3 does not change as t_2 is stepped because the E_{LO} is locked in time with E_3. The E_3/LO beam splitter is placed after the delay stage, so as t_2 is scanned the relative timing between E_{LO} and E_3 remains constant. The values of θ_R and θ_{NR}, however, need to be determined for each t_2 step. The phasing procedure described above is applied to each rephasing and nonrephasing spectrum for each value of t_2 to obtain the corresponding absorptive spectrum (approximately 3 hours of processing time for a typical data set consisting of ~100 t_2 time steps).

To demonstrate the effects of using a pump-probe spectrum having a time delay different from that of t_2 we obtained two absorptive spectra of $Mn_2(CO)_{12}$ in *n*-hexane at t_2 = 2 ps. For the phasing procedure we used a pump-probe spectrum with a time delay of 2 ps and one having a time delay of 5 ps. To compare the results, the projections of the absorptive spectra on to ω_3 obtained from the phasing procedure using the pump-probe at 2 ps (red line) and the pump-probe at 5 ps (blue dots) are displayed in Figure 3.11a. In comparing the projections there is no visible difference between the projection of the absorptive spectrum obtained from the 2 ps and 5 ps pump-probe. A plot of the difference between the two projections (Fig. 311b) shows that the two projections differ by less than 1%. This insensitivity to the specific time delay necessarily depends on the vibrational lifetime, and will not be universal.

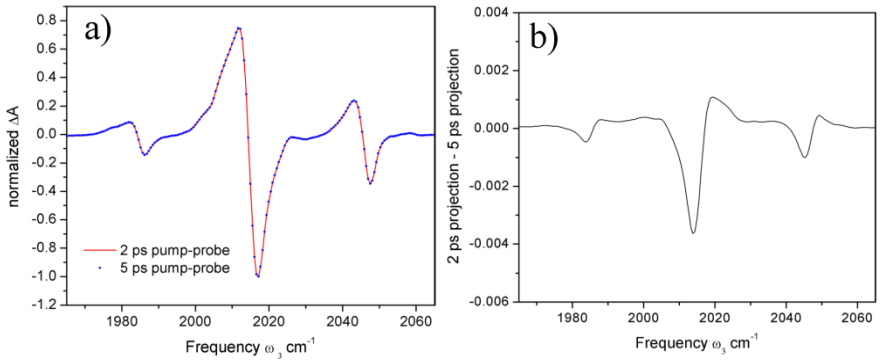

Figure 3.11 (a) The absorptive spectra of DMDC in *n*-hexane at t_2= 2 ps were obtained using pump-probe spectra at 2 ps and 5 ps and the projection of the absorptive spectra along ω_3 are shown, 2 ps pump-probe (red) and 5 ps pump-probe (blue). (b) The difference between the two projections is plotted.

3.9 Absorptive Spectra in a Polar Solvent

Since *n*-hexane is a weakly interacting non-polar solvent, the spectral features of the $Mn_2(CO)_{10}$ spectrum are particularly narrow, and provide a stringent test of the spectral resolution obtained using an absorptive 2D spectrum combined with CPU detection. Much of the chemical interest in 2DIR spectroscopy, however, concerns the presence of transient inhomogeneity which manifests itself as spectral diffusion. Due to a distribution of slightly different microscopic environments, transition frequencies are inhomogeneously distributed leading to a correlation between excited and detected frequencies, evident in a 2D spectrum as a diagonal elongation of the line shape for a given peak. In solution the individual sub-ensembles generally do not retain memory of their initial excitation frequencies indefinitely, so that increasing the waiting time delay t_2 leads to loss of the frequency correlation. The time scale of this frequency memory-loss is characterized by the frequency-frequency time correlation function.[25, 26, 35] Dissolving metal carbonyl complexes in polar solvents such as alcohols leads to slightly inhomogeneously broadened bands that exhibit spectral diffusion due to the polar solvent and the formation of hydrogen bonds.[19] Figure 3.12 shows absorptive 2DIR spectra of $Mn_2(CO)_{10}$ in methanol at two waiting time

delays, t_2 = 200 fs and 10 ps. The slight diagonal elongation seen at 200 fs is relaxed by 10 ps, a time scale for memory loss that is consistent with solvation dynamics. Although errors in phasing the absorptive spectrum seem more obvious and pronounced when the spectral features are narrow, the bulk of chemical interest concerns the analysis of 2D lineshapes in the presence of spectral diffusion. These data illustrate that chirped-corrected, CPU-detected 2DIR spectroscopy functions equally well for a system with some degree of inhomogeneity.

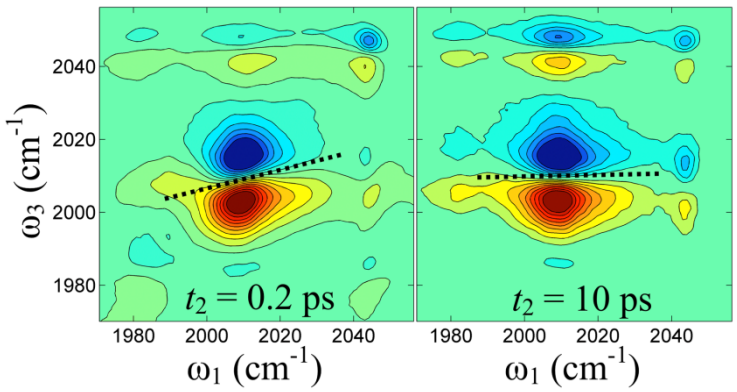

Figure 3.12 Absorptive 2DIR spectra of $Mn_2(CO)_{10}$ in methanol at (right) t_2 = 200 fs and (left) t_2 = 10 ps.

3.10 Conclusions

In this chapter, the general procedure for the removal of the cross-phase modulation acquired during sum-frequency generation[4] to CPU 2DIR spectroscopy was demonstrated and described in detail. For broad transitions and/or when phase sensitive measurements are not required, the correction is not necessary; however, to access the complete ultrafast dynamical information contained in the waiting-time evolution of the lineshapes, it is necessary to remove the distortions induced by the chirped pulse.

Along with demonstrating how to remove these phase distortions, giving a detailed step-by-step procedure, the method used for obtaining absorptive spectra from the corrected data was also described in detail. It was shown that this method

can be used to obtain spectra in both the homogeneous and inhomogeneous broadened cases. Though the correction of spectra obtained using the background-free beam geometry method of 2DIR spectroscopy was focused on, the approach can be applied to other implementation of 2DIR spectroscopy detected using CPU such as the pump-probe geometry or the hybrid frequency-time hole burning technique. We anticipate CPU to be an attractive method for detecting ultra-broadband mid-IR continuum probes in transient IR absorption and 2DIR spectroscopy.

References:

1. Nee, M., R. McCanne, K. Kubarych, and M. Joffre, *Two-dimensional infrared spectroscopy detected by chirped-pulse upconversion.* Opt. Lett., 2007. **32**(6): p. 713-715.

2. Lee, K.F., K.J. Kubarych, A. Bonvalet, and M. Joffre, *Characterization of mid-infrared femtosecond pulses [Invited]*. JOURNAL OF THE OPTICAL SOCIETY OF AMERICA B-OPTICAL PHYSICS, 2008. **25**(6): p. A54-A62.

3. Kubarych, K.J., M. Joffre, A. Moore, N. Belabas, and D.M. Jonas, *Mid-infrared electric field characterization using a visible charge-coupled-device-based spectrometer.* Opt. Lett., 2005. **30**(10): p. 1228-1230.

4. Lee, K., P. Nuernberger, A. Bonvalet, and M. Joffre, *Removing cross-phase modulation from midinfrared chirped-pulse upconversion spectra.* Optics Express, 2009. **17**: p. 18738-18744.

5. DeCamp, M., L. DeFlores, K. Jones, and A. Tokmakoff, *Single-shot two-dimensional infrared spectroscopy.* OPTICS EXPRESS, 2007. **15**(1): p. 233-241.

6. DeCamp, M. and A. Tokmakoff, *Upconversion multichannel infrared spectrometer.* Opt. Lett., 2005. **30**(14): p. 1818-1820.

7. Strasfeld, D., S. Shim, and M. Zanni, *NEW ADVANCES IN MID-IR PULSE SHAPING AND ITS APPLICATION TO 2D IR SPECTROSCOPY AND GROUND-STATE COHERENT CONTROL.* ADVANCES IN CHEMICAL PHYSICS, VOL 141, 2009. **141**: p. 1-28.

8. Shim, S., D. Strasfeld, Y. Ling, and M. Zanni, *Automated 2D IR spectroscopy using a mid-IR pulse shaper and application of this technology to the human islet amyloid polypeptide.* PROCEEDINGS OF THE NATIONAL ACADEMY OF

SCIENCES OF THE UNITED STATES OF AMERICA, 2007. **104**(36): p. 14197-14202.

9. DeFlores, L., R. Nicodemus, and A. Tokmakoff, *Two dimensional Fourier transform spectroscopy in the pump-probe geometry.* Opt. Lett., 2007. **32**(20): p. 2966-2968.

10. Myers, J., K. Lewis, P. Tekavec, and J. Ogilvie, *Two-color two-dimensional Fourier transform electronic spectroscopy with a pulse-shaper.* OPTICS EXPRESS, 2008. **16**(22): p. 17420-17428.

11. Tekavec, P., J. Myers, K. Lewis, and J. Ogilvie, *Two-dimensional electronic spectroscopy with a continuum probe.* Opt. Lett., 2009. **34**(9): p. 1390-1392.

12. Cook, D. and R. Hochstrasser, *Intense terahertz pulses by four-wave rectification in air.* Opt. Lett., 2000. **25**(16): p. 1210-1212.

13. Petersen, P.B. and A. Tokmakoff, *Source for ultrafast continuum infrared and terahertz radiation.* Opt. Lett., 2010. **35**(12): p. 1962-1964.

14. Armstrong, M., E. Reed, K. Kim, J. Glownia, W. Howard, E. Piner, and J. Roberts, *Observation of terahertz radiation coherently generated by acoustic waves.* NATURE PHYSICS, 2009. **5**(4): p. 285-288.

15. Kim, K., A. Taylor, J. Glownia, and G. Rodriguez, *Coherent control of terahertz supercontinuum generation in ultrafast laser-gas interactions.* NATURE PHOTONICS, 2008. **2**(10): p. 605-609.

16. Smith, A., *SNLO, free software for modeling nonlinear frequency conversion processes in nonlinear crystal.* http://www.as-photonics.com/SNLO.html.

17. O'Shea, P., M. Kimmel, X. Gu, and R. Trebino, *Increased-bandwidth in ultrashort-pulse measurement using an angle-dithered nonlinear-optical crystal.* OPTICS EXPRESS, 2000. **7**(10): p. 342-349.

18. Baum, P., S. Lochbrunner, and E. Riedle, *Tunable sub-10-fs ultraviolet pulses generated by achromatic frequency doubling.* Opt. Lett., 2004. **29**(14): p. 1686-1688.

19. Khalil, M., N. Demirdoven, and A. Tokmakoff, *Coherent 2D IR spectroscopy: Molecular structure and dynamics in solution.* J. Phys. Chem. A, 2003. **107**(27): p. 5258-5279.

20. Golonzka, O., M. Khalil, N. Demirdoven, and A. Tokmakoff, *Coupling and orientation between anharmonic vibrations characterized with two-dimensional infrared vibrational echo spectroscopy*. Journal of Chemical Physics, 2001. **115**(23): p. 10814-10828.

21. Demirdoven, N., M. Khalil, O. Golonzka, and A. Tokmakoff, *Correlation effects in the two-dimensional vibrational spectroscopy of coupled vibrations*. Journal of phySICAL CHEMISTRY A, 2001. **105**(34): p. 8025-8030.

22. Khalil, M. and A. Tokmakoff, *Signatures of vibrational interactions in coherent two-dimensional infrared spectroscopy*. Chemical Physics, 2001. **266**(2-3): p. 213-230.

23. Golonzka, O., M. Khalil, N. Demirdoven, and A. Tokmakoff, *Vibrational anharmonicities revealed by coherent two-dimensional infrared spectroscopy*. PHYSICAL REVIEW LETTERS, 2001. **86**(10): p. 2154-2157.

24. Khalil, M., N. Demirdoven, and A. Tokmakoff, *Obtaining absorptive line shapes in two-dimensional infrared vibrational correlation spectra*. Phys. Rev. Lett., 2003. **90**(4): p. 047401.

25. Faeder, S. and D. Jonas, *Two-dimensional electronic correlation and relaxation spectra: Theory and model calculations*. J. Phys. Chem. A, 1999. **103**(49): p. 10489-10505.

26. Roberts, S.T., J.J. Loparo, and A. Tokmakoff, *Characterization of spectral diffusion from two-dimensional line shapes*. JOURNAL OF CHEMICAL PHYSICS, 2006. **125**(8): p. -.

27. Tokmakoff, A., *Two-dimensional line shapes derived from coherent third-order nonlinear spectroscopy*. J. Phys. Chem. A, 2000. **104**(18): p. 4247-4255.

28. Okumura, K., A. Tokmakoff, and Y. Tanimura, *Two-dimensional line-shape analysis of photon-echo signal*. Chem. Phys. Lett., 1999. **314**(5-6): p. 488-495.

29. Baiz, C., P. McRobbie, J. Anna, E. Geva, and K. Kubarych, *Two-dimensional infrared spectroscopy of metal carbonyls*. Accounts of Chemical Research, 2009. **42**: p. 1395-1404.

30. Ding, F., P. Mukherjee, and M. Zanni, *Passively correcting phase drift in two-dimensional infrared spectroscopy*. Opt. Lett., 2006. **31**(19): p. 2918-2920.

31. Hybl, J., A. Albrecht, S. Faeder, and D. Jonas, *Two-dimensional electronic spectroscopy*. Chem. Phys. Lett., 1998. **297**(3-4): p. 307-313.

32. Gallagher, S., A. Albrecht, T. Hybl, B. Landin, B. Rajaram, and D. Jonas, *Heterodyne detection of the complete electric field of femtosecond four-wave mixing signals*. J. Opt. Soc. Am. B-Opt. Phys., 1998. **15**(8): p. 2338-2345.

33. Park, S., K. Kwak, and M. Fayer, *Ultrafast 2D-IR vibrational echo spectroscopy: a probe of molecular dynamics*. LASER PHYSICS LETTERS, 2007. **4**: p. 704-718.

34. Nagayama, K., P. Bachmann, K. Wuetrich, and R. Ernst, *USE OF CROSS-SECTIONS AND OF PROJECTIONS IN 2-DIMENSIONAL NMR-SPECTROSCOPY*. JOURNAL OF MAGNETIC RESONANCE, 1978. **31**(1): p. 133-148.

35. Kwak, K., D.E. Rosenfeld, and M.D. Fayer, *Taking apart the two-dimensional infrared vibrational echo spectra: More information and elimination of distortions*. JOURNAL OF CHEMICAL PHYSICS, 2008. **128**(20).

Chapter 4

Equilibrium Chemical Exchange: Determining Entropic and Enthalpic Barriers

The work presented in this chapter has been published in the following paper:

> Jessica M. Anna, Matthew R. Ross, and Kevin J. Kubarych, "*Dissecting Enthalpic and Entropic Barrier to Ultrafast Equilibrium Isomerization of a Flexible Molecule Using 2DIR Chemical Exchange Spectroscopy*," The Journal of Physical Chemistry A (letter), 113, 2009, 6544-6547.

4.1 Overview: Chapter 4

In this chapter 2DIR spectroscopy is used to study the dynamic equilibrium between the bridging and a non-bridging form of dicobalt octacarbonyl. The issue of extracting the rate constants to exchange from congested spectra having overlapping spectral features is addressed. Specifically, using the well-characterized coherent modulation of non-exchanging crosspeaks enables the isolation of the exchange contribution to the crosspeak from non-exchanging contributions. Through temperature dependent studies the barrier height for isomerization is extracted. An upper and lower limit to the barrier is obtained when the temperature dependence of the viscosity is accounted for. Analysis using the Eyring equation indicates a substantial entropic contribution to the free energy barrier ($\Delta S^{\ddagger}_{exp}>0$). Comparison to

quantum chemical calculations showed reasonable agreement for the activation energies but qualitative disagreement for the entropy of the transition state relative to the isomers ($\Delta S^{\ddagger}_{comp}<0$).

4.2 Dicobalt Octacarbonyl: Study of Dynamic Equilibrium

The equilibrium between two species is a dynamical process where reactants are consumed at the same rate they are regenerated. Despite the ubiquity of chemical equilibria, only with the development of ultrafast chemical exchange spectroscopy has it become possible to probe equilibrium kinetics of low-barrier reactions directly in the time domain.[1-8] 2DIR exchange spectroscopy has been applied to systems involving two different species such as solvent-solute complexes, free solute rotation about a carbon-carbon single bond, hydrogen bond formation and fluxionality. In this chapter we apply 2DIR exchange spectroscopy to dicobalt octacarbonyl [$Co_2(CO)_8$, DCO] which exists as three isomers in dynamic equilibrium.

Dicobalt octacarbonyl is known to be an important catalyst and precursor to catalysts of chemical reactions including the hydroformylation[9] and Pauson-Khand[10] reactions. DCO, is a flexible molecule, existing as three isomers at room temperature[11] that interconvert on the picosecond timescale (Fig. 4.1), and thus is an

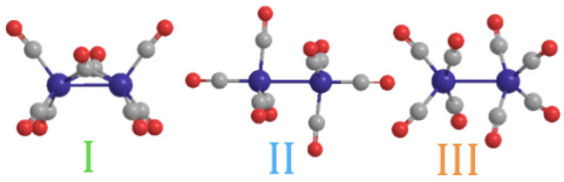

Figure 4.1 Three isomers of dicobalt octacarbonyl.

ideal model system to track with 2DIR exchange spectroscopy. Previous theoretical studies have explored both relative stabilities and isomerization barriers of DCO finding that some of the barriers were consistent with isomerization occurring on the picosecond timescale.[12, 13] Using 2DIR exchange spectroscopy we have directly observed interconversion between two of the three isomers, providing an

experimental measure of the isomerization barrier. Unlike the previous 2DIR exchange studies that had only two molecular species present, all three isomers of DCO have multiple overlapping vibrational transitions that complicate the isolation of the exchange component. We demonstrate a method that exploits predictable coherent quantum mechanical modulations of certain crosspeaks in the 2DIR spectrum to isolate the exchange signal, while extending chemical exchange to a system with more than two equilibrium species.

4.3 Linear FT-IR: Thermodynamics

The linear FT-IR spectrum of DCO in n-hexane at 25° C is shown in Fig. 4.2. The peaks in green have been previously assigned to isomer I (2040, 2044 and 2070 cm^{-1}), the peaks in blue to isomer II (2022 and 2067 cm^{-1}) and the peaks in orange to

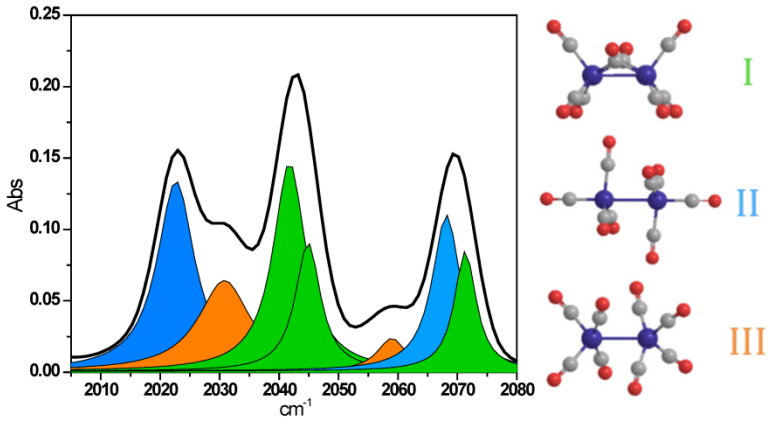

Figure 4.2 FT-IR spectrum of $Co_2(CO)_8$ in hexane is shown. The peaks in green at 2040, 2044 and 2070 cm^{-1} are assigned to isomer I. The peaks in blue at 2022 and 2067 cm^{-1} are assigned to isomer II, and the peaks in orange at 2030 and 2057 cm^{-1} are assigned to isomer III.

isomer III (2030 and 2057 cm^{-1}).[11] Fitting the linear FT-IR spectra to seven Lorentzians we obtain the areas of the peaks corresponding to the different isomers. Taking the ratio of the areas of the fitted peaks we can obtain the equilibrium constants. In a 2DIR spectrum, exchange crosspeaks grow with a rate constant that is the sum of the forward and reverse rate constants; the equilibrium constant is needed to find the separate rate constants.

2DIR spectra were collected at different temperatures, requiring the temperature-dependent equilibrium constants in order to extract the forward and reverse rate constants. We obtained several temperature-dependent linear FT-IR spectra ranging from 19C to 50°C which are displayed in Fig. 4.3a. The plotted

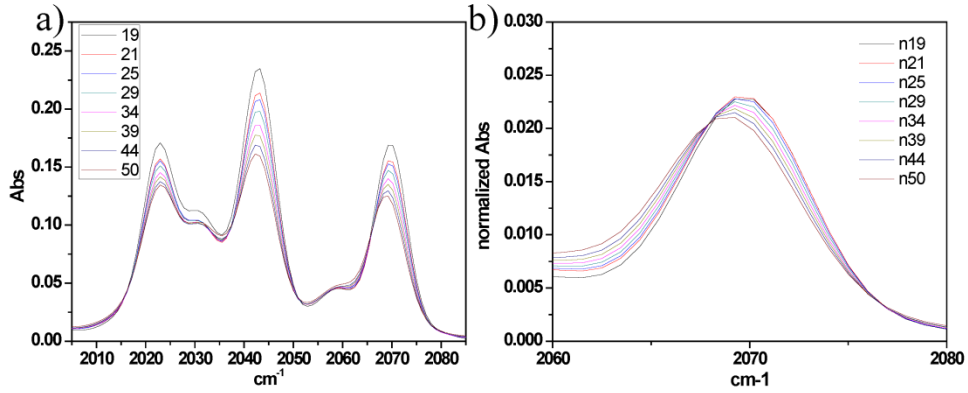

Figure 4.3 (a) Temperature dependent FT-IR spectra of $Co_2(CO)_8$ in n-hexane in terminal carbonyl region. (b) Focusing on the high frequency peak.

spectra are normalized to the total area. With increased temperature, the populations of the peaks assigned to isomer I and II decrease at different rates while the population of isomer III increases. Focusing on the peak centered at 2069 cm^{-1} (Fig. 4.3b) we see there is an isosbestic point indicating the presence of two distinct species, isomer I and isomer II. Isomer I is assigned to the higher frequency component and isomer II to the lower frequency. From the relative areas of the fitted peaks corresponding to isomer I and II we obtained equilibrium constants at 14, 25, and 50° C of $K_{I/II}$=1.13, 1.09 and 1.03.

We also obtained the relative enthalpy and entropy of isomer II to isomer I from the temperature dependent equilibrium constants. The van't Hoff equation (Eq. 4.1) describes how the equilibrium constant depends on temperature where K_{eq} is the equilibrium constant ΔH° is the change in enthalpy of the reaction and ΔS° is the change in entropy of the reaction.

$$\ln\left[K_{eq}\right] = -\frac{\Delta H^\circ}{RT} + \frac{\Delta S^\circ}{R} \qquad \textbf{Eq. 4.1}$$

Fig. 4.4 plots the natural log of the equilibrium constant versus 1/T. From the slope of the van't Hoff plot we obtain a $\Delta H°$= -0.49 kcal/mol and $\Delta S°$=-1.46 cal/(mol•K); both the entropy and enthalpy decrease upon isomerization from isomer II to isomer I.

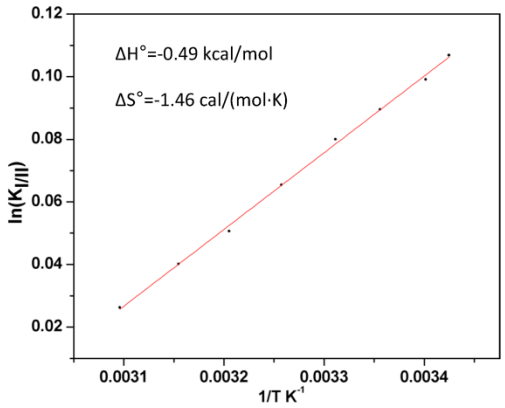

Figure 4.4 Van't Hoff plot using equilibrium constants determined from the relative total spectral amplitude for isomers I and II.

4.4 Two-Dimensional IR Spectra

From the linear FT-IR spectra we obtain information on the relative energy of the ground states; however, to obtain information on the forward and reverse rate constants and the height of the barrier we use 2DIR spectroscopy. Absolute value rephasing spectra for two different waiting times, t_2, are displayed in Fig. 4.5. The peaks on the diagonal ($\omega_{excite}=\omega_{detect}$) are due to the fundamental transitions seen in the linear spectrum. Crosspeaks present at t_2=0 ps indicate that the corresponding diagonal peaks share a common ground state and thus belong to the same isomer. The peaks lying along the diagonal correspond to the peaks in the linear FT-IR spectrum. In accord with earlier work[11], peak 1 is assigned to isomer II, peaks 2 and 5 are assigned to isomer III and peaks 3 and 4 are assigned to isomer I. Both isomer II and I contribute to peak 6 with isomer II lying at lower wavenumber (6a) and isomer I at higher wavenumber (6b). The composition of peak 6 has been confirmed by temperature-dependent FT-IR spectra (Fig. 4.3b). Crosspeaks 9, 10, 11 and 12 confirm the assignment of the diagonal peaks 3, 4 and 6b to isomer I, while the

crosspeaks 7 and 8 confirm the assignment of the diagonal peaks 1 and 6a to isomer II.

The peaks in the 2D spectrum change in magnitude with increased waiting time. Figure 4.5 shows the amplitudes of peaks 1, 6, and 7 at 25˚C as a function of t_2.

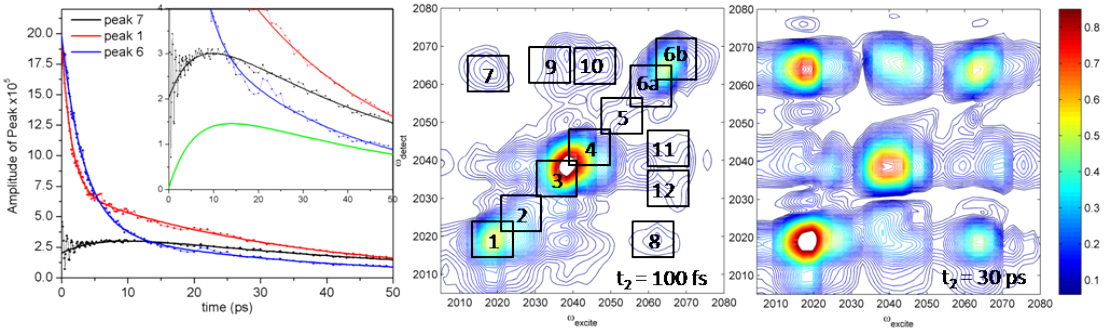

Figure 4.5 A plot of the amplitudes of peaks 1, 6 and 7 as a function of t_2 is shown. The inset shows the data focusing on the crosspeak along with the exchange part of the signal in green which was obtained from the described fitting procedure. Absolute value of the rephasing spectra of $Co_2(CO)_8$ in n-hexane at t_2=0 ps and t_2=30 ps are shown with the spectra normalized to the maximum amplitude.

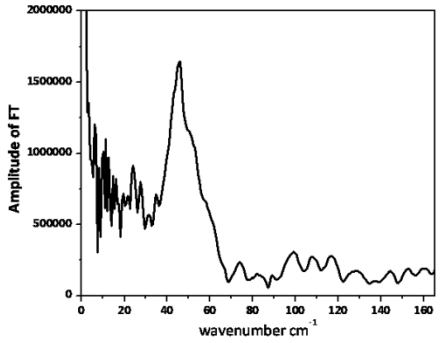

Figure 4.6 Fourier transform amplitude of t_2-dependent peak 7 amplitude showing a peak at 46 cm^{-1}.

Peak 7 is present at t_2=0 ps and markedly increases in amplitude by t_2=30 ps, whereas the diagonal peaks sim ply decay. Peaks 1, 6, and 7 were fit to a biexponential having the following form (Eq. 4.2):

$$f(t) = A_1 e^{-\frac{t_2}{t_a}} + A_2 e^{-\frac{t_2}{t_b}} \qquad \textbf{Eq. 4.2}$$

The resulting fit parameters are given in Table 4.1. Biexponential fits of the diagonal peaks indicate a fast decay of 2-3 ps ($1/e$) and a slower decay of 30 ps. Crosspeak 7, first oscillates as it grows in and then decays; a Fourier transform of the crosspeak 7 oscillations (Fig. 4.6) yields a frequency of 46 cm^{-1}, which equals the splitting between transitions 6a and 1 of isomer II, indicating an excited state coherence of isomer II.[14] Table 4.1 also reports the fitted parameters obtained from fitting the t_2 dependent amplitude of the peaks in 2D spectra recorded at 14 and 50 °C to Eq. 4.2. Figure 4.7 plots the amplitude or crosspeak 7 along with the biexponential fit at the three different temperatures. From Fig. 4.7 it can be seen that as the temperature increases the crosspeak maximum shifts to smaller t_2 values.

Table 4.1 Biexponential fit parameters for peaks 1, 6 and 7 at 14 25 and 50°C.

		A	t_a (ps)	B	t_b (ps)
14° C	peak1	6.7E+05	1.5	3.9E+05	32
	peak6	8.6E+05	3.5	3.2E+05	32
	peak7	-1.1E+05	8.6	2.2E+05	41
25° C	peak1	1.2E+06	1.5	7.2E+05	33
	peak6	1.6E+06	3.3	4.0E+05	33
	peak7	-2.2E+05	6.1	4.2E+05	47
50° C	peak1	7.2E+05	1.6	2.8E+05	26
	peak6	9.4E+05	2.9	2.0E+05	33
	peak7	-3.4E+04	3.4	1.4E+05	39

4.5 Growth of Crosspeak 7: IVR versus Exchange

As t_2 increases, crosspeak 7 first oscillates, grows in and then decays. There are two possible reasons for this growth due to the fact that there are two contributions to diagonal peak 6, from isomer I (6b) and isomer II (6a). The growth could be due to chemical exchange, population transfer between different chemical species, and the resulting crosspeak we refer to as the exchange crosspeak. Another possibility is that the growth could be due to intramolecular vibrational energy redistribution (IVR),

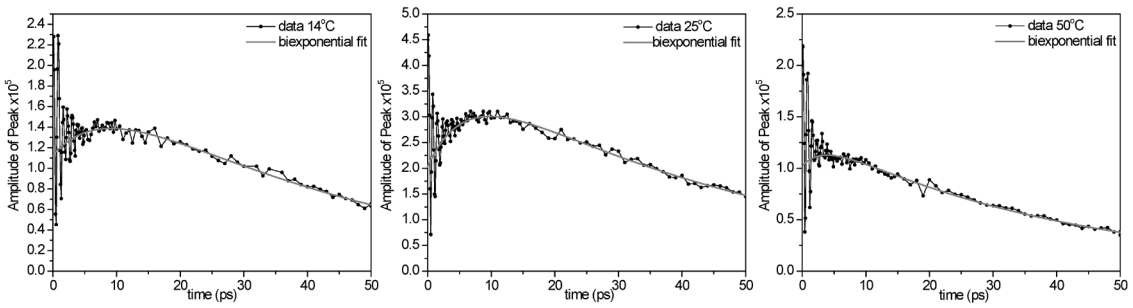

Figure 4.7 Waiting time dependent traces of peak 7 at 14, 25 and 50°C shown with (solid gray) a simple biexponential fit accounting for growth and decay is plotted in grey.

population transfer between different modes of the same chemical species, and the resulting crosspeak we refer to as the inherent crosspeak.

To establish evidence for the assignment of an exchange component in peak 7 we considered the difference in the temperature dependence of the diagonal and crosspeaks. Previous studies of IVR in metal carbonyls observed crosspeak growth with a rate constant similar to the fast decay of the corresponding diagonal peaks.[15] In order that the growth of peak 7 be due to IVR among the eigenstates of isomer II—both bright and dark—the growth of the crosspeak and IVR decay of the diagonal peaks should have the same temperature dependence. Fig. 4.8 plots the inverse of the rate constants for the fast decay of the diagonal peaks 1 and 6 and the growth of

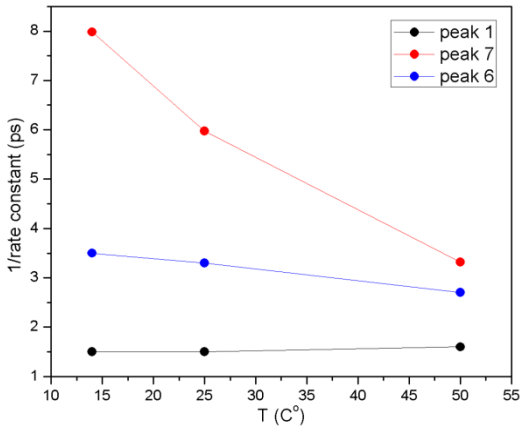

Figure 4.8 Temperature dependence of the fast decay component of two diagonal peaks and the growth component of the exchange peak 7.

crosspeak 7 as a function of temperature. The fast decay of the diagonal peaks is attributed to rapid IVR. If similar IVR is responsible for the growth of the crosspeak 7 we would expect the growth of the crosspeak and decay of the diagonal peaks to have the same temperature dependence. From Fig. 4.8 we see the growth has a greater dependence on temperature than the decay of peak 1 and 6, indicating the growth of crosspeak 7 is not due to IVR. Thus we assign the growth of peak 7 to chemical exchange between isomers II and I.

4.6 Separation of Inherent and Exchange Contributions

The key challenge in extracting the exchange component from crosspeak 7 is to remove the crosspeak contribution due to isomer II, the inherent crosspeak contribution. In absolute value rephasing spectra, inherent crosspeaks oscillate as a function of t_2 at a frequency corresponding to the difference in frequency between the two excited states involved.[14] The oscillating coherence is a delicate quantum mechanical condition easily disrupted by environmental fluctuations. The exchange process itself acts as a dephasing mechanism since once exchange occurs, the two states involved in the coherence are no longer eigenstates.[4] We therefore take the presence of the coherence to indicate *non-exchange*—that is, the coherence is due to molecules that never exchange during t_2. Removing the coherence from the total crosspeak amplitude leaves the part of the signal that is due primarily to exchange.

To extract the exchange component for isomerization between isomer I and II we have focused on peak 7. The t_2 time dependence of peak 7 can be modeled by accounting for the contribution of the exchange peak and a single non-exchange crosspeak; peaks 1, 3, 4 and 8 require less straightforward modeling due to multiple overlapping contributions.

4.7 Extraction of Rate Constants: Inherent and Exchange Crosspeak Models

This section first gives a detailed description of the kinetic model and resulting solutions to the rate laws for the exchange crosspeak. Next a detailed explanation of the model used to describe the t_2 dependence of the inherent crosspeak is given. In the last section, the fitting procedure used to extract the rate constants is described.

4.7.1 Exchange Crosspeak: t_2 Dependence

To model the equilibrium chemical exchange we use a two state kinetic model shown in Fig. 4.9 where A represents isomer II, B represents isomer I, k_f and k_r are the forward and reverse rate constants and k_V is the rate constant associated with vibrational population relaxation.

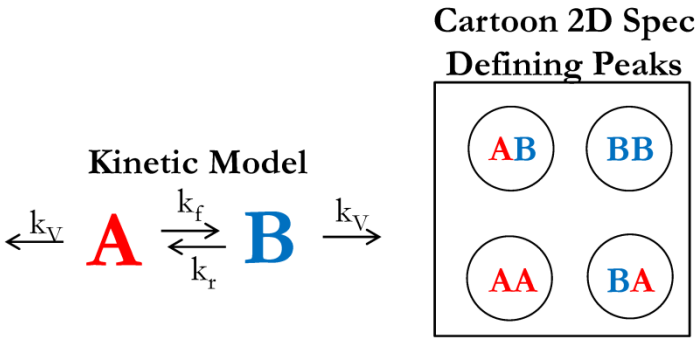

Figure 4.9 Kinetic model used to describe chemical exchange with corresponding 2D spectrum.

The following rate laws (Eq. 4.3-4.4) are obtained from the kinetic model where N_A and N_B are the effective populations of isomers II and I. The amplitude of the

$$\frac{dN_A}{dt} = -k_f[A] + k_r[B] - k_V[A] \qquad \textbf{Eq. 4.3}$$

$$\frac{dN_B}{dt} = +k_f[A] - k_r[B] - k_V[B] \qquad \textbf{Eq. 4.4}$$

signal depends on the concentration of the species, the oscillator strengths of the transitions, and the tuning of the incoming pulses. To avoid accounting for these contributions independently, we use the effective populations.

The solutions to these rate laws are given in Eq. 4.5-4.6 where N_{A0} is the initial effective population of A ($N_A(t=0)$) and N_{B0} is the initial effective population of B ($N_B(t=0)$) and $k_{ex}=k_f+k_r$.

$$N_A(t) = -\frac{e^{-(k_1+k_{ex})t}\left(N_{B0}\left(-1+e^{k_{ex}t}\right)k_f + N_{A0}\left(e^{k_{ex}t}k_f + k_r\right)\right)}{k_{ex}} \quad \textbf{Eq. 4.5}$$

$$N_B(t) = -\frac{e^{-(k_1+k_{ex})t}\left(N_{A0}\left(-1+e^{k_{ex}t}\right)k_r + N_{B0}\left(e^{k_{ex}t}k_r + k_f\right)\right)}{k_{ex}} \quad \textbf{Eq. 4.6}$$

The above solutions describe how the amplitudes of the diagonal peaks and crosspeaks change as a function of t_2. The waiting-time dependent amplitude of diagonal peak AA is determined by setting the initial effective population of B to zero ($N_{B0}=0$) and the initial effective population of A to A_0($N_{A0}=A_0$) in Eq. 4.5. For diagonal peak BB, N_{B0} is set to B_0 and N_{A0} is set to 0 in Eq. 4.6. For crosspeak AB (Fig. 4.9) N_{A0} is set to 0 and N_{B0} is set to B_0 in Eq. 4.5, and for crosspeak BA (Fig. 4.9) N_{A0} is set to A_0 and N_{B0} is set to 0 in Eq. 4.6. The resulting expressions for the t_2 dependent amplitudes of the peaks in Fig. 4.9 are given in Eq. 4.7-4.10.

$$AA(t) = \frac{A_0 e^{-(k_1+k_{ex})t}\left(e^{k_{ex}t}k_f + k_r\right)}{k_{ex}} \quad \textbf{Eq. 4.7}$$

$$BB(t) = \frac{B_0 e^{-(k_1+k_{ex})t}\left(e^{k_{ex}t}k_r + k_f\right)}{k_{ex}} \quad \textbf{Eq. 4.8}$$

$$AB(t) = \frac{B_0 e^{-(k_1+k_{ex})t}\left(-1+e^{k_{ex}t}\right)k_f}{k_{ex}} \quad \textbf{Eq. 4.9}$$

$$BA(t) = \frac{A_0 e^{-(k_1+k_{ex})t}\left(-1+e^{k_{ex}t}\right)k_r}{k_{ex}} \quad \textbf{Eq. 4.10}$$

4.7.2 Inherent Crosspeak: t_2 Dependence

For the inherent crosspeaks, we first determine how the crosspeak changes with waiting time by only accounting for dynamics of the coherences, and then we add

two phenomenological terms, one to account for the dephasing of the coherence and the other to account for overall decay of the signal due to vibrational population relaxation.

For the t_2 dependence of the inherent crosspeak, we are only concerned with contributions from the rephasing spectra, so we need only to consider contributions to the third-order nonlinear signal in the $-\mathbf{k}_1+\mathbf{k}_2+\mathbf{k}_3$ phase matched direction. Considering a three level system, the 8 contributing Feynman and ladder diagrams are shown in Fig. 4.10.[16]

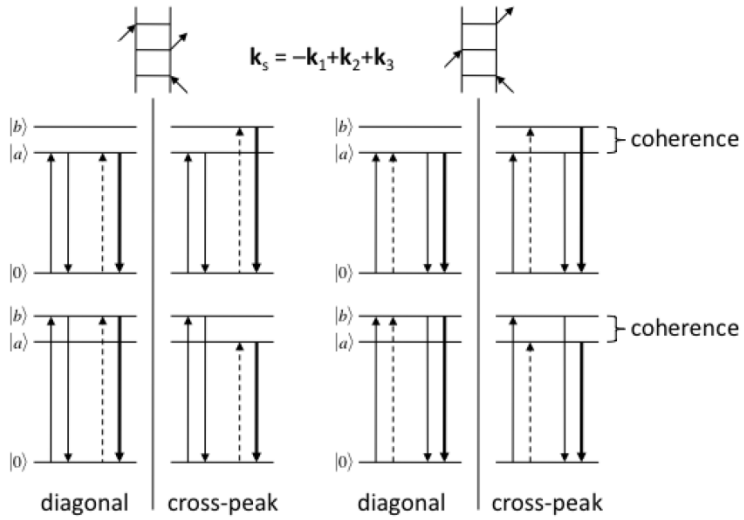

Figure 4.10 Double sided Feynman and wave matching energy level diagrams for the Liouville space pathways that contribute to the diagonal and cross-peak rephasing amplitude for a three-level system. Family I is on the left, and family II is on the right.

Considering family I first, the first interaction creates a coherence between the ground states and the first excited states, a and b, where the coherence evolves in time according to the field free Hamiltonian $G_{ij}(t) = \exp(-i\omega_{ij}t)$. The result follows:

$$\rho^I(t_1) = G_0(t_1)[\rho\mu] = \begin{pmatrix} 0 & e^{-i\omega_{0a}t_1}\mu_{0a}\rho_{00} & e^{-i\omega_{0b}t_1}\mu_{0b}\rho_{00} \\ 0 & 0 & 0 \\ 0 & 0 & 0 \end{pmatrix} \qquad \textbf{Eq. 4.11}$$

The second field-matter interaction returns the system to a ground state population. Since we are assuming that the only dynamics arise from coherences, we do not observe any t_2 time dependence of the population.

$$\rho^I(t_2) = G_0(t_2)\left[\rho^I(t_1)\mu\right] = \begin{pmatrix} e^{-i\omega_{0a}t_1}\mu_{0a}\mu_{a0}\rho_{00} + e^{-i\omega_{0b}t_1}\mu_{0b}\mu_{b0}\rho_{00} & 0 & 0 \\ 0 & 0 & 0 \\ 0 & 0 & 0 \end{pmatrix} \quad \textbf{Eq. 4.12}$$

The third field-matter interaction creates a coherence between the ground and first excited states.

$$\rho^I(t_3) = G_0(t_3)\left[\mu\rho^I(t_2)\right] = \begin{pmatrix} 0 & 0 & 0 \\ e^{i\omega_{0a}(t_3-t_2)}\mu_{a0}\left(e^{-i\omega_{0a}t_1}\mu_{0a}\mu_{a0}\rho_{00} + e^{-i\omega_{0b}t_1}\mu_{0b}\mu_{b0}\rho_{00}\right) & 0 & 0 \\ e^{i\omega_{0b}(t_3-t_2)}\mu_{b0}\left(e^{-i\omega_{0a}t_1}\mu_{0a}\mu_{a0}\rho_{00} + e^{-i\omega_{0b}t_1}\mu_{0b}\mu_{b0}\rho_{00}\right) & 0 & 0 \end{pmatrix} \quad \textbf{Eq. 4.13}$$

The final signal is proportional to the expectation value of the dipole operator,

$$\langle\mu\rangle = Tr\left[\mu\rho^I(t_3)\right] = Tr\begin{pmatrix} e^{i\omega_{0a}(t_3-t_2)}\mu_{0a}\mu_{a0}\left(e^{-i\omega_{0a}t_1}\mu_{0a}\mu_{a0}\rho_{00} + e^{-i\omega_{0b}t_1}\mu_{0b}\mu_{b0}\rho_{00}\right) + e^{i\omega_{0b}(t_3-t_2)}\mu_{0b}\mu_{b0}\left(e^{-i\omega_{0a}t_1}\mu_{0a}\mu_{a0}\rho_{00} + e^{-i\omega_{0b}t_1}\mu_{0b}\mu_{b0}\rho_{00}\right) & 0 & 0 \\ 0 & 0 & 0 \\ 0 & 0 & 0 \end{pmatrix}$$

thus,

$$\left\langle\mu^I\right\rangle = e^{i\omega_{0a}(t_3-t_2)}\mu_{0a}\mu_{a0}\left(e^{-i\omega_{0a}t_1}\mu_{0a}\mu_{a0}\rho_{00} + e^{-i\omega_{0b}t_1}\mu_{0b}\mu_{b0}\rho_{00}\right) \quad \textbf{Eq. 4.14}$$

$$+e^{i\omega_{0b}(t_3-t_2)}\mu_{0b}\mu_{b0}\left(e^{-i\omega_{0a}t_1}\mu_{0a}\mu_{a0}\rho_{00} + e^{-i\omega_{0b}t_1}\mu_{0b}\mu_{b0}\rho_{00}\right)$$

From Eq. 4.14, we see that the signal is composed of the four terms shown in the wave-matching energy level diagrams.

Now we consider family II, where an excited state coherence is created during t_2 for the pathways leading to crosspeaks. The first field matter interaction, which is the same as that for family I, creates a coherence.

$$\rho^{II}(t_1) = G_0(t_1)\left[\rho\mu\right] = \begin{pmatrix} 0 & e^{-i\omega_{0a}t_1}\mu_{0a}\rho_{00} & e^{-i\omega_{0b}t_1}\mu_{0b}\rho_{00} \\ 0 & 0 & 0 \\ 0 & 0 & 0 \end{pmatrix} \quad \textbf{Eq. 4.15}$$

The second interaction acts from the left creating both excited state coherences and excited state populations, which is difference. This differs from family I, where the second pulse created a ground state population.

$$\rho^{II}(t_2) = G_0(t_2)\left[\mu\rho^{II}(t_1)\right] = \begin{pmatrix} 0 & 0 & 0 \\ 0 & e^{-i\omega_{0a}t_1}\mu_{0a}\mu_{a0}\tilde{\rho}_{00} & e^{-i\omega_{0b}t_1}e^{-i\omega_{ab}(t_2-t_1)}\mu_{0b}\mu_{a0}\tilde{\rho}_{00} \\ 0 & e^{-i\omega_{0a}t_1}e^{i\omega_{ab}(t_2-t_1)}\mu_{0a}\mu_{b0}\tilde{\rho}_{00} & e^{-i\omega_{0b}t_1}\mu_{0b}\mu_{b0}\tilde{\rho}_{00} \end{pmatrix} \quad \textbf{Eq. 4.16}$$

After the second interaction we see that there is some time-dependence during t_2 due to the excited state coherences created. The third interaction creates a coherence between the ground state and the first excited states.

$$\rho^{II}(t_3) = G_0(t_3)\left[\rho^{II}(t_2)\mu\right] = \begin{pmatrix} 0 & 0 & 0 \\ e^{i\omega_{0a}(t_3-t_2)}\left(e^{-i\omega_{0a}t_1}\mu_{0a}\mu_{a0}\mu_{a0}\tilde{\rho}_{00} + e^{-i\omega_{0b}t_1}e^{-i\omega_{ab}(t_2-t_1)}\mu_{0a}\mu_{0b}\mu_{b0}\tilde{\rho}_{00}\right) & 0 & 0 \\ e^{i\omega_{0b}(t_3-t_2)}\left(e^{-i\omega_{0b}t_1}\mu_{0b}\mu_{b0}\mu_{b0}\tilde{\rho}_{00} + e^{-i\omega_{0a}t_1}e^{i\omega_{ab}(t_2-t_1)}\mu_{0b}\mu_{0a}\mu_{a0}\tilde{\rho}_{00}\right) & 0 & 0 \end{pmatrix} \quad \textbf{Eq. 4.17}$$

Again, the final signal is the trace of $\mu\rho$,

$$\begin{aligned} \langle\mu\rangle = {} & e^{i\omega_{0a}(t_3-t_2)}\left(e^{-i\omega_{0a}t_1}\mu_{0a}\mu_{a0}\mu_{0a}\mu_{a0}\rho_{00} + e^{-i\omega_{0b}t_1}e^{-i\omega_{ab}(t_2-t_1)}\mu_{0a}\mu_{a0}\mu_{0b}\mu_{b0}\rho_{00}\right) \\ & + e^{i\omega_{0b}(t_3-t_2)}\left(e^{-i\omega_{0b}t_1}\mu_{0b}\mu_{b0}\mu_{0b}\mu_{b0}\rho_{00} + e^{-i\omega_{0a}t_1}e^{i\omega_{ab}(t_2-t_1)}\mu_{0a}\mu_{a0}\mu_{0b}\mu_{b0}\rho_{00}\right) \end{aligned} \quad \textbf{Eq. 4.18}$$

and again we recover four terms corresponding to the four wave matching diagrams.

The total signal is the sum of the two families of paths derived above. Since we are primarily concerned with the t_2 dependence of a cross-peak, we now restrict our attention to one of the two crosspeaks in the simple three-level system model.

The 2D spectrum is obtained by performing a Fourier transform along t_1 and t_3 to obtain $\omega_1(\omega_{excite})$ and ω_3 (ω_{detect}). The crosspeak we wish to model occurs at $\omega_1 = \omega_{0a}$ and $\omega_3 = \omega_{0b}$. The component of the signal associated with this crosspeak is the following:

$$\begin{aligned} S(\omega_1 = \omega_{0a}; t_2; \omega_3 = \omega_{0b}) &= \mu_{0a}\mu_{a0}\mu_{0b}\mu_{b0}\rho_{00} + e^{i\omega_{ab}(t_2-t_1)}\mu_{0a}\mu_{a0}\mu_{0b}\mu_{b0}\rho_{00} \\ &= \left(e^{i\omega_{ab}(t_2-t_1)} + 1\right)\left|\mu_{0a}\right|^2\left|\mu_{0b}\right|^2\rho_{00} \end{aligned} \quad \textbf{Eq. 4.19}$$

It is important to note that Eq. 4.19 does not include any decay processes. We did not include any processes that would lead to the dephasing of the excited state coherence, and we add this dephasing rate constant, k_D, to the above equation. The result is given in equation 4.20.

$$S\left(\omega_1 = \omega_{0a}; t_2; \omega_3 = \omega_{0b}\right) = \left(e^{i(\omega_{ab} + ik_D)(t_2)} + 1\right)\left|\mu_{0a}\right|^2 \left|\mu_{0b}\right|^2 \rho_{00} \qquad \textbf{Eq. 4.20}$$

From the above equation it can be seen that the time dependence of the excited state coherence is completely predictable. Fig. 4.11 plots Eq. 20. We see that the signal oscillates at a frequency corresponding to the difference in frequency between the two excited states involved. We also see from Fig. 4.11 that the signal will decay to one-half its amplitude at t_2=0 when only the dephasing of the coherence is taken

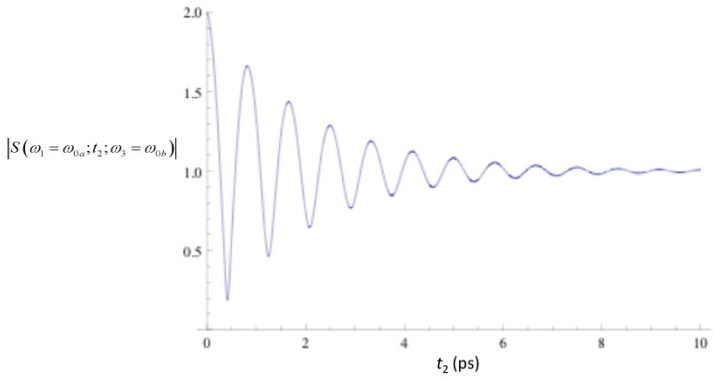

Figure 4.11 Plot of equation S11 for a coherence with a frequency in wavenumbers of 40 cm^{-1}, and a damping rate k_D of 0.5 ps^{-1}.

into account.

It is important to note that this derivation only included t_2 dynamics associated with coherences and that the inherent crosspeak amplitude will change according to all the typical mechanisms: IVR, orientational diffusion and vibrational relaxation. We did not include any dynamics associated with populations in our model, so in order to apply this model we add a decay constant to account for vibrational population relaxation, k_V, resulting in Eq. 4.21.

$$S\left(\omega_1=\omega_{0a};t_2;\omega_3=\omega_{0b}\right)=\left(e^{i(\omega_{ab}+ik_D)(t_2)}+1\right)\left|\mu_{0a}\right|^2\left|\mu_{0b}\right|^2\rho_{00}e^{-k_V t_2} \qquad \textbf{Eq. 4.21}$$

4.7.3 Fitting Procedure

The total amplitude of crosspeak 7 will be the sum of the contributions from the inherent (Eq. 4.21) and exchange (Eq. 4.9) crosspeak. Adding the inherent and exchange contributions we obtain the following expression where ω_{ab} is the frequency of the oscillation of the coherence, φ is the phase of the coherence, k_D is the rate constant for the dephasing of the coherence, k_V is the rate constant associated with vibrational population relaxation, k_{ex} is the exchange rate constant which is the sum

$$S\left(\omega_1=2021\text{cm}^{-1};t_2;\omega_3=2070\text{cm}^{-1}\right)=\left[-A_1e^{-(k_V+k_{ex})t_2}+A_2e^{-k_V t_2}\right] \qquad \textbf{Eq. 4.22}$$

$$+\left[\left(e^{(i\omega_{ab}-k_D)t_2+i\varphi}+1\right)Be^{-k_V t_2}\right]$$

of the forward and reverse rate constants, $A_1=A_2=B_0k_f/k_{ex}$, and $B=|\mu_{oa}|^2|\mu_{ob}|^2\rho_{00}$.

Using the coherence signal to lock onto the non-exchanging part of the signal, we can better estimate the exchange contribution to the crosspeak. Dividing the signal by the long time decay and subtracting the exchange leaves only the signal due to the non-exchange.

$$\left(e^{(i\omega_{ab}-k_D)t_2+i\varphi}+1\right)=\frac{S\left(\omega_1=2021cm^{-1};t_2;\omega_3=2070cm^{-1}\right)}{Be^{-k_V t_2}}-\left[-\frac{A_1}{B}e^{-(k_{ex})t_2}+\frac{A_2}{B}\right] \qquad \textbf{Eq. 4.23}$$

Since the rate of exchange is equal to the sum of the forward and reverse rate constant, knowing the equilibrium constant enables the separation of the forward and reverse rate constants.

To obtain the values of A_1, A_2, and B, which are needed in Eq. 4.23), we fit crosspeak 7 to the following biexponential:

$$f(t)=-P_1e^{-tk_1}+P_2e^{-tk_2} \qquad \textbf{Eq. 4.24}$$

The growth of the crosspeak is due to exchange, so $P_1=A_1$. Both the exchange and inherent contributions lead to the decay of the crosspeak, so $P_2=A_2+B$. Since we do not know the individual contributions of the inherent and exchange peak we weigh the two contributions by c: $(1-c)P_2=A_2$ and $cP_2=B$.

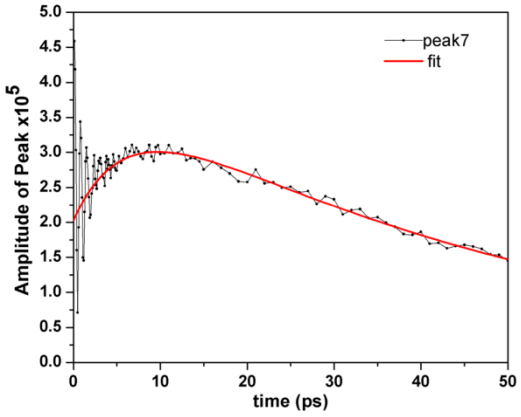

Figure 4.12 Biexponential fit of crosspeak 7.

Fitting crosspeak 7 to Eq. 4.24 we obtain $P_1=-2\text{-}2\text{x}10^5$ and $P_2=4.2\text{x}10^5$ (Fig. 4.12). For our fitting process we have two adjustable parameters; c and k_f. The parameter c can be thought of as the percentage of signal due to non-exchange and k_f is the forward rate constant which is related to the reverse rate constant through the equilibrium constant: $k_r=k_f/K_{eq}$. We can rewrite Eq. 4.23 in terms of k_f, P_1, P_2, and c.

$$\left(e^{(i\omega_{ab}-k_D)t_2+i\varphi}+1\right)=\frac{S\left(\omega_1=2021cm^{-1};t_2;\omega_3=2070cm^{-1}\right)}{P_2e^{-k_f t_2}}-\left[-\frac{P_1}{cP_2}e^{-(k_f+\frac{k_f}{K_{eq}})t_2}+\frac{(1-c)}{c}\right] \qquad \textbf{Eq. 4.25}$$

Using Eq. 4.25 to fit our data, we adjust parameters c and k_f to simulate our data. First, we vary parameter c so that the signal due to exchange is zero at t_2 = 0ps. This assumption would neglect exchange that occurs during t_1; however, for reactions that occur on the tens of picosecond timescale this is a valid assumption. Next we adjust k_f so that the non-exchange signal is centered around 1. Figure 4.13 shows each step of the fitting process.

To check the accuracy of our fit we modeled the non-exchange process with the following parameters: ω_{ab} = 1.38 THz (46 cm^{-1}), φ = -0.8 and k_d = 0.68 ps^{-1}. The

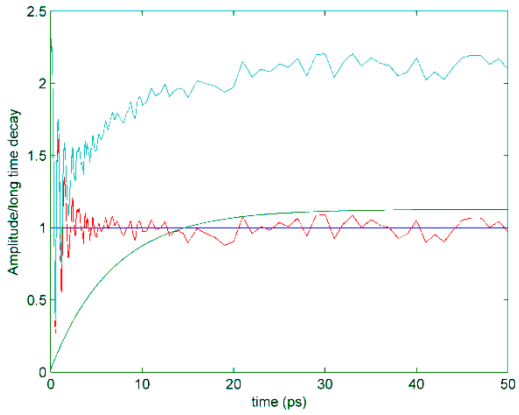

Figure 4.13 The cyan curve in the figure is the amplitude of peak seven divided by the long time decay; it contains both the non-exchange and exchange processes. The green curve is the exchange process only, a value of c = 0.47 was chosen so that the exchange signal would begin at t_2 = 0ps. The red curve, the non-exchange signal, was obtained by subtracting the green curve from the blue curve. A value of k_f = 0.077±0.007 ps^{-1} ($1/k_f$=13.0±1 ps) was chosen so the nonexchange signal was centered around 1. From the equilibrium constant we obtain a k_r = 0.077/1.03 = 0.071 ±0.007 ps^{-1} ($1/k_r$=14±1 ps).

model, data and residual are plotted in Fig. 4.14a. At t_2=0 ps the residual is large, this is due to artifacts that occur at t_2 = 0 ps. We also looked at the Fourier transform of

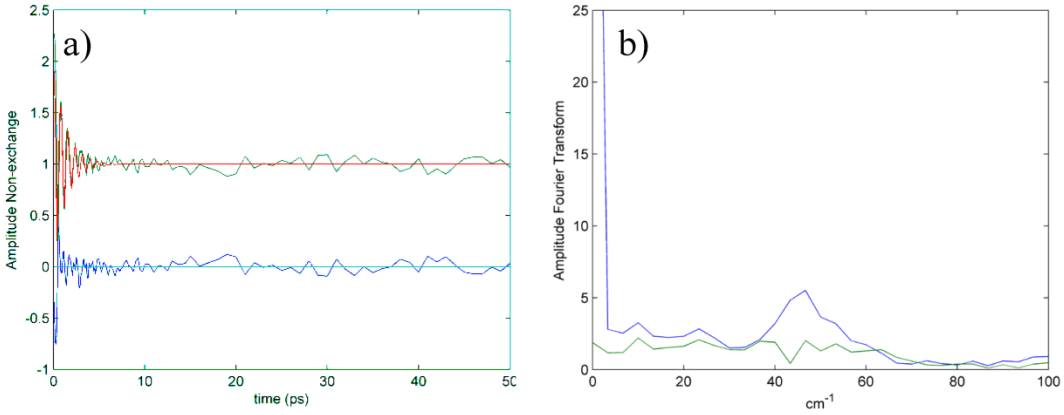

Figure 4.14 (a) The red curve is the model of the non-exchange, the green curve is the actual data and the blue curve is the residual. (b) The blue curve is the Fourier transform of the amplitude of peak 7, and the green curve is the Fourier transform of the residual. Comparing the two curves we see that the peak at 46 cm^{-1} is minimized.

the residual. Fig. 4.14b plots the Fourier transform of the data (blue) along with the Fourier transform of the residual (green). For the data, the peak at lower frequencies

is due to the biexponential growth and decay while the peak at 46 cm^{-1} is due to the oscillations. In the Fourier transform of the residual we see that both the growth and decay along with the oscillations are minimized.

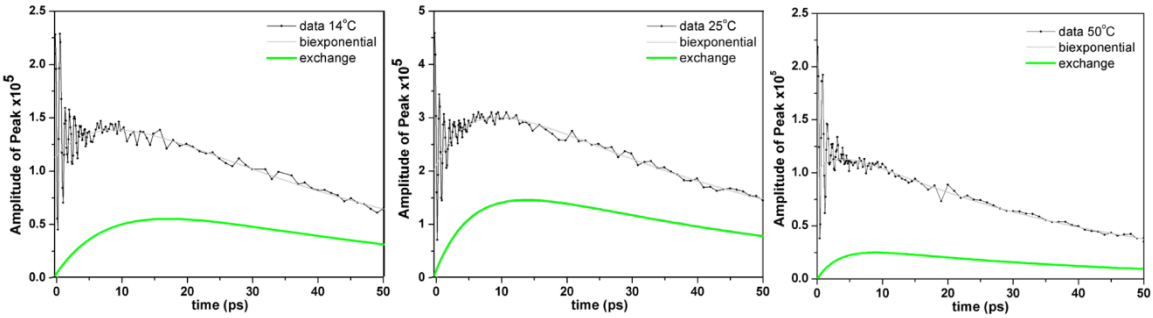

Figure 4.15 Waiting time dependent traces of peak 7 at 14, 25 and 50°C shown with (solid black) a simple biexponential fit accounting for growth and decay and (green) the isolated exchange component.

Fitting crosspeak 7 at 14, 25 and 50°C, we obtained the following rate constants for isomerization between the isomers. The extracted exchange contribution to the crosspeak is plotted in Fig. 4.15 along with the t_2 dependent trace of the amplitude of the temperature dependent crosspeaks. The forward rate constant describes the process of isomer II converting to isomer I, and the reverse rate constant corresponds to the process of isomer I converting to isomer II. From our fitting procedure we obtain a rate constant of k_f=0.077±0.007 ps^{-1} ($1/k_f$=13±1 ps) for isomer II to interconvert to isomer I at 25°C. Using the equilibrium constant

Table 4.2 Temperature dependent rate constants for forward and reverse reactions.

Temperature (°C)	k_f (ps^{-1})	$1/k_f$ (ps)	k_r (ps^{-1})	$1/k_r$ (ps)
14	0.047±0.004	21±2	0.042±0.004	24±2
25	0.077±0.007	13±1	0.071±0.007	14±1
50	0.139±0.021	7.0±1	0.135±0.021	7±1

obtained from FT-IR spectra (K_{eq}=1.09) we obtain a reverse rate constant of k_r=0.071±0.007 ps^{-1} (14±1 ps) for I-to-II interconversion. Fitting data from 2D spectra taken at 14 and 50°C results in rate constants of k_f=0.047±0.004 ps^{-1} (21±2

ps) and k_f=0.139±0.021 ps^{-1} (7.0±1 ps) for II-to-I. Reverse rate constants were determined to be k_r=0.042±0.004 ps^{-1} (24±2ps) and k_r=0.135±0.021 ps^{-1} (7±1 ps. The results are summarized in Table 4.2. Direct comparison of k_f to k_r shows that II-to-I interconversion is more rapid than I-to-II interconversion, consistent with a negative $\Delta G°_{II\rightarrow I}$.

4.8 Barrier Heights

From the temperature dependent rate constants we can obtain the barrier height. We used both the Arrhenius (Eq. 4.26) and Eyring (Eq. 4.27) equation to obtain the height of the barriers, with the Eyring analysis allowing for the extraction of the entropic contribution to the barrier.

$$k = Ae^{-\frac{E_a}{RT}} \qquad \textbf{Eq. 4.26}$$

$$k = \frac{k_B T}{h} e^{\frac{\Delta S^*}{R}} e^{-\frac{\Delta H^*}{RT}} \qquad \textbf{Eq. 4.27}$$

Plotting the natural log of the rate constants versus one over the temperature yields an Arrhenius plot (Eq. 4.28). From an Arrhenius plot the activation energy can be obtained from the slope of the plot. Plotting the natural log of the rate constants divided by the temperature versus one over the temperature yields an Eyring plot (Eq. 4.29) where the activation energy (ΔH^*) can be obtained from the slope and the change in entropy associated with the barrier crossing (ΔS^*) can be obtained from the intercept.

$$\ln(k) = \ln(A) - \frac{E_a}{RT} \qquad \textbf{Eq. 4.28}$$

$$\ln\left(\frac{k}{T}\right) = \ln\left(\frac{k_B}{h}\right) \frac{\Delta S^*}{R} - \frac{\Delta H^*}{R}\left(\frac{1}{T}\right) \qquad \textbf{Eq. 4.29}$$

For the forward isomerization reaction, II-to-I interconversion, Figure 4.16a displays the Arrhenius (black) and Eyring (red) plots. From the Arrhenius plot an activation energy of E_a=5.4 kcal/mol and the Eyring plot yields a $\Delta H^{\ddagger}$=4.8 kcal/mol and $\Delta S^{\ddagger}$=7.2 cal/(mol•K) (1.2 kcal/mol at 298 K) for II-to-I interconversion. Figure 4.16b displays the Arrhenius (black) and Eyring (red) plots for the reverse isomerization, I-to-II interconversion. From the Arrhenius plot an activation energy of E_a=5.8 kcal/mol was obtained and the Eyring plot yields a $\Delta H^{\ddagger}$=5.2 kcal/mol and $\Delta S^{\ddagger}$=8.4 cal/(mol•K) (2.7 kcal/mol at 298 K) for I-to-II interconversion. These values are similar to other ultrafast chemical exchange measurements of similar time scale processes, though the barrier observed here is larger than that measured for fluxional pseudorotation in $Fe(CO)_5$[6], consistent with the larger structural deformation in DCO.

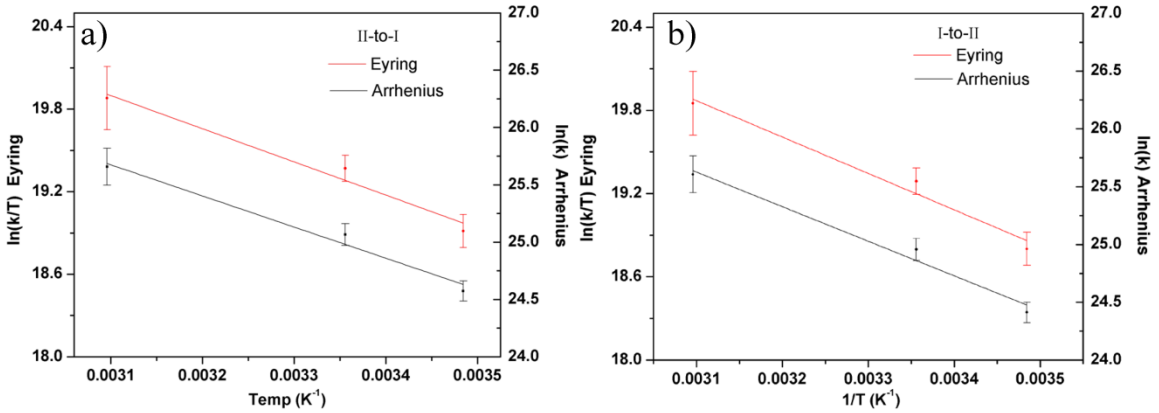

Figure 4.16 Arrhenius (black) and Eyring (red) plots for the II-to-I (a) and I-to-II (b) reactions.

It is important to note that these barrier heights do not take into account the temperature dependence of the solvent's viscosity (Eq. 4.30).

$$\eta = \eta_o e^{\left(\frac{E_a^{\eta}}{RT}\right)} \qquad \textbf{Eq. 4.30}$$

Plotting the natural log of the viscosity versus one over the temperature (Fig. 4.17) yields the activation energy associated with changing the temperature.[17] From Fig. 4.17 we find that over the temperature range of interest, the activation barrier due to the viscosity for *n*-hexane is $E_a^{\eta} = 1.6$ kcal/mol.

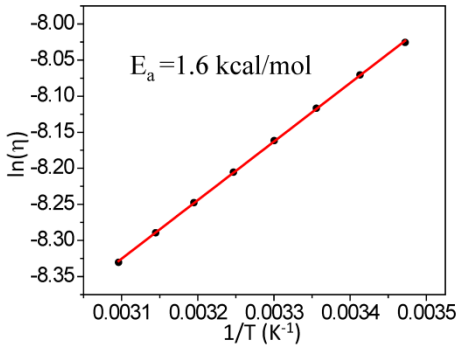

Figure 4.17 Plot of the ln(η) versus 1/T for hexane.

For barriers that are only a few kcals/mol the contribution from the viscosity to the activation energy associated with the barrier can be significant. Using the procedure described by Barbara *et. al.* we took into account the effect of the temperature dependence of the solvent's viscosity on the activation energy required for isomerization.[18] Barbara *et. al.* used the following expression to account for the viscosity's temperature dependence on the rate constant where they assumed that the rate constants was influenced by the solvent's viscosity (assuming the Stokes-Einstein equation for friction).[18]

$$k_f = F(\eta)e^{-\frac{E_a}{RT}} \quad \text{where } F(\eta) = c\eta^{-\alpha} \qquad \textbf{Eq. 4.31}$$

Combining Eq. 4.30 and Eq. 4.31 we obtain the following equation, from which we see that the measured activation energy is the sum of the energy associated with the barrier crossing process and the activation energy associated with the viscosity.

$$k_f = \frac{c}{\eta_o} e^{-\frac{E_a}{RT}} e^{-\frac{E_a^{\eta}}{RT}} \qquad \textbf{Eq. 4.32}$$

Assuming ideal Kramers behavior (which is discussed in detail in Chapter 5) in the high friction limit, α=1, we can obtain a lower limit for the activation energy while the Arrhenius E_a and Eyring ΔH^* give an upper limit for the activation energy.[18] When E_a^{η} is taken into account the barrier for I-to-II is E_a-E_a^{η}=4.2 kcal/mol and for II-to-I E_a-E_a^{η}=3.8 kcal/mol for the Arrhenius analysis, and for the Eyring analysis the barrier for I-to-II is 3.2 kcal/mol and for II-to-I interconversion the barrier is 3.6 kcal/mol.

From the Eyring plot both ΔH^* and ΔS^* were obtained for the forward and reverse interconversion. From ΔH^* and ΔS^* we can obtain the Gibbs free energy change associated with interconversion. At 298 K a ΔG^*= 2.70 kcal/mol for I-to-II interconversion and ΔG^*= 2.65 kcal/mol for II-to-I interconversion were obtained. However, these values do not take into account the temperature dependence of the viscosity. Again, assuming Kramers behavior in the high friction limit, the diffusive Smoluchowski regime, we can write the rate constant as the following

$$k = \frac{\omega_b I}{\zeta} k_{TST} \qquad \text{where } k_{TST} = \frac{k_b T}{h} \frac{Q^*}{Q} e^{-\frac{E_a}{RT}} \qquad \textbf{Eq. 4.33}$$

where k_{TST} is the rate constant from transition state theory, Q is the partition function, I is the moment if inertia, ω_b, is the frequency of the barrier and ζ is the friction coefficient[19].

The friction coefficient was obtained from the Stokes-Einstein relationship with slip boundary conditions, $\zeta = 4\pi\eta dr^2$ where d is the hydrodynamic radius and r is the radius of gyration, and η is the viscosity of the solvent. Using this relationship along with the Eq. 4.33 and Eq. 4.30, the rate constant can be written to include the temperature dependence of the solvent's viscosity.

$$k = \omega_b \left(\frac{I}{4\pi\eta_o dr^2} \right) \left(\frac{k_b T}{h} \right) e^{-\frac{E_a^{\eta}}{RT}} e^{\frac{\Delta S^*}{R}} e^{\frac{-E_a}{RT}} \qquad \textbf{Eq. 4.34}$$

In the above equation ω_b was obtained from DFT calculations. The imaginary frequency of the transition state was found to be 42.2 cm^{-1} which corresponds to $\omega_b = 2\pi c\,\bar{\nu}_b = 7.95x10^{12}s^{-1}$. From Fig. 4.17 both E_a^{η} and η_o were obtained. To obtain the moment of inertia, hydrodynamic radius, and radius of gyration, we use the DFT calculated transition state structure. Figure 4.18a shows the transition state with one of the moving groups associated with the isomerization reaction circled. Assuming

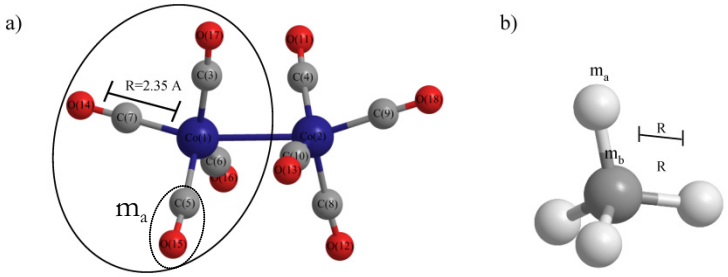

Figure 4.18 (a) Calculated structure of the transition state with one of the moving groups circled in a solid line and the substituent having mass m_a circled in a dotted line. (b) Spherical rotor.

the two moving groups are spherical rotors the moment of inertia can be calculated using the following equation for a spherical rotor (Fig. 4.18b): $I = \frac{8}{3} m_a R^2$.[20] The mass is the sum of the masses of C and O and R was taken to be the distance between Co and the center of the C-O bond. Using R = 2.35 Å, the moment of inertia was calculated to be I=6.8x10^{-45} kg•m^2. For a non-spherical moving group the values of the hydrodynamic radius and the radius of gyration may vary, but for a spherical group the values should be equivalent, d=r= 2.35 Å. Using these values and plotting the natural log of the rate constant divided by the temperature versus one over the temperature (Eq. 4.35) we can extract the $\Delta H^*$from the slope and the ΔS^* from the intercept while accounting for the temperature dependence of the viscosity.

$$\ln\left(\frac{k}{T}\right) = \left(\ln\left(\omega_b\left(\frac{I}{4\pi\eta_o dr^2}\right)\left(\frac{k_b}{h}\right)\right) + \frac{\Delta S^*}{R}\right) - \left(\frac{1}{T}\right)\left(\frac{E_a^{\eta}}{R} + \frac{E_a}{R}\right) \qquad \textbf{Eq. 4.35}$$

From this analysis values of ΔH^*=3.60 kcal/mol and ΔS^*=2.82 cal/(mol•K) were obtained for the I-to-II isomerization and for II-to-I isomerization ΔH^*=3.18

kcal/mol and ΔS^{*}=1.57 cal/(mol•K). Using these values a ΔG^{*}=2.76 kcal/mol for I-to-II interconversion and ΔG^{*}= 2.72 kcal/mol for II-to-I interconversion were obtained at 298 K.

In Fig. 4.19 the extracted experimental barriers are compared. The upper limit to the activation energy is shown in (black). When the temperature dependence of the viscosity is taken into account the barrier is lowered (purple). The E_a gives an upper limit to the barrier while E_a-E_a^{η} gives the lower limit to the enthalpic contribution to

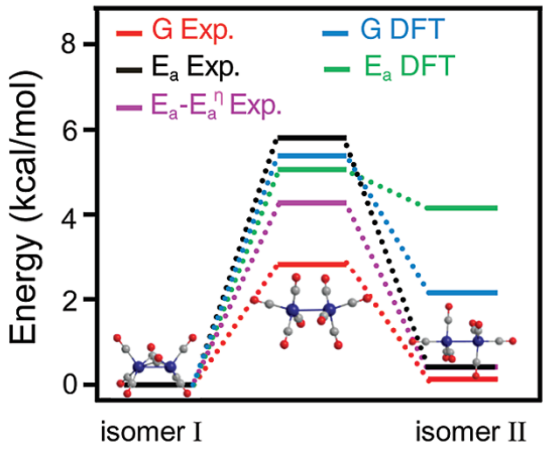

Figure 4.19 Summary of experimental and computationally-determined energies of the two isomers and the transition state.

the barrier. Comparing the E_a and ΔG^{*} allows one to see the effects of entropy on the energy required for isomerization. If $E_a \approx \Delta G^{*}$ then the effects of entropy on the isomerization barrier are relatively small and an Arrhenius plot is sufficient to obtain the barrier. If E_a and $\Delta G^{\ddagger}$ are not approximately equal to each other, the entropy does have a significant effect on the energy barrier and an Eyring plot can be used to obtain the energy barrier. When the entropy is taken into account the barrier is lowered (red). One reason for the large entropic contribution to the energy barrier could be due to the fact that the isomerization reaction induces a significant structural change: interconversion between bridged and unbridged isomers.

4.9 DFT Calculations

We have also performed DFT calculations on isomer I, isomer II and the transition state connecting the two. In the previous section we have used the results of the DFT calculations, specifically the structure and imaginary frequency of the transition state, to extract barrier heights. In this section we compare both the DFT calculated barriers and thermodynamic properties to our experimental results.

DFT calculations were carried out using the GAMESS package.[21] Using the B3LYP function and 6-31G(2df) basis, we obtained the optimized structures for isomer I, II and the corresponding transition state. Figure 4.20 displays the calculated

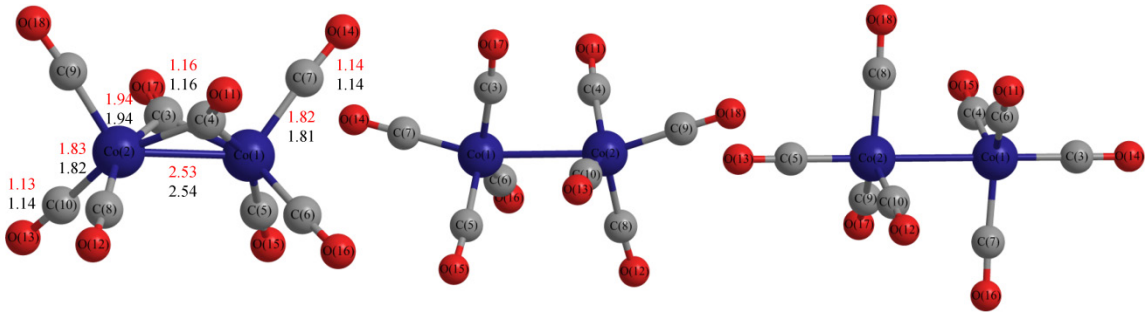

Figure 4.20 Optimized structure for isomer I (left) isomer II (middle) and isomer III(right). For isomer I, the distances in Angstroms are marked with the numbers in red being experimentally determined and the numbers in black are calculated values.

structures. For isomer I we compared the calculated bond lengths (black) to experimental bond lengths[22] (red), the crystal structures for the other two isomers could not be determined. We find that isomer I lies lower in energy than isomer II which is consistent with our experimental results and previous computational studies of DCO using DFT with the B3LYP functional.[12, 13]

Experimentally we have observed the direct isomerization between isomer I and II, as well as finding isomer I to lie lower in energy. From the calculated structures we find the barrier for I-to-II interconversion to be E_a=5.26 kcal/mol and E_a=1.05 kcal/mol for II-to-I (Table 4.3). The relative energies of the isomers are consistent with the previous computational studies using B3LYP[12, 13], and for the I-

to-II barrier, the agreement with the experimental results is surprisingly good (Fig. 4.19), but the II-to-I barrier differs by ~3 kcal/mol.

Though the activation enthalpies are in good agreement, the entropies are not. Experimentally, ΔS^* is found to play a role in determining the overall isomerization barrier; however, the DFT results found that ΔS^* does not have a large effect on computed barriers (Table 4.3 and Fig. 4.19). Comparing computed and experimentally determined ΔS^* we find $\Delta S^*_{exp}>0$ while $\Delta S^*_{comp}<0$. Computationally the isomerization is entropically unfavorable. The ground states being favored entropically stems from the fact that there are 3N-7 vibrational modes in the transition state while the ground states have 3N-6 vibrational modes. Experimentally the isomerization is entropically favored. We believe this disagreement could be due to the effect of the solvent, with the solvent lowering the entropy of the ground state relative to the transition state. The computational results indicate that the entropy does not have a large effect on the barrier for I-to-II isomerization, but the barrier for II-to-I isomerization increases by 2 kcal/mol when the entropy is taken into account. Experimentally we find that entropy does have a large effect on the energy barrier,

Table 4.3 Thermodynamic parameters obtained from DFT calculations and experiments.

	ΔH‡ (kcal/mol)	ΔS‡ (cal/mol•K)	ΔG‡ (kcal/mol) at 298 K
Experimental			
II→I	4.8 Eyring (5.4 Arrhenius)	7.2	2.65
I→II	5.2 Eyring (5.8 Arrhenius)	8.4	2.70
Experimental (account for viscosity)			
II→I	3.18 Eyring (3.8 Arrhenius)	1.57	2.72
I→II	3.60 Eyring (4.2 Arrhenius)	2.82	2.76
B3LYP			
II→I	1.05	-7.66	3.34
I→II	5.26	-0.56	5.43

the ΔG^* for isomerization, when entropy is taken into account, are approximately equal with $\Delta G^*_{I\rightarrow II}$ being 0.1 kcal/mol greater than $\Delta G^*_{II\rightarrow I}$. Though an isolated-molecule calculation cannot be expected to agree with a solution phase experiment, the reasonable enthalpy agreement suggests the solvent primarily influences the entropy of the molecules, perhaps by entropically stabilizing the two isomers relative to the transition state.

4.10 Conclusion

In this chapter we used 2DIR spectroscopy to probe the ultrafast equilibrium exchange between isomers of $Co_2(CO)_8$. Using the coherent modulation of the inherent crosspeak as an indicator of non-exchange, we have demonstrated that even in systems with complex multilevel vibrational structure it is possible to isolate the chemical exchange signature. Temperature dependent studies enabled separation of IVR from chemical exchange processes while yielding the activation barrier, E_a and ΔG^*, for equilibrium isomerization. Comparison of Arrhenius (E_a) and Eyring (ΔG^*) analysis shows that the entropy makes a substantial contribution to the energy barriers for isomerization, most likely due to the large structural changes associated with switching between bridging and nonbridging forms. Given the substantial entropic contribution the Eyring analysis indicates that the Arrhenius assumption of an isentropic, solvent viscosity independent reaction may be unwarranted. Comparison of our experimental data to DFT calculations suggests that relative to the isolated molecule case the solvent has a large effect on the relative free energies of the isomers.

References:

1. Woutersen, S., Y. Mu, G. Stock, and P. Hamm, *Hydrogen-bond lifetime measured by time-resolved 2D-IR spectroscopy: N-methylacetamide in methanol.* Chemical Physics, 2001. **266**(2-3): p. 137-147.

2. Zheng, J., K. Kwak, J. Asbury, X. Chen, I. Piletic, and M. Fayer, *Ultrafast dynamics of solute-solvent complexation observed at thermal equilibrium in real time.* SCIENCE, 2005. **309**(5739): p. 1338-1343.

3. Zheng, J., K. Kwak, J. Xie, and M. Fayer, *Ultrafast carbon-carbon single-bond rotational isomerization in room-temperature solution*. SCIENCE, 2006. **313**(5795): p. 1951-1955.

4. Kim, Y.S. and R.M. Hochstrasser, *Chemical exchange 2D IR of hydrogen-bond making and breaking*. Proceedings of the National Academy of Sciences of the United States of America, 2005. **102**(32): p. 11185-11190.

5. Ishikawa, H., K. Kwak, J. Chung, S. Kim, and M. Fayer, *Direct observation of fast protein conformational switching*. PROCEEDINGS OF THE NATIONAL ACADEMY OF SCIENCES OF THE UNITED STATES OF AMERICA, 2008. **105**(25): p. 8619-8624.

6. Cahoon, J., K. Sawyer, J. Schlegel, and C. Harris, *Determining Transition-State Geometries in Liquids using 2D-IR*. Science, 2008. **319**: p. 1820-1823.

7. Kim, Y.S. and R.M. Hochstrasser, *The 2D IR Responses of Amide and Carbonyl Modes in Water Cannot Be Described by Gaussian Frequency Fluctuations*. The Journal of Physical Chemistry B, 2007. **111**(33): p. 9697-9701.

8. Kim, Y.S., L. Liu, P.H. Axelsen, and R.M. Hochstrasser, *Two-dimensional infrared spectra of isotopically diluted amyloid fibrils from A beta 40*. Proceedings of the National Academy of Sciences of the United States of America, 2008. **105**(22): p. 7720-7725.

9. Tannenbaum, R. and G. Bor, *Selected reactions of cobalt carbonyl complexes placed under vacuum conditions*. Journal of Organometallic Chemistry, 1999. **586**(1): p. 18-22.

10. Keun Chung, Y., *Transition metal alkyne complexes: the Pauson-Khand reaction*. Coordination Chemistry Reviews, 1999. **188**(1): p. 297-341.

11. Sweany, R.L. and T.L. Brown, *Infrared spectra of matrix-isolated dicobalt octacarbonyl. Evidence for the third isomer*. Inorg. Chem., 1977. **16**(2): p. 415-421.

12. Kenny, J.P., R.B. King, and H.F. Schaefer, *Cobalt−Cobalt Multiple Bonds in Homoleptic Carbonyls? Co2(CO)x (x = 5−8) Structures, Energetics, and Vibrational Spectra*. Inorg. Chem., 2001. **40**(5): p. 900-911.

13. Aullón, G. and S. Alvarez, *The [M2(CO)8] Complexes of the Cobalt Group*. European Journal of Inorganic Chemistry, 2001. **2001**(12): p. 3031-3038.

14. Nee, M.J., C.R. Baiz, J.M. Anna, R. McCanne, and K.J. Kubarych, *Multilevel vibrational coherence transfer and wavepacket dynamics probed with multidimensional IR spectroscopy*. JOURNAL OF CHEMICAL PHYSICS, 2008. **129**(8): p. -.

15. Khalil, M., N. Demirdoven, and A. Tokmakoff, *Vibrational coherence transfer characterized with Fourier-transform 2D IR spectroscopy*. The Journal of Chemical Physics, 2004. **121**(1): p. 362-373.

16. Ogilvie, J.P. and K.J. Kubarych, *Multidimensional Electronic and Vibrational Spectroscopy: An Ultrafast Probe of Molecular Relaxation and Reaction Dynamics*. Adv Atom Mol Opt Phy, 2009. **57**: p. 249-321.

17. Rossini, F.D., K.S. Pitzer, R.L. Arnett, R.M. Braun, and G.C. Pimentel, *Selected values of physical and thermodynamic properties of hydrocarbons and related compounds*. 1953, Pittsburgh: Carnegie Press.

18. Flom, S.R., V. Nagarajan, and P.F. Barbara, *Dynamic Solvent Effects on Large-Amplitude Isomerization Rates .1. 2-Vinylanthracene*. J. Phys. Chem., 1986. **90**(10): p. 2085-2092.

19. Hynes, J.T., *CHEMICAL-REACTION RATES AND SOLVENT FRICTION*. Journal of Statistical Physics, 1986. **42**(1-2): p. 149-168.

20. Atkins, P. and R. Friedman, *Molecular Quantum Mechanics*. 2005, Oxford: Oxford University Press.

21. Schmidt, M.W., K.K. Baldridge, J.A. Boatz, S.T. Elbert, M.S. Gordon, J.H. Jensen, S. Koseki, N. Matsunaga, K.A. Nguyen, S. Su, T.L. Windus, M. Dupuis, and J.A. Montgomery, *General atomic and molecular electronic structure system*. Journal of Computational Chemistry, 1993. **14**(11): p. 1347-1363.

22. Leung, P.C. and P. Coppens, *Experimental charge density study of dicobalt octacarbonyl and comparison with theory*. Acta Cryst., 1983. **1983**(B39): p. 535-542.

Chapter 5

How Solvent Influences Equilibrium Isomerization

The work presented in this chapter has been published in the following paper:

> Jessica M. Anna and Kevin J. Kubarych, "*Watching solvent friction impede ultrafast barrier crossings: A direct test of Kramers theory*," The Journal of Chemical Physics, 133, 2010, 174506.

5.1 Overview: Chapter 5

In this chapter, the well characterized isomerization between two stable isomers of the metal carbonyl complex $Co_2(CO)_8$ is used to systematically investigate how the dynamics of the solvent influence an activated barrier crossing process. In the previous chapter the reaction between isomer I and II of DCO was characterized by developing a method for extracting the exchange signal from spectra having overlapping features. In this chapter, using ultrafast two-dimensional infrared (2DIR) chemical exchange spectroscopy the rate constants for isomerization in a series of linear alkane solvents and cyclohexane are extracted. These measurements facilitate a direct comparison with the widely-adopted Kramers theory of condensed phase reaction kinetics, and for the first time avoid the significant complication of electronic excitation to probe directly in the time domain a ground electronic state reaction with a well-defined transition state. Performing the reaction on a ground electronic state allows for the combination of experiment and computational results

for the removal of the non-dynamical barrier contribution to the rate constant, isolating the dynamical influence of solvent friction. The experimental data, supported with quantum and classical computations, show agreement with Kramers theory for the isomerization rate constant's dependence on solvent viscosity.

5.2 Kramers Theory

Activated barrier crossings are a cornerstone of molecular dynamical phenomena. The rate of a molecular transformation can be predicted entirely from static energetic considerations in the absence of strong coupling to an environment. In the solution phase, however, where the solvent couples strongly to the reacting species, the rate of a chemical reaction may be influenced by the dynamic nature of the solvent.[1-3] It has been a long standing goal of practical and theoretical chemistry to predict reaction rate constants in solution using simple bulk properties such as viscosity or polarity. The dynamical function of the solvent is to dissipate energy through microscopic friction, while supplying thermal excitation through collisions. For a molecule near the transition state of a reaction coordinate the solvent acts to induce recrossings back to the reactant or product well, effectively lowering the overall transmission through the barrier. Such recrossing is neglected by transition state theory (TST); the most common approach to treating the frictional solvent influence is due to Kramers.[4] Kramers theory has been applied to the study of many condensed phase reactions[5-19], finding particularly widespread utility in the kinetics of biopolymer folding, for example, where protein dynamics are slaved to solvent motions.[11-18]

Despite its broad adoption, precise tests of Kramers theory have proven to be somewhat difficult due to important details of experimental implementation. In the past, low-barrier, ultrafast reactions could only be studied using pump-probe transient absorption or time-resolved fluorescence measurements, requiring that the reaction take place on an excited electronic surface. Computing the nuclear coordinate dependence of electronic excited states is still at the frontier of quantum chemistry,

making accurate comparisons with numerical results effectively impossible. Adding further to the difficulty is the lack of a unique relationship between the physically well-defined microscopic friction and readily available bulk viscosity. At liquid densities, increasing the solvent viscosity certainly hinders the reaction, but the precise dependence is what is sought in testing the predictions of Kramers theory, and there are multiple approaches to mapping macroscopic transport to microscopic dissipation.[1, 20-24]

Current advances in ultrafast spectroscopy, particularly the development of two-dimensional infrared (2DIR) and its application to chemical exchange, has enabled us to revisit the fundamental basis of Kramers theory. 2DIR spectroscopy has elucidated chemical exchange phenomena in several systems including solute-solvent complexes, free rotation about a C–C single bond, protein conformational changes, hydrogen bond formation, and fluxional molecules.[25-30] By studying a reaction on the electronic ground state, robust quantum and classical computations can be combined with equilibrium one- and two-dimensional IR spectroscopy to generate a remarkably detailed picture of an activated barrier crossing in the condensed phase. The previous chapter characterized the isomerization reaction between isomer I and II of the flexible metal-carbonyl complex, $Co_2(CO)_8$, the cartoon representation of the isomerization reaction is shown in Fig. 5.1. In this chapter we use this reaction to implement the first direct test of Kramers theory in the time domain in a ground electronic state reaction in a series of solvents. Central to our analysis is the virtually complete insensitivity of the reaction energetics to linear alkane solvent, which enables the isolation of the dynamic friction due to the solvent.

Previous frequency domain studies of Kramers behavior in electronic ground states have been carried out using NMR[31] and Raman spectroscopy[32], where dynamical information is inferred using models of a frequency domain spectroscopic observable, such as the line width. In the Raman study, for example, which investigated the *gauche*-to-*trans* conformational isomerization of *n*-butane, temperature

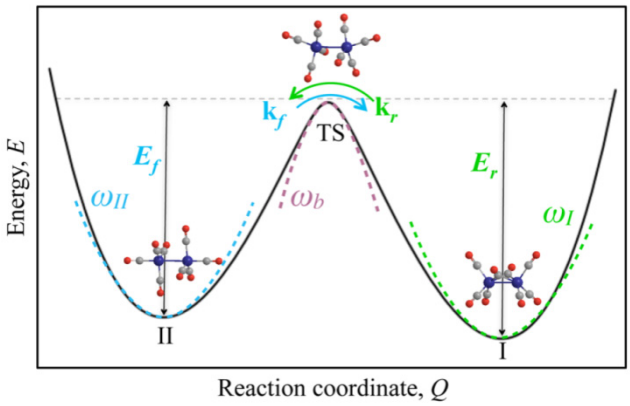

Figure 5.1 Cartoon representation of the potential energy surface along the reaction coordinate. The variables are defined in the text.

dependent line widths were analyzed with the assumption that coupling to the torsional reaction would serve as an additional dephasing mechanism and thus broaden the spectral line shape. Although reasonable, it is now well established that one-dimensional spectra and dephasing models are not always reliable. Indeed a major motivation for the development of multidimensional spectroscopy has been to develop refined descriptions of microscopic dynamics and how they are manifested in higher order spectra. In section 5.6, we also discuss complications associated with using temperature to study low-barrier reactions, where the viscosity, density and the available thermal energy change simultaneously.

In 1940, Kramers derived a correction to transition state theory (TST) using a one-dimensional Langevin equation (Eq. 5.1) where a particle with position x and mass m is subjected to a potential $V(x)$, with solvent dynamics modeled as a velocity v, dependent friction ζ, and a delta-correlated randomly fluctuating force $A(t)$.[4]

$$m\ddot{x}(t) = -\frac{dV(x)}{dx} - \zeta v(t) + A(t) \qquad \textbf{Eq. 5.1}$$

Subsequent development of linear response theory showed the friction to be proportional to the time integral of the fluctuating force autocorrelation function, providing an example of the fluctuation dissipation theorem. Assuming the timescale for the barrier crossing process is much slower than that of the random fluctuations

of the solvent molecules leads to a Markovian friction, which, by definition, lacks memory, and can be considered to be independent of the frequency of the motion along the reaction coordinate. The essence of the Langevin equation is that in the very low friction limit, environmental interactions assist the system to surmount the barrier, whereas at high friction the solvent induces the system to re-cross the barrier, slowing the reaction. The result of Kramers' analysis for the rate constant of a reaction, in the diffusion controlled regime, is given by the following equation :

$$k_{Kramers} = \frac{1}{\omega_b}\frac{\beta}{2}\left(\left(1+\left(\frac{2\omega_b}{\beta}\right)^2\right)^{1/2} - 1\right)k_{1DTST} = Fk_{1DTST} \qquad \textbf{Eq. 5.2}$$

where k_{1DTST} is the rate constant for one dimensional transition state theory, ω_a is the frequency of the reactant well, ω_b is the frequency of the barrier, β is proportional to the friction, E_a is the static energetic barrier, which is the energy difference between the transition state and the stable reactant minimum.

The expression for transition state theory is given in the following equation where Q^* is the partition function associated with the transition state, the partition function in the dividing surface, and Q_A is the partition function associated with the reactant.[33]

$$k_{TST} = \frac{k_B T}{h}\frac{Q^*}{Q_A}e^{-\frac{E_a}{RT}} \qquad \textbf{Eq. 5.3}$$

Considering a one-dimensional chemical reaction, the partition function associated with the transition state has 0 (n-1) degrees of freedom and therefore the partition function is equal to one. Assuming that the reactant potential well can be described as a harmonic oscillator having a frequency, ω_a, we can write the partition function associated with the reactant as the following:

$$Q_A = \frac{1}{1-e^{\frac{E_A}{k_B T}}} = \frac{1}{1-e^{\frac{h\omega_A}{2\pi k_B T}}} \qquad \textbf{Eq. 5.4}$$

Expanding the exponential term in a power series results in the following:

$$e^{\frac{h\omega_A}{2\pi k_B T}} = 1 + \frac{h\omega_A}{2\pi k_B T} \qquad \textbf{Eq. 5.5}$$

Combining Eq. 5.4 and 5.5 and making use of the fact that $Q^*=1$ we can write the ratio of the partition functions as the following:

$$\frac{Q^*}{Q_A} = \frac{h\omega_A}{2\pi k_B T} \qquad \textbf{Eq. 5.6}$$

Substituting Eq. 5.6 into the expression for k_{TST} (Eq. 5.3) results in the expression for k_{1DTST}:[3]

$$k_{1DTST} = \frac{k_B T}{h}\left(\frac{h\omega_A}{2\pi k_B T}\right) e^{\frac{-E_a}{RT}} = \frac{\omega_A}{2\pi} e^{\frac{-E_a}{RT}} \qquad \textbf{Eq. 5.7}$$

Kramers result can be thought of as a correction to transition state theory where the variable F in Eq. 5.2 takes into account the influence of the solvent on the barrier crossing process.

The first quantitative time-domain tests of the effects of solvent friction on activated barrier crossings used picosecond transient spectroscopy to monitor excited electronic state *trans*-to-*cis* isomerization of stilbene and several derivatives.[5-9, 19, 34] In contrast to the present work, these earlier studies required electronic excitation both to lower the isomerization barrier and to enable either transient absorption or fluorescence probes of the reaction progress. Rapid vibrational relaxation is thought to yield a system effectively at equilibrium with respect to the barrier crossing despite the inherently non-equilibrium electronic excitation. In general, precise agreement was not found with the simplest form of Kramers theory with a hydrodynamic Stokes-Einstein (SE) friction model. Experiments by multiple groups carried out in the diffusive regime found the solvent to be less effective than expected in hindering the reaction progress. Several proposals were made to account for the discrepancies including (1) introducing a non-Markovian friction via the Grote Hynes generalization[20]; (2) considering a multidimensional reaction coordinate[21, 23]; and (3)

using alternatives to the simple hydrodynamic model linking macroscopic viscosity to microscopic friction: the so-called Kramers-Hubbard model[8, 19].

Grote and Hynes generalized Kramers theory by replacing the constant friction ζ with a non-Markovian kernel $\int_0^t d\tau \zeta(\tau) v(t-\tau)$.[20] Grote-Hynes theory could be used to fit most of the experimental data.[5-7, 9, 35] However, some experimental data modeled using Grote-Hynes theory led to barrier frequencies (ω_b) that seemed unphysically low[5] or to barrier frequencies that did not agree with experimentally predicted results[7]. The discrepancies in the barrier frequencies were attributed to errors in the nontrivial calculation of the frequency-dependent friction. Later, Murarka *et al.*[36] readdressed the issue of calculating the frequency-dependent friction to find more reasonable barrier frequencies. Alternatively, agreement with a Markovian Kramers theory could be found by adopting a friction parameter due to Hubbard;[37] derived from the molecular reorientational time of the solute. The Hubbard friction retains some of the microscopic details of the solute-solvent interactions that are presumably neglected in the bulk shear viscosity of SE theory. The so-called Kramers-Hubbard model fit some of the available data well, while yielding reasonable barrier frequencies.[19]

Regardless of the specific model of dynamic friction, it is essential to highlight that the Kramers theory result is nearly linear in its dependence on friction, but retains the usual exponential energy dependence of an activated process. Thus it is always a concern that unexpected, non-dynamical changes to the reaction potential surface may dominate the dynamical contribution due to the solvent friction. From an energetic perspective, any changes in the transition state solvation shell structure or its conformational freedom would lead to non-dynamical changes in the rate constant. Despite the difficulty in quantitatively reproducing Kramers theory using systems that appear to be tailor-made benchmarks, Kramers theory is widely accepted in many areas of physical, chemical and biophysical research. In this chapter we describe the first direct test of the dynamical nature of Kramers' theory of activated

barrier crossings on a well-defined, unimolecular, ground electronic state reaction using the powerful methodology of ultrafast two-dimensional infrared (2DIR) chemical exchange spectroscopy.

5.3 2DIR Spectroscopy: Absorptive Spectra DCO

In this chapter we present absorptive 2DIR spectra of DCO at t_2= 100 fs and t_2= 30 ps in Fig. 5.2. In the previous chapter we presented absolute value of the

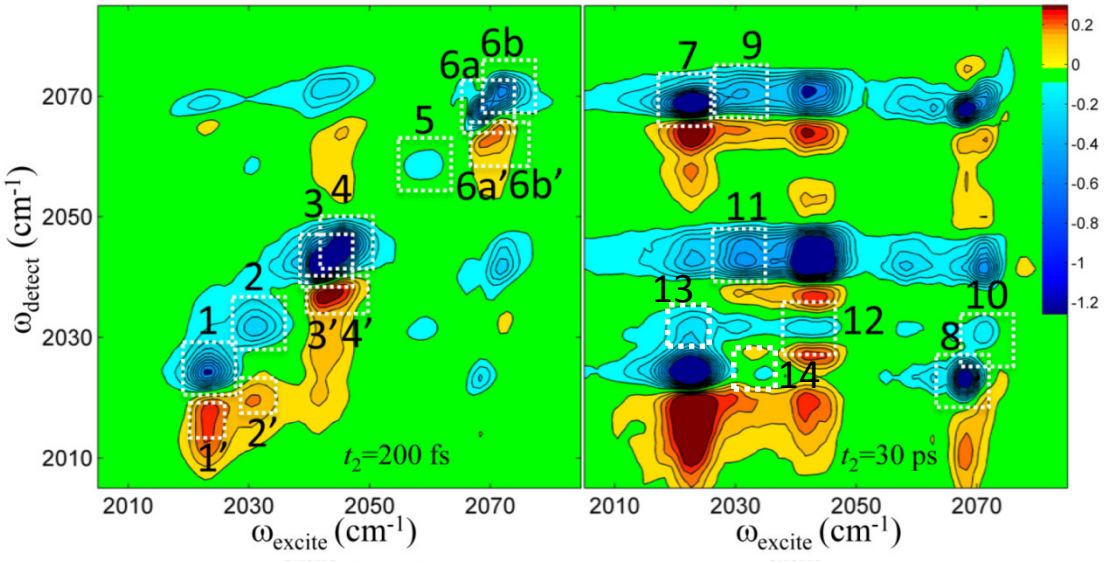

Figure 5.2 Absorptive spectra of DCO in hexane at t_2 =100 fs and t_2=30 ps.

rephasing spectra. In the absorptive spectra, negative peaks (blue) are due to fundamental transitions (i.e. ground state bleach and stimulated emission), while the positive peaks (red) are due to excited vibrational state absorption. Peaks lying along the diagonal correspond to the peaks in the FT-IR spectra; peaks 3, 4 and 6b are assigned to isomer I, peaks 1 and 6a to isomer II and peaks 2 and 5 to isomer III.[38] The induced absorptions appear at slightly lower frequencies along ω_{detect} axis with respect to the diagonal peaks because of the anharmonicity of the vibrations. Peaks 3', 4', and 6b' are assigned to induced excited state absorptions of isomer I, peaks 1' and 6a' are assigned to induced excited state absorptions of isomer II and peak 2' is assigned to the induced excited state absorptions of isomer III. At early t_2, crosspeaks

only arise from coupled modes on the same isomer; the inherent crosspeaks present at t_2= 200 fs confirm the assignment of the diagonal peaks illustrating the remarkable ability of a single 2DIR measurement to assign complex overlapping spectra arising from several distinct species that cannot be chemically separated—even in principle—due to the fact that they interconvert on a picosecond timescale. The negative crosspeaks are due to ground-state bleach and stimulated emission within the first excited state manifold while the positive crosspeaks arise because of excited-state absorption into combination bands between the two coupled modes.

At t_2= 30 ps, crosspeaks 7 and 8 grow with respect to the diagonal peaks. Fig. 5.3 plots the amplitudes of crosspeaks 7 (black) and 8 (red) along with the

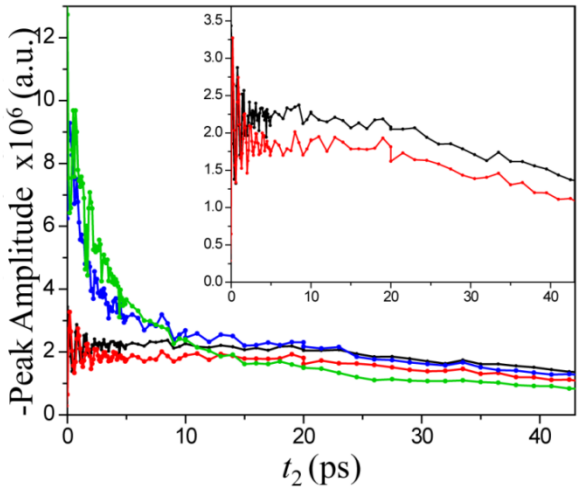

Figure 5.3 Plot of the negative amplitude of peaks 7 (red) , 8 (black), 1 (blue), and 6 (green) as a function of t_2.

corresponding diagonal peaks, 1 (blue) and 6 (green) as a function of t_2. Because of the inability to clearly separate diagonal peaks 6a and 6b, crosspeaks7 and 8 have two contributions: part of the amplitude is due to exchange and the remainder is due to the inherent crosspeak. The inherent crosspeak leads to the oscillations in the amplitude of the crosspeaks that arise from an excited state coherence between the two states of isomer II at 2022 cm^{-1} and 2067 cm^{-1}, and the beat frequency is consistent with the 45 cm^{-1} energy difference.

From the absolute value rephasing spectra we only see evidence of exchange between isomer I and II; however, looking at the absorptive spectra at later t_2 times we do see evidence of exchange between isomers I and III and between isomers II and III. The appearance of crosspeaks 9, 10, 11 and 12 indicate there is exchange between isomers I and III, and the appearance of crosspeaks 13 and 14 suggests that there may be exchange between isomer II and III. Previous studies have predicted a linear pathway to interconversion[38, 39], with experimental studies predicting that isomer I isomerizes to isomer II which then isomerizes to isomer III with the barrier between isomer II and III being very low and the barrier for II-to-I isomerization being ~6 kcal/mol.[38] Previous computational studies predicted a different pathway to interconversion with isomer I converting to isomer III which then isomerizes to isomer II.[39] These studies also predicted different barrier heights, with the barriers between I and II being a few kcal/mol, the barrier for III-to-II isomerization being ~8 kcal/mol and for II-to-III being ~3 kcal/mol. From the crosspeaks in the absorptive 2DIR spectra we see that the assumption of a linear isomerization pathway is not necessarily correct; all the isomers are free to interconvert between each other. The crosspeaks between isomers I and III appear at later t_2 times when compared to the crosspeaks between isomers I and II, indicating that the barrier to isomerization is greater for I-to-III isomerization The crosspeaks between isomers II and III appear at even later t_2 times indicating an even higher barrier for interconversion.

There is evidence of exchange between isomers III and I, isomers II and III, and isomer I and II; however, we focus on the exchange between isomers II and I. The exchange between isomers I and III and isomers II and III is slower than the exchange between II and I due to the fact that the barrier for isomerization between I and III and isomers II and III is larger. The slower exchange between isomers I and III and II and III leads to exchange crosspeaks that emerge at later t_2 times. Also, the population of isomer III is lower than that of II and I leading to a smaller contribution to the overall signal from isomer III. For these reasons we focus on the

exchange between isomer II and I. To extract the rate constants for exchange between isomers II and I, peak 7 provides the most direct probe because it is the least congested peak in the spectrum, there are no overlapping contributions from excited state absorption, and it consists of only two contributions from the exchange and the inherent crosspeaks.

We have used temperature dependent 2DIR spectra to confirm that the growth of crosspeak 7 is due to exchange and not solely due to intramolecular vibrational redistribution (IVR). Employing the model used by Cahoon *et al.*[26], in assuming the rate constant for IVR is directly proportional to the population of liquid phonons at an energy corresponding to the energy difference between the two modes involved in IVR, we found the temperature dependence of the growth of crosspeak 7 to be more consistent with exchange than IVR.

The rate of vibrational energy transfer between different vibrational states can be described by Fermi's golden rule where ρ is the density of states, the ket represents the initial states, the bra represents the final states, and V is the matrix element that couples the initial and final states.[40]

$$k_{IVR} = \frac{2\pi}{\hbar}\rho\left|\langle n, m, \ldots 0 | V | s, t \ldots 1\rangle\right|^2 \qquad \textbf{Eq. 5.8}$$

The occupation number of the initially excited vibrational modes is equal to 1, and it is assumed that the population of the other higher frequency vibrational modes is equal to zero. However, when considering the initial population of the lower frequency vibrational modes, the liquid phonons, we cannot assume that the initial occupation number will be equal to zero. The population of liquid phonons is given by Eq.5.9.[41]

$$n_P(T) = \left[e^{\frac{E_P}{RT}} - 1 \right]^{-1} \qquad \textbf{Eq. 5.9}$$

At room temperature kT=200 cm^{-1}; if the mode being considered is less than 200 cm^{-1} the initial occupation number must be accounted for. Accounting for the initial population of the phonon mode, Eq. 5.8 can be written as the following where n_P is given by Eq. 5.9.[40]

$$k_{IVR} = \frac{2\pi}{\hbar}\rho|V|^2(n_P+1) \qquad \textbf{Eq. 5.10}$$

Assuming that the density of states and the coupling does not significantly change with temperature, we can assume that the rate of IVR is directly proportional to the population of liquid phonons where E_P is the energy level corresponding to the difference in energy between the two modes involved in the IVR process:

$$k_{IVR} \propto n_P = \left[e^{\frac{E_P}{RT}} - 1\right]^{-1} \qquad \textbf{Eq. 5.11}$$

From Eq. 5.11, for an energy gap of 46 cm^{-1} between vibrational modes, we predict a 9% increase in the rate of the IVR constant when the temperature is increased from 25°C to 50°C.

Fig. 5.4 plots the amplitude of crosspeak 7 (from the absolute value rephasing spectra) at two different temperatures 25 (black) and 50°C (red). From a biexponential fit we find that the amplitude of crosspeak 7 grows with a rate constant of 0.164 ps^{-1} (6.1 ps) at 25°C and a rate constant of 0.294 ps^{-1} (3.4) at 50°C; the rate constant at 25°C increases by 79% when the temperature is increased to 50°C. IVR alone would not lead to such a large increase in the rate constant; the large increase in the rate constant is more consistent with exchange having a barrier of ~5 kcal/mol. Though it is possible that there is some IVR contribution to the temperature dependence of the rate constant, it is at most an order of magnitude smaller than the barrier contribution.

In order to test this further, we performed temperature-dependent 2DIR experiments on $Rh(CO)_2C_5H_7O_2$ (RDC Fig. 5.5) in hexane. RDC has been extensively studied by Tokmakoff *et al.*[42, 43] and is known to exist as one isomer that

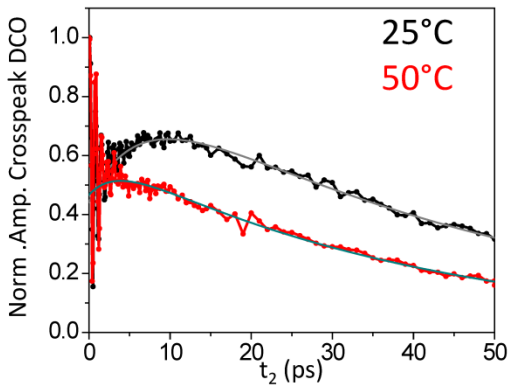

Figure 5.4 Normalized amplitude of peak 7 of DCO at 25°C (black) and 50°C (red) with biexponential fits shown.

has two IR active carbonyl modes exhibiting efficient and rapid IVR. In comparing the temperature dependence of the RDC crosspeaks to the temperature dependence of the DCO crosspeaks, we find a dramatic difference, with the growth of DCO crosspeak being more sensitive to temperature changes (Fig. 5.5). The comparisons of DCO to the IVR model and to RDC indicate that a substantial part of the growth of crosspeak 7 of DCO is due to exchange.

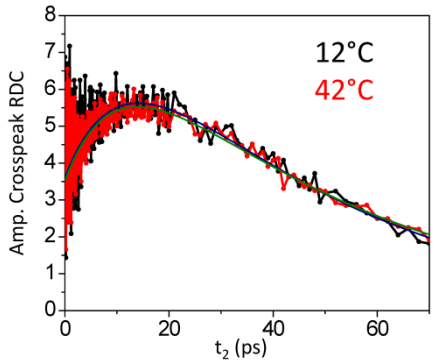

Figure 5.5 Amplitude of the RDC crosspeak at ω_1=2014 $cm^{-1}$$\omega_3$=2085 cm^{-1} plotted as a function of t_2 time at 12°C (black) and 42°C (red) with biexponential fits.

5.4 Solvent Dependent Rate Constants

In the previous chapter we have described a method for separating the contribution of the exchanging crosspeak from the contribution of the inherent crosspeak using t_2-dependent absolute-value rephasing spectra. In using absolute value rephasing spectra, which require half the acquisition time of absorptive spectra, a single t_2 scan for a given solvent can be collected within one hour, limiting long-time drift. Another benefit in using absolute-value rephasing spectra is the fact that the inherent crosspeaks oscillate as a function of t_2, and using these oscillations we are able to lock onto to the inherent contribution to the crosspeak; extracting the exchange contribution. In this chapter, we have expanded our kinetic model to include both IVR and exchange processes along with molecular reorientation times, the latter of which were obtained from molecular dynamics simulations. The total signal of crosspeak 7 is the sum of the signal from the exchange crosspeak and the signal from the inherent crosspeak.

$$S_{Total}(t) = S_{exchange}(t) + S_{inherent}(t) \qquad \textbf{Eq. 5.12}$$

We first describe the model we use for the exchange crosspeak then we describe the model used for the inherent crosspeak.

Using the same approach as Kwak *et al.*, the amplitude of a peak in the spectrum is given by Eq. 5.13 where A indicates the species, N_A is the effective population of the species A and p_A is the probability that the interacting dipole will be oriented at θ and φ at time t.[44]

$$S_A(t) \propto N_A(t)\left\langle p_A(\theta,\varphi,t)\right\rangle \qquad \textbf{Eq. 5.13}$$

The amplitude of the signal depends on the concentration of species A, the oscillator strength of the transition, and the tuning of the incoming pulses. In order to avoid accounting for each of these terms separately we use the effective population, which accounts for all of these contributions. The effective population

term and orientational term in Eq. 5.13 are treated independently for the case of the exchanging crosspeak and the inherent crosspeak.

5.4.1 Exchange Crosspeak

The kinetic model used to describe the equilibrium chemical exchange process is shown in Fig. 5.6.

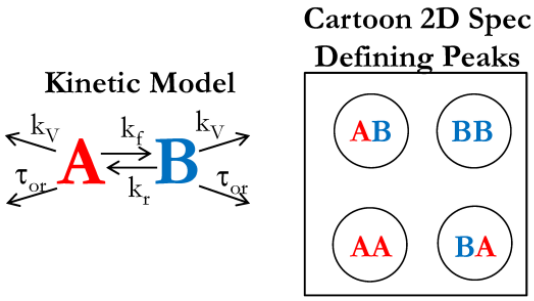

Figure 5.6 The kinetic model used for the exchange crosspeak along with the corresponding 2D spectrum.

Considering first the effective population term, we write the set of rate laws, Eq. 5.14, from the kinetic model in Figure 5.6, describing how the effective population changes with time where k_V is the rate constant associated with vibrational population relaxation, k_f and k_r are the forward and reverse rate constants, and N_{II} and N_I are the effective populations of isomer II and isomer I.

$$\frac{d}{dt}\begin{pmatrix} N_{II}(t) \\ N_I(t) \end{pmatrix} = \begin{pmatrix} -(k_V + k_f) & k_r \\ k_f & -(k_r + k_V) \end{pmatrix}\begin{pmatrix} N_{II}(t) \\ N_I(t) \end{pmatrix} \qquad \textbf{Eq. 5.14}$$

Now we discuss the molecular reorientation term. Considering the molecular reorientation to be diffusive, according to Debye's theory of rotational Brownian motion, the probability of a dipole being oriented at θ and φ at time t is given by Eq. 5.15 where D_A is the rotational diffusion constant for species A, which is related to the molecular reorientation time ($6D_A=(1/\tau_{or})$.[45, 46]

$$\frac{dp_A(\theta,\varphi,t)}{dt} = D_A\nabla^2 p_A(\theta,\varphi,t) \qquad \textbf{Eq. 5.15}$$

It is known that the solutions to Eq. 5.15 are the spherical harmonics and are given by Eq. 5.16 where the angles θ and φ are defined in Figure 5.7.[46]

$$p_A(\theta,\varphi,t) = \sum_{l,m} Y_{l,m}(\theta,\varphi) e^{-l(l+1)D_A t} \qquad \textbf{Eq. 5.16}$$

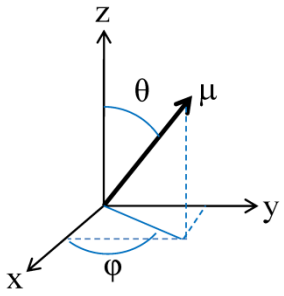

Figure 5.7 The angle θ and φ are shown. The incoming field, E, is polarized along the z axis, and μ is the transition dipole moment.

Assuming that the incoming light is polarized along the z-axis and neglecting the molecular reorientation that occurs during t_1 and t_3 we can write the boundary conditions as follows.[44]

$$p_A(\theta,\varphi,0) = \frac{3}{4\pi}\cos^2\theta \qquad \textbf{Eq. 5.17}$$

$$p_A(\theta,\varphi,\infty) = 1 \qquad \textbf{Eq. 5.18}$$

Making use of boundary conditions and the fact that the general solutions to Eq. 5.15 are the spherical harmonics, the solution follows.[44]

$$p_A(\theta,\varphi,t) = \frac{\sqrt{4\pi}}{4\pi} Y_{00} + \sqrt{\frac{4\pi}{5}} \frac{2}{4\pi} Y_{20} e^{-6D_A t} \qquad \textbf{Eq. 5.19}$$

Averaging over θ and φ we obtain the ensemble average and the orientational contribution to the signal is given by Eq. 5.20.

$$\langle p_A(t) \rangle = \frac{4}{15} e^{-6D_A t} + \frac{1}{3} \qquad \textbf{Eq. 5.20}$$

Combining the effective population and the orientational solutions, the general solutions for the exchange crosspeak follows where D_{II} and D_I are the rotational diffusion constants for isomer II and isomer I.

$$\begin{pmatrix} N_{II}(t)\langle p_{II}(t)\rangle \\ N_I(t)\langle p_I(t)\rangle \end{pmatrix} = \frac{4}{15}\exp\left[\begin{pmatrix} -(k_V+k_f+6D_{II}) & k_r \\ k_f & -(k_r+k_V+6D_I) \end{pmatrix} t\right]\begin{pmatrix} N_{II}(0) \\ N_I(0) \end{pmatrix} \qquad \textbf{Eq. 5.21}$$

$$+\frac{1}{3}\exp\left[\begin{pmatrix} -(k_V+k_f) & k_r \\ k_f & -(k_r+k_V) \end{pmatrix} t\right]\begin{pmatrix} N_{II}(0) \\ N_I(0) \end{pmatrix}$$

The analytical solutions for crosspeak 7 were obtained by solving the above equations and setting $N_{II}(0)=0$ and $N_I(0)=1$ for $N_{II}(t)\langle p_{II}(t)\rangle$ resulting in $S_{exchange}(t)$.

$$S_{exchange}(t) = A_{exchange}\left[-ae^{-(k_{exc}+k_V)t} + ae^{-(k_V)t} + \frac{8e^{-\frac{1}{2}ct}Sinh\left(\frac{bt}{2}\right)}{15b}\right] \qquad \textbf{Eq. 5.22}$$

In the above equation, $k_{ex}=k_f+k_r$, $A_{exchange}$ is the overall amplitude of the exchange crosspeak, $a=\frac{k_r}{3(k_f+k_r)}$, $b=\sqrt{(D_{II}-D_I+k_f)^2+2(-D_{II}+D_I+k_f)k_r+k_r^2}$, and $c=D_{II}+D_I+k_r+k_f+2k_V$.

5.4.2 Inherent Crosspeak

Here we treat the IVR process as an equilibrium process and the kinetic model in Fig. 5.8 is used to describe the process.

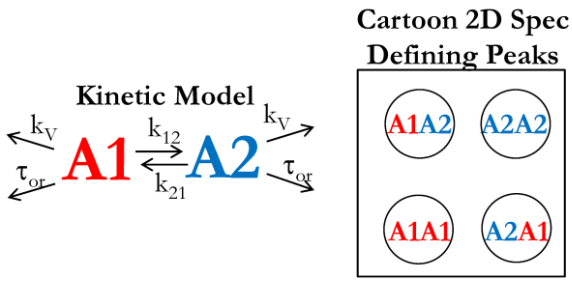

Figure 5.8 The kinetic model used for the inherent crosspeak along with the corresponding 2D spectrum.

Addressing the effective population term first, we write the set of rate laws, Eq. 5.23, from the kinetic model in Figure 5.8, describing how the effective population changes with time where k_V is the rate constant associated with vibrational population relaxation, k_{IVR} and k_{-IVR} are the forward and reverse rate constants associated with IVR, and N_{IIa} and N_{IIb} are the effective populations of the lower frequency mode (IIa) and higher frequency mode (IIb) of isomer II.

$$\frac{d}{dt}\begin{pmatrix} N_{IIa}(t) \\ N_{IIb}(t) \end{pmatrix} = \begin{pmatrix} -(k_V + k_{IVR}) & k_{-IVR} \\ k_{IVR} & -(k_{-IVR} + k_V) \end{pmatrix}\begin{pmatrix} N_{IIa}(t) \\ N_{IIb}(t) \end{pmatrix} \qquad \textbf{Eq. 5.23}$$

We now consider the orientational contribution for the inherent crosspeak. For the inherent crosspeak, we account for the orientational contribution according to the method established by Golonzka *et al.*.[47] Assuming the two transition dipole moments are oriented 90° to each other, the orientational contribution to the crosspeak for the rephasing spectrum is given by Eq. 5.24.[47] It is important to note that we are not accounting for orientational contributions during t_1 and t_3 period, only during the t_2 period.

$$\langle p_A(t)\rangle = \frac{3}{45}e^{-6D_A t} + \frac{1}{9} \qquad \textbf{Eq. 5.24}$$

Combining the effective population and the orientational solutions, the general solutions for the inherent crosspeak follow.

$$\begin{pmatrix} N_{IIa}(t)\langle p_{IIa}(t)\rangle \\ N_{IIb}(t)\langle p_{IIb}(t)\rangle \end{pmatrix} = \frac{3}{45}\exp\left[\begin{pmatrix} -(k_V + k_{IVR} + 6D_{II}) & k_{-IVR} \\ k_{IVR} & -(k_{-IVR} + k_V + 6D_{II}) \end{pmatrix}t\right]\begin{pmatrix} N_{IIa}(0) \\ N_{IIb}(0) \end{pmatrix} \qquad \textbf{Eq. 5.25}$$

$$+\frac{1}{9}\exp\left[\begin{pmatrix} -(k_V + k_{IVR}) & k_{-IVR} \\ k_{IVR} & -(k_{-IVR} + k_V) \end{pmatrix}t\right]\begin{pmatrix} N_{IIa}(0) \\ N_{IIb}(0) \end{pmatrix}$$

The analytical solution for the t_2 dependent amplitude of the inherent contribution to peak 7 is given by Eq. 5.27. It is important to note that the solution to the kinetic model for the inherent crosspeak was multiplied by a term that accounts for the t_2 time dependence of the coherence created between the two modes

of isomer II where we have derived the t_2 time dependence of the coherence in the previous chapter.

$$S_{inherent}(t) = A_{inherent}\left[\frac{1}{45}e^{-(d+k_V+D_{II})t}\left(fN_{IIa}(0) - gN_{IIb}(0) + \left(N_{IIa}(0) + N_{IIb}(0)\right)ge^{dt}\right)\right]* \quad \textbf{Eq. 5.26}$$

$$\left[\left(3+5e^{D_{II}t}\right)\left(abs\left(e^{(i\omega_{ab}-k_d)t+\varphi}\right)\right)\right]$$

In the above equation ω_{ab} is the frequency difference between modes IIa and IIb, k_d is the rate constant associated with the dephasing of the coherence and φ is the phase, $A_{inherent}$ is the overall amplitude of the inherent crosspeak, $d = k_{IVR} + k_{-IVR}$, $f = \frac{k_{IVR}}{k_{IVR} + k_{-IVR}}$, and $g = \frac{k_{-IVR}}{k_{IVR} + k_{-IVR}}$.

5.4.3 Extracted Rate Constants

Using the results from section 5.5.1 (Eq. 5.22) and section 5.5.2 (Eq. 5.26), we extract the forward and reverse exchange rate constants by fitting the t_2 dependent amplitude of crosspeak 7 to Eq. 5.27 where $S_{exchange}(t)$=Eq. 5.22 and $S_{inherent}(t)$=Eq. 5.26.

$$S_{Total}(t) = S_{exchange}(t) + S_{inherent}(t) \quad \textbf{Eq. 5.27}$$

Using a multivariable least squares fitting algorithm the data was fit to Eq. 5.27 by allowing five parameters to vary: k_f, k_d, φ, $A_{exchange}$, and $A_{inherent}$. The other parameters were determined through a combination of experimental and computational methods.

The effective populations of modes IIa and IIb are required for the inherent contribution to the crosspeak. Due to overlapping features from the three isomers of DCO the initial effective populations cannot be determined directly from experimental spectra. To obtain the effective populations we used the SPECTRON software package[48] to simulate the individual 2D spectra of the different isomers at t_2= 500 fs. DFT calculations were performed to obtain the transition dipole moments

of the IR active modes and the contribution of the individual spectra were weighted to reproduce the experimental absorptive spectra along with the experimental linear FT-IR spectra. Using the parameters that reproduced the experimental absorptive spectra, the effective population of modes IIa and IIb for the absolute value rephasing spectra were found to be $N_{IIa}(0)=0.95$ and $N_{IIb}(0)=1.16$.

For both the inherent and exchange crosspeaks the molecular reorientation times are needed. The molecular reorientation times of isomer I and II were obtained from MD trajectories. Molecular dynamics simulations were used rather than polarization dependent pump-probe spectra due to the fact that the pump-probe spectra are too congested to extract anisotropies of transitions on individual isomers. In the terminal carbonyl region the peaks in the pump-probe spectrum have contributions from two or more different isomers. Previous studies on a non-exchanging metal carbonyl system have shown good agreement between experimentally determined τ_{or} and the τ_{or} determined from MD simulations.[49]

To obtain the molecular reorientation times, the transition dipole moments of the IR active terminal carbonyl stretching modes, obtained from DFT calculations, were projected onto the coordinates of each isomer for each frame. This allows for the dipole-dipole time correlation function for each vibrational mode to be calculated. The dipole-dipole time correlation function is related to the anisotropy of a species according to Eq. 5.28 where P_2 is the second Legendre polynomial.[50]

$$r(t) = \frac{2}{5} C_2(t) \text{ where } C_2(t) = \left\langle P_2\left[\vec{\mu}(0)\cdot\vec{\mu}(t)\right]\right\rangle \qquad \textbf{Eq. 5.28}$$

Figure 5.9 shows a plot of $C_2(t)$ for the 2069 cm^{-1} mode isomer I in hexane. A single exponential fits the data well. Fitting the data to the Eq. 5.29 gives the molecular reorientation time, τ_{or}.

$$C_2(t) = Ae^{-t/\tau_{or}} \qquad \textbf{Eq. 5.29}$$

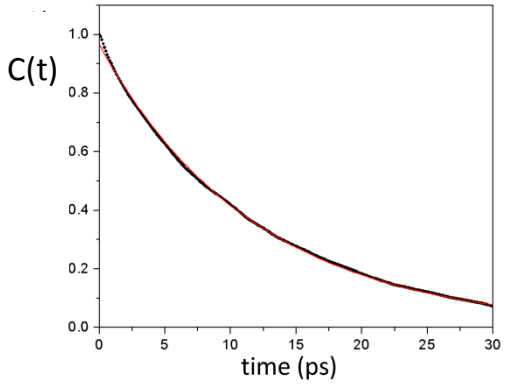

Figure 5.9 A plot of C(t) for highest frequency mode of isomer I in hexane (black) and the single exponential fit (red).

The molecular reorientation times of each IR active terminal carbonyl stretching mode for isomers I and II in the series of linear alkane solvents and cyclohexane were obtained in this fashion. The overall molecular reorientational times used were obtained by averaging the individual reorientational times of the

Table 5.1 The molecular reorientation times of Isomer I and Isomer II for the series of solvents.

	Isomer I τ_{or}(ps)	Isomer II τ_{or}(ps)
hexane	12.7	12.3
heptane	16.3	19.0
octane	20.7	22.7
decane	42.7	44.0
dodecane	57.7	84.7
cyclohexane	31.7	26.7

modes together and are given in Table 5.1.

To separate the forward and reverse rate constants we obtained the equilibrium constants from linear FTIR spectra of DCO in the different solvents. Fitting the peaks in the spectrum to seven Lorenzians and taking the ratios of the areas of the peaks corresponding to isomer I and isomer II results in the equilibrium constant. The equilibrium constants for the series of linear alkanes and cyclohexane follow:

hexane K_{eq} =1.09, heptane K_{eq} =1.07, octane K_{eq} =1.06, decane K_{eq} =1.06, dodecane K_{eq} =1.03 and cyclohexane K_{eq} =1.40.

The rate constant associated with vibrational population, k_V, and the rate constants associated with IVR, k_{IVR} and k_{-IVR}, are also needed. The rate constant corresponding to the vibrational population relaxation was set to k_V=0.02 ps^{-1} (50 ps). This value was determined by fitting crosspeak 7 in the different solvents to a biexponential consisting of a growth and decay. Although the long time decay varied between 43 and 58 ps, there was not a correlation between the long time decay constant and the solvent. Taking the average of the long time decays for crosspeak 7 in all the linear alkane solvents results in a rate constant corresponding to 0.02 ps^{-1} (50 ps).

For the rate constant associated with intramolecular vibrational relaxation, we chose to use an IVR rate of k_{IVR}=0.01 ps^{-1}. The timescale associated with IVR is thought to be longer because the normal modes involved in the IVR processes, IIa and IIb, involve displacement of different local carbonyl units[26], with the majority of the motion for mode IIb being motion of the axial carbonyl units and mode IIa only involves motion of equatorial carbonyl units. However, in order to determine how the extracted rate of exchange depends on the inputted IVR rate constant, we varied k_{IVR} for the linear alkanes and refit the data for six different k_{IVR} rates corresponding to 3 ps, 10 ps, 20 ps, 55 ps, 100 ps, and 1000 ps. For each of the IVR rates we also allowed the vibrational population relaxation rate to vary by ±5 ps and the molecular reorientation time to vary by ±5 ps. In comparing the average rate constants obtained from varying the IVR rate, vibrational population relaxation rate and molecular reorientation time to the average rate constant obtained from setting the IVR rate to correspond to 100 ps the vibrational population relaxation time to correspond to 50 ps and the molecular reorientation time to be that determined from the molecular dynamics simulations, we find that the resulting rate constants only vary by 0.0042 ps^{-1} at most.

Using these parameters as inputs and allowing the forward rate constant, k_f, the dephasing rate constant, k_D, the phase of the coherence, φ, and the amplitudes of the inherent and exchange crosspeaks, $A_{inherent}$ and $A_{exchange}$, to vary we fit the t_2 trace of the amplitude of crosspeak 7 to Eq. 5.27.

In Figure 5.10 we demonstrate our fitting process. Figure 5.10a plots the t_2 trace of the amplitude of crosspeak 7 in hexane along with the corresponding fit to Eq. 5.27 (black). The fit is obtained by minimizing the residual (Fig. 5.10c) along with

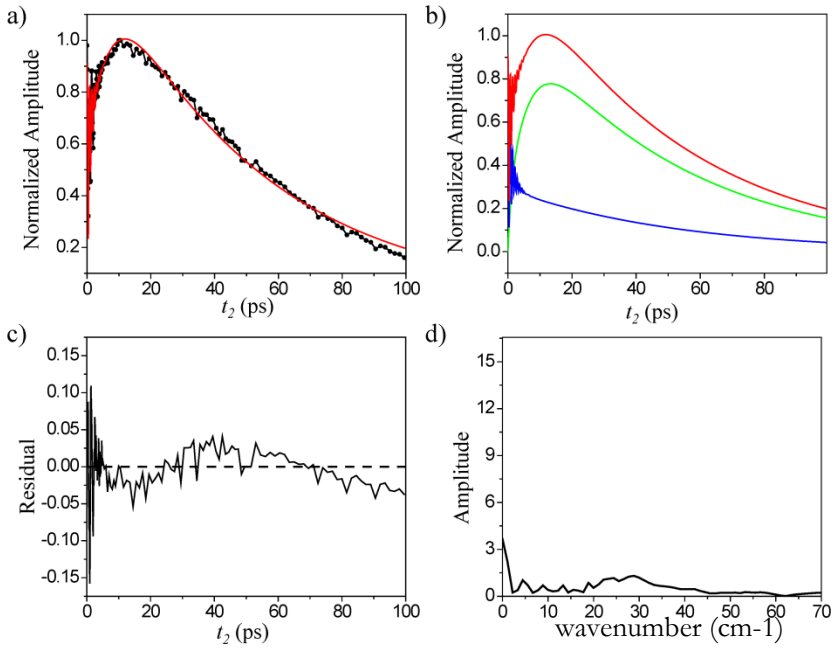

Figure 5.10 (a) The normalized amplitude of peak 7 is plotted as a function of t_2 (black). The fit is plotted in red. (b) The total fit to peak 7 is plotted in red, the contribution from the inherent crosspeak is plotted in blue and the contribution from the exchange crosspeak is plotted in green. (c) The residual is plotted. (d) The amplitude of the Fourier transform of the residual.

minimizing the amplitude of the Fourier transform of the residual (Fig. 5.10d). From Fig. 5.10c it can be seen that the residual is centered around zero. In the plot of the Fourier transform of the residual (Fig. 5.10d black curve), we see that the peak due to the exponential growth and decay is minimized along with the peak at 45 cm^{-1} The resulting extracted exchange and inherent contributions to the crosspeak are plotted

in Figure 5.10b. The inherent crosspeak (blue) first oscillates and then decays while the exchange crosspeak (green) first grows in and then decays.

Using this procedure we have extracted the forward and reverse rate constants from the absolute value rephasing spectra of DCO in the series of linear alkanes and in cyclohexane. The waiting time dependent rephasing spectra for each linear alkane solvent were taken at least twice, and the reported rate constants were obtained from averaging the individual rate constants. Figure 5.11 plots the amplitude of crosspeak 7 (absolute value rephasing spectra) for the series of linear solvents; from this data the

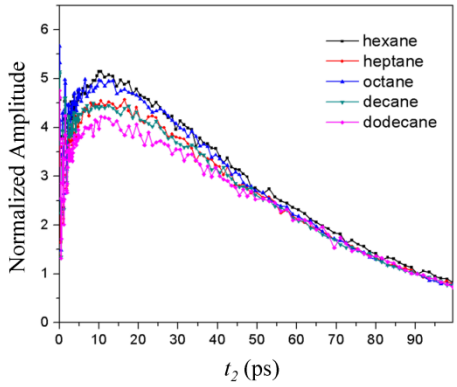

Figure 5.11 The amplitude of crosspeak 7 plotted as a function of t_2 time for the series of solvents, hexane (black) heptane (red) octane (blue) decane (green) and dodecane (pink). Each trace was normalized to its amplitude at 90 ps.

rate constants reported as Experiment 1 in Table 5.2 were obtained. The individual rate constants along with the R^2 value obtained from the fitting process are given in Table 5.2. The error bars were obtained by allowing the rate constants to vary until the R^2 value decreased by -0.01. From the forward rate constants the reverse rate constant was obtained from the equilibrium constant ($k_r=k_f/K_{eq}$).

Table 5.2 The forward rate constants obtained from the fits for the series of solvents

	Experiment 1		Experiment 2		Experiment 3	
	k_f(ps^{-1})	R squared	k_f(ps^{-1})	R squared	k_f(ps^{-1})	R squared
hexane	0.086 ± 0.010	0.977	0.100 ± 0.012	0.990		
heptane	0.069 ± 0.007	0.980	0.092 ± 0.011	0.989	0.069 ± 0.008	0.984
octane	0.066 ± 0.008	0.980	0.070 ± 0.008	0.992		
decane	0.042 ± 0.005	0.976	0.040 ± 0.004	0.986		
dodecane	0.026 ± 0.003	0.972	0.033 ± 0.004	0.971	0.025 ± 0.004	0.968
cyclohexane	0.062 ± 0.006	0.866				

The forward isomerization time (II-to-I), $1/k_f$, is less than the reverse isomerization time (I-to-II), $1/k_r$, which is consistent with isomer I lying lower in energy than isomer II. In the linear alkane series, as the carbon chain length of the solvent increases the isomerization time also increases (Fig. 5.12). There are two

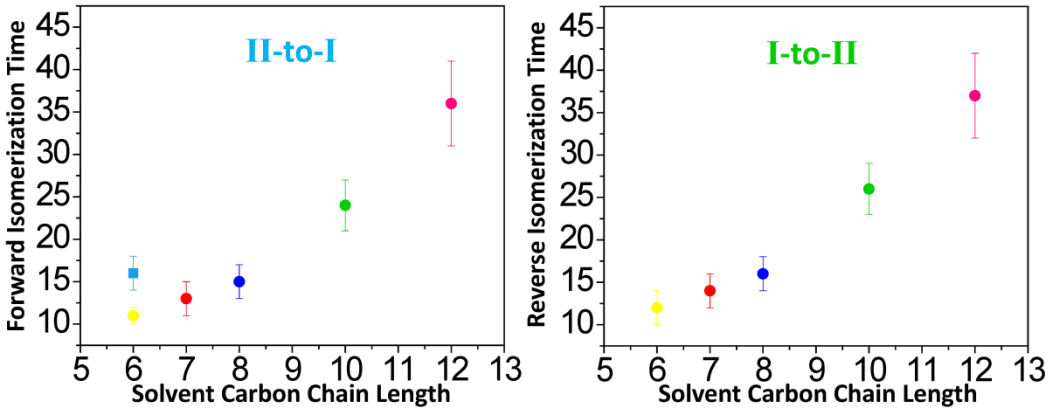

Figure 5.12 Plot of the forward (left) and reverse (right) isomerization times versus solvent carbon chain length.

possible reasons for this increase; either the solvent induces static modulations of the potential energy surface or the solvent causes dynamic changes by frictionally impeding the barrier crossing process.

5.5 Static Versus Dynamic Solvent Effects

One of the benefits to studying a picosecond isomerization reaction occurring on the ground electronic surface is that the static energetic contribution from the

solvent can be isolated from the dynamic friction using DFT calculations, MD simulations and linear FT-IR spectra. We first demonstrate, through the use of linear FT-IR spectra, that the relative energies of the isomers are invariant to linear carbon chain length. However, from the linear FT-IR spectra we do not gain any insight on how the energy of the TS is affected by the solvent. We employ both MD simulations and DFT calculations to determine how the solvent influences the energy of the transition state relative to the ground states. The entropic contribution associated with changing the solvent is accessed through the use of MD simulations, while DFT calculations are used to determine the solvent dependent activation energies.

5.5.1 Linear FT-IR Spectra

In the previous chapter we described the previous assignment of the linear IR spectrum of DCO in hexane; we briefly describe the assignment again here. The FT-IR spectrum of DCO in hexane along with the Lorentzian fits is shown in Fig. 5.13; the peaks in dashed green are assigned to isomer I, dashed blue to isomer II and dashed orange to isomer III.

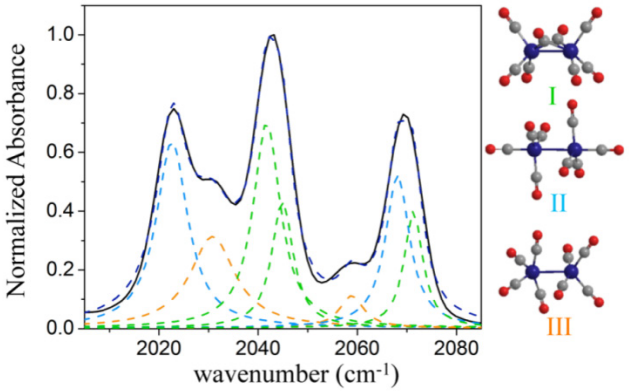

Figure 5.13 FT-IR spectra of DCO in hexane with the dashed green peaks assigned to isomer I, dashed blue to isomer II and dashed orange to isomer III.

In this section we look at the solvent dependent FT-IR spectrum of DCO. Figure 5.14 plots the FT-IR spectra of DCO in hexane (black), heptane (red), octane (blue), decane (green), dodecane (dark yellow) and cyclohexane (burgundy). Fitting each spectrum to 7 Lorentzains, we obtained the equilibrium constant ($K_{eq} = k_f/k_r$)

from taking the ratio of the fitted areas of peaks corresponding to isomer I and isomer II finding that K_{eq} only varies from 1.09 in hexane to 1.03 in dodecane for the linear alkanes, and for cyclohexane the equilibrium constant is 1.40.

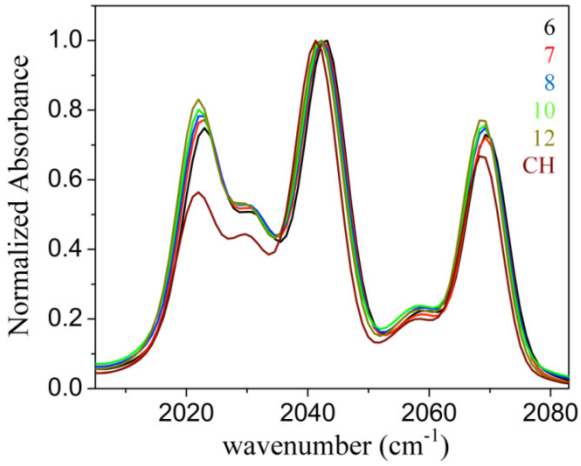

Figure 5.14 Normalized FT-IR spectra of DCO in the series of linear alkane solvents (length=6, 7, 8, 10, 12) and cyclohexane (CH).

For the linear alkanes, the nearly overlapping FT-IR spectra show that the relative energies of the two isomers do not vary among the linear solvents. From the equilibrium constants, using Eq. 5.30 we find a difference in ΔG of only 0.03 kcal/mol when the solvent is changed from hexane to dodecane.

$$\Delta G = -RT \ln\left(K_{eq}\right) \qquad \textbf{Eq. 5.30}$$

This small change among the linear alkanes indicates that changing the solvent does not result in a static modulation of the energy of the two isomers. In comparing the FT-IR spectra in the linear alkanes to that of cyclohexane, it is evident that the relative energies of the isomers have changed. In cyclohexane ΔG =-0.20 kcal/mol, compared to a ΔG =-0.05 kcal/mol in hexane and ΔG =-0.02 kcal/mol in dodecane, isomer I is stabilized with respect to isomer II in cyclohexane compared to the linear alkanes. Though the relative energy of the isomers is different in the cyclic alkane compared to the linear alkanes, the solvent does not modulate the relative energies of the isomers within the series of linear alkanes.

5.5.2 Molecular Dynamics Simulations

Using MD simulations we confirm the results from the FT-IR spectra and demonstrate the solvent does not entropically influence the energy of the different species within the linear alkane series.

Molecular dynamics (MD) simulations were performed on isomer I, isomer II and the transition state in all the solvents using the GROMACS package.[51] For each simulation an isomer (or transition state) was added to a cubic box containing between 300 to 340 solvent molecules and periodic boundary conditions were used in all directions. The simulations where performed using the NPT ensemble, (constant pressure and temperature) using the Berendsen coupling scheme to maintain a temperature of 298 K and a pressure of 1 bar.[52] Long range electrostatic interactions were accounted for by using the particle-mesh Ewald (PME) summation method with the interaction cutoff set to 1 nm.[53, 54] The nearest neighbor list was updated every 10 time steps, and time steps of 1 fs were taken. The length of the MD simulations varied depending on the solvent; for cyclohexane, hexane, heptane and octane 6 ns trajectories were obtained, for decane a 10 ns trajectory was obtained and for dodecane a 13 ns trajectory was obtained.

The radial distribution functions were obtained using 2 ns segments taken from the longer trajectories. The force fields for isomer I, II and the transition state were constructed from DFT calculations assuming a harmonic potential for the bonds and angles, and atomic charges were determined from using the CHarges from ELectroscatic Potential (CHELP) algorithm.[55] The force constants for the bonds and angles of the transition state were assumed to be the same as those for isomer II. The general AMBER force field (GAFF) was used to describe the solvent molecules.[56, 57] The structure of the geometry-optimized solvent molecule along with the atomic charges were obtained from DFT calculations using the B3LYP functional and the 6-31+G(d) basis set.[58, 59]

From MD simulations we obtained RDFs (Fig. 5.15) which provide a structural picture of the average solvation environment around the individual isomers and the transition state. Fig. 5.15 shows radial distribution functions (RDFs) obtained from MD trajectories of the distances between the center of mass of isomer I, isomer II, or the transition state and all the solvent atoms for the series of linear alkanes and cyclohexane. There is no apparent difference between the RDFs of the isomers or the transition state in the series of linear alkanes; however, in comparing the linear alkanes to cyclohexane, the differences in the RDFs are clear and are highlighted by the dashed grey lines in Fig. 5.15.

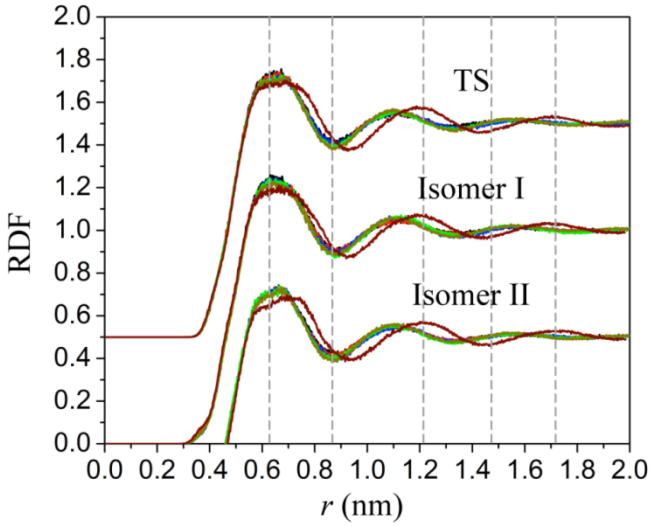

Figure 5.15 Radial distribution functions for isomer I, II (shifted by -0.5), and the transition state (shifted by +0.5) in the series of solvents (same key as in Fig. 5.14). The radial distribution functions are of the distances between the center of mass of the solute and all of the atoms of the solvent.

The invariance of the RDFs within the linear alkanes indicates that as the solvent changes the solvation environment is not altered, and since the radial distribution function is related to the thermodynamic properties of the system[60], the energies of the isomers are not altered. As would be anticipated from the differences in the linear FT-IR spectra, there is a considerable difference between the RDFs for the cyclic and the linear alkanes. The RDFs show that for the series of linear alkanes not only are the energies of the isomers independent of the solvent, but the energy of the transition state is also independent of the solvent.

For cyclohexane, the width of the first solvation shell is broader compared to the linear alkanes. We attribute this to structural aspects of the cyclohexane molecules. In Fig. 5.16, the probability distribution functions for above the xy plane and below the xy plane for isomer I and II in cyclohexane and hexane are plotted. The molecular axes used to define the xy planes are also shown in Fig. 5.16. For isomer II, we see that the distribution functions for above and below the planes are

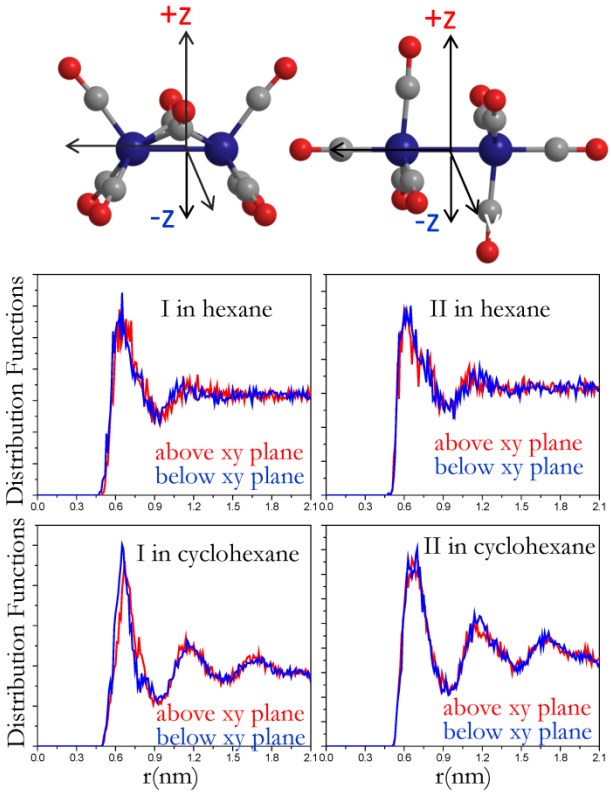

Figure 5.16 Directional dependent distribution functions for isomer I and isomer II in hexane and cyclohexane

the same in hexane and cyclohexane. However, for isomer I in cyclohexane the distribution functions for above and below the xy planes are different, with the first solvation shell for the below-the-plane distribution function being shifted closer. For isomer II in cyclohexane the distribution functions for above and below the planes are the same. The difference for isomer I indicates that the structural aspects of cyclohexane are playing a role in solvation, with solvent molecules being closer to isomer I below the xy plane.

5.5.3 DFT Calculations

DFT calculations also confirm the results from the MD simulations and the FT-IR spectra for the linear alkanes. Density functional theory (DFT) calculations were performed on Isomer I, Isomer II and the corresponding transition state using GAUSSIAN03.[61] The calculations were performed using the B3LYP functional with the 6-31+G(d) basis set for the carbon and oxygen atoms and the LANL2DZ pseudopotential was used for the cobalt atoms, the choices of functional and basis sets were based on previous computational studies performed on dicobalt octacarbonyl by Kenny *et al.*[62] and Aullón *et al*[39]; however, these previous calculations did not account for the solvent. In this study we accounted for three different solvents, hexane, decane and cyclohexane, using the polarized continuum model.[63-65] The transition states in hexane, decane and cyclohexane were determined and optimized using synchronous transit-guided quasi-Newton methods.[66, 67] Performing a frequency calculation on the optimized transition state structures results in one imaginary frequency, confirming the structure is a transition state.

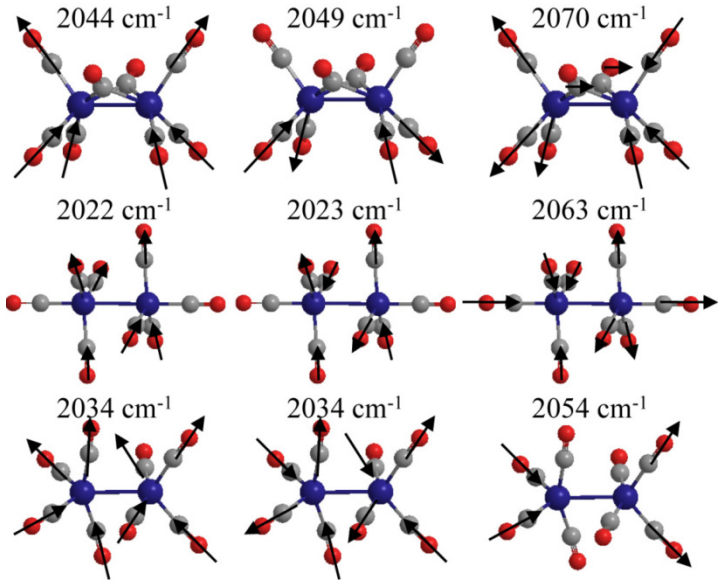

Figure 5.17 The motion of the carbonyl units corresponding to the normal modes are indicated with arrow.

To determine whether the functional and basis set represent the system well; we compared our calculated frequencies and bond lengths to experimentally determined values. For hexane, the calculated vibrational frequencies, weighted by the scaling factor 0.9725, are shown in Table 5.3 along with the experimentally determined frequencies. The calculated vibrational frequencies only differ from the experimental values by ± 5 cm^{-1} at most. The normal modes corresponding to the calculated frequencies are also shown in Fig. 5.17 with the arrows indicating the motion of the carbonyl units. It is important to note that the normal modes in the terminal carbonyl region are not part of the reaction coordinate. The motion along the reaction coordinate is a low frequency motion, and the coupling between the high frequency motions and low frequency motions is small as is indicated by the slow vibrational population relaxation. Comparing the metal-metal bond length of the calculated structure for isomer I (2.55 Å for hexane, decane and cyclohexane) to the experimentally determined bond length (2.53 Å)[68], we see a difference of only 0.02 Å. In comparing the vibrational frequencies and metal-metal bond lengths we find good agreement between the experimental and theoretical results indicating that the basis

Table 5.3 The calculated vibrational frequencies and intensities weighted by the scaling factor 0.9725 along with the experimentally determined vibrational frequencies and intensities are given in parentheses.

	DFT Harmonic Frequencies (cm^{-1})	Experimental Frequencies (cm^{-1})
Isomer I	2044 (2183)	2042 (0.88)
	2049 (1783)	2045 (0.54)
	2070 (2104)	2071 (0.50)
Isomer II	2022 (2538) 2023 (2537)	2023 (0.80)
	2063 (2808)	2068 (0.66)
Isomer III	2034 (2191) 2034 (2193)	2031 (0.39)
	2054 (2297)	2059 (0.14)

set and functional represent the system well.

From the DFT calculated energies of isomers I, II and III we have obtained the activation energy for the forward and reverse reactions, defined in Fig. 5.1, by taking the difference between the energy of the transition state and the ground states. The results follow: E_f(hexane)= 2.35 kcal/mol, E_f(decane)= 2.39 kcal/mol, E_f(cyclohexane)= 2.33 kcal/mol; and E_r(hexane)= 3.06 kcal/mol, E_r(decane)= 3.09 kcal/mol, E_r(cyclohexane)= 3.11 kcal/mol. These values are comparable to the experimental values that we determined in the previous chapter. We also note that for the metal carbonyl system iron pentacarbonyl, previous studies by Cahoon *et. al.* (using similar basis set and functional) have reported reasonable agreement between their DFT computed activation energies and experimental results.[26] Though it should be noted that they did not account for the temperature dependent viscosity in their Arrhenius analysis, suggesting that their experimentally determined barriers are likely too high.

For the linear alkanes, as the solvent is changed from hexane to decane the activation energies only vary by 0.04 kcal/mol confirming that the relative energy of the transition state with respect to the isomers does not greatly change as the solvent is changed. However, if the change in experimental rate constants were due solely to static solvent effects, the change in E_a between hexane and decane would be 0.5 kcal/mol, which is an order of magnitude larger than the calculated difference. Since the difference between E_f and E_r is equivalent to the $\Delta H_{II \rightarrow I}$ we can also compare the DFT results to temperature dependent FT-IR spectra. In the previous chapter, we have determined the experimental value for $\Delta H_{II \rightarrow I}$=-0.49 kcal/mol in hexane, which when compared to the DFT results, $\Delta H_{II \rightarrow I}$=-0.72 kcal/mol, the difference is only 0.23 kcal/mol. For cyclohexane, we have also obtained temperature dependent FTIR spectra of DCO between 5°C and 50°C (Fig. 5.18a). As the temperature increases the peaks corresponding to isomer I decrease while the peaks corresponding to isomer II increase. The temperature dependent equilibrium constants were obtained by fitting

the individual spectra, and from the equilibrium constants a van't Hoff plot was constructed (Fig. 5.18b) and yielded values of $\Delta H°_{II\rightarrow I}$=-1.69 kcal/mol and $\Delta S°_{II\rightarrow I}$=-5.14 cal/(mol·K). Comparing the experimental value $\Delta H_{II\rightarrow I}$=-1.69 kcal/mol (DCO in cyclohexane) to the DFT calculated value of $\Delta H_{II\rightarrow I}$=-0.78 kcal/mol, we see that the experimental value is larger with the difference between the results being 0.91 kcal/mol. Though the experimental and calculated values of $\Delta H_{II\rightarrow I}$ do not agree quantitatively, the DFT calculations produce the trend observed between the linear alkanes and cyclohexane, with the asymmetry of the barrier being more pronounced in cyclohexane. One possible reason for the larger difference between the

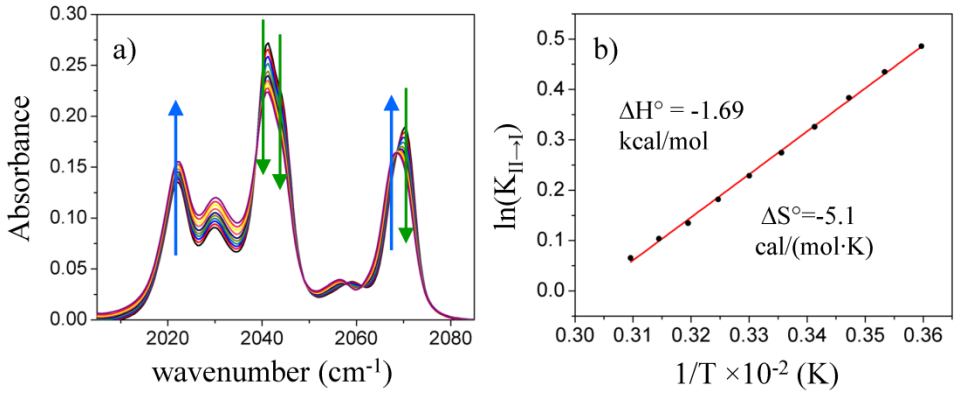

Figure 5.18 (a) Temperature dependent FT-IR spectra of DCO in cyclohexane. The arrows indicate the change in the peaks amplitude as temperature is increased with the green arrows indicating isomer I and the blue arrows indicating isomer II. (b) Van't Hoff plot.

experimental and calculated $\Delta H_{II\rightarrow I}$ in cyclohexane could be attributed to the failure of the PCM to capture the structural components of cyclohexane, which are evident from the more structured RDFs of the different isomers in cyclohexane.

We have also used the DFT calculated structures to obtain the volumes of the isomers and the transition state, the volumes follow: isomer II=180.5 Å^3; isomer I=174.5 Å^3; and the transition state=179.1 Å^3. The change in volume for isomer II to the transition state is ΔV=-1.4 Å^3 and the change in volume for isomer I to the transition state is ΔV=4.6 Å^3. The ΔV between isomer II and the transition state is

negative indicating that the solvent displacement is small for this reaction. For isomer I to the transition state the ΔV is positive and slightly larger indicating that the solvent displacement might be more significant. Since the structure of the isomers are virtually unaffected by the solvent the ΔV is also unaffected. The ΔV is relatively small indicating that the amplitude of the motion is also small compared to the free volumes of the solvents.

5.6 Dynamic Solvent Effect

Combining the results from solvent and temperature dependent linear FT-IR spectra, MD simulations and DFT calculations, there is ample evidence that changing the solvent within the series of linear alkanes does not modulate the potential energy surface. Therefore, for the linear alkanes, the observed change in the rate constants is a purely dynamic solvent effect. In comparing cyclohexane to the series or linear alkanes, we note that there is a static modulation to the potential energy surface. In the next section we will first explore the dynamic solvent effects for the series of linear alkanes. Then, through the use of the FT-IR spectra and DFT calculations, we will demonstrate how to isolate the static and dynamic modulations caused by cyclohexane.

5.6.1 Linear Alkanes

In order to isolate the dynamic effect of the solvent, we remove the static contributions from the barrier crossing process resulting in the reduced rate constant given in Eq. 5.31, where k_{exp} is the experimental rate constant and E_a is the activation energy.

$$k_{\text{red}} = k_{\text{exp}} e^{\frac{E_a}{RT}} \qquad \textbf{Eq. 5.31}$$

To obtain the reduced rate constant the activation energy term must be removed. Though it is common to vary temperature in order to extract activation energies, in changing the temperature, the viscosity is also changed, effectively linking

the static and dynamic aspects of the rate constant. The viscosity's contribution to the perceived barrier can also be on the order of a few kcal/mol, and for reactions taking place on the ps timescale, which also have barriers of only a few kcal/mol, the viscosity's contribution to the barrier could be nontrivial. If the reaction is completely diffusive and the solvent friction is assumed to be proportional to the solvent's viscosity, the temperature dependence of the viscosity can be accounted for by simply subtracting it from the experimentally measured activation energy.[7] In the previous chapter, we measured the E_f=5.4 kcal/mol and E_r =5.8 kcal/mol of DCO in hexane. Over the temperature range probed the activation energy associated with the temperature dependence of the viscosity was estimated to be 1.6 kcal/mol using the hydrodynamic model. Assuming the reaction was in the Smoluchowski limit and that the solvent's friction was proportional to the viscosity we accounted for the contribution of the viscosity and found E_f=3.8 kcal/mol and E_r=4.2 kcal/mol. Though we could approximate the effect of the solvent on the barrier crossing process, we necessarily had to assume a model for the solvent. Complications arise when the barrier crossing process is not in the Smoluchowski limit and/or the friction is not directly proportional to the viscosity, because the assumed model is no longer correct. Since the goal of this chapter is to test the solvent model, assuming a solvent model in order to obtain the activation energy is not valid. To avoid assuming a solvent model, we have chosen to use the activation energy determined from DFT calculations to calculate the reduced rate constant in the linear alkanes.

To gain insight into the microscopic solvent dynamics affecting the barrier crossing process we examine the solvent dependence of k_{red} using two friction models: the hydrodynamic and the Hubbard models[37], given in Eqs. 5.32-5.33.

$$\beta = \frac{4\pi\eta d r^2}{I} \quad \text{hydrodynamic} \qquad \textbf{Eq. 5.32}$$

$$\beta = \frac{6kT}{I_{rxn}} p\tau_{or} \quad \text{Hubbard} \qquad \textbf{Eq. 5.33}$$

In the above equations, η is the macroscopic viscosity of the solvent, d is the diameter of the isomerizing group, r is the radius of gyration, and I is the moment of inertia. For the Hubbard relationship, τ_{or} is the molecular reorientation time of the solute (which was determined from MD simulations according to the procedure described in Section 5.4.3), I_{rxn} is the moment of inertia corresponding to the motion along the reaction coordinate and p is a factor that accounts for the possibility that the isomerization friction is proportional (but not necessarily equal) to the full molecular orientational friction. The p factor is added to account for the fact that not every interaction that leads to molecular reorientation will necessarily coincide with the rotational motion along the reaction coordinate. It is important to note, that in using the Hubbard friction we are assuming that the motion along the reaction coordinate is rotational. For the case of DCO the motion along the reaction coordinate does consist of some small translations; however, the motion is mostly rotational.

The reaction coordinate is not obvious from looking at the structures of isomer I, II and the transition state in Fig. 5.1; however, by observing the motion corresponding to the mode with imaginary frequency, the reaction coordinate

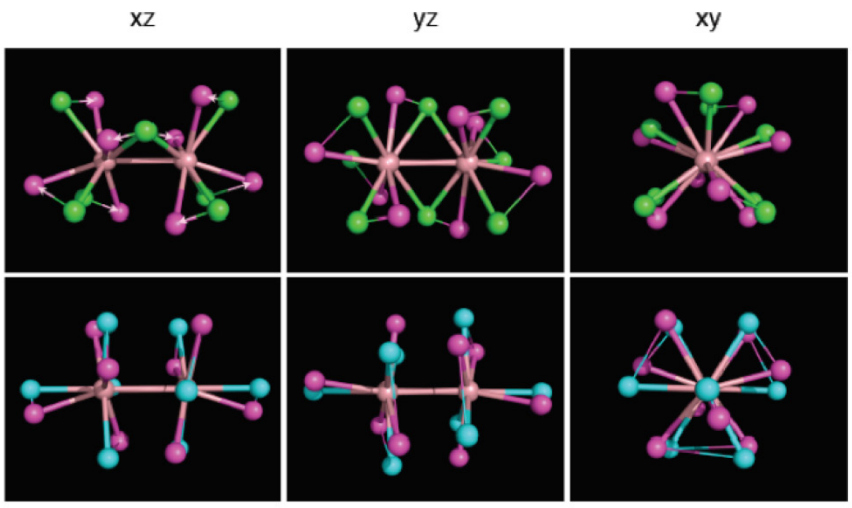

Figure 5.19 (top) The projections of the transition state (pink) and isomer I (green) and (bottom) the projections of the transition state (pink) and isomer II (blue) onto the y-z, x-z, and x-y planes.

becomes more clear and can be thought of as a series of rotations about the x, y and z axis of the molecular frame. Projections of the transition state (pink) along with the structure of the isomer II (blue) and isomer I (green) onto the x-y, y-z, and x-z planes are given in Fig. 19, which suggests the reaction coordinate consists of a series of rotations about the x, y and z axes. The arrows point in the direction of rotation about the axis to obtain the transition state structure. In considering the reaction coordinate to consist of a series of rotations about the x, y and z axes, the moment of inertia for the motion along the reaction coordinate can be written as the following:

$$I_{rxn} = \left(\left(c_x I_x \right)^2 + \left(c_y I_y \right)^2 + \left(c_x I_z \right)^2 \right)^{\frac{1}{2}} \qquad \textbf{Eq. 5.34}$$

where I_x, I_y and I_z, obtained from DFT calculations, are the principle moments of inertia along the x, y and z axes, and c_x^2, c_y^2 and c_z^2 are coefficients that account for an uneven distribution of motion about the x, y and z axes.

In order to determine the coefficients in Eq. 5.34 we use a least squares fitting method to determine the angles of rotations, α, β and γ, about the x, y and z axes that minimize the difference between the transition state's coordinates and the rotated coordinates of the isomer. The rotated coordinates are obtained by using the rotation matrices R_x, R_y, and R_z, Eq. 5.35-5.37.

$$R_x = \begin{pmatrix} 1 & 0 & 0 \\ 0 & \cos(\alpha) & -\sin(\alpha) \\ 0 & \sin(\alpha) & \cos(\alpha) \end{pmatrix} \qquad \textbf{Eq. 5.35}$$

$$R_y = \begin{pmatrix} \cos(\beta) & 0 & \sin(\beta) \\ 0 & 1 & 0 \\ -\sin(\beta) & 0 & \cos(\beta) \end{pmatrix} \qquad \textbf{Eq. 5.36}$$

$$R_z = \begin{pmatrix} \cos(\gamma) & -\sin(\gamma) & 0 \\ \sin(\gamma) & \cos(\gamma) & 0 \\ 0 & 0 & 1 \end{pmatrix} \qquad \textbf{Eq. 5.37}$$

The angles of rotation can be used as a measurement of the amount of movement about a given axis; the larger the angle, the more motion about the specific axis. In order to relate the resulting angles to the coefficients in Eq. 5.34, we represent the angles as components of a normalized vector, θ. The components of θ are the coefficients, c_x, c_y and c_z in Eq. 5.34.

Applying the fitting method to isomer II and the transition state we estimate the moment of inertia along the reaction coordinate to be 6.73×10^{-44} kg·m^2. Since the isomerization motion is symmetric about the Co–Co bond we only consider one half of the molecule. Figure 5.20a shows half the molecule of isomer II and half of the transition state (pink) before applying the fitting procedure. Figure 5.20b plots the rotated coordinates of isomer II, obtained by minimizing the difference between the two structures and the transition sate. Rotations alone cannot map the stable isomer to the transition state because the motion along the reaction coordinate is not strictly rigid. However, since the amount of translation is small, we can assume that most of the rearrangement along the reaction coordinate is due to rotation about the axes. Applying this same procedure to isomer I and the transition state we estimate the

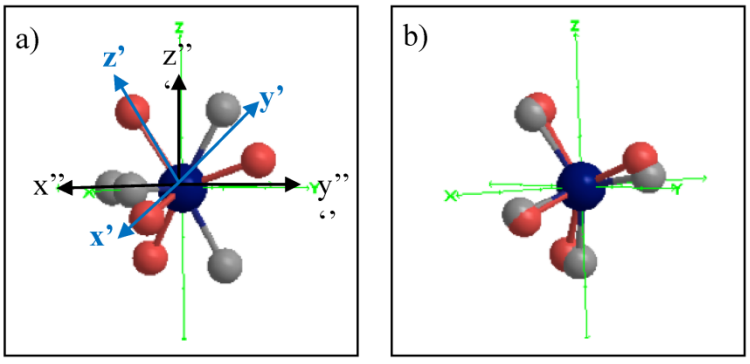

Figure 5.20 (a) The transition state structure (pink) and the structure of isomer II before rotation. (b) The rotated structure of isomer II and the transition state structure (pink).

moment of inertia along the reaction coordinate to be 6.96×10^{-44} kg·m^2.

The hydrodynamic model uses the macroscopic properties of the solvent and the size of the solute as an approximation of the friction. In contrast, the Hubbard

model uses the molecular reorientation time of the solute and the moment of inertia along the reaction coordinate as a measure of the friction, taking into account the microscopic environment sampled by the solute. In using the Hubbard and hydrodynamic frictional models, a Markovian friction is assumed. For low flat barriers, Grote-Hynes theory reduces to Kramers's result (the frequency-dependence of the friction becomes unimportant); however, as the frequency of the barrier becomes larger, when $\omega_b \geq 10^{13}$ s^{-1}, the frequency-dependence of the friction may need to be considered.[35, 36] For DCO, the DFT calculated barrier frequencies are ~7×10^{12} s^{-1} which implies that the friction can be considered to be frequency independent.

It follows from Eq. 5.2 that the reduced rate constant is equivalent to $F(\omega_a/2\pi)$ for a barrier crossing process that behaves according to Kramers theory. In the high friction limit, $F(\omega_a/2\pi)$ is inversely proportional to the friction and reduces to the Smoluchowski result, Eq 5.38, where the variables have been previously defined.

$$k_{red} = \frac{\omega_a \omega_b}{2\pi\beta} \qquad \textbf{Eq. 5.38}$$

To determine whether the barrier crossing process is in the high friction limit, previous studies have fit the reduced rate constants to the following expression and $k_{red}=C\beta^{-\alpha}$,[6, 69, 70] assuming a hydrodynamic friction ($\beta \propto \eta$).

$$k_{red} = c\beta^{-\alpha} \qquad \textbf{Eq. 5.39}$$

By fitting the experimental data to this equation, information on the barrier crossing process is gained from the value of α obtained from fit.[71] A value $\alpha=1$ corresponds to a barrier crossing process that is in the high friction limit (Smoluchowski limit), and as α deviates from 1 the barrier crossing process is described by an intermediate friction.[70] Our data deviate from the Smoluchowski result indicating the barrier crossing process is not in the high friction limit. Fig. 5.21 shows the results of the fits of the $\ln(k_{red})$ versus (a) $\ln(\eta)$, for the hydrodynamic

friction where the literature values of the viscosity were used,[72, 73] and (b) $\ln(\tau_{or})$, for the Hubbard friction along with the resulting α values obtained from the slopes of the fit. The barrier crossing process is not in the high-friction limit, for the

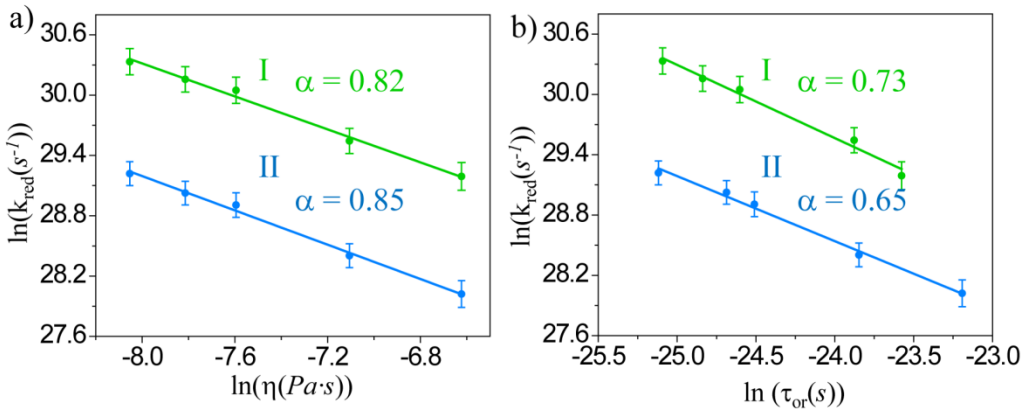

Figure 5.21 Plots of $\ln(k_{red}(s^{-1}))$ versus (a) $\ln(\eta(Pa{\cdot}s))$ and (b) $\ln(\tau_{or}(s))$.

hydrodynamic or Hubbard friction, the barrier crossing process lies within the intermediate friction regime being more like the high-friction limit than TST-like.

Since the Smoluchowski limit does not hold in the present case, we fit our data to the full Kramers expression. Fig. 5.22 shows multivariable fits to the full Kramers expression, $F(\omega_d/2\pi)$, using (a) the hydrodynamic and (b) Hubbard friction models. The extracted basin frequencies (defined in Fig. 5.1) are also given in Fig. 5.22 along

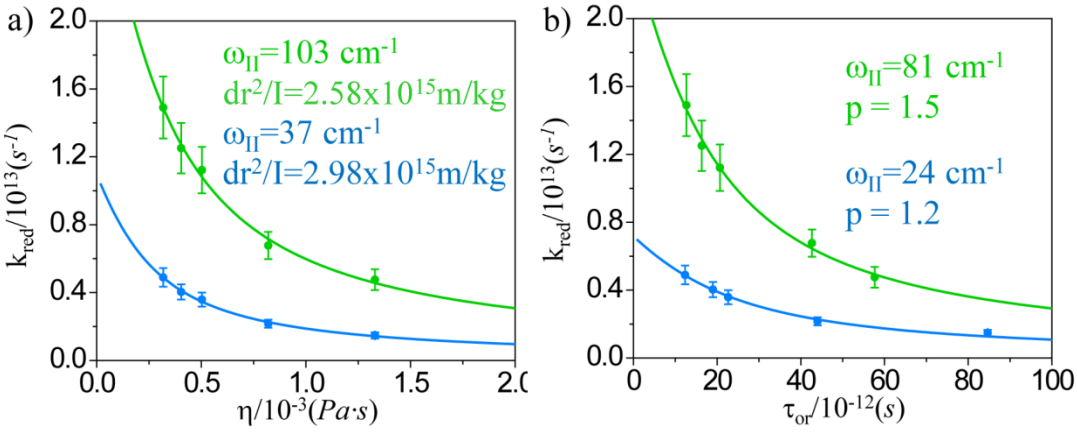

Figure 5.22 Reduced rate constants with the (a) Kramers-hydrodynamic fit and the (b) Kramers-Hubbard fit.

with the other fitted parameters. In both cases, ω_b was fixed with the DFT-computed imaginary frequency of the transition state, 35 cm^{-1}. It is important to note that the imaginary frequency obtained here is slightly less than the imaginary frequency computed in the previous chapter. This is attributed to the fact that a different basis set was used to describe the system in the previous chapter, and in the previous chapter the solvent was not taken into account. For both models we allowed two parameters to vary; the value of dr^2/I and the basin frequency for the hydrodynamic model, and for the Hubbard model the value of p and the basin frequency. Though the Hubbard friction yielded smaller basin frequencies, the two models gave the same trend, indicating a shallower potential well for isomer II than for isomer I. The calculated basin frequencies for isomer II are comparable to the lowest vibrational frequency calculated from DFT results. The calculated basin frequencies of isomer I are slightly higher ~100 cm^{-1} which is still comparable to the DFT calculated low frequency modes. For the hydrodynamic friction, the value of dr^2/I is larger for isomer II than isomer I. The difference in these values is not surprising because the size and shape of the isomers differ, due to the fact that isomer I, having bridging carbonyls, has a smaller metal-metal bond length and isomer II, lacking bridging carbonyls, has a larger metal-metal bond. For the Hubbard friction, the value of p for isomer I is larger than the value of p for isomer II. Again, this is not surprising given the fact that the structure of isomer I and II are very different leading to different moments of inertia along the reaction coordinate due to the fact that the rotational motions along the reaction coordinate are different.

Previous studies have found the Kramers-Hubbard model to produce better fits than the hydrodynamic Kramers model.[19] The success of the Kramers-Hubbard model was apparent in solvents that deviated from the Stokes-Einstein-Debye (SED) relation for orientational relaxation. In the viscosity range probed here, our results indicate that both models yield adequate fits. Orientational diffusion times of DCO in the different solvents computed using MD simulations show a linear dependence on viscosity, which is consistent with the applicability of both friction models (Fig 5.23).

Since the SED equation breaks down with increased solvent size, we expect that with further increased carbon chain length, the isomerization time would also increase. Though we would anticipate agreement with the Hubbard friction, slowing the reaction with higher viscosity will extend the kinetics beyond the vibrational-lifetime-

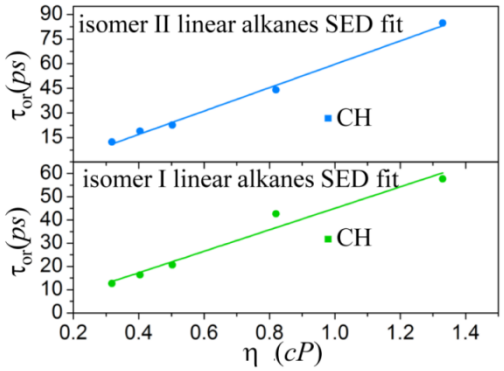

Figure 5.23 Plots of the reorientation time versus viscosity. The linear alkanes are fit to a line, according to the SED equation.

limited window (~50-100 ps) available using 2DIR chemical exchange spectroscopy.

5.6.2 Cyclic Alkane

It could be considered fortuitous—and certainly not general—that the linear alkanes induce no static energetic shifts. In some sense, the motivation to use Kramers theory at all is to retain a simple continuum-like picture of solvation while adapting the parameters to suit the specific solvent system. When the solvent alters the energy landscape, however, verifying Kramers theory is more subtle since the non-dynamical contribution must be removed. In order to compare the dynamic solvent effect of cyclohexane to the linear alkanes, we must first account for the static differences in the potential energy surface.

The parameters related to the potential energy surface in the Kramers model (Eq. 5.2) are the activation energy, E_a, the frequency of the basin, ω_a, and the frequency of the barrier, ω_b. Manipulating Eq. 5.2 by dividing the reduced rate constants by ω_a and incorporating ω_b into the friction yields Eq. 5.40 where B =

β/ω_b which entirely isolates the potential energy surface from the dynamic effects of the solvent.

$$\frac{k_{red}}{\omega_a} = \frac{B}{2}\left(\left[1+\left(\frac{2}{B}\right)^2\right]^{1/2} - 1\right) \qquad \textbf{Eq. 5.40}$$

Fig. 5.24 plots Eq. 5.40 for the linear alkanes with their corresponding fits for the Hubbard friction. The values of ω_a and p used were taken from the Hubbard fits (Fig. 5.22b). As can be seen from Fig. 5.24, removing the static contributions from

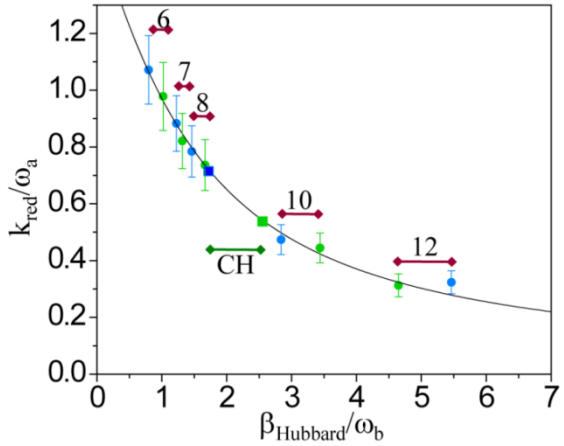

Figure 5.24 Plot of k_{red}/ω_a versus β/ω_b resulting in the isolated solvent dynamics.

the potential energy surface results in reduction of the fits to Kramers model for the two isomers to a single curve, with both the k_{red}/ω_a for isomer I (green circles) and isomer II (blue circles) lying along a single curve. Fig. 5.24 can be thought of as a look-up plot, if the static energetics are known and the solvent friction is known, the decrease in the rate constant due to the solvent impeding the barrier crossing processes can be determined. For the case of cyclohexane, we utilize Fig. 5.24 to isolate the static and dynamic contributions to the rate constant.

For cyclohexane we only consider the Hubbard friction since the molecular reorientation time of DCO in cyclohexane deviates from the SED equation. Fig. 5.23 shows the molecular reorientation of isomer I (green circles) and isomer II (blue circles) in the linear alkanes versus the viscosity along with the linear fit. It is apparent

from Fig 5.23 that the molecular reorientation times of the isomer I (green square) and isomer II (blue square) in cyclohexane deviate from SED behavior.

Unlike the linear alkanes, where the difference in the activation energy corresponds to the experimentally determined enthalpy, the experimentally determined enthalpy difference between the two isomers in cyclohexane is not equivalent to the DFT results. In order to explain the difference between the experimental and calculated results we compare the RDFs of the cyclic and linear alkanes. It is apparent from the RDFs that cyclohexane is more structured than the linear alkanes. One possible reason for the lack of agreement between the DFT calculations and the experimental results could be attributed to the inability of the polarized continuum model to account for the solvent structure of cyclohexane. Since the DFT results do not seem to capture the solute-solvent interactions for cyclohexane, we cannot use the activation energies to obtain the reduced rate constants. However, the molecular reorientation time of isomer I and II should account for the influence of the structured environment of the solvent molecules on the microscopic environment sampled by the solute. Using the reorientational time of isomer I and II in cyclohexane along with the results from the previous section—that the isomerization between isomers II and I in the linear alkanes behaves according to Kramers theory—the static and dynamic contributions to the rate constant can be isolated. Assuming that the inherent properties of cyclohexane do not lead to deviations from Kramers theory, when the static potential is accounted for, the k_{red}/ω_a for cyclohexane should also lie along the fitted curve in Fig. 5.24.

Using the values of p determined from the fit of the linear alkanes and the DFT calculated frequency of the barrier in cyclohexane, 35 cm^{-1}, the values of k_{red}/ω_a for cyclohexane are determined from Fig. 5.24 to be equal to 0.7149 for the forward reaction (blue square Fig. 5.24) and 0.5377 for the reverse reaction (green square Fig. 5.24).

Using a multivariable searching algorithm the following static energetic parameters that result in $k_{f,red}/\omega_{II}$ =0.7149 and $k_{r,red}/\omega_{I}$=0.5377 were obtained: E_f=2.4 kcal/mol ω_{II}=26 cm^{-1}, and E_r=4.1 kcal/mol, ω_{I}=415 cm^{-1}. The searching method required initial guesses for the activation energy, for which we used the DFT results for cyclohexane, and for the basin frequencies we used the linear alkane results as initial guesses. The results form temperature dependent FT-IR spectra were also used in the searching method by constraining the difference between the activation energies to be equivalent to the experimentally determined ΔH.

In this section we have shown that using the well characterized dynamic solvent dependence of the linear alkanes enables the extraction of the static energetics characterizing the potential energy surface corresponding to the isomerization between isomer II and I of DCO in cyclohexane. Using this technique, information on the static potential energy surface can be extracted from a single temperature independent t_2 dependent 2DIR measurement, representing a significant step towards the goal of being able to predict condensed phase reaction rate constants from bulk dynamic properties such as viscosity and from "gas phase" enthalpy barriers. This technique should be applicable when the potential energy surface is not drastically altered by the solvent. For instance, a large increase in the barrier frequency could lead to a friction which may no longer lie within the Markovian regime, and a treatment using Grote-Hynes theory might be more appropriate. For solvents that do not drastically alter the potential energy surface, however, the method described here offers a means of extracting static energetic parameters from a single experimental measurement of the rate constant combined with DFT calculations and molecular dynamics simulations.

5.7 Conclusion

In solution and other dense media transition state theory is not valid since it cannot account for the important solvent dynamics that induce recrossing of the barrier separating reactants and products. Kramers theory does admit solvent

dynamics as frictional drag and random force fluctuations, leading to testable predictions provided one has a means to map bulk solvent properties to the microscopic friction. The test can be made even more stringent with knowledge of the static energetic profile of the stable basins and the transition state. In this chapter we have presented the first direct and systematic time-domain investigation of the effects of dynamic solvent friction on an equilibrium chemical reaction occurring on the ground electronic state. Ultrafast 2DIR chemical exchange spectroscopy has enabled the study of an isomerization reaction under conditions where static energetic changes are negligible. By isolating the dynamic solvent effects we found the rate constant to decrease with increased solvent viscosity according to the Kramers model. Using cyclohexane as an example where the energetics are solvent dependent, we have suggested a method for the separation of static modulations to the potential energy surface from the dynamic effects of the solvent. In the viscosity region studied, we determined that a frequency-independent, memory-less, Markovian friction was sufficient to describe the influence of the solvent on the barrier crossing process, regardless of the choice of the particular friction model. This behavior remains to be verified at higher viscosities, but we predict that the Kramers-Hubbard relation will offer an adequate description of the interactions between the reacting species and the solvent. The validation of Kramers theory in a well characterized reactive system suggests that, much as it has been shown to be the case in the gas phase, quantitative predictions of chemical kinetics in solution are possible.

References:

1. Hanggi, P., P. Talkner, and M. Borkovec, *REACTION-RATE THEORY - 50 YEARS AFTER KRAMERS*. Reviews of Modern Physics, 1990. **62**(2): p. 251-341.

2. Fleming, G.R. and P. Hanggi, *Activated Barrier Crossing: Applications in Physics, Chemistry and Biology*, ed. G.R. Fleming and P. Hanggi. 1993, Singapore: World Scientific Publishing Co. Pte. Ltd.

3. Talkner, P. and P. Hanggi, *New Trends in Kramers' Reaction Rate Theory*. 1995, Netherlands: Kluwer Academic Publishers.

4. Kramers, H.A., *Brownian motion in a field of force and the diffusion model of chemical reactions*. Physica, 1940. **7**: p. 284-304.

5. Rothenberger, G., D.K. Negus, and R.M. Hochstrasser, *Solvent Influence on Photo-Isomerization Dynamics*. Journal of Chemical Physics, 1983. **79**(11): p. 5360-5367.

6. Velsko, S.P., D.H. Waldeck, and G.R. Fleming, *Breakdown of Kramer Theory Description of Photochemical Isomerization and the Possible Involvement of Frequency-Dependent Friction*. Journal of Chemical Physics, 1983. **78**(1): p. 249-258.

7. Brearley, A.M., S.R. Flom, V. Nagarajan, and P.F. Barbara, *Dynamic Solvent Effects on Large-Amplitude Isomerization Rates .2. 2-(2'-Propenyl)Anthracene and (E)-2-(but-2'-En-2'-Yl)Anthracene*. J. Phys. Chem., 1986. **90**(10): p. 2092-2099.

8. Courtney, S.H., S.K. Kim, S. Canonica, and G.R. Fleming, *Rotational Diffusion of Stilbene in Alkane and Alcohol-Solutions*. Journal of the Chemical Society-Faraday Transactions Ii, 1986. **82**: p. 2065-2072.

9. Flom, S.R., V. Nagarajan, and P.F. Barbara, *Dynamic Solvent Effects on Large-Amplitude Isomerization Rates .1. 2-Vinylanthracene*. J. Phys. Chem., 1986. **90**(10): p. 2085-2092.

10. Gegiou, D., K.A. Muszkat, and E. Fischer, *TEMPERATURE DEPENDENCE OF PHOTOISOMERIZATION .6. VISCOSITY EFFECT*. Journal of the American Chemical Society, 1968. **90**(1): p. 12-&.

11. Ansari, A., C.M. Jones, E.R. Henry, J. Hofrichter, and W.A. Eaton, *The Role of Solvent Viscosity in the Dynamics of Protein Conformational-Changes*. Science, 1992. **256**(5065): p. 1796-1798.

12. Ansari, A., C.M. Jones, E.R. Henry, J. Hofrichter, and W.A. Eaton, *Conformational Relaxation and Ligand-Binding in Myoglobin*. Biochemistry, 1994. **33**(17): p. 5128-5145.

13. Frauenfelder, H. and P.G. Wolynes, *RATE THEORIES AND PUZZLES OF HEMEPROTEIN KINETICS*. Science, 1985. **229**(4711): p. 337-345.

14. Venable, R.M. and R.W. Pastor, *FRICTIONAL MODELS FOR STOCHASTIC SIMULATIONS OF PROTEINS*. Biopolymers, 1988. **27**(6): p. 1001-1014.

15. Honeycutt, J.D. and D. Thirumalai, *THE NATURE OF FOLDED STATES OF GLOBULAR-PROTEINS*. Biopolymers, 1992. **32**(6): p. 695-709.

16. Beece, D., L. Eisenstein, H. Frauenfelder, D. Good, M.C. Marden, L. Reinisch, A.H. Reynolds, L.B. Sorensen, and K.T. Yue, *Solvent Viscosity and Protein Dynamics*. Biochemistry, 1980. **19**(23): p. 5147-5157.

17. Kleinert, T., W. Doster, H. Leyser, W. Petry, V. Schwarz, and M. Settles, *Solvent composition and viscosity effects on the kinetics of CO binding to horse myoglobin*. Biochemistry, 1998. **37**(2): p. 717-733.

18. Bolhuis, P.G., C. Dellago, and D. Chandler, *Reaction coordinates of biomolecular isomerization*. Proceedings of the National Academy of Sciences of the United States of America, 2000. **97**(11): p. 5877-5882.

19. Lee, M., A.J. Bain, P.J. McCarthy, C.H. Han, J.N. Haseltine, A.B. Smith, and R.M. Hochstrasser, *Picosecond Photoisomerization and Rotational Reorientation Dynamics in Solution*. Journal of Chemical Physics, 1986. **85**(8): p. 4341-4347.

20. Grote, R.F. and J.T. Hynes, *The Stable States Picture of Chemical-Reactions .2. Rate Constants for Condensed and Gas-Phase Reaction Models*. Journal of Chemical Physics, 1980. **73**(6): p. 2715-2732.

21. Vanderzwan, G. and J.T. Hynes, *Reactive Paths in the Diffusion Limit*. Journal of Chemical Physics, 1982. **77**(3): p. 1295-1301.

22. Pollak, E., *Theory of Activated Rate-Processes - a New Derivation of Kramers Expression*. Journal of Chemical Physics, 1986. **85**(2): p. 865-867.

23. Nitzan, A., *Non-Markovian Theory of Activated Rate-Processes .6. Unimolecular Reactions in Condensed Phases*. Journal of Chemical Physics, 1987. **86**(5): p. 2734-2749.

24. Berne, B.J., M. Borkovec, and J.E. Straub, *Classical and Modern Methods in Reaction-Rate Theory*. J. Phys. Chem., 1988. **92**(13): p. 3711-3725.

25. Woutersen, S., Y. Mu, G. Stock, and P. Hamm, *Hydrogen-bond lifetime measured by time-resolved 2D-IR spectroscopy: N-methylacetamide in methanol.* Chemical Physics, 2001. **266**(2-3): p. 137-147.

26. Cahoon, J., K. Sawyer, J. Schlegel, and C. Harris, *Determining Transition-State Geometries in Liquids using 2D-IR.* Science, 2008. **319**: p. 1820-1823.

27. Fayer, M., *Dynamics of Liquids, Molecules, and Proteins Measured with Ultrafast 2D IR Vibrational Echo Chemical Exchange Spectroscopy.* ANNUAL REVIEW OF PHYSICAL CHEMISTRY, 2009. **60**: p. 21-38.

28. Kim, Y. and R. Hochstrasser, *Applications of 2D IR Spectroscopy to Peptides, Proteins, and Hydrogen-Bond Dynamics.* J. Phys. Chem. B, 2009. **113**(24): p. 8231-8251.

29. Zheng, J.R., K. Kwak, X. Chen, J.B. Asbury, and M.D. Fayer, *Formation and dissociation of intra-intermolecular hydrogen-bonded solute-solvent complexes: Chemical exchange two-dimensional infrared vibrational echo spectroscopy.* Journal of the American Chemical Society, 2006. **128**(9): p. 2977-2987.

30. Zheng, J.R. and M.D. Fayer, *Hydrogen bond lifetimes and energetics for solute/solvent complexes studied with 2D-IR vibrational echo spectroscopy.* Journal of the American Chemical Society, 2007. **129**(14): p. 4328-4335.

31. Campbell, D.M., M. Mackowiak, and J. Jonas, *CYCLOHEXANE REVISITED - HIGH-PRESSURE NUCLEAR-MAGNETIC-RESONANCE ROTATING FRAME RELAXATION STUDY OF THE DYNAMIC SOLVENT EFFECTS ON THE CONFORMATIONAL ISOMERIZATION OF CYCLOHEXANE.* Journal of Chemical Physics, 1992. **96**(4): p. 2717-2723.

32. Macphail, R.A. and R.G. Snyder, *TORSIONAL DAMPING AND SOLVENT FRICTION IN LIQUID N-BUTANE - EXPERIMENTAL ESTIMATES FROM RAMAN-SPECTROSCOPY.* Journal of Chemical Physics, 1989. **91**(7): p. 3895-3902.

33. Hynes, J.T., *CHEMICAL-REACTION DYNAMICS IN SOLUTION.* Annual Review of Physical Chemistry, 1985. **36**: p. 573-597.

34. Waldeck, D.H., *PHOTOISOMERIZATION DYNAMICS OF STILBENES.* Chem. Rev., 1991. **91**(3): p. 415-436.

35. Bagchi, B. and D.W. Oxtoby, *THE EFFECT OF FREQUENCY-DEPENDENT FRICTION ON ISOMERIZATION DYNAMICS IN SOLUTION*. Journal of Chemical Physics, 1983. **78**(5): p. 2735-2741.

36. Murarka, R.K., S. Bhattacharyya, R. Biswas, and B. Bagchi, *Isomerization dynamics in viscous liquids: Microscopic investigation of the coupling and decoupling of the rate to and from solvent viscosity and dependence on the intermolecular potential*. Journal of Chemical Physics, 1999. **110**(15): p. 7365-7375.

37. Hubbard, P.S., *THEORY OF NUCLEAR MAGNETIC RELAXATION BY SPIN-ROTATIONAL INTERACTIONS IN LIQUIDS*. Physical Review, 1963. **131**(3): p. 1155-&.

38. Sweany, R.L. and T.L. Brown, *Infrared spectra of matrix-isolated dicobalt octacarbonyl. Evidence for the third isomer*. Inorg. Chem., 1977. **16**(2): p. 415-421.

39. Aullón, G. and S. Alvarez, *The [M2(CO)8] Complexes of the Cobalt Group*. European Journal of Inorganic Chemistry, 2001. **2001**(12): p. 3031-3038.

40. Tokmakoff, A., B. Sauter, and M.D. Fayer, *TEMPERATURE-DEPENDENT VIBRATIONAL-RELAXATION IN POLYATOMIC LIQUIDS - PICOSECOND INFRARED PUMP-PROBE EXPERIMENTS*. Journal of Chemical Physics, 1994. **100**(12): p. 9035-9043.

41. McQuarrie, D.A., *Statistical Mechanics*. 2000, Sausalito, California: University Science Books.

42. Golonzka, O., M. Khalil, N. Demirdoven, and A. Tokmakoff, *Coupling and orientation between anharmonic vibrations characterized with two-dimensional infrared vibrational echo spectroscopy*. Journal of Chemical Physics, 2001. **115**(23): p. 10814-10828.

43. Khalil, M., N. Demirdoven, and A. Tokmakoff, *Coherent 2D IR spectroscopy: Molecular structure and dynamics in solution*. J. Phys. Chem. A, 2003. **107**(27): p. 5258-5279.

44. Kwak, K., J.R. Zheng, H. Cang, and M.D. Fayer, *Ultrafast two-dimensional infrared vibrational echo chemical exchange experiments and theory*. J. Phys. Chem. B, 2006. **110**(40): p. 19998-20013.

45. Debye, P., ed. *Polar Molecules*. 1945, Dover Publications: New York.

46. Carrington, A. and A.D. McLachlan, *Introduction to Magnetic Resonance* 1967, New York: Harper and Row Publishers.

47. Golonzka, O. and A. Tokmakoff, *Polarization-selective third-order spectroscopy of coupled vibronic states.* Journal of Chemical Physics, 2001. **115**(1): p. 297-309.

48. Zhuang, W., D. Abramavicius, T. Hayashi, and S. Mukamel, *Simulation protocols for coherent femtosecond vibrational spectra of peptides.* J. Phys. Chem. B, 2006. **110**(7): p. 3362-3374.

49. Baiz, C.R., R. McCanne, M.J. Nee, and K.J. Kubarych, *Orientational Dynamics of Transient Molecules Measured by Nonequilibrium Two-Dimensional Infrared Spectroscopy.* Journal of Physical Chemistry A, 2009. **113**(31): p. 8907-8916.

50. Gordon, R.G., *Molecular Collisions and Depolarization of Fluorescence in Gases.* Journal of Chemical Physics, 1966. **45**(5): p. 1643-&.

51. Hess, B., C. Kutzner, D. van der Spoel, and E. Lindahl, *GROMACS 4: Algorithms for highly efficient, load-balanced, and scalable molecular simulation.* Journal of Chemical Theory and Computation, 2008. **4**(3): p. 435-447.

52. Berendsen, H.J.C., J.P.M. Postma, W.F. Vangunsteren, A. Dinola, and J.R. Haak, *Molecular-Dynamics with Coupling to an External Bath.* Journal of Chemical Physics, 1984. **81**(8): p. 3684-3690.

53. Essmann, U., L. Perera, M.L. Berkowitz, T. Darden, H. Lee, and L.G. Pedersen, *A Smooth Particle Mesh Ewald Method.* Journal of Chemical Physics, 1995. **103**(19): p. 8577-8593.

54. Darden, T., D. York, and L. Pedersen, *Particle Mesh Ewald - an N.Log(N) Method for Ewald Sums in Large Systems.* Journal of Chemical Physics, 1993. **98**(12): p. 10089-10092.

55. Chirlian, L.E. and M.M. Francl, *Atomic Charges Derived from Electrostatic Potentials - a Detailed Study.* Journal of Computational Chemistry, 1987. **8**(6): p. 894-905.

56. Wang, J.M., R.M. Wolf, J.W. Caldwell, P.A. Kollman, and D.A. Case, *Development and testing of a general amber force field.* Journal of Computational Chemistry, 2004. **25**(9): p. 1157-1174.

57. Wang, J.M., W. Wang, P.A. Kollman, and D.A. Case, *Automatic atom type and bond type perception in molecular mechanical calculations*. Journal of Molecular Graphics & Modelling, 2006. **25**(2): p. 247-260.

58. Singh, U.C. and P.A. Kollman, *An Approach to Computing Electrostatic Charges for Molecules*. Journal of Computational Chemistry, 1984. **5**(2): p. 129-145.

59. Besler, B.H., K.M. Merz, and P.A. Kollman, *Atomic Charges Derived from Semiempirical Methods*. Journal of Computational Chemistry, 1990. **11**(4): p. 431-439.

60. Chandler, D., *Introduction to Modern Statistical Mechanics*. 1987, New York: Oxford University Press.

61. Frisch, M.J., G.W. Trucks, H.B. Schlegel, G.E. Scuseria, M.A. Robb, J.R. Cheeseman, J. Montgomery, J. A., T. Vreven, K.N. Kudin, J.C. Burant, J.M. Millam, S.S. Iyengar, J. Tomasi, V. Barone, B. Mennucci, M. Cossi, G. Scalmani, N. Rega, G.A. Petersson, H. Nakatsuji, M. Hada, M. Ehara, K. Toyota, R. Fukuda, J. Hasegawa, M. Ishida, T. Nakajima, Y. Honda, O. Kitao, H. Nakai, M. Klene, X. Li, J.E. Knox, H.P. Hratchian, J.B. Cross, V. Bakken, C. Adamo, J. Jaramillo, R. Gomperts, R.E. Stratmann, O. Yazyev, A.J. Austin, R. Cammi, C. Pomelli, J.W. Ochterski, P.Y. Ayala, K. Morokuma, G.A. Voth, P. Salvador, J.J. Dannenberg, V.G. Zakrzewski, S. Dapprich, A.D. Daniels, M.C. Strain, O. Farkas, D.K. Malick, A.D. Rabuck, K. Raghavachari, J.B. Foresman, J.V. Ortiz, Q. Cui, A.G. Baboul, S. Clifford, J. Cioslowski, B.B. Stefanov, G. Liu, A. Liashenko, P. Piskorz, I. Komaromi, R.L. Martin, D.J. Fox, T. Keith, M.A. Al-Laham, C.Y. Peng, A. Nanayakkara, M. Challacombe, P.M.W. Gill, B. Johnson, W. Chen, M.W. Wong, C. Gonzalez, and J.A. Pople, *Gaussian 03*. 2004, Gaussian, Inc: Wallingford CT.

62. Kenny, J.P., R.B. King, and H.F. Schaefer, *Cobalt−Cobalt Multiple Bonds in Homoleptic Carbonyls? Co2(CO)x (x = 7−8) Structures, Energetics, and Vibrational Spectra*. Inorg. Chem., 2001. **40**(5): p. 900-911.

63. Cances, E., B. Mennucci, and J. Tomasi, *A new integral equation formalism for the polarizable continuum model: Theoretical background and applications to isotropic and anisotropic dielectrics*. Journal of Chemical Physics, 1997. **107**(8): p. 3032-3041.

64. Mennucci, B. and J. Tomasi, *Continuum solvation models: A new approach to the problem of solute's charge distribution and cavity boundaries*. Journal of Chemical Physics, 1997. **106**(12): p. 5151-5158.

65. Cossi, M., V. Barone, B. Mennucci, and J. Tomasi, *Ab initio study of ionic solutions by a polarizable continuum dielectric model.* Chemical Physics Letters, 1998. **286**(3-4): p. 253-260.

66. Peng, C.Y. and H.B. Schlegel, *Combining Synchronous Transit and Quasi-Newton Methods to Find Transition-States.* Israel Journal of Chemistry, 1993. **33**(4): p. 449-454.

67. Peng, C.Y., P.Y. Ayala, H.B. Schlegel, and M.J. Frisch, *Using redundant internal coordinates to optimize equilibrium geometries and transition states.* Journal of Computational Chemistry, 1996. **17**(1): p. 49-56.

68. Leung, P.C. and P. Coppens, *Experimental charge density study of dicobalt octacarbonyl and comparison with theory.* Acta Cryst., 1983. **1983**(B39): p. 535-542.

69. Velsko, S.P. and G.R. Fleming, *PHOTOCHEMICAL ISOMERIZATION IN SOLUTION - PHOTOPHYSICS OF DIPHENYL BUTADIENE.* Journal of Chemical Physics, 1982. **76**(7): p. 3553-3562.

70. Keery, K.M. and G.R. Fleming, *INFLUENCE OF SOLVENT ON PHOTOCHEMICAL ISOMERIZATION - PHOTOPHYSICS OF DIPHENYL BUTADIENE IN POLAR-SOLVENTS.* Chemical Physics Letters, 1982. **93**(4): p. 322-326.

71. Fleming, G.R., S.H. Courtney, and M.W. Balk, *Activated Barrier Crossing - Comparison of Experiment and Theory.* Journal of Statistical Physics, 1986. **42**(1-2): p. 83-104.

72. Nayak, J.N., M.I. Aralaguppi, and T.M. Aminabhavi, *Density, viscosity, refractive index, and speed of sound for the binary mixtures of ethyl chloroacetate with n-alkanes (C-6 to C-12) at (298.15, 303.15, and 308.15) K.* Journal of Chemical and Engineering Data, 2001. **46**(4): p. 891-896.

73. Silva, A.A., R.A. Reis, and M.L.L. Paredes, *Density and Viscosity of Decalin, Cyclohexane, and Toluene Binary Mixtures at (283.15, 293.15, 303.15, 313.15, and 323.15) K.* Journal of Chemical and Engineering Data, 2009. **54**(7): p. 2067-2072.

Chapter 6

Intramolecular Vibrational Energy Redistribution: A Study of $[CpFe(CO)_2]_2$ and $[CpRu(CO)_2]_2$

The work presented in this chapter has been submitted for publication.

Jessica M. Anna, John T. King and Kevin J. Kubarych, "*Multiple Structures and Dynamics of $[CpRu(CO)_2]_2$ and $[CpFe(CO)_2]_2$ in Solution Revealed with Two-Dimensional Infrared Spectroscopy*," [submitted to Inorganic Chemistry].

6.1 Overview: Chapter 6

In this chapter 2DIR spectroscopy is applied to both cyclopentadienyliron dicarbonyl, $Cp_2Fe_2(CO)_4$, and its ruthenium analog, $Cp_2Ru_2(CO)_4$, in order to observe energy transfer in the different systems and to assign the transition frequencies of the individual isomers. For both metal complexes, the previous assignment of the linear IR spectra is confirmed, and the assignment is further refined by determining the transition frequencies associated with different isomeric forms of a given metal complex. Density functional theory (DFT) calculations were performed to obtain the relative energies of the different isomers of $Cp_2Fe_2(CO)_4$ and $Cp_2Ru_2(CO)_4$ along with the structures and energies of the transition states connecting the stable isomers. Combining the DFT and experimental results, a detailed understanding of the differences between the two metal complexes is obtained. Monitoring the waiting

time dependent amplitude of the crosspeaks in the 2DIR spectrum, provides a direct probe of the energy transfer dynamics between different vibrational modes. Treating the energy transfer as an equilibrium process enables the extraction of both the uphill and downhill energy transfer rate constants, and the rate constants for the two metal complexes are compared.

6.2 $[CpFe(CO)_2]_2$ and $[CpRu(CO)_2]_2$: Multiple Structures and Dynamics

Binulcear $Cp_2Fe_2(CO)_4$, and the ruthenium analog, $Cp_2Ru_2(CO)_4$, have been studied for over 50 years.[1] One motivation for ongoing investigations of these complexes arises from the dynamical and structural complexity of fluxional interconversion between multiple isomeric forms. Earlier IR[2-7], x-ray crystallography[8-12], and NMR[7, 13] studies identified and characterized these different isomeric forms, finding that $Cp_2Fe_2(CO)_4$ exists mainly as two isomers in equilibrium at room temperature (Fig. 6.1 top) while $Cp_2Ru_2(CO)_4$ exists as four isomers (Fig. 6.1 bottom).[5-7, 13] More recently $Cp_2Fe_2(CO)_4$ and $Cp_2Ru_2(CO)_4$ have been studied because of the rich photochemistry that accompanies the presence of multiple isomers in equilibrium.[14]

Since $Cp_2Fe_2(CO)_4$ was first isolated by Piper and Wilkinson in 1955[15], the assignment of the linear IR spectrum has been debated. From the first crystal structure of $Cp_2Fe_2(CO)_4$ it was determined that it exists in the *trans*-B form (Fig. 6.1).[8] However, the peaks in the solution phase linear IR spectrum could not be explained by the *trans*-B isomer alone, indicating that the solvent environment significantly perturbs the structure.[2] In order to explain the linear IR spectrum several temperature and solvent dependent studies were conducted. From these studies, it was first suggested that the spectrum of $Cp_2Fe_2(CO)_4$ could be attributed to one isomeric form, a distorted *trans*-B isomer.[3] This assignment was soon challenged, and the peaks in the IR spectrum were attributed to a *cis*-B form and to a minute amount of a non-bridging form.[4] This same study also considered the IR spectrum of

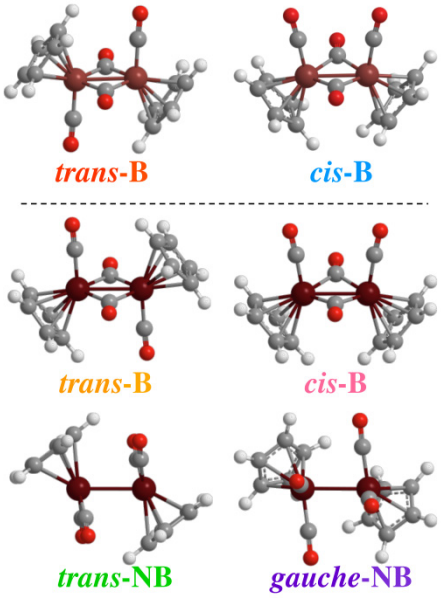

Figure 6.1 Equilibrium structures for both $Cp_2Fe_2(CO)_4$ (top) and $Cp_2Ru_2(CO)_4$ (bottom).

$Cp_2Ru_2(CO)_4$ assigning the peaks to two isomeric forms: a *cis*-B and a *cis*-NB form or another NB rotamer.[4] This assignment was also challenged, from solvent dependent IR spectra it was concluded that there are three isomeric forms contributing to the spectrum of $Cp_2Fe_2(CO)_4$, a *trans*-B, *cis*-B and a negligible amount of a non-bridging form and for the $Cp_2Ru_2(CO)_4$ complex there are four isomeric forms contributing to the spectrum: a *trans*-B, *trans*-NB, *cis*-B, and a *cis*-NB.[5, 6] From NMR and IR studies it was determined that what was thought to be the *cis*-NB isomer of $Cp_2Ru_2(CO)_4$ was actually the *gauche*-NB form.[7]

Seventeen years after the first linear IR spectrum was reported for the iron complex, the equilibrium compositions of both the iron and ruthenium complexes were determined. This required several temperature and solvent dependent studies and though these studies assigned the peaks in the linear spectrum to have different contributions from different isomeric forms, the exact transition frequency and corresponding amplitudes of the overlapping peaks could not be determined. In this chapter, we demonstrate the ability of 2DIR spectroscopy to aide in the assignment of the linear IR spectra. From temperature independent spectra in a single solvent,

not only can we determine the composition of the peaks in the linear spectrum, but we can also determine the transition frequencies and amplitudes of the individual peaks.

In addition to resolving the individual transition frequencies, we also explore the energy transfer dynamics between the different modes of the different isomeric forms. We observe intramolecular vibrational energy redistribution (IVR) between different modes of the *cis*-B isomer of $Cp_2Fe_2(CO)_4$ and the *gauche*-NB isomer of $Cp_2Ru_2(CO)_4$. We find that the rate of intramolecular energy transfer (IVR) varies between the two species, and that the difference in the rate maps to the difference in energy between the two states exchanging vibrational excitation.

Though we see evidence of energy transfer between different modes of the same isomer, we do not see evidence of chemical exchange. Previous NMR studies were able to observe chemical exchange between the different isomers of these complexes.[7, 13] The pathway by which chemical exchange takes place was proposed by Bullit, Cotton, and Marks in 1972 where interconversion between the bridging forms occurs through non-bridging intermediates for both $Cp_2Fe_2(CO)_4$ and $Cp_2Ru_2(CO)_4$.[7] An activation energy of 16.7 kcal/mol for the *trans*-B-to-*cis*-B interconversion for $Cp_2Fe_2(CO)_4$ was also obtained. For the ruthenium complex, an activation energy was not obtained because it did not reach the slow exchange limit over the temperature range probed; however, it was suggested that the activation energy was less than 8 kcal/mol. Bridging terminal carbonyl exchange was also observed for $Cp_2Fe_2(CO)_4$ and $Cp_2Ru_2(CO)_4$ by Gasnow and Vernon.[13] From NMR studies they found the activation energies ranged from 6.5 to 11.1 kcal/mol for the bridging terminal carbonyl exchange for both $Cp_2Fe_2(CO)_4$ and $Cp_2Ru_2(CO)_4$. They also obtained an activation energy of 6.5 kcal/mol for *trans*-NB-to-*gauche*-NB interconversion for $Cp_2Fe_2(CO)_4$; however they did not observe rotation about the metal-metal bond for the $Cp_2Ru_2(CO)_4$ complex due to the faster timescale of the interconversion compared to $Cp_2Fe_2(CO)_4$. 2DIR spectroscopy probes processes that occur on the picosecond timescale; therefore, the fast interconversion between the non-bridging

isomers of $Cp_2Ru_2(CO)_4$ should be observed with 2DIR spectroscopy. However, in this study we do not see evidence of chemical exchange between these two species.

6.3 Linear FTIR Spectroscopy

The linear FT-IR spectrum of $Cp_2Fe_2(CO)_4$ in the terminal carbonyl stretching region is shown in Fig. 6.2a. Previous studies[5] have assigned peak 1 at 1961 cm^{-1}, to the *trans*-B isomer with a small contribution from the *cis*-B isomer. Peak 2, at 2006 cm^{-1}, was assigned to the *cis*-B isomer. It has also been suggested that there is a small

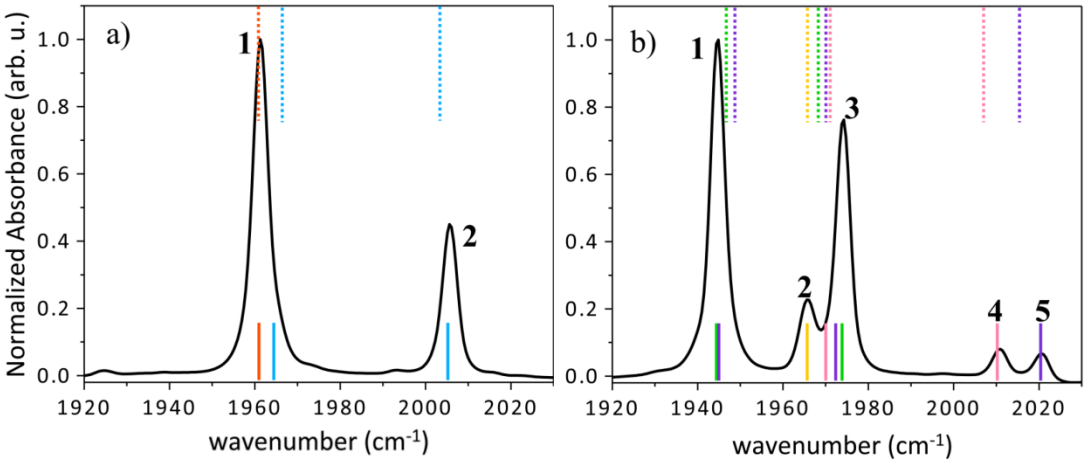

Figure 6.2 Linear FTIR spectra of $Cp_2Fe_2(CO)_4$ (a) and $Cp_2Ru_2(CO)_4$ (b) in *n*-hexane. Scaled DFT calculated frequencies are indicated with dashed lines and 2DIR experimentally determined frequencies are indicated with solid lines.

contribution, a negligible amount, of the *trans*-NB form present. The presence of the *trans*-NB form leads to absorptive features in the linear IR spectrum at 1938 cm^{-1}, 1973 cm^{-1} and 2015 cm^{-1}.[16, 17] We do not see absorptive features at these frequencies in our linear FT-IR spectrum indicating that the non-bridging form is not significantly populated at room temperature in *n*-hexane.

The linear FTIR spectrum of $Cp_2Ru_2(CO)_4$ in the terminal carbonyl stretching region is shown in Fig. 6.2b. Previous studies[6, 7] have assigned peak 1 at 1945 cm^{-1} to the *trans*-NB and *gauche*-NB isomers. Peak 2 at 1965 cm^{-1} was assigned to the *trans*-B. Three components were assigned to peak 3 at 1974 cm^{-1}; the *trans*-NB, *gauche*-NB, and

cis-B isomers. Peak 4 at 2011 cm^{-1} was assigned the *cis*-B isomer and peak 5 at 2021 cm^{-1} was assigned to the *gauche*-NB form.

6.4 Structure and Energetics

In this section we discuss the characterization of the multiple isomeric forms for the iron and ruthenium complex using 2DIR spectroscopy along with DFT calculations. We first discuss the 2DIR spectra and DFT calculations performed on both the metal complexes in general, and then we discuss the spectra and calculations for each metal complex separately in detail.

6.4.1 2DIR spectroscopy

In previous chapters we have extracted rate constants associated with dynamic processes from absolute-value rephasing 2DIR spectra. In the previous studies we chose to use the rephasing spectra in order to separate exchange and inherent crosspeak contributions by locking onto the coherent oscillations that only arise from inherent crosspeaks. In this chapter we choose to use the absolute-value nonrephasing spectra to obtain dynamic information on the iron and ruthenium complex. In the nonrephasing spectra the inherent crosspeaks do not oscillate as function of t_2. Since we are extracting the rate constants associated with IVR from the inherent crosspeaks we use the nonrephasing spectra to avoid increasing the number of fitting parameters that would be required to fit the oscillations. It is also important to note, that we do not observe exchange in these complexes, so we do not need to isolate exchange and inherent crosspeak contributions.

6.4.2 Density Functional Theory Calculations

Previous studies have suggested the pathway for isomerization from *trans*-B to *cis*-B proceeds through non-bridging intermediates, *trans*-NB and *gauche*-NB.[7] DFT calculations were performed on these isomers for both $Cp_2Fe_2(CO)_4$ and $Cp_2Ru_2(CO)_4$ and the transition states connecting the stable states specified by the suggested pathway.

Table 6.1 The 2DIR experimentally determined frequencies and DFT calculated frequencies for both $Cp_2Fe_2(CO)_4$ and $Cp_2Ru_2(CO)_4$ are tabulated

	Exp. Frequencies (cm-1)	DFT Frequencies (cm-1)
$Cp_2Fe_2(CO)_4$		
trans-B	1962	1962
cis-B	1965	1967
	2006	2003
$Cp_2Ru_2(CO)_4$		
trans-B	1966	1966
cis-B	1970	1971
	2011	2008
gauche-NB	1943	1949
	1972	1970
	2021	2015
trans-NB	1943	1946
	1974	1969

The DFT calculations were performed on both $Cp_2Fe_2(CO)_4$ and $Cp_2Ru_2(CO)_4$ using Gaussian03.[18] All the calculations were performed using the B3LYP functional. For $Cp_2Fe_2(CO)_4$ we used the following basis sets, which were taken from previous computational studies on $Cp_2Fe_2(CO)_4$ performed by Schaefer *et. al.*.[19] For carbon, oxygen, and hydrogen we used the double-ζ plus polarization (DZP) basis sets. For the iron atoms we used the 14s11p6d/10s8p3d basis which was also used by Schaefer *et. al.*.[19] For $Cp_2Ru_2(CO)_4$ we again used the DZP basis sets for the carbon, oxygen and hydrogen atoms. For the ruthenium atoms we used the LANL2DZ pseudopotential. We chose to use the pseudopotential for the ruthenium atoms based on previous calculations by Schaefer *et. al.* which compared triruthenium dodecacarbonyl to triiron dodecacarbonyl, where the same basis sets used for

$Cp_2Fe_2(CO)_4$ were also used for triiron dodecacarbonyl.[20, 21] The transition states connecting the different isomers were determined using the synchronous transit-guided quasi Newton methods.[22, 23] For each transition state a single imaginary frequency was obtained and the transition states were confirmed by observing that the single imaginary frequency connected the two corresponding stable isomers.

Frequency calculations were also performed. Table 6.1 displays the experimentally determined frequencies with the corresponding DFT calculated frequencies scaled by 0.9636 for $Cp_2Fe_2(CO)_4$ and 0.9651 for $Cp_2Ru_2(CO)_4$. The theoretically determined frequencies only differ from the experimentally determined frequencies by 6 cm^{-1}. The scaled DFT calculated frequencies are also shown as dashed lines in Fig. 6.2.

6.4.3 $[CpFe(CO)_2]_2$: 2DIR Spectroscopy and DFT Calculations

The absolute value of the 2DIR nonrephasing spectra of $Cp_2Fe_2(CO)_4$ in hexane at t_2=200 fs and t_2=10 ps are shown in Fig. 6.3. The peaks lying along the diagonal, peaks 1 and 2, correspond to the two peaks in the linear FT-IR spectrum (Fig. 6.2). Peaks 1' and 2', which are shifted to slightly lower frequencies along ω_{detect}, are due to excited state absorptions and are red-shifted due to the vibrational anharmonicity. Peaks 3 and 4 are present at t_2=200 fs and as t_2 increases we see the appearance of peaks 4' and 5.

The 2DIR spectra of $Cp_2Fe_2(CO)_4$ (Fig. 6.3) confirm the assignment of the linear IR spectra. Crosspeaks 4 and 5 are inherent crosspeaks, arising because there are two transitions from the *cis*-B isomer lying within the ~200-cm^{-1} bandwidth of the incoming 100-fs pulses. Peak 4 arises because during t_1, a coherence exists between the ground state and the first excited state of the lower frequency *cis*-B mode, followed by a ground state population during t_2, and ultimately a coherence exists during t_3 between the ground and first excited state of the higher frequency *cis*-B mode. This final coherence radiates the signal and is detected.

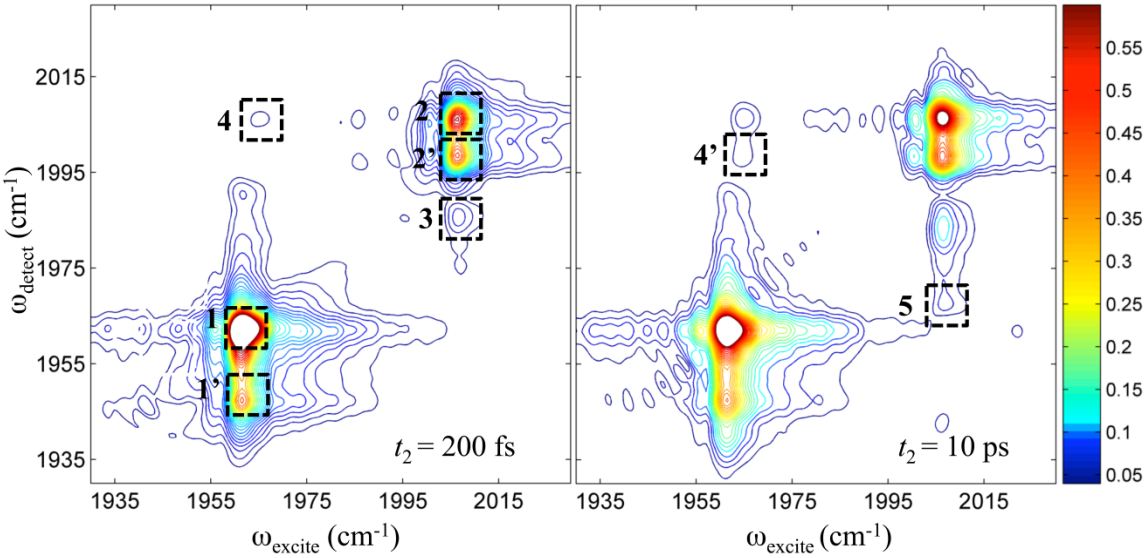

Figure 6.3 Absolute-value non-rephasing spectra of $Cp_2Fe_2(CO)_4$ in *n*-hexane at t_2=200 fs and t_2=10 ps. The spectra are normalized to the maximum peak at the given t_2 value.

We can obtain the transition frequency of the lower frequency mode of the *cis*-B isomer from the corresponding crosspeak (crosspeak 4). The transition frequency of the lower frequency mode of the *cis*-B isomer was found to be 1965 cm^{-1}. The transition frequencies determined from the 2DIR spectra are indicated in Fig. 6.2 as solid lines and given in Table 1. We also determined the transition frequencies between the first and second excited state manifolds from peaks 1', 2', 4' and 3. Peaks 1' and 2' are due to excited state absorptions. The difference between the shifted peaks and the corresponding diagonal peaks is a measure of the anharmonicity. Peak 1' is shifted by 15 cm^{-1} along ω_{detect} compared to peak 1 and peak 2' is shifted by 8 cm^{-1} with respect to peak 2. Peak 3 is due to a transition from the first excited state manifold of the *cis*-B isomer to the corresponding combination band. Peak 4', which has the same ω_3 frequency as peak 2', arises because intramolecular vibrational energy transfer has occurred between the two modes of the *cis*-B isomer; population has been transferred from the lower frequency mode to the higher frequency mode during t_2. In the next section we discuss the rate of IVR between the two modes of the *cis*-B isomer.

Along with the transition frequencies we can also determine the relative magnitude of the transition dipole moments of the two modes of the *cis*-B isomer. In nonrephasing spectra, for a molecular system having two transitions, B and B', where the transition dipole moments, μ, are 90° with respect to one another and neglecting dynamics that may occur during t_1 and t_3, the amplitude of the diagonal peak B' is proportional to the transition dipole moments as described by Eq. 6.1 at t_2=0.[24]

$$S_{B'}(t_2 = 0) \propto \frac{1}{15}\left|\mu_{0B'}\right|^2\left[6\left|\mu_{0B'}\right|^2 + \left|\mu_{0B}\right|^2\right] \qquad \textbf{Eq. 6.1}$$

In nonrephasing spectra, given the same conditions stated for the diagonal peak, the amplitude of the inherent crosspeaks is proportional to the magnitude of the square of the transition dipole moments of the corresponding diagonal peaks (Eq. 6.2).[24]

$$S_{BB'}(t_2 = 0) \propto \frac{1}{15}\left|\mu_{0B'}\right|^2\left|\mu_{0B}\right|^2 \qquad \textbf{Eq. 6.2}$$

From these two expressions, it can be determined that the amplitude of the crosspeak will always be less than the amplitude of the weakest diagonal peak. For the case where one of the diagonal peaks is very weak, the initial amplitude of the crosspeak may not be distinguishable from the noise. However, as t_2 increases the crosspeaks may grow in with respect to the diagonal peaks due to IVR. This could result in what seems like the appearance of a crosspeak at later t_2 times, but is actually attributable to an inherent crosspeak that becomes more pronounced compared to the corresponding diagonal peaks due to IVR. If the amplitude of a diagonal peak is small, the amplitude of the corresponding crosspeak will also be small, but it may nevertheless be "amplified" relative to the FT-IR spectrum if the other diagonal peak is strong enough.

From DFT calculation we determined that the angle between the two *cis*-B transition dipole moments is 87. Since the measured angle only d iffers from 90° by 3°, we can approximate the magnitude of the transition dipole moments from the amplitudes of crosspeak 4 and diagonal peak 2 at t_2=0 ps using Eq. 6.1 and Eq. 6.2.

We determined, for the lower frequency mode, the magnitude of the transition dipole moment to be 0.74 and for the higher frequency mode the magnitude to be 1.10. Since the amplitude of the diagonal peak is related to the transition dipole moment by Eq. 6.1, the relative amplitude of the diagonal peaks can be determined. For the higher frequency mode the amplitude is 0.63 and the amplitude of the lower frequency peak is 0.16. This indicates that the contribution of the *cis*-B isomer to peak 1 is small and that peak 1 is mostly attributed to the *trans*-B isomer.

The results of the DFT calculations (Fig. 6.4) support our experimental results. The *trans*-B and *cis*-B isomers lie lowest in energy with the two non-bridging isomers

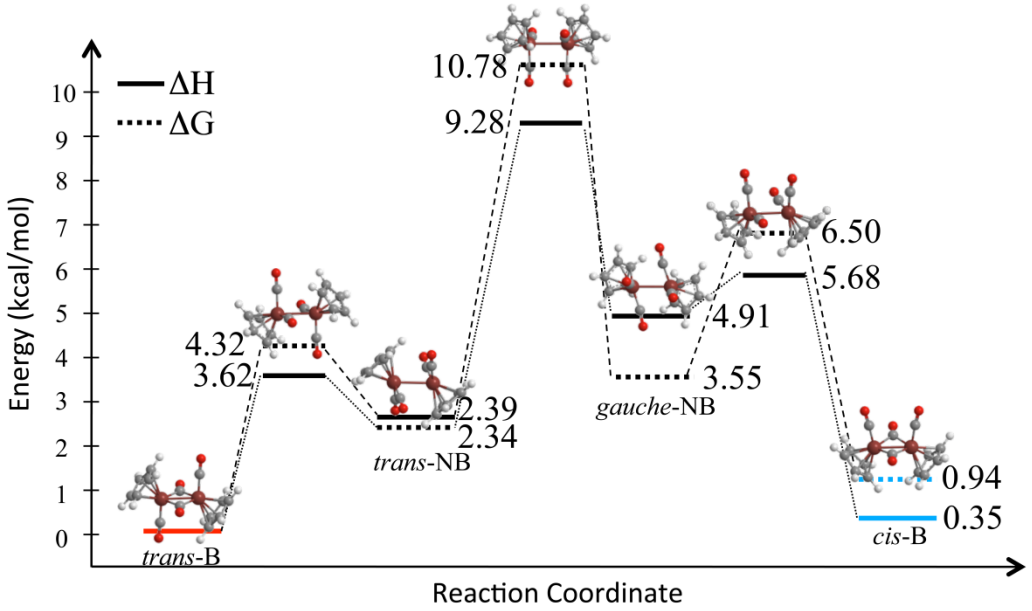

Figure 6.4 DFT calculated ground state energies of $Cp_2Fe_2(CO)_4$ along with the corresponding transition states. The calculated ΔG (dashed lines) and ΔH (solid lines) are indicated.

lying higher in energy. The *trans*-NB isomer lies ΔG=2.34 kcal/mol higher than the *trans*-B isomer. This is consistent with previous computational studies performed on the *trans*-B, *trans*-NB, and *cis*-B isomers.[19] This ΔG value is equivalent to an equilibrium constant of 0.02, indicating that the relative populations of the non-bridging isomers are negligible compared to the bridging isomers, and explains why we do not see any signature from the *trans*-NB isomer in our spectra. Previous studies did see evidence of the *trans*-NB isomer, but indicated that the amount present was

negligibly small (<0.1%) which is also consistent with our DFT calculations. The equilibrium constant for the *gauche*-NB isomer is 0.002 leading to an even smaller population, and is consistent with its absence in IR studies.

We have also calculated the activation energy associated with interconversion between the different stable isomers. For *trans*-B-to-*trans*-NB E_a=3.62 kcal/mol and for the *cis*-B-to-*gauche*-NB E_a=5.33 kcal/mol. Previous NMR studies have observed bridging terminal carbonyl exchange with a *trans*-B-to-*trans*-NB activation energy of E_a=6.5 kcal/mol.[13] The study also observed exchange between the two non-bridging forms, with an activation energy of 6.2 kcal/mol for *trans*-NB-to-*gauche*-NB.[13] This is comparable to the DFT calculations which predict an activation energy of 6.89 kcal/mol. Previous NMR studies have also observed the chemical exchange between the two bridging forms and have determined the activation energy to be 16.7 kcal/mol.[7] From our DFT calculations, the activation energy for the *trans*-B-to-*cis*-B isomer is 11.28 kcal/mol, and for the reverse reaction *trans*-B-to-*cis*-B is 11.75 kcal/mol. We offer two possible reasons for the disagreement between the experimental and calculated activation energies. One reason for disagreement could be due to the fact that the DFT calculations were performed in vacuum and do not take into account the influence of the solvent molecules. Another reason for the discrepancies could be due to the fact that the dynamic and static solvent effects were not taken into account in either of the previous NMR studies. One of the most common ways of experimentally determining the activation energy is to measure the rate constant as a function of temperature. However, in the condensed phase, varying the temperature also leads to changes in the viscosity of the solvent effectively linking the static and dynamic contributions to the rate constants. The activation energy associated with the temperature dependence of the viscosity can be on the order of a few kcal/mol and for barriers that are a few kcal/mol this contribution from the viscosity cannot be neglected and acts to lower the overall measured activation energy. In chapter 4 we demonstrated that for the fluxional metal carbonyl complex dicobalt octacarbonyl in hexane that the barrier to isomerization could have a

contribution of 1.6 kcal/mol from the viscosity alone. Another possibility for the disagreement could be due to the fact that one of the previous NMR studies used three different solvents in order to broaden the temperature range probed. The studies did not attempt to account for changes that the solvent could have on the potential energy surface, which if the potential energy surface was altered upon changing the solvent, the measured activation energy could end up being a combination of different barriers in the different solvents.

6.4.4 $[CpRu(CO)_2]_2$: 2DIR Spectroscopy and DFT Calculations

The absolute value of the 2DIR nonrephasing spectra of $Cp_2Ru_2(CO)_4$ in hexane at t_2=150 fs and t_2=10 ps are shown in Fig. 6.5. In order to highlight the higher frequency peaks, the incoming beams were tuned to the higher frequency peaks leading to skewed 2DIR spectra. Because of the tuning of the incoming beams, the amplitudes of the higher frequencies peaks compared to the lower frequency peaks in the 2DIR spectra seem larger than what would be predicted from the linear FT-IR spectrum. The peaks along the diagonal, peaks 1-5, correspond to the peaks in the linear FT-IR spectrum. Peaks 4' and 5' are due to excited state absorptions. Peaks 6, 7, 8, and 9 are present at t_2=150 fs and as t_2 increases we see the appearance of peaks 11 and 10.

The IR spectra of $Cp_2Ru_2(CO)_4$ are more complex than the iron analog due to the significant populations of the two non-bridging isomers. For $Cp_2Ru_2(CO)_4$ the transition frequencies for the two bridging structures are shifted to higher frequencies compared to $Cp_2Fe_2(CO)_4$. In the 2DIR spectra of $Cp_2Ru_2(CO)_4$ the *trans*-B isomer is assigned to peak 2 and the *cis*-B isomer is assigned to peak 4 and has a small contribution to peak 3. The shift to higher frequencies can be simply explained by the increased bond length between the carbonyl carbon atoms and the metal atom. As the bond length increases, the carbonyl more closely resembles a free carbonyl group, shifting the frequency higher. We do not observe a crosspeak between the two modes of the *cis*-B isomer; this may be due to the crosspeak being dominated by the wings of

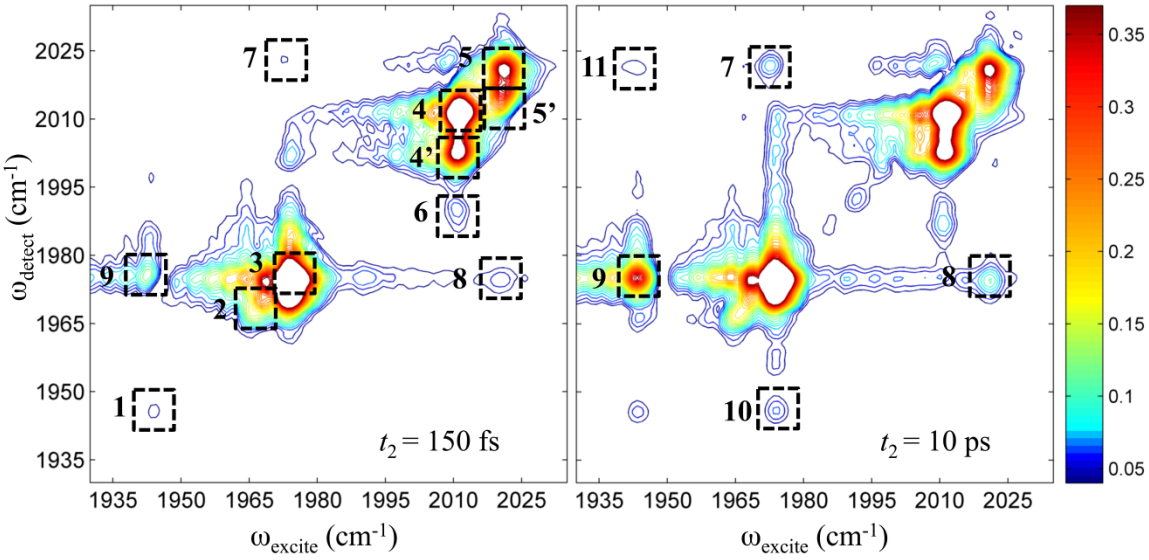

Figure 6.5 Absolute-value non-rephasing spectra of $Cp_2Ru_2(CO)_4$ in *n*-hexane at t_2=150 fs and t_2=10 ps. The spectra are normalized to the maximum peak at the given t_2 value.

diagonal peak 3. However, we still see evidence that there are two modes from the *cis*-B isomer because of the presence of peak 6, which arises from transitions to the combination band. Though we cannot determine the transition frequency of the lower frequency mode of the *cis*-B isomer from the crosspeaks, we can use the information obtained from the $Cp_2Fe_2(CO)_4$ complex in order to obtain the transition frequency. The frequency of the *trans*-B (1966 cm^{-1}) and higher frequency (2011 cm^{-1}) *cis*-B mode are shifted for the ruthenium complex; however, the spacing between the two modes only differs by 1 cm^{-1} indicating that the lower frequency *cis*-B mode should also maintain the same frequency spacing. Using this comparison we determined a frequency of 1970 cm^{-1} for the lower frequency *cis*-B mode.

$Cp_2Ru_2(CO)_4$ also exists as two non-bridging forms at room temperature. Peaks 1 and 3 have some contribution from both the *trans*-NB and *gauche*-NB form and peak 5 is assigned the *gauche*-NB form alone. As was the case for $Cp_2Fe_2(CO)_4$, we can obtain the transition frequencies of the overlapping peaks from the crosspeaks in the 2DIR spectra.

Crosspeaks 9 and 10 are inherent crosspeaks arising from the two transitions of the *trans*-NB species. Peak 10 is not observed at t_2=150 fs which we attribute to the tuning of the incoming pulses. As t_2 increases peak 10 becomes more prominent because of IVR. From the position of crosspeak 9 the transition frequencies for the two modes of the *trans*-NB isomer are found to be 1943 cm^{-1} and 1975 cm^{-1}. Crosspeaks 7, 8 and 11 are inherent crosspeaks arising from the three modes of the *gauche*-NB isomer. From the position of these peaks we can obtain the transition frequencies for the modes; 1943 cm^{-1}, 1972 cm^{-1}, and 2021 cm^{-1}. We have also compared our experimentally determined frequencies to the DFT calculated frequencies. The frequencies are given in Table 6.1 and are represented graphically in Fig. 6.2 with the experimental frequencies indicated as solid lines and the scaled DFT frequencies as dashed lines. The calculated frequencies differ from the experimentally determined frequencies by 6 cm^{-1} at most. In general the relative ordering of the DFT calculated frequencies are correct, except for the ordering of the frequencies making up peak 3.

We also obtained information on the second excited state manifold for the *gauche*-NB isomer from peak 5'. An anharmonicity of 4 cm^{-1} was obtained, which is less than the 8-cm^{-1} anharmonicity of the *cis*-B isomer. Unlike the case for $Cp_2Fe_2(CO)_4$, we are unable to determine the relative amplitudes of the dipole moments for the $Cp_2Ru_2(CO)_4$ complex due to the tuning of the incoming beams.

DFT calculations (Fig. 6.6) were performed on the isomers of $Cp_2Ru_2(CO)_4$. Here the *trans*-NB species lies lowest in energy with the *trans*-B species lying only slightly higher at ΔG=0.10 kcal/mol. Previous experimental studies found that the *trans*-B species lies the lowest in energy.[7] However, this energy difference is very small and since the calculations are performed in vacuum, the solvent interactions may be capable of inverting the ordering of these energies. The *gauche*-B isomer lies the highest in energy at ΔG=1.49 kcal/mol, which corresponds to an equilibrium constant of 0.08. Compared to the iron complex, the non-bridging species for the

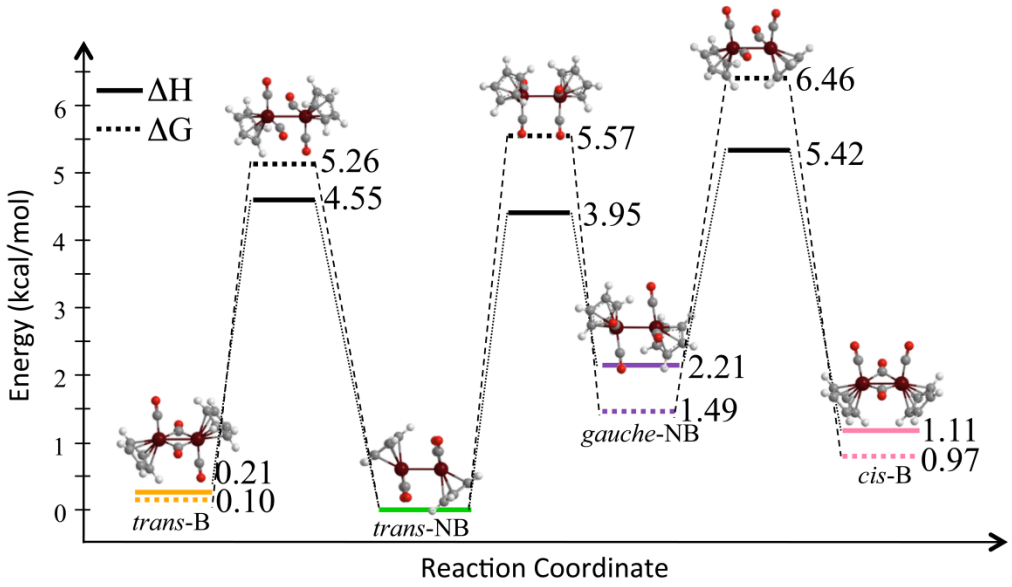

Figure 6.6 DFT calculated ground state energies of $Cp_2Ru_2(CO)_4$ along with the corresponding transition states. The calculated ΔG (dashed lines) and ΔH (solid lines) are indicated.

ruthenium complex lie lower in energy. One reason for this difference is that fact that the metal-metal bond length in the ruthenium complex is longer than that of the iron complex and the increased bond length leads to reduced steric hindrance resulting in a decrease in energy.

We also calculated the activation barrier for isomerization between the different isomers. For bridging terminal carbonyl exchange the activation energy for *trans*-B-to-*trans*-NB is E_a=4.34 kcal/mol and for *cis*-B-to-*gauche*-NB the activation energy is E_a=4.31 kcal/mol. Previous NMR studies have determined the activation energy for bridging terminal carbonyl exchange to be 7.6 kcal/mol *trans*-B-to-*trans*-NB and ~8.1 kcal/mol for *cis*-B-to-*gauche*-NB. Again we do not see quantitative agreement, but we do see that the difference between the two calculated energies is smaller than the difference in energies for the iron complex, as is the difference in energy between the two experimentally determined energies when compared to the iron complex. DFT and experiment indicate that the barrier for rotation about the Ru-Ru bond is lower than it is about the Fe-Fe bond, which is consistent with the greater Ru-Ru bond length. The increased bond length results in reduced steric

hindrance and reduced barrier to rotation about the metal-metal bond. The DFT calculated barrier is 3.95 kcal/mol for the *trans*-NB-to-*gauche*-NB interconversion. Previous NMR studies have suggested the barrier to be below 5 kcal/mol; however, these studies were not able to determine the barrier directly because the process was occurring on a timescale that was faster than could be probed with NMR.[7, 13] Barrier heights of this magnitude generally correspond to picosecond timescales for interconversion, which in principle may be observable using 2DIR spectroscopy. In this study, however, we do not observe exchange between the two non-bridging forms for reasons that are discussed below.

One impediment to observing exchange is the small equilibrium population of the *gauche*-NB isomer. To demonstrate this point we used the simple two-state kinetic model shown in Fig. 6.7, where we have two states A and B which interconvert with forward and reverse rate constants, k_{for} and k_{rev}, and vibrationally decay with a rate constant k_{Vib}.

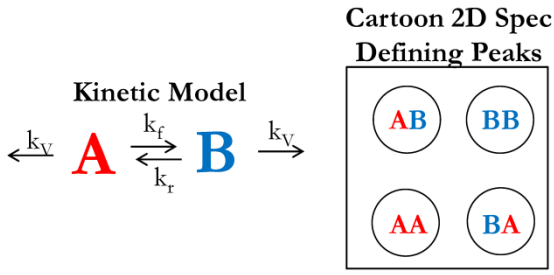

Figure 6.7 Two-state kinetic model where species A and B interconvert with forward and reverse rate constants, k_{for} and k_{rev}, and decay due to vibrational population relaxation k_{Vib}.

The solutions to this kinetic model are given in chapter 4.7.1 Eqs. 4.7-4.10, here we just present the solution for crosspeak AB (Fig. 6.7).

$$AB(t) = \frac{B_0 e^{-(k_V + k_{ex})t}\left(-1 + e^{k_{ex}t}\right)k_f}{k_{ex}} \qquad \textbf{Eq. 6.3}$$

Taking the derivate of Eq. 6.3, we determined the maximum amplitude that would be due to the exchange signal for the crosspeak at $\omega_{excite}=\omega_A$, $\omega_{detect}=\omega_B$ (Eq. 6.4) where $k_{Sum}=k_{for}+k_{rev}+k_{Vib}$ and B_0 is the initial effective population.

$$S_{\max} = \frac{B_0 k_{for}\left(\frac{k_{Sum}}{k_{Vib}}\right)^{-\left(\frac{k_{Sum}}{k_{for}+k_{rev}}\right)}}{k_{Vib}} \qquad \textbf{Eq. 6.4}$$

Taking the initial effective population, B_0, which we choose to use here to avoid accounting for the concentration, oscillator strength and tuning of the incoming pulses separately, to be equal to the initial amplitude of peak 5, $k_{Vib}=0.050$ ps^{-1}, $k_{rev}=0.050$ ps^{-1} where k_{for} is related to k_{rev} through the equilibrium constant K_{eq}, $k_{for}=k_{rev}/K_{eq}$, where $K_{eq}=0.08$ which was taken from the DFT calculations, we simulated the time dependent amplitudes of peaks AA, BB and AB (Fig. 6.7). The simulated diagonal peaks, AA and BB, along with the crosspeak AB are plotted in Fig. 6.8 (left). We see that the diagonal peaks decay and that the amplitude of the crosspeak is much less compared to the diagonal peaks.

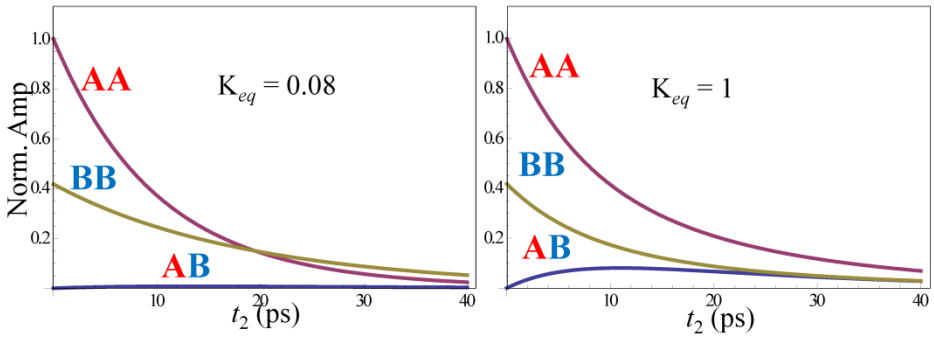

Figure 6.8 (left) Plot of the waiting time dependent amplitude of diagonal peaks AA (purple), BB(mustard), and crosspeak AB (green) for $K_{eq}=0.08$. (right) Plot of the waiting time dependent amplitude of diagonal peaks AA (purple), BB(mustard), and crosspeak AB (blue) for $K_{eq}=1$.

From the simulated data, we are able to approximate the maximum amplitude of the exchange signal contributing to crosspeak 7 to be only 1.9% of the maximum amplitude of diagonal peak 5. Fig. 6.8 (right) plots the simulated data keeping all parameters the same, except for the equilibrium constant which was set to 1. As the

energy of the species corresponding to B is lowered with respect to the species corresponding to A we see an increase in the amplitude of the exchange crosspeak. Comparing the two figures, we see that the relative populations of the two species affects the amplitude of exchange signal observed.

It is important to note that the above model predicts the maximum possible exchange signal and that this model does not account for the redistribution of vibrational energy upon isomerization. If energy is not significantly distributed to the IR active *gauche*-NB mode, upon isomerization from the *trans*-NB form to the *gauche*-NB, this would result in a decrease in the amplitude of the exchange crosspeak. Since there are three other modes in the terminal carbonyl stretching region of the *trans*-NB form, with one of the three being IR active, we would not expect all of the vibrational energy to be redistributed to the specific *gauche*-NB mode corresponding to diagonal peak 3, and our estimate of exchange would be an overestimate. It is also important to note that the conjugate crosspeak, peak 8, would have more of an exchange contribution according to the simple model; the equation corresponding to the maximum amplitude of exchange signal from this crosspeak is given in the Eq. 6.5.

$$S_{\max} = \frac{A_0 k_{rev} \left(\frac{k_{Sum}}{k_{Vib}} \right)^{-\left(\frac{k_{Sum}}{k_{for}+k_{rev}} \right)}}{k_{Vib}} \qquad \textbf{Eq. 6.5}$$

Though we would see more exchange signal from crosspeak 8, we choose not to focus on crosspeak 8 because it is in the more congested region of the spectrum and is already being dominated by the wings of diagonal peak 3.

6.5 Dynamics: Intramolecular Vibrational Energy Transfer

We do not observe any evidence of exchange between the two non-bridging isomers of the ruthenium complex; however, we do observe intramolecular vibrational energy redistribution between the two higher frequency modes of the *gauche*-NB isomer for $Cp_2Ru_2(CO)_4$ and between the modes of the *cis*-B isomer for $Cp_2Fe_2(CO)_4$. We have chosen to study the *gauche*-NB modes for the $Cp_2Ru_2(CO)_4$

complex because the crosspeak, peak 7, and corresponding diagonal peak, peak 5, are in the least congested region of the spectrum. To obtain the rate of IVR between the two *trans*-NB modes we would have to account for more than one process, because the crosspeak 9 has contributions from both the *gauche*-NB and *trans*-NB species and the corresponding diagonal peak 3 has contributions from three different isomers. For these reasons we focus on peaks 7 and 5 to isolate the rate of IVR for the *gauche*-NB isomer.

From Figs. 6.9a-b we see that for both metal complexes the diagonal peaks (blue) decay due to molecular reorientation, vibrational population relaxation and IVR. The crosspeaks (green) behave differently for the two metal complexes. For $Cp_2Fe_2(CO)_4$ the crosspeak decays. When compared to the corresponding diagonal peak the extent of decay is less. This is attributed to the IVR process which

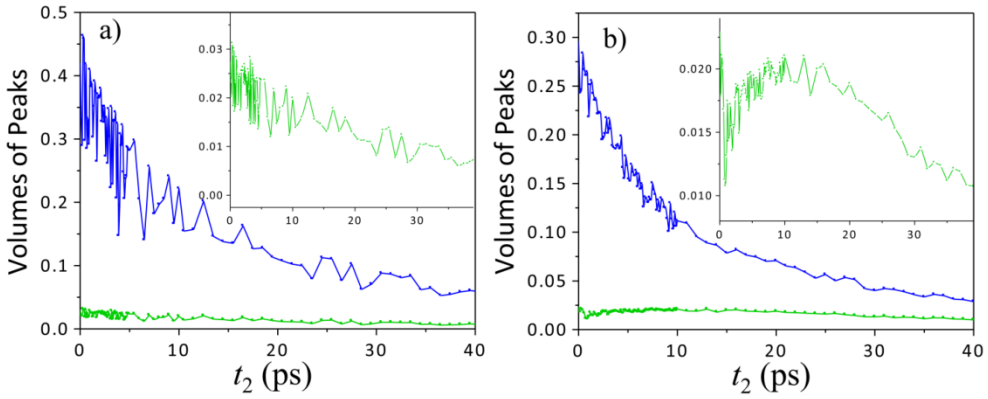

Figure 6.9 (a) Plot of the volumes of peaks 2 (blue) and 4 (green) for $Cp_2Fe_2(CO)_4$ in *n*-hexane. (b) Plot of the volumes of peaks 5 (blue) and 7 (green) for $Cp_2Ru_2(CO)_4$ in *n*-hexane.

contributes to the growth of the crosspeak. For $Cp_2Ru_2(CO)_4$, the crosspeak first grows in and then decays. The decay is due to molecular reorientation and population relaxation. There are two possible origins for the signal growth, either there is exchange between the two non-bridging species or there is IVR between the two modes of the *gauche*-NB isomer. As discussed previously, the barrier for interconversion between these two species is consistent with an exchange process that occurs on the picosecond timescale, but that the contribution of exchange to the

total amplitude of the crosspeak is expected to be too small to observe given the limitations of our data. To show that the growth is due to IVR and not to exchange we first examine the excitation frequency of the crosspeak. The *trans*-NB isomer has a transition frequency of 1974 cm^{-1}. For the growth of crosspeak 7 to be from exchange the peak should appear at ω_{excite} = 1974 cm^{-1} , ω_{detect} = 2021 cm^{-1}. The excitation and detection frequencies for crosspeak 7 are ω_{excite} = 1972 cm^{-1}, ω_{detect} = 2021 cm^{-1} indicating that the growth of the crosspeak is due to IVR. If there were some contribution from exchange to crosspeak 7 we would expect to see a broadening of the crosspeak to include the excitation frequency at ω_{excite} = 1974 cm^{-1}. We have also looked at the solvent dependence of crosspeak 7 and we found that the growth was not affected by the solvent. In chapter 5 it has been shown that in solution, 2DIR spectroscopy can be used to probe the influence of the solvent on isomerization reactions, with a slower exchange times obtained in solvents with higher viscosities. Fig. 6.10 plots the normalized volumes of crosspeak 7 in hexane (blue) and dodecane (green) as a function of t_2. The viscosities of the two solvents differ by 1.1 cP, which led to a factor of 3.3 increase in the reaction time in the flexible metal carbonyl complex $Co_2(CO)_8$. From the traces it is obvious that the solvent does not influence the growth of the crosspeak, further indicating the growth is not due to exchange.

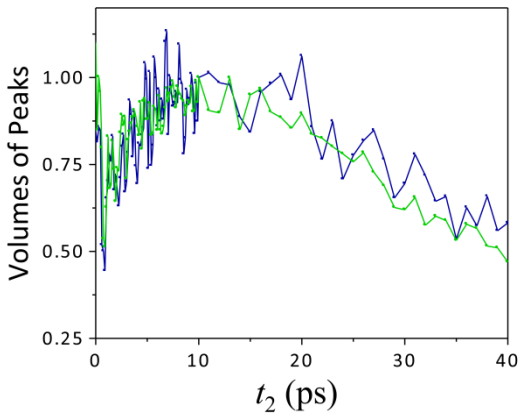

Figure 6.10 The volumes of crosspeak 7 for $Cp_2Ru_2(CO)_4$ in *n*-hexane (blue) and dodecane (green).

To extract the IVR rate constants we modeled IVR as an equilibrium process. The kinetic model we used is given in Fig. 6.11 where k_V is the rate of population relaxation, τ_{or} is the molecular reorientation time, k_{IVR} and k_{-IVR} are the forward and reverse rate constants for IVR, and A1 indicates the lower frequency mode involved in the IVR process while A2 indicates the higher frequency mode.

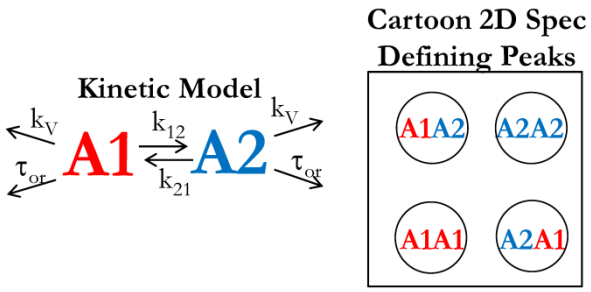

Figure 6.11 Two-state kinetic model where modes A1 and A2 exchange vibrational energy with a forward and reverse rate constant, k_{IVR} and k_{-IVR}, and decay due to vibrational population relaxation, k_{Vib}, and molecular reorientation, τ_{or}.

The general solutions to this kinetic model are given in Eq. 6.6 and a detailed explanation of the general solutions is given in chapter 5.4.2.

$$\begin{pmatrix} A1(t) \\ A2(t) \end{pmatrix} = \frac{3}{45}\exp\left[\begin{pmatrix} -(k_V + k_{12} + D) & k_{21} \\ k_{12} & -(k_V + k_{21} + D) \end{pmatrix} t\right]\begin{pmatrix} A1_0 \\ A2_0 \end{pmatrix} \qquad \textbf{Eq. 6.6}$$

$$+\frac{1}{9}\left[\begin{pmatrix} -(k_V + k_{12}) & k_{21} \\ k_{12} & -(k_V + k_{21}) \end{pmatrix} t\right]\begin{pmatrix} A1_0 \\ A2_0 \end{pmatrix}$$

The analytical solutions to Eq. 6.6 for the peaks in Fig. 6.11 are given in Eqs. 6.7-6.10.

$$A1A1(t) = \frac{2}{45}A1_0 e^{-(D+k_{12}+k_{21}+k_V)t}(4+5e^{Dt})(g+he^{(k_{12}+k_{21})t}) \qquad \textbf{Eq. 6.7}$$

$$A2A2(t) = \frac{2}{45}A2_0 e^{-(D+k_{12}+k_{21}+k_V)t}(4+5e^{Dt})(h+ge^{(k_{12}+k_{21})t}) \qquad \textbf{Eq. 6.8}$$

$$A1A2(t) = \frac{1}{45}e^{-(D+k_{12}+k_{21}+k_V)t}(3+5e^{Dt})(-A2_0 h + A1_0 g + (A1_0 + A2_0)he^{(k_{12}+k_{21})t}) \qquad \textbf{Eq. 6.9}$$

$$A2A1(t) = \frac{1}{45} e^{-(D+k_{12}+k_{21}+k_V)t}(3+5e^{Dt})(+A2_0 h - A1_0 g + (A1_0 + A2_0) g e^{(k_{12}+k_{21})t}) \quad \textbf{Eq. 6.10}$$

In order to reduce the number of fitting parameters, we take the ratio of the crosspeak A1A2, Eq. 6.9, to the diagonal peak A2A2, Eq.6.8, this eliminates the vibrational population relaxation term. Taking the ratio of the crosspeak and diagonal peak, results in the following equation (Eq. 6.11) which we use to fit the data, where A is the amplitude of the inherent crosspeak, $6D_{or}=1/\tau_{or}$, $k_{IVR}=k_{-IVR}\exp(-\Delta cm^{-1}/207cm^{-1})$ where Δcm^{-1} is the splitting between the two modes involved, N_A is the effective initial population of mode A and N_B is the effective initial population of mode B, $g=k_{IVR}/(k_{IVR}+k_{-IVR})$, and $h=k_{-IVR}/(k_{IVR}+k_{-IVR})$.

$$S_{CP/DP}(t_2) = A\left(3+5e^{6D_{or}t_2}\right)\left(N_A g - N_B h + h\left(N_A + N_B\right)e^{(k_{IVR}+k_{-IVR})t_2}\right)/ \quad \textbf{Eq. 6.11}$$

$$2N_B\left(4\_5e^{6D_{or}t_2}\right)\left(h + ge^{(k_{IVR}+k_{-IVR})t_2}\right)$$

The IVR rate constants are obtained by fitting the data to Eq. 6.11 and allowing for the following 4 parameters to vary: A, k_{-IVR}, N_A, N_B. The molecular reorientation times were determined from molecular dynamic simulations for the *gauche*-NB isomer for $Cp_2Ru_2(CO)_4$ using the same process described in chapter 4. We have used this molecular reorientation time for both the $Cp_2Ru_2(CO)_4$ and $Cp_2Fe_2(CO)_4$ complex since we do not expect the molecular reorientation time to change significantly between the two species. Also we found that varying the molecular reorientation time by ± 10 ps results in the variation of the rate constants by 2% at the most.

The ratio of the volumes of crosspeak 4 to diagonal peak 2 for the iron complex (a) and the ratio of crosspeak 7 to diagonal peak 5 for the ruthenium complex (b) along with the fits obtained from fitting to the Eq. 6.11 are shown in Figs. 6.12. For $Cp_2Fe_2(CO)_4$, the IVR rate constants for energy exchange between the two modes of the *cis*-B isomer were determined to be $k_{-IVR}= 0.072\pm0.012$ ps^{-1} (14±3 ps) and $k_{IVR}= 0.059\pm0.013$ ps^{-1} (17±5 ps). The two modes involved are shown in Fig

6.13. The higher frequency mode is the symmetric stretch of the terminal carbonyls and the lower frequency mode is the antisymmetric stretch of the terminal carbonyls. For $Cp_2Ru_2(CO)_4$, the IVR rates between the two modes of the *gauche*-NB were determined to be k_{-IVR}= 0.057±0.007 ps^{-1} (17±2 ps) and k_{IVR}= 0.045±0.007 ps^{-1}

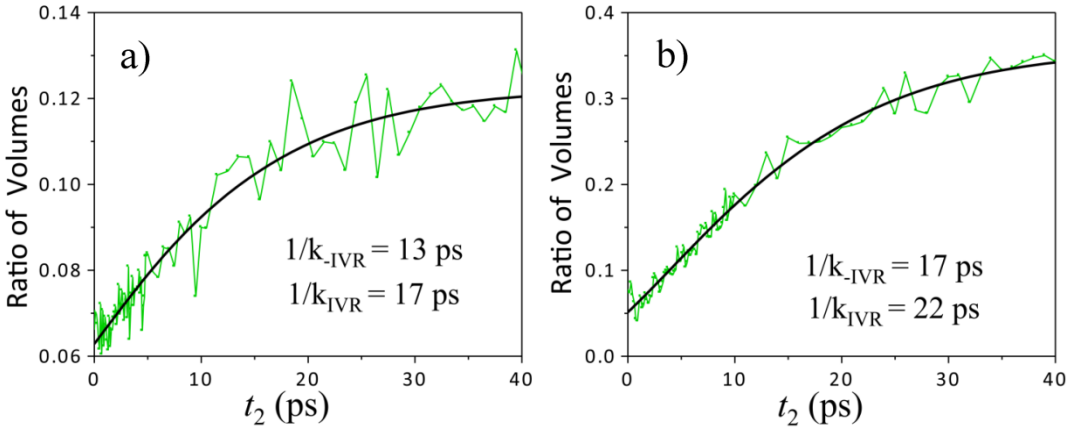

Figure 6.12 (a) Plot of the ratio of crosspeak 4 to diagonal peak 2 for $Cp_2Fe_2(CO)_4$ (green) along with the resulting fit to Eq. 6.11 (black). (b) Plot of the ratio of crosspeak 7 to diagonal peak 5 for $Cp_2Ru_2(CO)_4$ (green) along with the resulting fit to Eq. 6.11 (black).

(22±4 ps). The two modes involved are shown in Fig. 6.13. The higher frequency mode is the symmetric stretch and the lower frequency mode is the antisymmetric stretch.

For both metal complexes, we find that the IVR rate constant is slower for the uphill transfer compared to the downhill transfer, which is due to the weighting by the Boltzmann factor. We also find that for the ruthenium complex the rate of IVR is slightly slower compared to the iron complex. One of the main differences between the two metal complexes is the difference in frequency between the two modes involved. For $Cp_2Fe_2(CO)_4$ the difference in frequency is 41 cm^{-1} and for $Cp_2Ru_2(CO)_4$ it is 49 cm^{-1}. Assuming that the rate of IVR is directly proportional to the population of liquid photons at an energy corresponding to the difference in energy between the two modes involved in IVR[25, 26], we find that the rate of IVR for a splitting of 41 cm^{-1} should decrease by 18% as the splitting is increased to 49 cm^{-1}.

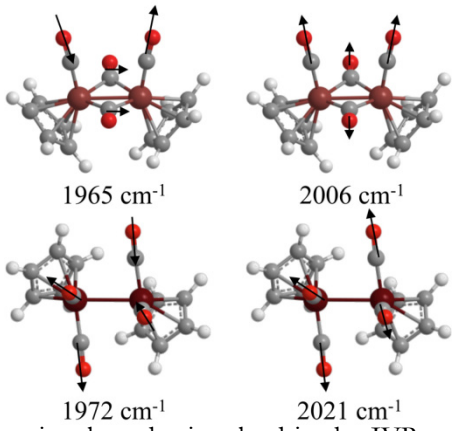

Figure 6.13 The vibrational modes involved in the IVR process are shown for $Cp_2Fe_2(CO)_4$ and $Cp_2Ru_2(CO)_4$. Arrows indicate displacements of the carbonyl units.

The measured IVR rate constant for $Cp_2Ru_2(CO)_4$ is 21±10% slower than that of $Cp_2Fe_2(CO)_4$. The agreement with the simple description of IVR as a barrierless process free of solvent-solute interactions, indicates that the linear alkane solvents do not modify the solvation shell environment or the associated energetics. This lack of solvent specificity is in stark contrast to our recent observation of solvent-hindered vibrational energy redistribution in metal carbonyl complexes in hydrogen bonding alcohols.[27] The present work lays the foundation for future studies in more strongly interacting solvents capable of forming hydrogen bonds with the complex.

6.6 Conclusion

Congested linear IR spectra obscure the assignment of peaks requiring several solvent and temperature dependent spectra to determine the contributions from different species to individual spectral features. Even with such data, the exact transition frequencies of the contributing species may be difficult to extract unambiguously. In this chapter we have utilized 2DIR spectroscopy to aid in the interpretation of the linear FT-IR spectrum for $Cp_2Fe_2(CO)_4$ and $Cp_2Ru_2(CO)_4$, two structurally related complexes whose energetics and IR spectra differ due primarily to the metal-metal bond distance From the 2DIR spectrum we are able to obtain the transition frequencies for the individual isomers from inherent crosspeaks in the spectra. Combining our experimental and DFT results leads to a detailed

understanding of the spectroscopic and energetic differences between these two metal complexes.

Not only do the crosspeaks aid in assignment, but by monitoring the picosecond change in the volume of the crosspeaks as a function or waiting time we are able to obtain the rate of vibrational energy transfer (IVR) for both the uphill and downhill transfer of energy. We find the rate of IVR for the iron complex is faster compared to the ruthenium complex, and is consistent with an explanation based solely on the energy gap between the two modes, which is smaller for the iron case.

Though we did see energy transfer in both complexes, we did not see any population transfer between two distinct chemical species due to chemical exchange. However, the DFT calculations and previous NMR experiments suggest that it should be possible to observe chemical exchange between the *gauche*-NB and *trans*-NB forms of $Cp_2Ru_2(CO)_4$ on the timescale probed by 2DIR spectroscopy. We propose that our inability to observe exchange is due to the very small population of the *gauche*-NB form. One way to address this issue in future work would be to perform the experiment in solvents that stabilize the polar isomers, namely the *gauche*-NB and *cis*-B isomers, increasing the population of the *gauche*-NB isomer relative to the *trans*-NB. If the relative free energies of the two isomers were equal, we predict that the amplitude of the exchange signal would increase by an order of magnitude (i.e. 10% of the maximum of diagonal peak 5 (Fig. 6.8)). Performing the experiments using different solvents may facilitate the observation of chemical exchange, while perhaps introducing a structured solvation shell environments to spatially modulate the reaction barrier and vibrational energy transfer. This work emphasizes the power that 2DIR spectroscopy has to resolve structure and dynamics in condensed phase systems, which is crucial information needed to understand current inorganic-based catalysis as well as to design future catalysts.

References:

1. Jaworska, M., W. Macyk, and Z. Stasicka, *Structure, spectroscopy and photochemistry of the M(eta(5) -C5H5)(CO)(2) (2) complexes (M=Fe, Ru)*, in *Optical Spectra and Chemical Bonding in Inorganic Compounds, Vol 1*. 2004. p. 153-172.

2. Cotton, F.A., H. Stammreich, and G. Wilkinson, *THE RAMAN AND INFRA-RED SPECTRA AND STRUCTURE OF DI-(PI-CYCLOPENTADIENYLIRON) TETRACARBONYL*. Journal of Inorganic & Nuclear Chemistry, 1959. **9**(1): p. 3-7.

3. Noack, K., *INFRA-RED SPECTRUM AND STRUCTURE OF DI-CYCLOPENTADIENYL DI-IRON TETRACARBONYL*. Journal of Inorganic & Nuclear Chemistry, 1963. **25**(11): p. 1383-1388.

4. Cotton, F.A. and G. Yagupsky, *TAUTOMERIC CHANGES IN METAL CARBONYLS .I. PI-CYCLOPENTADIENYLIRON DICARBONYL DIMER AND PI-CYCLOPENTADIENYLRUTHENIUM DICARBONYL DIMER*. Inorg. Chem., 1967. **6**(1): p. 15-&.

5. Manning, A.R., *STRUCTURE OF BIS-PI-CYCLOPENTADIENYLDI-IRON TETRACARBONYL IN SOLUTION*. Journal of the Chemical Society a - Inorganic Physical Theoretical, 1968(6): p. 1319-&.

6. McArdle, P. and A.R. Manning, *STRUCTURES OF DICARBONYLCYCLOPENTADIENYLRUTHENIUM DIMER (RU(PI-C5H5)(CO)2)2! AND SOME RELATED COMPLEXES IN SOLUTION*. Journal of the Chemical Society a -Inorganic Physical Theoretical, 1970(12): p. 2128-&.

7. Bullitt, J.G., F.A. Cotton, and T.J. Marks, *STRUCTURAL AND DYNAMIC PROPERTIES OF PENTAHAPTOCYCLOPENTADIENYLMETAL DICARBONYL DIMERS*. Inorg. Chem., 1972. **11**(4): p. 671-&.

8. Mills, O.S., *STUDIES OF SOME CARBON COMPOUNDS OF THE TRANSITION METALS .1. THE CRYSTAL STRUCTURE OF DICYCLOPENTADIENYLDI-IRON TETRACARBONYL*. Acta Crystallographica, 1958. **11**(9): p. 620-623.

9. Mills, O.S. and J.P. Nice, *Carbon compounds of the transition metals : V. The structure of bis(cyclopentadienyldicarbonyl-rutheium)*. Journal of Organometallic Chemistry, 1967. **9**(2): p. 339-344.

10. Bryan, R.F. and P.T. Greene, *METAL-METAL BONDING IN CO-ORDINATION COMPLEXES .9. CRYSTAL STRUCTURE OF TRANS-DI-MU-CARBONYL-DICARBONYLDI-PI-CYCLOPENTADIENYLDI-IRON (FE-FE), A REDETERMINATION*. Journal of the Chemical Society a -Inorganic Physical Theoretical, 1970(18): p. 3064-&.

11. Bryan, R.F., P.T. Greene, M.J. Newlands, and D.S. Field, *METAL-METAL BONDING IN CO-ORDINATION COMPLEXES .10. PREPARATION, SPECTROSCOPIC PROPERTIES, AND CRYSTAL STRUCTURE OF CIS-ISOMER OF DI-MU-CARBONYL-DICARBONYLDI-PI-CYCLOPENTADIENYLDI-IRON (FE-FE)*. Journal of the Chemical Society a -Inorganic Physical Theoretical, 1970(18): p. 3068-&.

12. Mague, J.T., *A REDETERMINATION OF THE CRYSTAL-STRUCTURE OF BIS(CYCLOPENTADIENYLDICARBONYLRUTHENIUM)*. Acta Crystallographica Section C-Crystal Structure Communications, 1995. **51**: p. 831-833.

13. Gansow, O.A., A.R. Burke, and W.D. Vernon, *C-13 AND PROTON MAGNETIC-RESONANCE EXAMINATION OF SOLUTE STRUCTURES, EQUILIBRIA, AND STRUCTURAL INTERCONVERSIONS IN SOME DINUCLEAR ETA5-DIENYLRUTHENIUM, DIENYLIRON, AND DIENYLNICKEL CARBONYLS*. Journal of the American Chemical Society, 1976. **98**(19): p. 5817-5826.

14. Bitterwolf, T.E., *Photochemistry and reaction intermediates of the bimetallic Group VIII cyclopentadienyl metal carbonyl compounds, (eta(5)-C5H5)(2)M-2(CO)(4) and their derivatives*. Coordination Chemistry Reviews, 2000. **206**: p. 419-450.

15. Piper, T.S., F.A. Cotton, and G. Wilkinson, *CYCLOPENTADIENYL-CARBON MONOXIDE AND RELATED COMPOUNDS OF SOME TRANSITIONAL METALS*. Journal of Inorganic & Nuclear Chemistry, 1955. **1**(3): p. 165-174.

16. Fischer, R.D., A. Vogler, and K. Noack, *ISOMERISM IN METAL COMPLEXES OF TYPE C5H5M(CO)2 2*. Journal of Organometallic Chemistry, 1967. **7**(1): p. 135-&.

17. Noack, K., *ENTHALPY AND ENTROPY DIFFERENCE OF BRIDGED AND NON-BRIDGED FORMS OF CYCLOPENTADIENYLRUTHENIUM DICARBONYL DIMER*

RUC5H5(CO)2 2 AND ANALOGOUS IRON COMPOUND FEC5H5(CO)2 2. Journal of Organometallic Chemistry, 1967. **7**(1): p. 151-&.

18. Frisch, M.J., G.W. Trucks, H.B. Schlegel, G.E. Scuseria, M.A. Robb, J.R. Cheeseman, J. Montgomery, J. A., T. Vreven, K.N. Kudin, J.C. Burant, J.M. Millam, S.S. Iyengar, J. Tomasi, V. Barone, B. Mennucci, M. Cossi, G. Scalmani, N. Rega, G.A. Petersson, H. Nakatsuji, M. Hada, M. Ehara, K. Toyota, R. Fukuda, J. Hasegawa, M. Ishida, T. Nakajima, Y. Honda, O. Kitao, H. Nakai, M. Klene, X. Li, J.E. Knox, H.P. Hratchian, J.B. Cross, V. Bakken, C. Adamo, J. Jaramillo, R. Gomperts, R.E. Stratmann, O. Yazyev, A.J. Austin, R. Cammi, C. Pomelli, J.W. Ochterski, P.Y. Ayala, K. Morokuma, G.A. Voth, P. Salvador, J.J. Dannenberg, V.G. Zakrzewski, S. Dapprich, A.D. Daniels, M.C. Strain, O. Farkas, D.K. Malick, A.D. Rabuck, K. Raghavachari, J.B. Foresman, J.V. Ortiz, Q. Cui, A.G. Baboul, S. Clifford, J. Cioslowski, B.B. Stefanov, G. Liu, A. Liashenko, P. Piskorz, I. Komaromi, R.L. Martin, D.J. Fox, T. Keith, M.A. Al-Laham, C.Y. Peng, A. Nanayakkara, M. Challacombe, P.M.W. Gill, B. Johnson, W. Chen, M.W. Wong, C. Gonzalez, and J.A. Pople, *Gaussian 03*. 2004, Gaussian, Inc: Wallingford CT.

19. Wang, H.Y., Y.M. Xie, R.B. King, and H.F. Schaefer, *Unsaturation in binuclear cyclopentadienyliron carbonyls*. Inorg. Chem., 2006. **45**(8): p. 3384-3392.

20. Peng, B., Q.S. Li, Y.M. Xie, R.B. King, and H.F. Schaefer, *Unsaturated trinuclear ruthenium carbonyls: large structural differences between analogous carbonyl derivatives of the first, second, and third row transition metals*. Dalton Transactions, 2008(48): p. 6977-6986.

21. Wang, H.Y., Y.M. Xie, R.B. King, and H.F. Schaefer, *Remarkable aspects of unsaturation in trinuclear metal carbonyl clusters: The triiron species Fe-3(CO)(n) (n=12, 11, 10, 9)*. Journal of the American Chemical Society, 2006. **128**(35): p. 11376-11384.

22. Peng, C.Y. and H.B. Schlegel, *Combining Synchronous Transit and Quasi-Newton Methods to Find Transition-States*. Israel Journal of Chemistry, 1993. **33**(4): p. 449-454.

23. Peng, C.Y., P.Y. Ayala, H.B. Schlegel, and M.J. Frisch, *Using redundant internal coordinates to optimize equilibrium geometries and transition states*. Journal of Computational Chemistry, 1996. **17**(1): p. 49-56.

24. Golonzka, O. and A. Tokmakoff, *Polarization-selective third-order spectroscopy of coupled vibronic states*. Journal of Chemical Physics, 2001. **115**(1): p. 297-309.

25. Cahoon, J., K. Sawyer, J. Schlegel, and C. Harris, *Determining Transition-State Geometries in Liquids using 2D-IR.* Science, 2008. **319**: p. 1820-1823.

26. Tokmakoff, A., B. Sauter, and M.D. Fayer, *TEMPERATURE-DEPENDENT VIBRATIONAL-RELAXATION IN POLYATOMIC LIQUIDS - PICOSECOND INFRARED PUMP-PROBE EXPERIMENTS.* Journal of Chemical Physics, 1994. **100**(12): p. 9035-9043.

27. King, J.T., J.M. Anna, and K.J. Kubarych, *Solvent-hindered intramolecular vibrational redistribution.* Phys. Chem. Chem. Phys., 2011.

Chapter 7

Conclusion

7.1 General Conclusions

Linear spectra can be congested – obscuring the assignment of spectral features. Because spectral features arising from different chemical species could have different dependencies on temperature and solvent, several solvent and temperature dependent studies may be performed, in order to gain insight on the assignment of linear spectrum. However, assignments based solely on these perturbations are not always accurate. For example, if two species were to have the same dipole moment, changing the solvent may not have a large effect on the linear spectrum, leading to the conclusion that only one species was present. If two species had an equilibrium constant of ~1, then changing the temperature would not have a large effect on the linear spectrum, which could also lead to incorrect interpretations. Even if one were to assign a congested linear spectrum using these techniques, the exact transition frequencies of the contributing species may be difficult to extract unambiguously.

Spreading the congested information contained in a linear spectrum over two frequency axes aids in the assignment of the peaks in the spectrum. For the metal carbonyl complexes $Co_2(CO)_8$, $Fe_2Cp_2(CO)_4$, and $Ru_2Cp_2(CO)_4$, it was demonstrated that 2DIR spectroscopy can be used to assign the linear spectrum. From inherent crosspeaks in a 2DIR spectrum, the transition frequency of a given mode can also be determined unambiguously as opposed to the case in linear spectrum. This

aspect of 2DIR spectroscopy makes it a competitive alternative for the assignment and characterization of chemical species.

Along with assignment and determination of transition frequencies, 2DIR spectroscopy has been shown to be an effective tool in the study of equilibrium dynamics. Though dynamic information is contained in the lineshapes of the peaks in linear spectra, the abstraction of this dynamic information is not trivial.[1-3] 2DIR spectroscopy, where the signal results from the third-order nonlinear polarization, separates homogeneous and inhomogeneous broadening, aiding in the extraction of dynamic information specific to solvent-solute interactions.[4, 5]

We obtain our 2DIR spectra via the chirped pulse upconversion method of 2DIR spectroscopy, where the mid-IR signal is transferred to the visible region allowing for detection via a CCD camera.[6] Conventionally, HgCdTe detectors are used for direct detection of mid-IR signals; however, these detectors can be costly; only detect in the mid-IR; and have a low intrinsic sensitivity compared to CCD cameras. Also, a 100x1340 CCD camera has an order of magnitude multiplex advantage over a state of the art 128 pixel HgCdTe detector, which also contributes to the benefits of using a CCD camera for detection. One of the disadvantages associated with CPU 2DIR spectroscopy arises from the inherent cross-phase modulation resulting from the upconversion process. However, as was demonstrated in chapter 3, the phase distortions resulting from the upconverion process are easily removed. In chapter 3 we have given a detailed procedure for the removal of these distortions along with a detailed description for obtaining absorptive spectra. The removal of these distortions is not necessary for broad transitions, but is necessary when the lineshapes of spectra are desired or when phase sensitive measurements are required.

We have also utilized 2DIR spectroscopy to study the equilibrium dynamics of the three metal carbonyl complexes, $Co_2(CO)_8$, $Fe_2Cp_2(CO)_4$, and $Ru_2Cp_2(CO)_4$. We probed the dynamic equilibrium between the different isomers of $Co_2(CO)_8$. For

$Fe_2Cp_2(CO)_4$, and its ruthenium analog, $Ru_2Cp_2(CO)_4$, we observed intramolecular energy transfer between different vibrational modes for a given metal complex.

Previous studies have observed chemical exchange using 2DIR spectroscopy, where the exchange occurred between two different species for which the peaks were well resolved.[7-11] Studying $Co_2(CO)_8$, we furthered these studies by applying 2DIR chemical exchange spectroscopy to a system existing as three isomers in dynamic equilibrium which have overlapping spectral features. We observed evidence of chemical exchange between all three isomers, indicating previous suggestions of a linear pathway of interconversion are not strictly true. Focusing on exchange between two of the isomers, we characterized the picosecond isomerization. Temperature dependent forward and reverse rate constants were obtained from the congested spectra by locking onto the well characterized quantum oscillations of the inherent crosspeak enabling the separation of exchange and inherent crosspeak contributions to the signal. By modeling the waiting time dependent dynamics of overlapping spectral features, we demonstrated how to characterize a barrier crossing process from congested 2DIR spectra. From the temperature dependent rate constants, we extracted the height of the barrier for isomerization and found a significant entropic contribution to the barrier. We also highlighted the importance of the solvent in condensed phase measurements. Changing the temperature in order to extract the barrier heights, leads to changes in the viscosity of the solvent. We stressed the importance of including this aspect in the measurements of the barrier height, giving a lower and upper bound to the activation energy.

Understanding the role solvent plays in barrier crossing processes leads to being able to influence the outcome of chemical reactions, whether biasing the formation of a specific product or altering the rate of a reaction. Using the well-characterized isomerization reaction between the two isomers of dicobalt octacarbonyl we probed how the solvent influences a barrier crossing process. We performed the first direct test of Kramers theory in the time-domain for an isomerization reaction occurring on the ground electronic state. Through a combination of quantum and classical

computations along with FTIR measurements, we found for a series of linear alkanes that the potential energy surface is not modulated, and the change in isomerization time is solely a dynamic solvent effect that could be modeled using Markovian Kramers theory. Kramers theory has been used to describe many reactions in the condensed phase[12-26], yet it has not been systematically investigated for reactions occurring on the ground electronic state. We provide this systematic test, finding that Kramers theory is capable of predicting chemical reaction dynamics in the condensed phase.

This thesis also presents the study of equilibrium dynamics of iron cyclopentadienyl dicarbonyl dimer ($Fe_2(Cp)_2(CO)_4$) and its ruthenium analog ($Ru_2(Cp)_2(CO)_4$). Previous NMR studies have suggested that the isomerization between the *trans*-NB and *gauche*-NB forms of $Ru_2(Cp)_2(CO)_4$ occurs on the picosecond timescale.[27, 28] This is also consistent with our DFT calculated barrier heights. However, we did not observe chemical exchange between these two species. We attribute the lack of chemical exchange to the relatively small population of the *gauche*-NB species at room temperature. The equilibrium constant for *trans*-NB to *gauche*-NB isomerization is much less than one. The *trans*-NB species is much more populated: there are ~13 *trans*-NB molecules for every *gauche*-NB molecule. From the kinetic model, we have shown that as the equilibrium constant approaches one, the exchange signal will increase. The static solvent effect could lead to alterations in the potential energy surface resulting in the stabilization of the *gauche*-NB species with respect to the *trans*-NB species. Current work is underway, in which the static solvent effect is being used to shift the equilibrium constant in hopes of facilitating the observation of chemical exchange between these two species.

Although we do not observe chemical exchange in the ruthenium complex, we did observe intramolecular vibrational energy transfer. How vibrational energy is transferred between different modes is also important in understanding chemical dynamics in solution. The flow of vibrational energy can influence outcomes of chemical reactions[29, 30], and in the condensed phase the solvent can manipulate the

flow of vibrational energy transfer.[31, 32] We observed intramolecular vibrational energy transfer between two modes of the *cis*-B $Fe_2(Cp)_2(CO)_4$ and the *gauche*-NB $Ru_2(Cp)_2(CO)_4$ isomers. Treating IVR as an equilibrium process we extracted the timescales of IVR for both the uphill and downhill transfer of energy finding that the rate of energy transfer maps directly to the splitting in energy between the two modes involved in the IVR process.

7.2 Future Outlooks

This thesis demonstrated that 2DIR spectroscopy is a powerful tool for studying condensed phase dynamics and assigning spectra. It explored both dynamic equilibrium isomerization between two different isomers and intramolecular vibrational energy transfer.

As was demonstrated, the presence of inherent crosspeaks makes 2DIR spectroscopy a powerful tool for assigning species, especially in the case where different species cannot be isolated, such as different isomeric forms of a given chemical species. Though the 2DIR experimental setup can be complicated, certain aspects of the apparatus are commercially available, making 2DIR spectroscopy a competitive tool for assigning and characterizing chemical species.

Along with being able to characterize chemical species, 2DIR spectroscopy is also a powerful tool for studying condensed phase dynamics. In solution and other dense media, transition state theory is not valid since it cannot account for the important solvent dynamics that induce recrossing of the barrier separating reactants and products. Through our studies we have shown that Kramers theory is capable of making quantitative predictions of chemical kinetics in solution. Further studies of condensed phase reactions and solvent dynamics will lead to more accurate predictions of condensed phase processes.

References:

1. Loring, R.F. and S. Mukamel, *Selectivity in Coherent Transient Raman Measurements of Vibrational Dephasing in Liquids*. Journal of Chemical Physics, 1985. **83**(5): p. 2116-2128.

2. Tanimura, Y. and S. Mukamel, *2-Dimensional Femtosecond Vibrational Spectroscopy of Liquids*. Journal of Chemical Physics, 1993. **99**(12): p. 9496-9511.

3. Mukamel, S., *Principles of Nonlinear Optical Spectroscopy*. 1995, New York: Oxford University Press.

4. Cho, M.H., *Coherent two-dimensional optical spectroscopy*. Chem. Rev., 2008. **108**(4): p. 1331-1418.

5. Jonas, D.M., *Two-dimensional femtosecond spectroscopy*. Annual Review of Physical Chemistry, 2003. **54**: p. 425-463.

6. Nee, M., R. McCanne, K. Kubarych, and M. Joffre, *Two-dimensional infrared spectroscopy detected by chirped-pulse upconversion*. Opt. Lett., 2007. **32**(6): p. 713-715.

7. Zheng, J., K. Kwak, J. Asbury, X. Chen, I. Piletic, and M. Fayer, *Ultrafast dynamics of solute-solvent complexation observed at thermal equilibrium in real time*. SCIENCE, 2005. **309**(5739): p. 1338-1343.

8. Zheng, J., K. Kwak, J. Xie, and M. Fayer, *Ultrafast carbon-carbon single-bond rotational isomerization in room-temperature solution*. SCIENCE, 2006. **313**(5795): p. 1951-1955.

9. Woutersen, S., Y. Mu, G. Stock, and P. Hamm, *Hydrogen-bond lifetime measured by time-resolved 2D-IR spectroscopy: N-methylacetamide in methanol*. Chemical Physics, 2001. **266**(2-3): p. 137-147.

10. Kim, Y.S. and R.M. Hochstrasser, *Chemical exchange 2D IR of hydrogen-bond making and breaking*. Proceedings of the National Academy of Sciences of the United States of America, 2005. **102**(32): p. 11185-11190.

11. Cahoon, J., K. Sawyer, J. Schlegel, and C. Harris, *Determining Transition-State Geometries in Liquids using 2D-IR*. Science, 2008. **319**: p. 1820-1823.

12. Velsko, S.P., D.H. Waldeck, and G.R. Fleming, *Breakdown of Kramer Theory Description of Photochemical Isomerization and the Possible Involvement of Frequency-Dependent Friction*. Journal of Chemical Physics, 1983. **78**(1): p. 249-258.

13. Rothenberger, G., D.K. Negus, and R.M. Hochstrasser, *Solvent Influence on Photo-Isomerization Dynamics*. Journal of Chemical Physics, 1983. **79**(11): p. 5360-5367.

14. Brearley, A.M., S.R. Flom, V. Nagarajan, and P.F. Barbara, *Dynamic Solvent Effects on Large-Amplitude Isomerization Rates .2. 2-(2'-Propenyl)Anthracene and (E)-2-(but-2'-En-2'-Yl)Anthracene*. J. Phys. Chem., 1986. **90**(10): p. 2092-2099.

15. Courtney, S.H., S.K. Kim, S. Canonica, and G.R. Fleming, *Rotational Diffusion of Stilbene in Alkane and Alcohol-Solutions*. Journal of the Chemical Society-Faraday Transactions Ii, 1986. **82**: p. 2065-2072.

16. Flom, S.R., V. Nagarajan, and P.F. Barbara, *Dynamic Solvent Effects on Large-Amplitude Isomerization Rates .1. 2-Vinylanthracene*. J. Phys. Chem., 1986. **90**(10): p. 2085-2092.

17. Lee, M., A.J. Bain, P.J. McCarthy, C.H. Han, J.N. Haseltine, A.B. Smith, and R.M. Hochstrasser, *Picosecond Photoisomerization and Rotational Reorientation Dynamics in Solution*. Journal of Chemical Physics, 1986. **85**(8): p. 4341-4347.

18. Gegiou, D., K.A. Muszkat, and E. Fischer, *TEMPERATURE DEPENDENCE OF PHOTOISOMERIZATION .6. VISCOSITY EFFECT*. Journal of the American Chemical Society, 1968. **90**(1): p. 12-&.

19. Ansari, A., C.M. Jones, E.R. Henry, J. Hofrichter, and W.A. Eaton, *The Role of Solvent Viscosity in the Dynamics of Protein Conformational-Changes*. Science, 1992. **256**(5065): p. 1796-1798.

20. Ansari, A., C.M. Jones, E.R. Henry, J. Hofrichter, and W.A. Eaton, *Conformational Relaxation and Ligand-Binding in Myoglobin*. Biochemistry, 1994. **33**(17): p. 5128-5145.

21. Frauenfelder, H. and P.G. Wolynes, *RATE THEORIES AND PUZZLES OF HEMEPROTEIN KINETICS*. Science, 1985. **229**(4711): p. 337-345.

22. Venable, R.M. and R.W. Pastor, *FRICTIONAL MODELS FOR STOCHASTIC SIMULATIONS OF PROTEINS*. Biopolymers, 1988. **27**(6): p. 1001-1014.

23. Honeycutt, J.D. and D. Thirumalai, *THE NATURE OF FOLDED STATES OF GLOBULAR-PROTEINS*. Biopolymers, 1992. **32**(6): p. 695-709.

24. Beece, D., L. Eisenstein, H. Frauenfelder, D. Good, M.C. Marden, L. Reinisch, A.H. Reynolds, L.B. Sorensen, and K.T. Yue, *Solvent Viscosity and Protein Dynamics*. Biochemistry, 1980. **19**(23): p. 5147-5157.

25. Kleinert, T., W. Doster, H. Leyser, W. Petry, V. Schwarz, and M. Settles, *Solvent composition and viscosity effects on the kinetics of CO binding to horse myoglobin*. Biochemistry, 1998. **37**(2): p. 717-733.

26. Bolhuis, P.G., C. Dellago, and D. Chandler, *Reaction coordinates of biomolecular isomerization*. Proceedings of the National Academy of Sciences of the United States of America, 2000. **97**(11): p. 5877-5882.

27. Bullitt, J.G., F.A. Cotton, and T.J. Marks, *STRUCTURAL AND DYNAMIC PROPERTIES OF PENTAHAPTOCYCLOPENTADIENYLMETAL DICARBONYL DIMERS*. Inorg. Chem., 1972. **11**(4): p. 671-&.

28. Gansow, O.A., A.R. Burke, and W.D. Vernon, *C-13 AND PROTON MAGNETIC-RESONANCE EXAMINATION OF SOLUTE STRUCTURES, EQUILIBRIA, AND STRUCTURAL INTERCONVERSIONS IN SOME DINUCLEAR ETA5-DIENYLRUTHENIUM, DIENYLIRON, AND DIENYLNICKEL CARBONYLS*. Journal of the American Chemical Society, 1976. **98**(19): p. 5817-5826.

29. Crim, F.F., *Vibrational state control of bimolecular reactions: Discovering and directing the chemistry*. Accounts of Chemical Research, 1999. **32**(10): p. 877-884.

30. Elles, C.G. and F.F. Crim, *Connecting chemical dynamics in gases and liquids*. Annual Review of Physical Chemistry, 2006. **57**: p. 273-302.

31. Stewart, A.I., I.P. Clark, M. Towrie, S.K. Ibrahim, A.W. Parker, C.J. Pickett, and N.T. Hunt, *Structure and vibrational dynamics of model compounds of the FeFe - hydrogenase enzyme system via ultrafast two-dimensional infrared spectroscopy*. J. Phys. Chem. B, 2008. **112**(32): p. 10023-10032.

32. King, J.T., J.M. Anna, and K.J. Kubarych, *Solvent-hindered intramolecular vibrational redistribution.* Phys. Chem. Chem. Phys., 2011.